



FLUID PROPERTIES AT NANO/MESO SCALE


A Numerical Treatment

Peter Dyson

Rajesh S. Ransing

Paul M. Williams

P. Rhodri Williams

 WILEY

The Wiley Microsystem and Nanotechnology Series | Ronald Pethig, Series Editor

Fluid Properties at Nano/Meso Scale

The Wiley Microsystem and Nanotechnology Series

Editor: Ronald Pethig

Gerlach	Introduction to Microsystem Technology: A Guide for Students	March 2008
Koch, Evans & Brunnschweiler	Microfluidic Technology and Applications	November 2000

Fluid Properties at Nano/Meso Scale: A Numerical Treatment

Peter Dyson

Rajesh S. Ransing

Paul M. Williams

P. Rhodri Williams

*School of Engineering
Swansea University, UK*



A John Wiley and Sons, Ltd, Publication

This edition first published 2008

© 2008 John Wiley & Sons, Ltd

Registered office

John Wiley & Sons Ltd, The Atrium, Southern Gate, Chichester, West Sussex, PO19 8SQ,
United Kingdom

For details of our global editorial offices, for customer services and for information about how to apply for permission to reuse the copyright material in this book please see our website at www.wiley.com.

The right of the author to be identified as the author of this work has been asserted in accordance with the Copyright, Designs and Patents Act 1988.

All rights reserved. No part of this publication may be reproduced, stored in a retrieval system, or transmitted, in any form or by any means, electronic, mechanical, photocopying, recording or otherwise, except as permitted by the UK Copyright, Designs and Patents Act 1988, without the prior permission of the publisher.

Wiley also publishes its books in a variety of electronic formats. Some content that appears in print may not be available in electronic books.

Designations used by companies to distinguish their products are often claimed as trademarks. All brand names and product names used in this book are trade names, service marks, trademarks or registered trademarks of their respective owners. The publisher is not associated with any product or vendor mentioned in this book. This publication is designed to provide accurate and authoritative information in regard to the subject matter covered. It is sold on the understanding that the publisher is not engaged in rendering professional services. If professional advice or other expert assistance is required, the services of a competent professional should be sought.

Library of Congress Cataloging-in-Publication Data

Fluid properties at nano/Meso scale : a numerical treatment / Rajesh S. Ransing ... [et al].
p. cm.

Includes bibliographical references and index.

ISBN 978-0-470-75124-4 (cloth)

1. Fluid dynamics. 2. Fluid dynamics—Data processing. I. Ransing, R. S.

QA911.F5645 2008

620.1'06—dc22

2008024095

A catalogue record for this book is available from the British Library.

ISBN: 978-0-470-75124-4

Set in 10/12pt Times by Aptara Inc., New Dehli, India

Printed in Singapore by Markono

Contents

Biographies	ix
Series Preface	xi
Preface	xiii
Symbols and Abbreviations	xvii
1 The Nature of Fluid Flow	1
1.1 Introduction	1
1.2 Basics of fluid motion	1
1.2.1 Continuum/bulk properties	3
1.2.2 Continuum approximations	8
1.2.3 Continuum scale simulation	11
1.3 Molecular mechanics	16
1.3.1 Molecular properties	16
1.3.2 Molecular simulations	18
1.4 Types of simulation	20
1.4.1 Monte Carlo simulation	22
1.4.2 Molecular dynamics	25
1.4.3 Introduction to the physics of MD simulations	25
1.4.4 Hard sphere model	32
1.4.5 Soft sphere model	35
1.5 Effects at molecular scale	36
1.5.1 Phase change in confined systems	36
1.5.2 Adsorption/desorption in pores	39
1.6 Summary	43

2 Fluid Physics at Meso Scales	45
2.1 Introduction	45
2.2 Top-down approach for meso scale computation	46
2.2.1 Continuum limit	46
2.2.2 Top-down meso scale methods	50
2.3 Bottom up approach for meso scale computation	55
2.3.1 Molecular dynamics model	55
2.3.2 Boundary conditions	57
2.3.3 Bottom-up meso scale methods	60
2.4 Summary	65
3 Meso Scale Model Based on First Principles	67
3.1 Introduction	67
3.2 Fluid physics model	68
3.2.1 Book keeping	68
3.2.2 Force interactions	70
3.2.3 Time integration scheme	70
3.2.4 Boundary conditions	75
3.2.5 Modified boundary potential	80
3.3 Extracting local bulk properties	81
3.3.1 Approximation method	82
3.3.2 Bin averaging	82
3.3.3 Smooth particle hydrodynamics (SPH)	83
3.3.4 Moving least squares	86
3.3.5 Weight functions	92
3.3.6 Grid structure implementation	94
3.3.7 Sampling	95
3.4 Verification of proposed meso scale model	96
3.5 Summary	102
4 Enhancements to the Meso Scale Model	103
4.1 Introduction	103
4.2 Driving forces	104
4.3 Thermostats	106
4.3.1 Gaussian thermostat	106
4.3.2 Nosé–Hoover	108
4.4 Case studies	110
4.4.1 Sampling	110
4.4.2 Gradient study	119
4.5 Summary	125

5 Modelling Fluid Regimes at Nano/Meso Scales	127
5.1 Introduction	127
5.2 Flow regimes	128
5.2.1 Laminar flow	130
5.2.2 Turbulent flow	132
5.3 Fluid flow characterization from molecular simulation	133
5.3.1 Characteristics of low-speed molecular flow	134
5.3.2 Characteristics of high-speed molecular flow	136
5.3.3 Comparisons and data analysis	137
5.4 Summary	142
6 Performance of Proposed Meso Scale Model	143
6.1 Introduction	143
6.2 Issues in using large numbers of molecules	143
6.2.1 Processing large numbers of molecules	144
6.2.2 Boundary conditions	150
6.2.3 Bulk property extraction	150
6.3 Meso scale simulations	151
6.3.1 Performance of meso scale simulations	155
6.4 Summary	158
7 Experimental Aspects of Fluid Properties at the Nano/Meso Scale	159
7.1 Introduction	159
7.2 Colloidal interactions in nano-fluids	160
7.2.1 Particle-particle interactions	161
7.3 Osmotic phenomena and osmotic pressure	163
7.3.1 Measurement of osmotic pressure	164
7.3.2 Numerical calculation of the osmotic pressure for nano-fluids	170
7.4 Gradient diffusion coefficient	172
7.4.1 Experimental measurement of the gradient diffusion coefficient	173
7.4.2 Experimental data analysis	174
7.4.3 Gradient diffusion coefficient calculation	176
7.5 Viscosity	180
7.5.1 Viscosity experiments	181
7.5.2 Viscosity calculation	184
7.6 Membrane separations	184
7.7 Membrane ultrafiltration models	185
7.7.1 Frontal ultrafiltration model	185
7.7.2 Cross-flow ultrafiltration model	186
7.7.3 Comparison of experimental and theoretical data	189

viii CONTENTS

7.8 Tensile and other rheological properties of liquids on the meso scale	190
7.8.1 Metastability and cavitation phenomena	190
7.8.2 Experimental techniques	194
7.9 Summary	202
8 Future Advancement	203
8.1 Future advancement	203
References	205
Index	215

Biographies

Dr Peter Dyson

Specialist Subjects: Mechanical Engineering, Fluid Systems, Computer Simulation, Mathematical Modelling, Data Analysis and Pattern Recognition

Dr Peter Dyson, MEng, PhD did his first degree at Swansea University, which followed on to his PhD in 'The Numerical Computation of Fluid Systems at Nano-Meso Scale'. This developed into other research positions and he is now Vice President for a Swansea University spin-out company, MetaCause Solutions Ltd, providing advanced data analysis and optimization strategies for industry.

Dr Rajesh S. Ransing

Specialist Subjects: Data Analysis, Machine Learning, Optimization Techniques, Computer Simulation and Mathematical Modelling

Dr Rajesh S. Ransing, BE, ME, PhD is a Senior Lecturer in the School of Engineering and has over fifteen years of experience in numerical methods, optimization techniques and machine learning algorithms to improve quality and productivity in manufacturing processes. He has co-authored over 80 refereed publications and has two pending patent applications in the field of data analysis. He is currently on the Executive Committee of Natural Computing Applications Forum (www.ncaf.org.uk) and has edited many journal issues, conference proceedings and has organized/co-organized many conferences and research symposiums. Dr Ransing is also the CEO of a Swansea University spin-out company, MetaCause Solutions Ltd, that has developed a data analysis software – MetaCause. MetaCause converts production data into process optimization opportunities (www.metacause.com). He was the Regional Winner of the Technium Challenge 2004 Competition and received an award from the Hon Minister Mr

Andrew Davies, Welsh Assembly Government, for MetaCause Solutions Ltd's business plan.

Dr Paul M. Williams

Specialist Subjects: Membrane Separation Processes, Colloid Science, Computer Simulation, Mathematical Modelling

Dr Paul M. Williams, MEng, PhD, works in membrane separation processing and modelling. His first degree was in Chemical Engineering at Nottingham University. He later got his PhD in 'Protein Ultrafiltration, a Colloidal Interaction Approach' at Swansea University where he now works. He is currently the owner of an EPSRC Fellowship (2005–present) looking into the effects of colloidal interactions in bioseparation processes.

Professor P. Rhodri Williams

Specialist Subjects: Non-Newtonian Fluid Mechanics, Rheology, Haemorheology, Rheometry, Process Engineering, Cavitation

Professor P. Rhodri Williams, CEng, CPhys, FInstP, FICHEM, works in rheology and cavitation. For his rheometrical work, conducted under an EPSRC Advanced Fellowship (1990–1995, 1995–1998), he received the British Society of Rheology's Annual Award (1997) and a Royal Society Brian Mercer Award (2007). He is the leading author of over 100 papers. His work has also been supported by NSF (USA), NATO and industry and has consistently received EPSRC's highest assessments. He currently leads an EPSRC Portfolio Partnership in 'Complex Fluids and Complex Flows'.

Series Preface

Books in this series are intended to serve researchers and scientists who wish to keep abreast of advances in the expanding field of nano- and micro-technology, and as a resource for teachers and students of specialized undergraduate and post-graduate courses.

The earlier book *Microfluidic Technology and Applications*, by Michael Koch, Alan Evans and Arthur Brunnschweiler, provided a comprehensive introduction to the theory, modelling and fabrication of fluidic systems whose characteristic dimensions do not get smaller than a micron. The modelling and understanding of the operation of such systems can rely on Navier-Stokes-type equations, that assume conventional continuum laws, without the need to consider localised molecular interactions. Recent advances in fabrication now provide electronic components and fluidic systems in the nanometric scale. Thus, molecular interactions can no longer be ignored in our approach, either by numerical modelling or through the design of suitable experiments, to understand key phenomena such as viscosity, boundary layers, and fluid flow, for example.

In this book Peter Dyson, Rajesh Ransing, Paul Williams and Rhodri Williams take us step by step through the fluidic world bridging the nanoscale, where molecular physics is required as our guide, and the microscale where macro continuum laws operate. The pedagogic treatment is suitable for inclusion in taught Masters Degrees, and the book as a whole should be considered as essential reading for all researchers in Nanotechnology. I know of no other book that covers this material, and of no other authors who could have tackled their task with such clarity and authority.

Ronald Pethig

*Professor of Micro- and Nano-Systems
University of Edinburgh*

Preface

BACKGROUND

Fluid simulation at the nano/meso scale (50 nm–500 nm) presents a current stumbling block for the numerical modelling community. The traditional consideration of fluids assumes that the influence of molecular interactions is negligible, but at nano/meso scales this is not the case. This book aims to tackle this problem by providing the reader with the knowledge necessary to approach fluid simulation at this scale. Techniques and tools are also presented to give a detailed insight into how simulations in this area can be performed successfully. The core problem faced at the meso scale is the multiscale nature of the problem and the tradeoff between molecular and bulk fluid properties and physics. As well as providing the reader with simulation techniques, this book will also illustrate some experimental examples that show where these theoretical methods may be applied.

Current advances in nano and micro technology have allowed engineering to take place at smaller and smaller scales. IBM's research in nanotechnology now allows electronic components to be manufactured with dimensions as small as 29.9 nm, which allows the continuation of 'Moore's law' that has been followed for the last 40 years. Other critical advances include a nano-engineered bio-silicone drug delivery system developed by QinetiQ, which can attack cancers by taking drugs directly to tumour sites. These applications are at the forefront of science today and it is essential to maintain the ability to predict the behaviour of these devices to exploit the technology.

To design such systems successfully requires the ability to simulate complete fluid systems at scales above and below the actual device dimensions, which saves time and experimental costs. However, it is not currently possible with existing simulation methods. Experimental techniques also need to be developed or refined in order to measure properties of interest at this scale.

A wide range of simulation techniques are available, at macro and nano scales, but the scales they tackle contain very different physics models. Unfortunately,

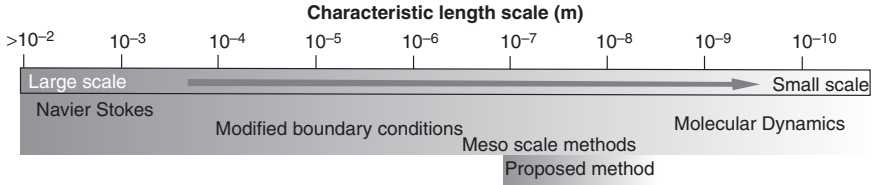


Figure 1 Length scales of simulations, showing the targeted location of the method proposed in this book.

at meso scale dimensions the conventional macro scale continuum simulations become less effective, as they fail to capture all the key physical nano scale interactions. Figure 1 shows the regimes of simulation methods over a range of scales; existing meso scale methods such as lattice Boltzmann (LB) [1] and dissipative particle dynamics (DPD) [2] tackle problems at the high end of the meso scale region. This work focuses on the lower end of the meso scale where molecular physics plays a larger part.

Despite advances in numerical simulation techniques care must be taken not to go too far down the simulation-only road. Experimental measurements and techniques that rely on nano/meso scale properties are required to verify the simulations. Advances in experimental and simulation techniques should be considered in tandem.

All fluid is constructed of molecules under continuous motion and it is the arrangement of these molecules that defines the bulk behaviour of a fluid. For example, a fluid flowing over a solid boundary displays layers of fluid of different velocities at varying distances from the boundary. At a molecular level, the constant molecular interchange between fluid layers causes slower layers to exert a net drag force on faster layers, and vice versa. This causes a velocity profile that can be used to quantify this molecular exchange effect in terms of the macroscopic quantity of viscosity.

At meso scales, fluid displays macro scale effects such as viscosity, laminar and turbulent flow regimes, boundary layers, etc., but at such small scales, the number of molecules and molecular interactions is no longer effectively infinite and the conventional continuum laws are not able to describe them adequately. The continuum laws are unable to include the localized molecular physics that dominates the behaviour of the fluid at this scale.

Even though the conventional continuum laws do not apply in the meso scale regime, modelling engineering problems at these scales require us to quantify the macro scale effects resulting from the molecular interactions as these properties are key to characterizing fluid behaviour in engineering systems. Addressing this challenge forms the kernel of this book, which is to be met by looking at meso scale systems in terms of both bulk and molecular scale physics.

OUTLINE

This book is divided into eight chapters. The following is a synopsis of each.

- *Chapter 1.* A discussion of fluid flow behaviour on scales between the continuum and molecular scale is presented. This chapter presents a background in the continuum view of fluid and how it can be described and modelled at these scales. The discussion then moves to the molecular scale and how fluid at these scales differs from the continuum model. The basic outline of the construction of molecular simulation models is given and conditions when molecular scale effects dominate the behaviour of fluid systems are discussed.

Aim. To provide the reader with basic knowledge on the treatment of fluid at scales above and below the meso scale.
- *Chapter 2.* A review of existing meso scale modelling schemes is presented in two sections, ‘top down’ and ‘bottom up’ approaches. Top-down methods operate by adding molecular information into a continuum simulation, which includes a discussion of the limits and breakdown of the continuum laws. Bottom-up approaches tackle meso scale problems by using molecular physics, which are simplified in regions of low activity.

Aim. By the end of this chapter, the reader should be aware of and understand existing simulation techniques and their advantages/disadvantages when applied to fluid systems at meso scales.
- *Chapter 3.* A meso scale simulation method is developed based on a ‘bottom-up’ approach. This chapter shows the implementation of the molecular model and the upscaling of information to characterize the bulk properties of the fluid system.

Aim. The reader should understand how fluid modelling at the meso scale can be undertaken by employing molecular physics models to characterize bulk properties.
- *Chapter 4.* The developed method is extended to deal with flowing fluids with the implementation of a flow generation method, balanced by additional thermodynamic controls. Case studies are presented in two sections, sampling and gradient studies. The sampling case studies explore the parameters of the bulk property characterization and explain their use. The gradient studies show examples of use with thermally driven and pressure driven flows, validated against published results.

Aim. This chapter explores the limitations of the meso scale approach discussed in the previous chapter. Using these case studies the reader should see the depth of knowledge available from molecular models and how it may be used to characterize fluid systems.
- *Chapter 5.* The developed method is applied to a molecular scale flow through a slit pore to demonstrate the depth of information that this method can

extract from a meso scale molecular model by looking only at the distribution of velocity across the pore. Different flow regimes are examined and shown to exhibit similar behaviour to laminar/turbulent flow.

Aim. The reader should see how a fluid system can be explored using meso scale methods. This chapter also shows some of the current limitations faced by this meso scale approach.

- *Chapter 6.* The developed meso scale method is applied to large scale systems containing between 20 000 and 100 000 molecules. An investigation is also performed to examine the behaviour of the method in terms of performance with large numbers of molecules.

Aim. The reader should understand the computational performance issues faced by molecular physics models at these scales.

- *Chapter 7.* A discussion of various experimental measurements and techniques that depend on fluid flow and properties at the nano/meso scale is presented. These measurements range from macro scale measurements, such as rates of membrane filtration, down to nano scale measurements performed using the atomic force microscope (AFM). Comparison between simulation and experiment is shown for several cases.

Aim. By the end of this chapter the reader should be aware of and understand experimental techniques that can be used to study fluid systems at different scales and should also be aware of how events at the nano/meso scale can affect experimental results at the macro scale.

- *Chapter 8.* This chapter summarizes the approaches considered in this book and the current challenges faced in the meso scale simulation of fluid systems. Some suggestions are given for further work required in the area.

Peter Dyson
Rajesh S. Ransing
Paul M. Williams
P. Rhodri Williams

Symbols and Abbreviations

The following notation will be used unless otherwise stated.

a	Acceleration (m/s^2)
a	Particle radius (m)
a_{hyd}	Hydrodynamic particle radius (m)
A	Area (m^2)
A	Baseline (counts/s)
A_h	Area of a hexagon (m^2)
A_H	Hamaker constant (J)
A_m	Area of membrane surface (m^2)
B	Instrument factor ≤ 1
c	Solute concentration (kg/m^3)
c_o	Feed concentration at the inlet (kg/m^3)
c_w	Solute concentration at the membrane (kg/m^3)
C_b	Solution feed concentration (m^3/m^3)
d	Distance to OHP (m)
d_{eff}	Effective particle diameter (m)
D	Interparticle surface–surface separation (m)
D_{B_o}	Dilute limit Brownian diffusion coefficient (m^2/s)
D_{eff}	Effective diffusion coefficient (m^2/s)
D_m	Gradient (or mutual) diffusion coefficient (m^2/s)
D_{mon}	Monomer diffusion coefficient (m^2/s)
D_s	Self (or tracer) diffusion coefficient (m^2/s)
D_w	Gradient diffusion coefficient at the membrane surface (m^2/s)
e	Elementary charge (C)
E	Energy (J)
E_{KE}	Kinetic energy (J)
E_{PE}	Potential energy (J)
ΔE	Energy cost of forming bubble (J)
f	Tangential momentum accommodation coefficient

xviii SYMBOLS AND ABBREVIATIONS

F	Force (N)
F	Hydrodynamic force (N)
F_{ATT}	London–van der Waals force (N)
F_{ELEC}	Electrostatic force (N)
F_{EXTRA}	Extra interaction force (N)
F_{TOT}	Total force between two particles (N)
g	Gravitational acceleration (m/s^2)
$g_1(\tau)$	Field autocorrelation function
$G_1(\tau)$	Normalized field autocorrelation function
$G_2(\tau)$	Intensity autocorrelation function
h	Half-channel height (m)
h	Smoothing length (m)
h_o	Separation distance (m)
H	Height (m)
$I(t)$	Observed scattered intensity
k	Boltzmann constant (J/K)
k_b	Boltzmann constant (J/K)
K	Spring constant of cantilever (N/m)
$K(\phi)$	Hydrodynamic (or hindered settling) coefficient
K_{HAPP}	Happel's permeability coefficient (m^2)
K_n	The n th cumulant
Kn	Knudsen number
l	Channel length (m)
l	Characteristic length (m)
λ	Mean free path (m)
L_s	Slip length (m)
m	Mass (kg)
n	Number of moles
n^o	Ion number concentration (m^{-3})
n_o	Refractive index of solvent
N	Number of molecules
p	Momentum (kg m/s)
p	Pressure (N/m^2)
p_B	Interior bubble pressure (N/m^2)
p_D	Disjoining pressure (N/m^2)
p_V	Saturated vapour pressure (N/m^2)
P	Pressure (Pa)
P_c	Critical pressure (Pa)
P_{ENT}	Entropic pressure (N/m^2)
Pr	Prandtl number
$P(\Gamma)$	Unknown distribution function of the decay rates
ΔP	Applied pressure (N/m^2)
q	Scattering vector (m^{-1})

Q	Volume flow rate (m^3/s)
r	Centre-to-centre separation distance (m)
r	Radius (m)
r_{ij}	Separation distance between two particles i and j (m)
R	Bubble radius (m)
R	Universal gas constant ($\text{J}/\text{kg K}$)
R_c	Critical bubble radius (m)
R_m	Membrane resistance (m^{-1})
Re	Reynolds number
S	Surface tension (J/m^2)
S_β	Surface area of spherical cell (m^2)
$S(\phi)$	Thermodynamic coefficient (or structure factor)
t	Filtration time (s)
t	Time (s)
T	Temperature (K)
T_c	Critical temperature (K)
u	Axial bulk velocity component in the x direction (m/s)
u	Velocity (m/s)
u_o	Average inlet bulk velocity (m/s)
U	Applied velocity (m/s)
U	Potential energy (J)
U	Relative viscosity (m/s)
$U(r_{ij})$	Molecular potential between nano-particles (J)
v	Speed (m/s)
v	Transverse bulk velocity in the y direction (m/s)
v_{av}	Average or measured permeate flux (m/s)
v_w	Wall permeation velocity (m/s)
\hat{v}	Unit vector
$\langle v \rangle$	Ensemble average
V	Volume (m^3)
V	Volume filtered (m^3)
V_{ATT}	Attractive interaction energy (J)
V_{TOT}	Total interaction energy (J)
$w(r)$	Weighting function
x	Axial direction (m)
x, y, z	Cartesian coordinates
\bar{x}	Average value
$x_{x,y,z}$	Cartesian components
$x_{i,j,k}$	Identifiers
y	Transverse direction (m)
z	Valency of ion
Z	Number of charges on the particle surface

xx SYMBOLS AND ABBREVIATIONS

α	Concentrated disordered dispersion exponent
α	Polynomial constants
β	Boltzmann factor
β	Rejection coefficient
γ	Strain
Γ	Decay rates (h)
ε	Fractional cake voidage at the membrane surface
ε_0	Permittivity of vacuum (C/V m)
ε_r	Dielectric constant of the background solvent
ϵ	Well depth (reduced units, K)
η	Viscosity of the solution (kg/m s)
$[\eta]$	Intrinsic viscosity
η_a	Apparent viscosity of the solvent (kg/m s)
η_p	Viscosity of protein solution (kg/m s)
η_s	Viscosity of the solvent (kg/m s)
θ	Characteristic angle (deg)
θ	Scattering angle (deg)
κ	Debye–Hückel parameter (m^{-1})
λ	Order parameter
λ_o	Wavelength of scattered light (m)
μ	Dynamic viscosity (Pa s)
ν	Dynamic viscosity (Pa s)
ξ	Thermostat parameter
π	Ratio of the circumference to the diameter of a circle
$\pi(\phi)$	Osmotic pressure (N/m^2)
$\Delta\Pi_m$	Osmotic pressure difference across the membrane (N/m^2)
ρ	Density (kg/m^3)
ρ	Density of the solution (kg/m^3)
σ	Collision diameter (nm)
σ	Range of additional repulsion (m)
τ	Molecular frequency scale (ns)
τ	Shear stress (Pa)
τ	Time (s)
ϕ	Volume fraction
ϕ_{eff}	Effective volume fraction
ϕ_{max}	Maximum packing fraction
$\phi_{o/d}$	Order/disorder phase transition volume fraction
ψ_β	Potential at the outer boundary of the cell (V)
ψ_o	Electrostatic potential at the particle surface (V)

1

The Nature of Fluid Flow

Aim. To provide the reader with basic knowledge on the treatment of fluid at scales above and below the meso scale.

1.1 INTRODUCTION

The fundamentals of fluid flow on a wide range of scales are introduced in this chapter. The characterizing properties of a fluid and their relevance at large scales (kilometre to millimetre scale) and small scale (nanometre and angstrom scale) will be discussed. The continuum approach to describing the behaviour of a fluid will be presented along with the methods of simulation at the continuum scale. In contrast, the molecular scale is considered along with fluid structure and simulation methods used at this scale. Examples of the change in physics and fluid behaviour that occur as the scale is reduced are presented, concentrating on the effect of confinement on a fluid.

This chapter highlights the special requirements of meso scale systems. Elements from both the continuum scale and the molecular scale are needed to model and describe a meso scale fluid systemfully.

1.2 BASICS OF FLUID MOTION

The basic characteristic property that defines a fluid is viscosity. Fluid, unlike solids, is unable to offer any permanent resistance to a shearing force. The fluid will continue to deform as long as the force is applied, taking the shape of any solid boundary it touches. The deformation of a fluid occurs from shearing forces

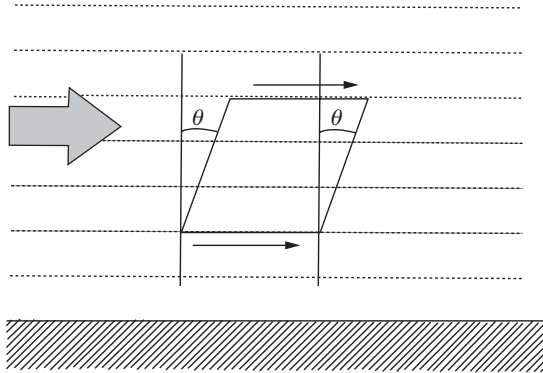


Figure 1.1 Internal shear between fluid layers.

acting tangentially to any solid surface. The fluid can be considered as layers parallel to a surface, which slide over each other, as shown in Figure 1.1. Each fluid layer applies a shear force to the next, and is in turn sheared by those it touches.

The ability to deform continuously under an applied force makes fluids behave differently from solids. Solid bodies are capable of maintaining an unsupported shape and structure, and can resist finite shear.

Fluids themselves fall into two categories, liquids and gases. To a fluid dynamist, who is interested in flows at the macro scale, there are two characterizing differences between them:

- Liquids have densities an order of magnitude larger than gases.
- Liquids and gases respond very differently to changes in pressure and temperature.

Gases can also be expanded and compressed more easily than liquids due to the lower density and spacing between molecules. The motion of all fluids relies on the interaction and internal shear between fluid layers, but the actual interaction between layers occurs from collisions between many molecules on the molecular scale ($\sim 10^{-9}$ m). In fact, all fluid effects and properties occur from molecular interactions, but at the macro scale ($\sim 10^{-4}$ m) the detailed molecular physics of this behaviour can be neglected as the number of molecules within the characteristic length can be considered as sufficiently large. At these scales the fluid can be viewed as having physical properties corresponding to the statistical averages of the underlying molecules and are known as continuum or bulk properties. Molecular physics, manifested in a continuum framework, has the ability to be defined as continuous functions of time and space.

1.2.1 Continuum/Bulk Properties

Bulk or continuum properties such as velocity, density and pressure remain constant at a point and changes due to molecular motion are assumed to be negligible. These properties are also assumed to vary smoothly from point to point with no jumps or discontinuities. This assumption is correct as long as the characteristic distance of the system is of an order of magnitude greater than the distance between molecules.

This assumption of bulk physical properties allows the behaviour of fluid systems to be approximated by a set of deterministic equations that represent the underlying infinite chaotic molecular motion on a much larger scales. The definition and basis of these bulk properties will be of significant importance in later discussions, so it is necessary to explain the origin of some of these bulk properties to clarify concepts.

1.2.1.1 Density

The density of a fluid is defined as the mass contained within a unit volume. It is computed as a function of mass (m) and volume (V) of a sample as follows:

$$\rho = \frac{m}{V}. \quad (1.1)$$

This expression of density is represented in terms of mass per unit volume (kg/m^3). Other expressions of density used are specific weight (weight per unit volume, N/m^3), relative density (relative to another density, *dimensionless*) and specific volume (reciprocal of density, m^3/kg). Density can also be computed from molecular properties, in terms of sample volume, V , containing N molecules of individual mass, m_{molecule} [3]:

$$\rho = \frac{Nm_{\text{molecule}}}{V}. \quad (1.2)$$

This expression also has units of kg/m^3 and can be defined from $N = 1$ to $N = \infty$.

1.2.1.2 Temperature

The temperature (T) at any point in a fluid is derived from the internal kinetic energy of the underlying N molecules, each with velocity, v_i , and mass, m [4]:

$$E_{\text{KE}} = \sum_{i=1}^N \frac{1}{2}mv_i^2. \quad (1.3)$$

4 THE NATURE OF FLUID FLOW

At continuum or bulk scales the number of molecules is assumed to be infinite, but the distribution of the velocity of this (almost) infinite number of molecules can be assumed to follow the Boltzmann distribution, which in one dimension appears as

$$f(v) = \sqrt{\frac{m}{2\pi k_b T}} e^{-mv^2/2k_b T}, \quad (1.4)$$

where k_b is the Boltzmann constant. This distribution can then be used to calculate the average squared velocity in the system to relate the velocity distribution to the kinetic energy,

$$\langle v^2 \rangle = \sqrt{\frac{m}{2\pi k_b T}} \int_{-\infty}^{\infty} v^2 e^{-mv^2/2k_b T} dv, \quad (1.5)$$

which gives

$$\langle v^2 \rangle = \sqrt{\frac{m}{2\pi k_b T}} \frac{\sqrt{\pi}}{2} \left(\frac{2k_b T}{m} \right)^{3/2} = \frac{k_b T}{m}. \quad (1.6)$$

The equation for the translational kinetic energy of the molecules can now be related to the temperature of the system in one dimension:

$$E_{KE} = \frac{1}{2} m \langle v^2 \rangle = \frac{k_b T}{2}. \quad (1.7)$$

For three dimensions, this simply becomes

$$\frac{1}{2} m \langle v^2 \rangle = \frac{3}{2} N k_b T, \quad (1.8)$$

which describes the temperature of a local system of N molecules. In terms of bulk properties, where locally $N \rightarrow \infty$, the temperature is considered constant and varies smoothly from over the whole domain.

1.2.1.3 Pressure

The pressure is explained by kinetic theory as arising from the force exerted by colliding gas molecules on to the walls of the container [5]. To explain the mechanics of pressure, consider a single molecule with velocity, v , along the x direction contained within two walls perpendicular to its direction of travel and separated by length, l , as shown in Figure 1.2.

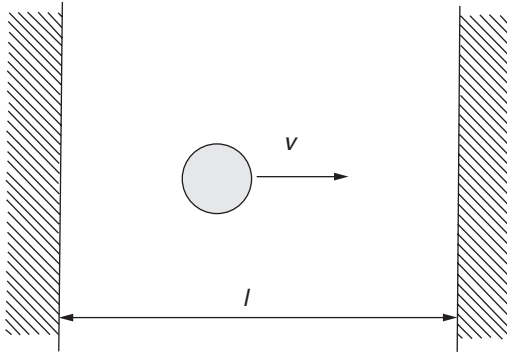


Figure 1.2 Single molecules oscillating between two walls.

By considering the collision between the molecule and one of the walls, the momentum lost by the molecule and the wall is

$$\Delta p = p_{\text{initial}} - p_{\text{final}} = mv_x - (-mv_x) = 2mv_x. \quad (1.9)$$

The time between successive collisions on this particular wall will be

$$\Delta t = 2 \frac{l}{v_x} \quad (1.10)$$

Force is the rate of change of momentum, so the force on the wall from the single molecule is

$$F = \frac{\Delta p}{\Delta t} = \frac{2mv_x}{2l/v_x} = \frac{mv_x^2}{l}. \quad (1.11)$$

For a large number (j) of molecules and collisions with the wall, this becomes

$$F = \frac{m \sum_j v_{jx}^2}{l}. \quad (1.12)$$

Now, by adding in collisions with walls in all six directions this gives

$$F = 2 \frac{m}{l} \sum_j (v_{jx}^2 + v_{jy}^2 + v_{jz}^2). \quad (1.13)$$

For equilibrium conditions and a sufficiently high collision rate with the walls, the force on all six walls can be assumed to be the same. Therefore the force on a

single wall becomes

$$F = \frac{1}{6} \left(2 \frac{m \sum_j v_j^2}{l} \right) = \frac{m \sum_j v_j^2}{3l}, \quad (1.14)$$

where v_j is the velocity of molecule j in three dimensions. It is now possible to talk in terms of the average velocity of the molecules, $(1/N) \sum_j v_j^2$, which can be represented by \bar{v}^2 :

$$F = \frac{Nm\bar{v}^2}{3l}. \quad (1.15)$$

This can then be divided by the area, A , of the wall to give the pressure

$$P = \frac{F}{A} = \frac{Nm\bar{v}^2}{3lA}. \quad (1.16)$$

The cross-sectional area multiplied by length yields a volume, $Al = V$, which when combined with Equation (1.2) yields

$$P = \frac{1}{3} \rho \bar{v}^2, \quad (1.17)$$

thereby describing pressure as a function of density and kinetic energy of molecules, which, as shown in Equation (1.8), is in turn directly related to the temperature of the system. As with temperature, at continuum scales the number of molecules tends to infinity, and any fluctuations or statistical differences become approximately zero. In this case both pressure and temperature may be considered as constant at any point in the fluid domain.

1.2.1.4 Viscosity

Viscosity quantifies the resistance put up by a fluid undergoing finite shearing forces and can commonly be perceived as internal fluid friction, or resistance to pouring. This effect occurs from the drag forces occurring between adjacent fluid layers moving with different velocities. The concept of viscosity is best demonstrated by example.

Figure 1.3 shows a fluid trapped between two parallel plates separated by distance H . The top plate moves with constant velocity U and the bottom plate is at rest. The fluid in between them adheres to both plates, so that the fluid layers at each of the plates has the same velocity at the plate. The velocity of the fluid changes linearly in this case, so the velocity at any point between the plates can

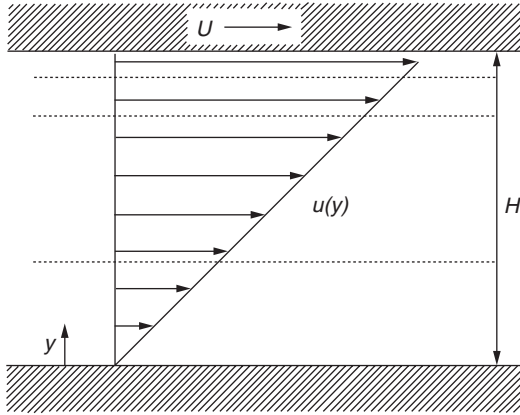


Figure 1.3 Viscous flow between parallel plates; the bottom plate is at rest and the top plate moves with velocity U .

be computed as follows:

$$u(y) = \frac{y}{H}U. \quad (1.18)$$

It is known from experiments that, for Newtonian fluids, the frictional force per unit area, τ , is proportional to the difference in velocity between the two plates and inversely proportional to the separation, H . Together, this is interpreted as the frictional force being proportional to the velocity gradient, du/dy ,

$$\tau = \mu \frac{du}{dy}, \quad (1.19)$$

with the proportionality factor being the fluid parameter μ , which characterizes the drag between fluid layers and is known as the dynamic viscosity. This is known as Newton's law of viscosity, where a linear relationship between velocity gradient and shear stress is assumed. While this is valid for most simple fluids such as water and most gases, non-Newtonian fluids such as plastics and pseudo plastics exhibit a more complex relationship and Newton's law does not apply.

To obtain the coefficient of viscosity, μ , for a Newtonian fluid, the situation shown above in Figure 1.3 is used. The coefficient is then extracted by comparing the applied U and the drag force on the opposite plate, τ .

The concept of kinematic viscosity is described in fluid systems where frictional and inertial forces interact. It is defined as the ratio of dynamic viscosity,

μ , to the fluid density, ρ ,

$$v = \frac{\mu}{\rho}, \quad (1.20)$$

Causes of viscosity Viscous effects occur due to internal friction between fluid layers, and it is important to consider the nature and cause of this drag. The molecules in a fluid are continuously moving and have little, if any, structure. Consequently, they are in constant molecular exchange between fluid layers. This exchange occurs via two mechanisms, the transfer of mass, by a fluid molecule physically crossing between fluid layers, and the transfer of energy via interlayer collisions/potential energy interactions.

This constant exchange occurring over a sufficiently large number of collisions causes energy and momentum to propagate smoothly throughout the fluid at a rate governed by the physical properties of the molecular interactions and the conditions of the fluid. However, the condition of the fluid in terms of pressure and temperature causes different effects in liquids and gases.

Viscosity of gases In a gas, the molecules are widely spaced and interact relatively little, so an increase in temperature increases the kinetic energy of the molecules and viscosity increases as a result of increased mass transfer between layers. According to the kinetic theory of gases [5], the viscosity is proportional to the square root of the absolute temperature. This, however, is an exact solution to an approximate model while in reality, the rate of increase of viscosity is much higher [3]. In gases, viscosity is found to be independent over the normal range of pressures, with the exception of extremely high pressure.

Viscosity in liquids In liquids, which have much higher densities, the distance between molecules is much shorter and the cohesive/attractive forces between them increase the viscous effect. The response to an increase in temperature, and hence kinetic energy, decreases the effect of these cohesive forces, which reduces the viscosity. However, the increased molecular interchange between fluid layers increases the viscosity [3]. The net result is that liquids show a reduction in viscosity for an increase in temperature.

Due to the close packing of the molecules in a liquid, high pressures also affect the viscosity. At high pressures, the energy required for the relative movement of a molecule is increased, causing an increase in viscosity.

1.2.2 Continuum Approximations

At distances above the micro scale, approximately $\geq 10^{-6}$ m, the number of molecules in the system can be in the order of millions! In these cases, the number of molecular interactions occurring over length and time scales is also huge. Because of this, it can be considered acceptable to assume that the influence

of any individual molecular exchange/interaction is negligible as the number of molecules in any volume tends to infinity. The continuum assumption considers an infinite number of molecules in a domain and neglects their individual contributions. The interpretation of continuum is given as:

Continuum. A continuous thing, quantity, or substance; a continuous series of elements passing into each other [6].

If a fluid is considered as a continuum, then each part is considered as identical (i.e. the fluid is homogenous) to the next and infinitely divisible, and the molecular structure of the fluid is ignored. This means that the fluid is assumed to have the same properties even if the domain dimensions are 100 nm, 1 mm or 1 km.

By making the continuum assumption, molecular scale effects are neglected and the bulk properties are defined by the physical observable relationships between them. These properties can then be used to characterize fluid flows, as done in experiments by Reynolds [7] whose number, the Reynolds number, presents a criteria for dynamic similitude.

$$Re = \frac{\rho u L}{\mu}. \quad (1.21)$$

The Reynolds number is the ratio of inertial (u/ρ) to viscous (μ/L) forces, where L is the characteristic dimension of a flow with speed u . This can be used both to determine kinematic and dynamic similitude for comparing scale models to real applications and also to characterize the point of transition between laminar and turbulent flow (critical Reynolds number).

A large Reynolds number indicates that the inertial forces dominate the system, with a low viscosity causing the small scales of fluid motion to be relatively undamped. A low Reynolds number flow, however, has high viscous forces, which damp out small scale motion.

The Reynolds number represents simple characterization of the behaviour of a fluid system. To look more in depth at the measure and description of fluid behaviour, a set of continuum governing equations is used. However, before these are considered it is important to set out the rules for the fluid mechanics interpretation of a continuum, which are known as the continuum assumptions/approximations.

1.2.2.1 Continuum approximations

- *Infinitely Divisible.* The characteristic length of the fluid should be several orders of magnitude larger than molecular diameters, such that the number of molecules in the system is large enough to be considered as approximately infinite. By assuming an infinite number of molecules, the fluid is considered homogenous at all scales, and can be divided up/decomposed into an infinite number of identical sections. If the fluid is considered in terms of a finite

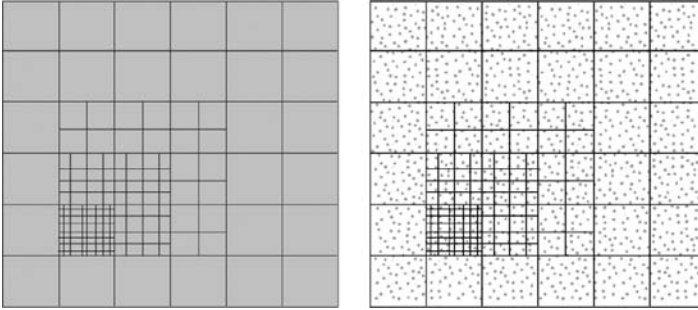


Figure 1.4 Left: continuous and infinitely divisible. Right: finite number of molecules, mass and energy localized and not continuously distributed.

number of molecules, when it is divided up even in a finite number of sections, some will contain mass (a molecule) and energy and some will not (Figure 1.4).

- *Thermodynamic Equilibrium.* To maintain the assumption of continuum mater with an infinite number of molecules, there must also be an approximately infinite number of intermolecular interactions occurring over length and time scales in the system. This means that there is a continuous propagation of energy throughout the system. Discontinuities cannot occur as the fluid is continuous (infinitely divisible) and an infinite number of infinitely small intermolecular energy exchanges smooth out and propagate fluid properties and energy through the system.

This is also essential to maintain the linear relationship between the stress and strain rate and the heat flux and temperature gradient. The thermodynamic equilibrium condition also states that there are sufficient interactions or collisions to smooth out any statistical variations occurring from the molecular scale (Figure 1.5).

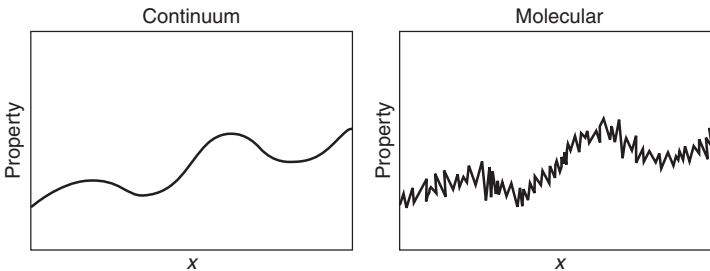


Figure 1.5 Statistical variations in properties arising from a finite number of molecules in the system,

If these conditions are met, the fluid system can be considered as a continuum. This is an important classification, as it means the flow can be approximated using continuum laws.

The continuum laws can be applied in both simple analytical form, as in the Bernoulli equation (inviscid flows),

$$\frac{P}{\rho} + \frac{v^2}{2} + gh = \text{constant}, \quad (1.22)$$

or for more complex situations that require numerical solution. For cases such as simple pipe flows, the Bernoulli equation can be of use where little information is required. However, in complex systems or geometries, a more detailed analysis and interrogation is required. In this case, fluid behaviour can be simulated using a set of conservative governing equations solved numerically. These simulations, based on the continuum assumptions and continuum scale observations and laws, provide a detailed and accurate model of fluid behaviour, where experiments are difficult or expensive, or a greater amount of information is needed.

1.2.3 Continuum Scale Simulation

Both simple and complex fluid systems can be investigated, within the limits of the continuum assumptions, by sets of governing differential equations that describe fluid behaviour. The mathematical solution of these equations throughout a fluid domain is known as *computational fluid dynamics* (CFD). The governing equations describe the mathematical representation of a physical model that is derived from experimental flow measurements and observations. These representative equations are then replaced with an equivalent numerical description, which is solved using numerical techniques for the dependent variables of velocity, density, pressure and temperature. One of the most widely used sets of governing equations are the Navier–Stokes equations.

1.2.3.1 Navier–Stokes governing equations

The Navier–Stokes equations are a set of governing equations that describe the behaviour of fluids in terms of continuous functions of space and time. They state that changes of momentum in the fluid are based on the product of the change in pressure and internal viscous dissipation forces acting internally. The scheme works by not considering instantaneous values of the dependent variables, but their flux, which in mathematical terms is interpreted as the derivative of the variables. The equation set is separated into three conservation laws for mass, energy and momentum.

Mass The conservation of mass, known as the continuity equation, is obtained by considering the mass flux into and out of any elemental control volume within the flow field. In the Cartesian coordinate system, x , y , z , fluid velocities along those directions are u , v , w respectively. The continuity equation then becomes

$$\frac{\delta\rho}{\delta t} + \frac{\delta(\rho u)}{\delta x} + \frac{\delta(\rho v)}{\delta y} + \frac{\delta(\rho w)}{\delta z} = 0. \quad (1.23)$$

The first term accounts for any change in density over time, while the rest of the terms describe the change in density in the x , y and z directions.

Energy The expression for the conservation of energy in a fluid system is

$$\begin{aligned} & \frac{\delta(\rho e)}{\delta t} + \frac{\delta(\rho ue)}{\delta x} + \frac{\delta(\rho ve)}{\delta y} + \frac{\delta(\rho we)}{\delta z} \\ &= \rho Q + \frac{\delta}{\delta x} \left(k \frac{\delta T}{\delta x} \right) + \frac{\delta}{\delta y} \left(k \frac{\delta T}{\delta y} \right) + \frac{\delta}{\delta z} \left(k \frac{\delta T}{\delta z} \right) \\ & - P \left(\frac{\delta u}{\delta x} + \frac{\delta v}{\delta y} + \frac{\delta w}{\delta z} \right) - \varphi \left(\frac{\delta u}{\delta x} + \frac{\delta v}{\delta y} + \frac{\delta w}{\delta z} \right)^2 \\ & + \mu \left\{ 2 \left[\left(\frac{\delta u}{\delta x} \right)^2 + \left(\frac{\delta v}{\delta y} \right)^2 + \left(\frac{\delta w}{\delta z} \right)^2 \right] \right. \\ & \left. + \left(\frac{\delta v}{\delta x} + \frac{\delta u}{\delta y} \right)^2 + \left(\frac{\delta w}{\delta y} + \frac{\delta v}{\delta z} \right)^2 + \left(\frac{\delta u}{\delta z} + \frac{\delta w}{\delta x} \right)^2 \right\}, \quad (1.24) \end{aligned}$$

where φ is the bulk viscosity, Q is the heat added per unit mass, k is the thermal conductivity and e is the internal energy

Momentum The conservation of momentum equations are as follows:

$$\begin{aligned} & \frac{\delta(\rho u)}{\delta t} + \frac{\delta(\rho u^2)}{\delta x} + \frac{\delta(\rho uv)}{\delta y} + \frac{\delta(\rho uw)}{\delta z} \\ &= \rho X - \frac{P}{x} + \frac{\delta}{\delta x} \left\{ \mu \left[2 \frac{\delta u}{\delta x} - \frac{2}{3} \left(\frac{\delta u}{\delta x} + \frac{\delta v}{\delta y} + \frac{\delta w}{\delta z} \right) \right] \right\} \\ & + \frac{\delta}{\delta y} \left[\mu \left(\frac{\delta u}{\delta y} \frac{\delta v}{\delta x} \right) \right] + \frac{\delta}{\delta z} \left[\mu \left(\frac{\delta w}{\delta x} \frac{\delta u}{\delta z} \right) \right], \quad (1.25) \end{aligned}$$

$$\begin{aligned}
 & \frac{\delta(\rho v)}{\delta t} + \frac{\delta(\rho v u)}{\delta x} + \frac{\delta(\rho v^2)}{\delta y} + \frac{\delta(\rho v w)}{\delta z} \\
 &= \rho Y - \frac{P}{y} + \frac{\delta}{\delta y} \left\{ \mu \left[2 \frac{\delta v}{\delta y} - \frac{2}{3} \left(\frac{\delta u}{\delta x} + \frac{\delta v}{\delta y} + \frac{\delta w}{\delta z} \right) \right] \right\} \\
 &+ \frac{\delta}{\delta z} \left[\mu \left(\frac{\delta v}{\delta z} \frac{\delta w}{\delta y} \right) \right] + \frac{\delta}{\delta x} \left[\mu \left(\frac{\delta u}{\delta y} \frac{\delta v}{\delta x} \right) \right], \quad (1.26)
 \end{aligned}$$

$$\begin{aligned}
 & \frac{\delta(\rho w)}{\delta t} + \frac{\delta(\rho w u)}{\delta x} + \frac{\delta(\rho w v)}{\delta y} + \frac{\delta(\rho w^2)}{\delta z} \\
 &= \rho Z - \frac{P}{z} + \frac{\delta}{\delta z} \left\{ \mu \left[2 \frac{\delta w}{\delta z} - \frac{2}{3} \left(\frac{\delta u}{\delta x} + \frac{\delta v}{\delta y} + \frac{\delta w}{\delta z} \right) \right] \right\} \\
 &+ \frac{\delta}{\delta x} \left[\mu \left(\frac{\delta w}{\delta x} \frac{\delta u}{\delta z} \right) \right] + \frac{\delta}{\delta y} \left[\mu \left(\frac{\delta v}{\delta z} \frac{\delta w}{\delta y} \right) \right], \quad (1.27)
 \end{aligned}$$

where X , Y and Z are components of body force.

Equations (1.23) to (1.27) represent the Navier–Stokes set of conservation equations used to compute fluid properties numerically. For these properties to be used to simulate a fluid system, they need to be localized at discrete points within the flow domain before they are solved using a numerical scheme.

1.2.3.2 Solving continuum equations

There are a number of schemes for solving the fluid conservation equations in a simulation environment, such as the finite difference, finite volume, finite element, boundary element, etc. However, the three most developed and widely used of the bunch will be considered: the finite difference method, the finite element method and the finite volume method.

Finite difference method (FDM) The finite difference method is a simple and efficient method for solving the continuum governing differential equations. Instead of derivatives being computed over infinitesimal elements, increments of finite width are used as an approximation. There are three varieties of finite difference, the forward, backward and central difference, which are highlighted in Figure 1.6 and are calculated as follows for parameter p at point P:

Forward difference:

$$\left(\frac{\partial p}{\partial y} \right)_{i,j} = \frac{p_{i,j+1} - p_{i,j}}{h} \quad (1.28)$$

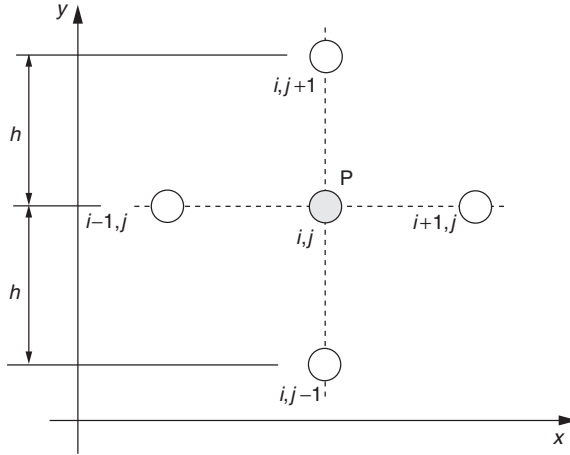


Figure 1.6 Illustrating the finite difference method calculations at point P.

Backward difference:

$$\left(\frac{\partial p}{\partial y}\right)_{i,j} = \frac{p_{i,j} - p_{i,j-1}}{h} \quad (1.29)$$

Central difference:

$$\left(\frac{\partial p}{\partial y}\right)_{i,j} = \frac{p_{i,j+1} - p_{i,j-1}}{2h} \quad (1.30)$$

Using this method the partial differential equations can be replaced with simple algebraic equations that can be solved either iteratively or by matrix inversion. This can be implemented for fluid flow simulations to yield the values of the flow variables at discrete points in the flow field. Due to the structures of the FDM, problems are limited to ones with simple boundaries where a structured mesh can be used. For more complex problems, the finite element method allows for more versatility but is much more complex.

Finite element method (FEM) The aim of the finite element method is to determine the values of the dependent variables of the conservative flow equations. The FEM achieves this by dividing the flow domain into a finite number of cells or elements, each containing a small portion of the continuous fluid. At points placed at the corners or sides of these elements, points that are known as nodes, the governing equations are evaluated (see Figure 1.7). Instead of working with the differential equations directly, the FEM uses these nodes to discretize and evaluate the governing equations in an integral form using weighting functions.

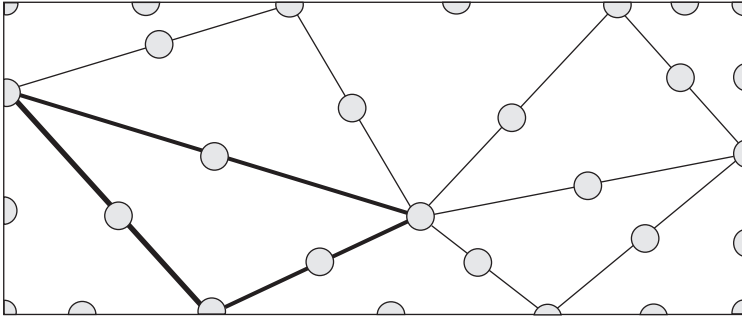


Figure 1.7 Governing equations evaluated at nodes surrounding fluid elements.

Finite volume method (FVM) Similar to the finite element method, the FVM discretizes the flow domain into elemental control volumes surrounding a node. Flow parameters are then treated as fluxes between control volumes, and conservation is maintained in each element. This allows for better treatment of flows with discontinuities such as shock waves.

1.2.3.3 Advantages

Continuum simulations are able to provide an accurate model for fluid behaviour in a wide range of applications and systems. The division of the flow field into discrete elements allows complex geometries to be simulated, and smaller elements can be used to refine the solution in areas of high gradients or where a greater accuracy is needed.

By approximating the fluid as a continuum and ignoring the underlying molecular behaviour, a great deal of computational effort is saved and accuracy has been proved to be sufficient in many applications. The molecular information can be approximated at these scales, as the molecular motion cancels out, yielding only bulk properties at this scale.

Continuum simulations also have the flexibility to prescribe a wide variety of boundary conditions capable of replicating almost any system, while still maintaining global conservation laws.

1.2.3.4 Limitations

Continuum mechanics, however, has its drawbacks. It is dependent on the generation of the mesh of elements and nodes it uses in the approximation. The generation of these meshes can be almost as time consuming and challenging as the actual simulation. These meshes can also have a significant effect on the solution,

either through resolution or the distribution of nodes, and must be generated with consideration for the system of interest.

The scale of the system is also limited by the continuum approximations. Because of the continuum approximations, the matter of interest must be uniform throughout and infinitely divisible. This removes the ability to deal with discrete objects, such as, at the top of the scale, extreme planetary systems and, at the lower end, molecules. As the continuum governing equations are approximate relationships which are approximated in their solution, careful validation and testing must also be performed, which is true of any simulation method. Particular care must also be taken close to the continuum limit.

The breakdown of these approximations in the meso scale region between the continuum and molecular scales was studied in detail and the transition from continuum to molecular scale effects is explained in depth in later sections.

1.3 MOLECULAR MECHANICS

At very small scales ($\leq 10^{-8}$), the mechanics of fluid take on an entirely different form. The continuum approximations and laws are not valid as the number of molecules in the system is of the order of tens to thousands. At this scale the molecular interactions dominate the physics of the fluid, and it is debatable whether fluid is an accurate description as it is better described as a molecular flow.

1.3.1 Molecular Properties

The properties at a molecular scale ($\sim 10^{-9}$) are very different from those considered at the bulk/continuum scale. At this scale, the characteristic length of the flow is comparable to the diameters of individual molecules. There is no concept of bulk properties, and fluid-like motion is in the form of the motion of individual molecules. The fluid is now not continuous, as the molecular centres represent discontinuities in both density and energy.

The molecular chemistry of the making or breaking of bonds or changes to the internal structure of molecules is not considered in this research, although it is important to understand the mechanisms by which molecules interact in a chemically stable fluid.

A molecule is formed of an aggregate of two or more atoms bonded together by special bonding forces. The examination of interactions between bonded molecules was first undertaken by a Dutch chemist, Johannes Diderik van der Waals, whose studies into noble gases led to the characterization of the forces between molecules [8]. The van der Waals force was originally considered to

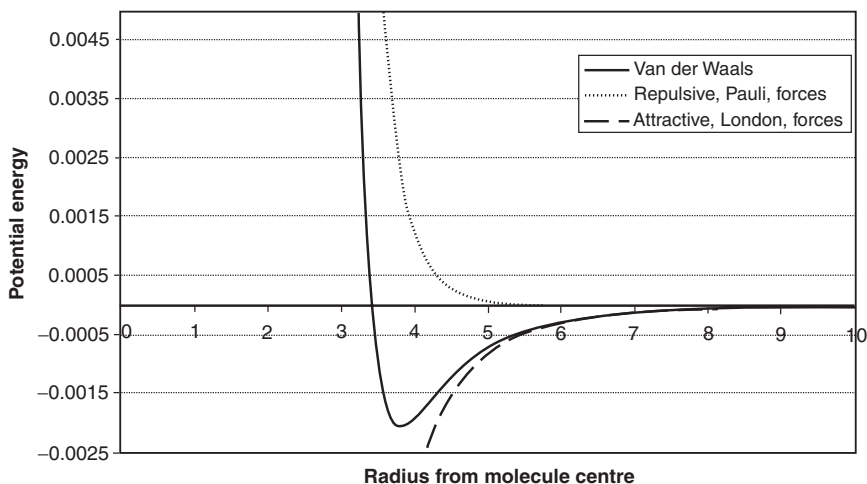


Figure 1.8 Van der Waals potential, as the sum of attractive, London, and repulsive, Pauli, forces.

describe the force between all molecules,

$$U(r) = \frac{Ae^{br}}{r} - \frac{C_6}{r^6}, \quad (1.31)$$

where A , b and C_6 are characterizing parameters for the molecules and r is the distance from the molecule centre. However, it is now mainly used to describe the polarization of molecules into dipoles.

The interaction forces are characterized in two parts, a long-range attractive force, C_6/r^6 , and a short-range but strongly repulsive force, Ae^{br}/r , as shown in Figure 1.8.

The repulsive forces, or London forces [9], named after the physicist Fritz London, represent the weak forces that occur between transient dipoles/ multipoles. This occurs from an uneven distribution of electrons surrounding the nucleus of the molecule, creating a temporary multipole.

The electron density in a molecule's electron cloud varies due to the finite number of electrons orbiting the atom, but the variation of density in the cloud created hotspots of high charge, creating a temporary multipole that attracts hotspots of opposite charge on other molecules. A molecule with a temporary multipole can also attract/repel electrons from neighbouring molecules, thereby propagating the multipole effect. These short-term multipoles produce the net affect of a weak attractive force between neutral molecules such as nitrogen, methane and many others. The London forces are higher for larger molecules with more dispersed electron clouds.

The attractive part of the potential comes from the strong short-range repulsive forces between two overlaps between negatively charged electron clouds, based on the Pauli principle [10]. The Pauli principle states that as the clouds of electrons of the two interacting particles intersect, the energy increases dramatically.

The behaviour of a molecular system is defined by the properties of a system of molecules. However, the individual properties of molecules can be combined together to describe the state, or global, properties of the system or region. An analogy can be found with the macro scale ideal gas equation of state, which relates the pressure, P , volume, V , and temperature, T , of an ideal gas of n moles:

$$PV = nRT. \quad (1.32)$$

The van der Waals equation of state [11] describes a similar relationship for the molecular system,

$$P = \frac{RT}{V - b} - \frac{a}{v^2}nRT = \left(P + a\frac{n^2}{V^2}\right)(V - nb), \quad (1.33)$$

where n is the number of moles and the gas law is corrected for the internal volume of the molecules using correction factor b and adjusted with parameter a , which characterizes the cohesion/attraction between molecules. Parameters a and b can also be obtained from the critical properties of the fluid [12]:

$$a = \frac{27R^2T_c^2}{64P_c}, \quad (1.34)$$

$$b = \frac{RT_c}{8P_c}. \quad (1.35)$$

The equation of state approaches the ideal gas law as these correction factors approach zero. This allows the description of the fluid to be made in terms of the state of the fluid, rather than as a large number of chaotic molecules. The van der Waals equation is best suited to low-temperature and pressure systems, but there are other equations of state that can be applied to other situations, e.g. Lennard–Jones equation, Clausius equation, etc.

1.3.2 Molecular Simulations

Molecular simulations play a vital role in science today by providing a framework on which to investigate theories and solutions in a relatively low-risk and low-cost environment. At the molecular scale, investigations and experiments are very costly to perform, and in some situations it is not possible with current technology. Because of this, molecular simulations are often thought of as blurring the line

between experiment and simulation, as they can be used to investigate theories that otherwise could not be tested.

Molecular simulation is the study of material/fluid by considering the individual interactions of atoms or molecules, and will be described in detail in Chapter 2. General simulation schemes involve representative molecules interacting with some sort of boundary and each other to achieve a change in position and momentum. There are many different forms of simulation methods and techniques that can be applied to many different situations, each offering different advantages. The basic mechanism behind almost all molecular simulations is relatively basic, relying on a system of particles that represent atoms or molecules that interact using Newton's law,

$$F = ma, \quad (1.36)$$

where the force acting on a particle, F , is equal to its mass, m , multiplied by its acceleration, a . The force acting on any one of the many particles in the system is determined by the movement of those around it. There are two branches of molecular simulation, stochastic and deterministic. The deterministic approach is in the form of a molecular dynamic (MD) simulation, where the outcome could theoretically be worked out. Stochastic methods, such as the Monte Carlo simulation method, have an element of unpredictability and chance and the result cannot be exactly calculated in advance; these will be discussed in more detail later. Despite the deterministic approach of standard molecular dynamics, it remains a statistical mechanics method, as system property values are developed from ensemble averages over the system.

Molecular simulations rely on representative molecules interacting with each other, so each molecule must possess individual properties that determine how it will move in the next time step; these are position, r , and momentum, p , applied in the number of dimensions present in the simulation. It is from these properties that interactions and collisions are found and evaluated, thus allowing the simulation to proceed. Given that the state of the whole system is governed by a function of the properties of all the individual particles, the concept of 'phase space' can be introduced. At any time in the simulation, the state of the system can be defined by a single point in a $6N$ -dimensional 'phase space', where N is the number of particles in a three-dimensional system. Each three-dimensional particle contains information about its momentum (p_x , p_y , p_z) and position (x , y , z) in each of the three dimensions, so for N particles there are $6N$ variables. As the simulation progresses, the phase point will move throughout phase space, sampling more of the regions accessible without violating any of the rules set at the start of the simulation, such as constant energy, pressure or temperature.

In the following sections the basics behind simulations of molecular systems will be described, before proceeding to a description of how it applies to real fluid flow problems and situations.

1.4 TYPES OF SIMULATION

The above sections have described the general form of molecular simulations used to explore the constant energy surface of a system. However, the simulation so far can describe the positions and momentum of the molecules in the system. These properties are useful within the simulation, but cannot be compared with a real situation because such information is not available. Available system properties such as temperature, entropy, pressure, etc., are the result of the motion of many particles and not properties of individual molecules. Such bulk properties are extracted from the simulation data with the use of statistical mechanics, by averaging the properties of a large number of molecules over a specified period of time.

This method of property evaluation relies on Boltzmann's ergodic hypothesis [4]. The hypothesis assumes a quantum description of the system of particles and for any system there are i different possible energy states conforming to a constant energy E (proportional to the system volume). Over a sufficiently long period of time the hypothesis assumes that the phase space trajectory will sample almost all of these energy state configurations resulting in an average value, known as the ensemble average and considered to be representative of the system (over all state configurations, see Figure 1.9). The ergodic hypothesis therefore states that over a sufficient period of time, the ensemble average is equal to the statistical average obtained by simulation. This is a reasonable assumption for most cases, but it does not apply when considering meta-stable phases or glasses.

The ergodic hypothesis leads to the construction of many different conservation laws that can be applied to simulate different properties and situations. These groups sample different ensemble averages and conserve different properties in molecular simulations, the most common of which are listed below:

- *Microcanonical Ensemble (NVE)*. a constant number of particles, volume and energy. It is also common to control the temperature of the simulation during the equilibrium stage so that the target system temperature is reached within a

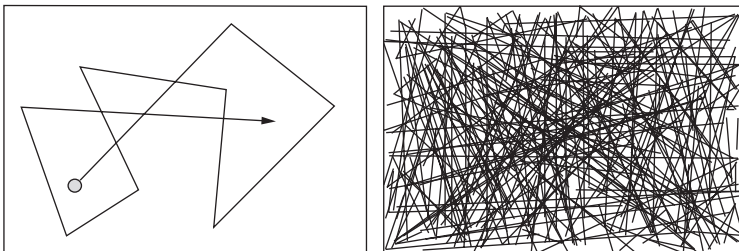


Figure 1.9 Left: poor phase space sampling. Right: excellent phase space sampling, resulting in excellent ensemble averages of bulk properties.

suitable number of time steps. The simplest form of temperature control is to scale the velocities periodically, but this is not a truly isothermal method and must be removed before the properties are collected.

Although energy is considered to be conserved, there will be slight fluctuations and the possibility of a small drift due to truncation and rounding errors from the calculations.

This type of ensemble is useful for predicting thermodynamic response functions.

- *Canonical Ensemble (NVT)*. a constant number of particles, volume and temperature. As in the microcanonical ensemble, during the initialization stage the velocities are scaled to the desired value for the set temperature. Although useful for initialization, velocity scaling is not suitable to use as a control for a simulation as it is crude and not a truly isothermal method. Therefore, other thermostatic methods must be used to apply the temperature control, which will be explained in detail in Chapter 3. This ensemble is used to perform conformational (spatial arrangements of a molecule) searches of models evaluated in a vacuum without periodic boundary conditions. Even when periodic boundary conditions are used, this ensemble can be useful if pressure is not a significant factor, as the constant temperature and volume provides less perturbation due to the absence of pressure coupling.
- *Isobaric–Isothermal Ensemble (NPT and NST)*.
 - NPT: a constant number of particles, pressure and temperature. Temperature is controlled using one of the thermostatic schemes detailed in Chapter 3 and the pressure is controlled by varying the volume of the system using the Berendsen, Anderson or the Parrinello–Rahman schemes [13]. The Berendsen and Anderson schemes work by varying the size of the system, while the Parrinello–Rahman scheme is also capable of varying the shape of the system.
 - NST: a constant number of particles, stress and temperature. This is an extension to the constant pressure ensemble, which adds extra control on the stress components xx , yy , zz , xy , yz and zx .

Both methods are mainly used in structural applications. NST can be used to evaluate stress/strain relationships and NPT is generally used when the correct pressure, volume and temperature are important.
- *NPH and NSH*.
 - NPH: a constant number of particles, pressure and enthalpy. This ensemble is similar to the NVT ensemble, only the size on the cell is allowed to vary.

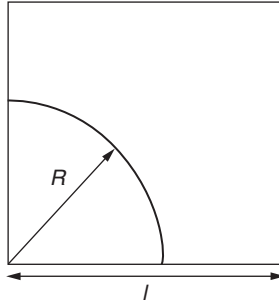


Figure 1.10 Monte Carlo integration.

- NSH: a constant number of particles, stress and enthalpy. The control of the stress of the system implies the use of one of the variable volume schemes, of which the Parrinello–Rahman scheme is used to vary the size and shape. This ensemble can only be used in fully three-dimensional periodic systems. In both ensembles, enthalpy, h , is conserved but it is also common, as with many of these methods, to use temperature scaling in the initialization and equilibration stages to stabilize the system. NPH and NSH are commonly used to investigate natural response functions such as specific heat (at constant temperature), thermal expansion, adiabatic compressibility and adiabatic compliance tensors.
- *Grand Canonical Ensemble* (μVT). Simulations with constant chemical potential μ , volume and temperature are used widely to investigate capillary phenomena and other chemically driven effects.

These ensembles are used within statistical mechanics, both for stochastic and deterministic approaches, to investigate different environments and systems. The Monte Carlo molecular simulation method represents the stochastic approach, which incorporates an element of randomness in the molecular model.

1.4.1 Monte Carlo Simulation

The Monte Carlo simulation method is a powerful tool for integrating complex equations using a relatively simple probability theory [14]. This is best illustrated by a simple example, where the value of π is calculated using a brute force approach to Monte Carlo integration. To approach this problem, first consider an arc with radius R , within a square domain of side l , as shown in Figure 1.10. The domain is probed using a number of test points, randomly distributed over the area, as shown in Figure 1.11

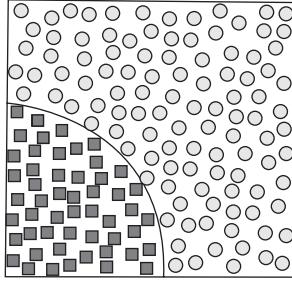


Figure 1.11 Monte Carlo integration; domain is interrogated by random points, some of which lie within the arc.

The area inside the arc is then estimated by the ratio of the number of points inside its constraints (squares) and the total number of points (squares + circles):

$$\frac{\text{Squares}}{\text{Circles} + \text{squares}} = \frac{\text{area of arc}}{\text{area of square}}, \quad (1.37)$$

which becomes

$$\text{Area of arc} = \frac{\text{Number of squares}}{\text{Number of circles} + \text{number of squares}} \times \text{area of square}. \quad (1.38)$$

The equation for the area of an arc is known as πR^2 , so this becomes

$$\frac{\pi R^2}{4} = \frac{\text{squares}}{\text{circles} + \text{squares}} \times l^2. \quad (1.39)$$

Rearranging for π gives

$$\pi = \frac{\text{squares}}{\text{circles} + \text{squares}} \frac{4l^2}{R^2}. \quad (1.40)$$

Equation (1.40) relates the ratio of particles within the arc to the value of π . The accuracy of the estimation is mainly dependent on the number of points used to probe the domain. This approach is known as the brute force approach, and is the less sophisticated form of Monte Carlo integration, where there is an equal probability for a sample point to be taken from anywhere within the domain.

Monte Carlo simulation uses elements from this technique to move the molecules in the system in the following way:

1. A molecule is selected at random from the system.
2. The molecule is then moved a random distance in a random direction.

3. The resulting change in potential energy of the whole system is then evaluated and if it is reduced, the move is accepted.
4. Some failed moves are also accepted according to a probability value, P . Completely rejected moves are ignored.

The distance a particle is moved is often scaled to alter the acceptance ratio of moves making the simulation more efficient.

When applied to molecular simulation there is a need to improve computational efficiency by making certain approximations for solving equations on relatively inactive regions. It is at this point that importance sampling techniques are introduced into the Monte Carlo method, as described by Metropolis *et al.* [15].

The Metropolis Monte Carlo method biases the contribution of each move to the statistical average based on the Boltzmann factor. The probability of a particle being selected is also influenced by the Boltzmann factor as follows:

1. The overall system energy is calculated, E_i .
2. From the system, one molecule is picked out. The probability of selection for each particle is determined by the probability parameter A .
3. The molecule is assigned a small perturbation, such as a small displacement in position, and the new system energy is calculated, E_j .
4. If the new system energy is smaller than the old system energy, accept the addition of the perturbation.
5. If the new system energy is greater than the old system energy, accept the perturbation with probability $B = e^{-E_j - E_i/k_b T}$ (note that $\beta = e^{-E/k_b T}$ is the Boltzmann factor).
6. Repeat steps 1 to 5.

This gives the probability value that an added perturbation will be accepted as A multiplied by B . Allowing a small proportion of moves that increase the system energy to be accepted provides a limited amount of protection against settling in meta-stable configurations on quasi-equilibrium states. By doing this, the system is pushed towards the configuration that is most likely to occur, thus speeding up the simulation run time.

Another modified form of the Monte Carlo technique is the force biased method [16]. This adds some extra calculation overheads into each molecule evaluation to determine the resultant force acting on the particle by its neighbours, biasing the random move performed within the simulation. This also improves the computational efficiency as statistical averages need to sample fewer configurations.

Additional information on the Monte Carlo simulation method and its different ensembles can be found in the book by Gould *et al.* [17]. Gould provides examples of Monte Carlo methods, focusing on its advantages at simulating phase changes, which has been used to good effect by Levesque *et al.* [18] applied to hydrogen storage in carbon nanotubes.

1.4.2 Molecular Dynamics

Molecular dynamic (MD) simulations model fluid in two ways, with molecules being represented as hard or soft spheres. Modelling with hard sphere models provides a relatively simple approach to approximating a system of molecules but still has valid applications, such as looking into the liquid–gas phase transition and diffusion, and hard sphere fluids have a well-defined critical point. The drawbacks are mainly to do with the discontinuous nature of the model. The collisions are performed instantaneously and spheres only interact repulsively, whereas real systems have some form of attraction between particles. Because of this, it is also used for gas simulations where the distances between molecules are far greater than their diameter, and intermolecular interactions occur rarely. Despite these disadvantages, the model is still widely and successfully used, but care must be taken to ensure that it is appropriate to the situation being simulated.

A more realistic, but more complex and computationally demanding approach, is the soft sphere model. In this model, the long-range attractive and repulsive forces are modelled as a continuous function of the separation between pairs of molecules. The use of a continuous interaction function improves the accuracy of the simulation at the cost of increasing the computational load.

1.4.3 Introduction to the Physics of MD Simulations

Molecular dynamic simulations work on the same basic principles regardless of the actual interaction laws (hard or soft spheres) and rely on the following three steps: initialization, equilibrium and production. These stages are detailed below following the example of a molecular scale cubic cell suspended in a fluid away from any physical boundaries, as shown in Figure 1.12.

1.4.3.1 Initialization

When the simulation is run, the first task performed is to define the problem; this is known as initialization. This stage of the simulation accounts for only one time step and is used to create the system of spheres based on a set of user-defined parameters. In the example used, a control volume suspended in a fluid of set volume and density is simulated (Figure 1.12). The initialization stage is where

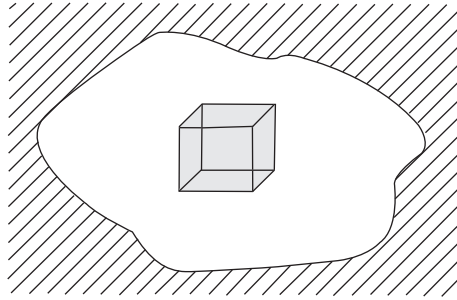


Figure 1.12 Control volume of fluid suspended away from any solid boundaries.

the dimensions of the considered volume of the system are defined and representative molecules are placed within. Therefore a method is needed to position N spheres within the system. If the spheres were to be randomly assigned positions, there is a quite high probability that some of them may overlap, creating extremely high interaction forces, disrupting the system with unnatural forces. It is therefore more practical to assign positions based on a lattice or crystal structure.

However, this creates a problem, as fluid molecules do not conform to a static lattice, but move constantly within the domain. This means that the fluid molecules need to break out of the initial lattice structure and find a natural, randomized, equilibrium position. A degree of randomization is added to the molecules to allow them to break out of this structure. This can either be done by adding a degree of randomization to the initial molecular positions or to assign random initial velocities. Randomized positions, however, are generally used for very large systems to reduce the simulation time taken to settle into a random ‘cloud’. By assigning random initial velocities to the molecules it is also possible to control the initial temperature of the system by assigning velocities based on the Boltzmann velocity distribution (Equation (1.4)).

Once all of the initial positions and velocities for all of the spheres have been defined, the forces on each of the atoms must be evaluated, giving the overall force on the particle. The force calculations are used to perform changes to the dynamics of the particles in the system, but these changes are performed within the time loops of the simulation. There are two time loops within the simulation, one in the equilibrium stage and one in the production stage.

1.4.3.2 Equilibration

The simulation time allotted to the equilibrium period immediately follows the initialization stage. This provides a buffering/settling time for the particles to mix

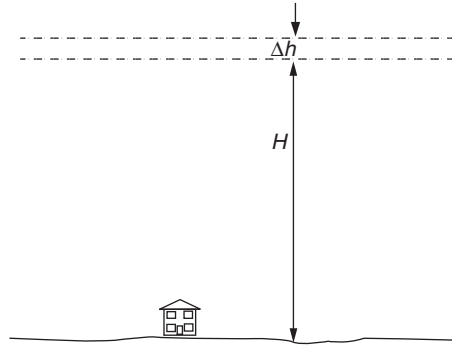


Figure 1.13 Boltzmann factor derived from an elemental change in height in the atmosphere.

themselves up and reach a maintainable equilibrium state that is sufficiently randomized. Once a stable, but randomized, situation is reached, the production stage can proceed, which provides all the useful information about the run.

While the simulation is proceeding, there needs to be some way to measure how well randomized the simulation has become and whether or not an equilibrium state has been reached.

Monitoring Initially, the positions and velocities of all the molecules in the system are defined, both of which need to be relaxed before the production phase can take place. To ensure this has been completed, there needs to be ways of detecting the state of the simulation. The state of the dynamics of the particles are measured against the Maxwell–Boltzmann velocity distribution, while the breakdown of the positions is evaluated using the order parameter (see below).

The Maxwell–Boltzmann velocity distribution is strongly linked to the Boltzmann factor, derived from the kinetic theory of gases. By looking at a small change in height of the atmosphere, and relating the pressure to kinetic theory, the Boltzmann factor is derived from the change in pressure and can be found as shown in Figure 1.13.

Boltzmann distribution The force exerted on the boundary of a fluid is described as n , the number density (number of molecules divided by volume) multiplied by the volume and the weight of each molecule (force due to momentum exchange at collision at the boundary)

$$F = mgAn\Delta h. \quad (1.41)$$

Therefore pressure becomes

$$\Delta P = -\frac{F}{A} = -\frac{mgAn\Delta h}{A}, \quad (1.42)$$

$$\Delta P = -mgn\Delta h. \quad (1.43)$$

The ideal gas law can be rearranged for n :

$$Pv = Nk_bT, \quad n = \frac{N}{V} = \frac{P}{k_bT}, \quad (1.44)$$

which when substituted into the expression for ΔP gives

$$\Delta P = -\frac{mg\Delta h}{k_bT}P. \quad (1.45)$$

Thus, for $h \rightarrow 0$,

$$\int \frac{1}{P} dP = -\frac{mg}{k_bT} \int dh \quad (1.46)$$

gives

$$P = P_0 e^{-mgh/k_bT}, \quad (1.47)$$

where e^{-mgh/k_bT} is known as the Boltzmann factor. This form of the Boltzmann factor has been derived from potential energy, and as potential energy, can be written as mgh , the factor can be rewritten as

$$\beta = e^{-E_{PE}/k_bT}, \quad (1.48)$$

where E is the energy. A similar derivation can be performed using kinetic energy, resulting in a Boltzmann factor of

$$\beta = e^{-E_{KE}/k_bT}. \quad (1.49)$$

This describes the probability that a molecule is at a certain energy level for a prescribed temperature, T . By normalizing probability values so they add to a unit value, the Boltzmann factor can be evaluated over a range of speeds to obtain the Maxwell–Boltzmann distribution for speeds. Where speed $v = \sqrt{v_x^2 + v_y^2 + v_z^2}$,

$$f(v) = 4\pi \left(\frac{m}{2\pi RT} \right)^{2/3} v^2 e^{-mv^2/(2RT)}. \quad (1.50)$$

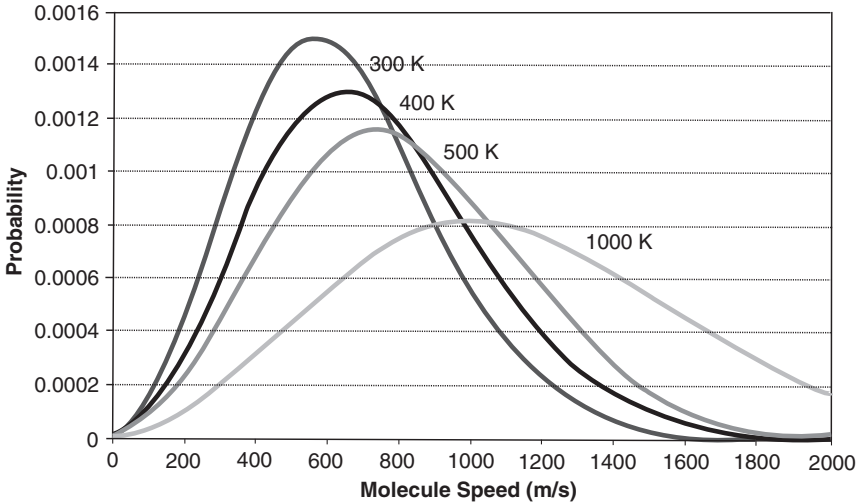


Figure 1.14 Maxwell distribution of velocity for temperatures of 300 K, 400 K, 500 K and 1000 K.

This velocity–probability distribution (Figure 1.14) can therefore be used to assess the dynamics of a simulation, by comparing the distribution of the resultant velocity of molecules with this distribution. This is an important test, as even for systems at steady state, as the velocity of individual particles does not remain constant, they are constantly interacting and colliding with each other. It is sensible to consider the overall distribution of velocities within the system to get a view of how the system is behaving and how it is approaching equilibrium.

By monitoring the distribution of velocities and its resemblance to the Maxwell–Boltzmann distribution, a measure of the approach to equilibrium is developed. It is then used to identify stability in the simulation. If the simulation is not stable, the temperature would fluctuate and the system would not be in equilibrium. It is therefore necessary to observe the development of the distribution over a period of time, ensuring that it converges with minimal oscillations. The graphs in Figure 1.14 show examples of the distribution at different temperatures.

The variations arise from statistical noise that occurs due to the finite number of molecules in the simulation. The greater the number of molecules, the lower is the noise in the extracted distribution. For an infinite number of molecules, the distribution would be followed perfectly, going the possibility of a continuum description.

Other measured thermodynamic properties, such as pressure and density, are also sensitive to the state of the system. By looking at these properties and seeing how they behave is another tool in the identification of equilibrium and smooth running of the simulation. Properties are averaged over a period of time and need

time to adjust themselves to the correct, stable value. If some instabilities are present and the properties are not converging, the system cannot be in a steady state.

The stability of a property does not just imply that the value remains approximately constant, but it should also be able to recover its value after a small amount of perturbation, such as a temperature adjustment.

The order parameter The order parameter gives an indication of the randomization of the positions of the particles within the system. There are many formulations of this parameter relating to different initial structures, but only an example of a face centred cubic (f.c.c.) lattice is considered here.

First, the system of particles is broken down and the three Cartesian coordinates are considered independently. The form of the order parameter must be such that it is possible to detect when a particle is on or near an original lattice site.

The form of such a function is described for a single particle as

$$\lambda_i = \cos\left(\frac{4\pi x_i}{a}\right), \quad (1.51)$$

where a is the spacing between lattice sites and x_i is the position of molecule i . By summing this over all particles the average value can be calculated for all molecules, for each of the three directions:

$$\begin{aligned} \lambda_x &= \frac{1}{N} \sum_{i=1}^N \cos\left(\frac{4\pi x_i}{a}\right), & \lambda_y &= \frac{1}{N} \sum_{i=1}^N \cos\left(\frac{4\pi y_i}{a}\right), \\ \lambda_z &= \frac{1}{N} \sum_{i=1}^N \cos\left(\frac{4\pi z_i}{a}\right). \end{aligned} \quad (1.52)$$

The overall value can then be calculated from the three directional components:

$$\lambda = \frac{1}{3} (\lambda_x + \lambda_y + \lambda_z). \quad (1.53)$$

This is the order parameter for the system. After the initialization of the simulation, the order parameter can be used to confirm that the lattice has been constructed correctly; if $\lambda = 1$, all lattice sites are occupied. During the run the particles move from their initial position, which alters their individual order parameter to a value between -1 and 1 (Figure 1.15). For a fully randomized simulation, the parameter should be approximately zero, indicating an even distribution of

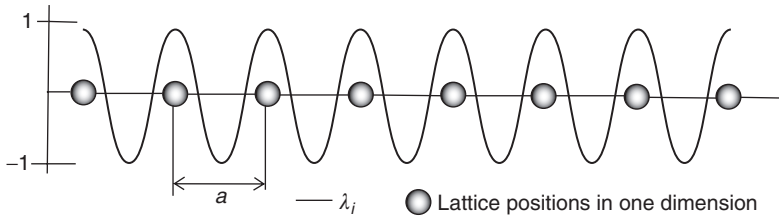


Figure 1.15 Order parameter relative to lattice positions.

particles between the bounds of the simulation. The order parameter can also be used to determine the point of solidification and the quality of the lattice, as used by Radhakrishnan and Gubbins [19].

A successfully equilibrated system should be sufficiently randomized and have reached a stable equilibrium point from which the production phase can begin. The stable point should have the same global properties regardless of the initial positions of the molecules, and can be tested by applying random noise to the positions of the molecular lattice and examining several equilibration phases. A fully equilibrated system will have the following properties:

- Stable levels of kinetic, potential and total energy. Variations in energy levels are to be expected, but there should be no drift in average values of energy.
- The order parameter should be zero, indicating that the molecules are sufficiently randomized.
- Velocities of all molecules should conform to velocity distributions for the set temperature for the system.
- Stable state which is independent of initial positions of molecules.

Although the above criteria help identify equilibrium, there is still a chance for undetected instabilities to be present, so care must be taken to be certain that a steady state has been reached. After sufficient randomization, the production phase of the simulation can begin.

1.4.3.3 Production

After the successful randomization of the system of molecules, the production phase can take place. This is basically an extension of the equilibrium phase to calculate the properties of the stable system over a set period of time. As the system is assumed to be sufficiently equilibrated, some of the controlling factors and adjustments are removed to allow the simulation to progress freely. Although the

controls are removed, the parameters such as the order parameter and velocity distribution are still monitored to check for anomalies. At the end of the equilibration phase, all property averages are reset to zero so that when the production phase starts, the properties are not affected by the approach to equilibrium and are the result of the production phase only.

This is the stage of the simulation where the interrogation and investigation of the system may start. There are two main types of dynamic models used in simulation to describe molecular dynamics, hard sphere and soft sphere. They differ in the way they handle interactions between particles. The hard sphere model considers interactions as binary collisions, whereas the soft sphere approach considers the molecules to be continually interacting via long-range potential functions with their neighbours.

1.4.4 Hard sphere model

Hard sphere simulations only interact by colliding with one another and exchanging linear momentum in a perfectly elastic way. The forces present in the hard sphere model are relatively simple and easy to calculate. As there are no long-range interactions, spheres only interact when they are colliding. The hard sphere models are generally event driven, where the simulation time only steps forward to the next event, or collision. This is based on the assumption that all spheres have an initial position and velocity, and that sphere travels along the same direction at a constant speed (as there is no acceleration), such that the position at any time can be calculated as follows [4]:

$$r_i(t) = r_i(t_0) + (t - t_0)v_i(t_0) \quad (1.54)$$

where r_i and v_i are the position (of the centre of the sphere) and velocity of particle i , t_0 is the start time and t is the new time. As all molecules move in this way the time until two spheres overlap, i.e. when a collision occurs, can be predicted, highlighting the deterministic nature of the molecular dynamics approach.

At any collision between two spheres, each with diameter σ , the distance between the centres will be σ . Therefore a collision occurs between two molecules with position at time t , of $r_1(t)$ and $r_2(t)$, when

$$|r_1(t) - r_2(t)| = \sigma, \quad (1.55)$$

which can be calculated as

$$[r_1(t) - r_2(t)]^2 = \sigma^2. \quad (1.56)$$

At this time, t , a collision is occurring and in a simulation of N molecules the molecules that are colliding next need to be determined. By substituting Equation 1.54 for r_1 and r_2 in Equation (1.56) and rearranging for t , the time at which the two spheres will collide is given as

$$t_c = t_0 + \frac{(-v_{12}r_{12}) \pm \sqrt{(v_{12}r_{12})^2 - v_{12}(r_{12}^2 - \sigma^2)}}{v_{12}^2}, \quad (1.57)$$

where

$$v_{12} = (t_c - t_0)v_1 - (t_c - t_0)v_2, \quad (1.58)$$

$$r_{12} = r_1(t) - r_2(t). \quad (1.59)$$

This gives the collision time, t_c , for two spheres providing they are moving towards each other. Therefore, before t_c is calculated, the state of the collision for the colliding pair must be determined.

For example, take molecule 1 from the simulation and consider the possibility that it may collide with molecule 37. There are two basic possibilities, either they are moving towards each other or away. Mathematically, this is described by the projection of the velocity difference along the line of the centres of the spheres by finding the product of v_{12} and r_{12} . If the result is less than zero, the spheres are moving together:

$$v_{12}r_{12} < 0. \quad (1.60)$$

If the spheres satisfy this condition, they are said to be moving towards each other, but this does not guarantee a collision. To determine if they will collide we need to consider the limiting case where they come in contact as they pass each other.

By considering the one sphere to be fixed and the other to have velocity equal to the velocity difference, Figure 1.16 shows the limiting case for collision. It can be seen that, there must be a limiting value of θ that, if exceeded, ensure no collisions occur and the spheres pass each other [4].

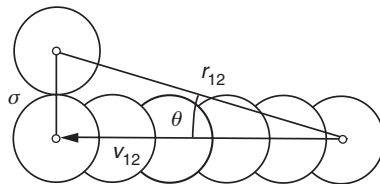


Figure 1.16 Hard sphere collision detection.

This collision test is evaluated for every possible colliding pair within the system by looping over all molecules and calculating the next collision time for each. From these times, a table of collision times is created containing predictions for when each sphere will have its next collision. The calculation of this table is the last step in the initialization stage.

The table can then be used and updated in the equilibrium and production stages to advance the simulation and evaluate the next collision.

Collisions are modelled as binary interactions, occurring instantaneously, where the molecules exchange linear momentum.

1.4.4.1 Time steps

The first task in the time step loop is to look at the table of predicted collision times and find which collision will occur next. The first collision to happen is the only reliable prediction as the collisions afterwards may occur in a different order. The simulation is then progressed by advancing to the time of this collision and moving all spheres using

$$r(t + \Delta t) = r(t) + v(t)\Delta t. \quad (1.61)$$

The new position for each sphere, $r(t + \Delta t)$, is calculated from the old position, $r(t)$, by adding the distance travelled at constant velocity, $v(t)$, during Δt . When all spheres have been moved, the two that are colliding will be in contact and the momentum exchange can take place. As the masses of the spheres are the same, the mass terms can be cancelled out of the momentum equation completely, leaving just an exchange of velocity. The velocities of the two spheres are projected along the line of their centres, as in the two-dimensional example in Figure 1.17. At the collision, the component of velocity along the line connecting the two

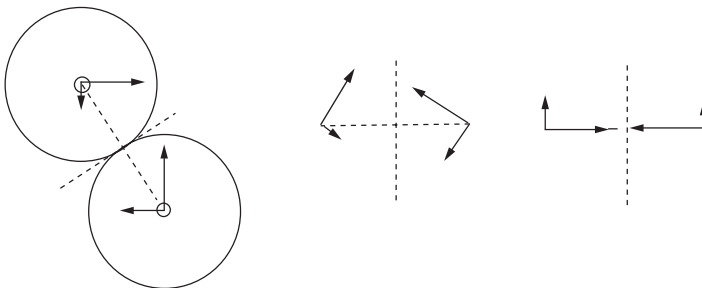


Figure 1.17 Hard sphere collision evaluation. Momentum is transformed from physical coordinates along the line between the centres of the molecules, along which they exchange momentum.

centres is exchanged, while the component of velocity perpendicular to this line remains the same for both spheres. The velocities of both spheres are updated and can be used to update the prediction table for the next collision time for the pair. There is no need to update the table for all the molecules, as only the colliding pair experience a change in velocity. The updated tables can then be used to predict the time step to the next collision.

1.4.5 Soft sphere model

The soft sphere model of molecular interactions considers molecules to interact by exerting a force on each other relative to the distance between them. These interactions occur continually, with each molecule having a 'zone' in which any other molecule present is influenced. Hard spheres will only interact when contact is made.

The initialization stage starts as stated above, where the initial positions and velocities have been defined for all molecules in the system. Force calculation for soft sphere models is more complex due to the addition of long-range interactions. Particles in the system continually attract and repel their neighbours through a predefined potential function, as opposed to the instantaneous and perfectly elastic collisions of the binary collisions described above.

This is best described with the use of Figure 1.18, where the centre particle is interacting with particles within a set radius, R_C . The most common potential used is the Lennard–Jones 12-6 potential, which provides an approximation of the attractive and repulsive forces experienced by nonbonded molecules.

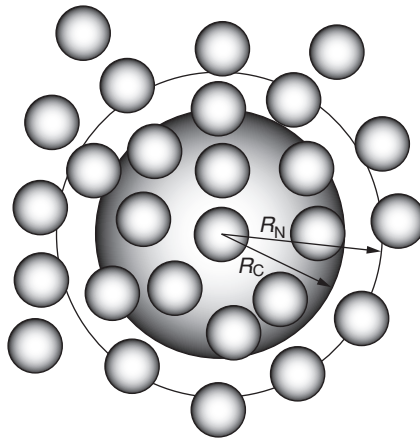


Figure 1.18 Soft sphere interaction detection.

The potential functions are continuous and become weaker as the distance between molecules increases, so it is therefore convenient to set a limit to the ‘zone of influence’ (typically around 2 to 3 times the interaction radius of the molecules) of any one molecule (outside which the potential is approximately zero). This finite limit cuts off the weak, long-range interactions between far-off particles, interactions that can be approximated by ‘long-range correction factors’ [4] to increase the efficiency of the simulation. Despite this streamlining, the process of finding a particle neighbour is time consuming and there needs to be an effective method of storing the lists of neighbouring particles for each sphere.

Soft sphere molecular dynamics provides an accurate model for molecular scale fluids and is generally used for dense fluids, where the cohesive part of the intermolecular interaction plays a more important role. Travis and Gubbins [20] and Tuzun *et al.* [21] show good examples of general molecular simulations. Other applications include chemical gradient driven flows [22] and studies of pore roughness [23] on flow parameters.

1.5 EFFECTS AT MOLECULAR SCALE

In this section, the effect of scale on the mechanics of a fluid at molecular scale are discussed along with the different mechanisms that are present which cannot be modelled on a continuum scale. The most obvious effects are present in highly porous media, where there is a high mix of fluid and solid molecules.

1.5.1 Phase Change in Confined Systems

The process of changing phases is in some cases modelled relatively well with hard spheres, but with soft sphere models when thawing, the melting temperature is often overestimated by up to 30 % [24]. The melting temperature is the point at which solid and liquid can coexist, but for there to be liquid present, there needs to be a section within the simulation domain where the structure starts to break down (nucleation of the new phase). At any phase change a good indication is a jump in the caloric curve relating to the adsorption of latent heat.

If the system properties come close to the temperature and pressure of the phase boundary, the dynamics of the system can change quite substantially, and this needs to be taken into consideration. The change between liquid and gas is not as drastic as the change between liquid and solid, where the molecules fall into or out of a structured formation. As the temperature of the molecules is lowered, molecules possess less energy and do not interact with each other as strongly, and consequently they move less and less. The kinetic energy of the particles then reaches a point where, for a given density, they are kept in the same position by

all the other particles. At this point, the particles do not possess enough energy to break out of their position, due to the proximity of other molecules. During a phase change, energy is absorbed or discharged in the form of latent heat at constant temperature; this is the extra amount of energy needed by the molecules to break out of the lattice and start moving around the container.

Phase change is a well-understood mechanism, but the molecules behave slightly differently when the solid/fluid is confined. Simulations of hard sphere fluids confined between hard walls were found to exhibit quasi-one-dimensional motion near the wall [25], where the molecules near the walls were pushed up against the container and could only move approximately parallel to the wall. This effectively creates different phase behaviour parallel and perpendicular to the boundary. The compressibility factor parallel and perpendicular was measured using the radial free space distribution function (RFSDF) within a Monte Carlo simulation of hard spheres [26]. The study showed that as the distance between the plates was reduced from a separation to sphere diameter ratio of 21 to 3, the difference between the compressibility factors was increased between the parallel and perpendicular directions (with respect to the wall). This indicates that there is also a difference in pressure between the two components.

The RFSDF has components from both the compressibility factor and the order parameter, so by looking at the order parameter the phase of the fluid can be determined as a function of distance from the wall. Molecules away from the walls are still in the liquid phase and are free to move, but molecules closer to the wall are trapped between a nonmoving boundary and the moving particles colliding against them.

The quasi-one-dimensional motion combined with the difference in pressure results in the phenomena of anisotropic phases, where close to the wall molecules are in the solid phase perpendicular to the wall and in the liquid phase parallel to the wall. Taking this quasi-one-dimensional theory one step further, and constraining a fluid within a cylindrical pore only two molecular diameters wide (between centres of molecules within the wall), freezing of the fluid is not observed to occur. The study by Peterson *et al.* [27] showed that no phase transitions are observed in a single nano-pore with a diameter twice that of the molecule diameter (between the centres of wall molecules), right down to absolute zero. However, Radhakrishnan and Gubbins [28] showed that phase change was possible when the nano-tubes were arranged in a cluster, due to correlation effects. Using a grand canonical Monte Carlo (GCMC) simulation (constant chemical potential, volume and temperature) they first showed that a phase change was not observed in a single pore; however, this also highlighted the problem of fluctuations in thermodynamic properties due to the limited number of particles in the system. The investigation then turned to simulating a hexagonal cluster of pores, and the same cluster surrounded by periodic images of itself. The walls were oxygen molecules and the transported molecules were methane, and the periodic pore model showed that clusters of pores do show evidence of freezing at a temperature of about 40 K.

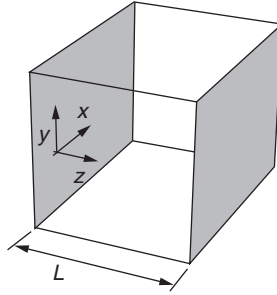


Figure 1.19 Confined geometry for simulation of liquid–liquid phase coexistence, $L = 10.95$, periodic boundary conditions along the x and y axes. Two parallel plates in the xy plane are separated by length L in the z direction.

The simulation also replicated the hysteresis effect of regular phase change, but highlighted the importance of the correlation effect between pores.

In a Monte Carlo simulation of water, Meyer and Stanley [29] investigated the coexistence of two liquid phases of water within a strongly confined geometry, shown in Figure 1.19. The theory of this is based on the fact that amorphous solidified water displays two distinct phases, one with a lower density than the other, and by extrapolating the transition line to a higher temperature to the meta-stable liquid region, there is a possibility of two liquid phases being present. This has been shown for bulk liquids, so Meyer and Stanley [29] investigated the same theory, where the geometry is confined as above. It was found that the pressures normal and parallel to the wall were different and, furthermore, at temperatures below 230 K the pressure parallel to the wall was found to become density independent, typical of the coexistence of phases of different densities in constant volume simulations [30]. The pressure normal to the wall, however, remained density dependent right down to absolute zero. They concluded that it was possible for these high and low density phases to coexist within the simulation.

A combination of these works was looked at by Gatica *et al.* [31] to investigate the adsorption of fluids within carbon nanotubes. As with the work above, adsorbed fluid was expected to exhibit one-dimensional or quasi-one-dimensional behaviour. The study found the corrugation experienced by an adsorbed molecule to be much less when compared to planar graphite [31, 32], leading to fluid adsorbed on to the wall, showing what is known as a cylindrical shell phase. When the density within the nanotube is increased significantly, the cylindrical shell phase solidifies and becomes similar to the incommensurate monolayer solid film on graphite, which is well known and studied [33]. At some point there must be a transition between the solid and fluid, and at this threshold there must also be the possibility of coexistence of the two phases. The solid ‘axial phase’ is recognized when the fluid becomes confined close to the axis of the tube as the number of

molecules in the system is increased (hence increasing the density of the fluid). This axial phase transition operates in a similar way to capillary condensation and layering transition. The layering transitions are known to occur at higher temperature, but the one-dimensionality of the system limits the transition to occur at $T = 0^\circ\text{C}$. It has also been shown that a bundle of adsorbing tubes exhibits correlation effects, which raises the transition temperature above zero [30, 34].

The work of Radhakrishnan and Gubbins [19] agrees with the above discussion of confined phase change, but applied to slit shaped pores. As with the cylindrical pores, fluids confined within slit shaped pores showed strong evidence of a third phase close to the walls. They investigated the effect of the wall–fluid interaction strength on the phase change, varying it from strongly attractive to repulsive, with respect to the fluid–fluid interaction strength.

Previous work by Miyahara and Gubbins [35] had already found that the strength of the interaction affects the hysteresis loop of the freezing temperature relative to the bulk material. However, Maddox and Gubbins [36] also found that the reduced confinement of the fluid in slit pores, as opposed to cylindrical pores, leads to higher freezing temperatures.

The study found that for strongly attractive walls the layer of particles nearest the wall froze at a higher temperature than those in the middle of the pore, similar to many of the examples described above for cylindrical pores. However, as the interaction swings the other way, becoming repulsive, the freezing effect also switches so that the centre of the pore freezes before the layer in contact with the walls. This implies that there must be a level of attraction or repulsion where the fluid freezes at one temperature, making the intermediate shell phase metastable, or disappear completely. The attractive/repulsive interaction potentials at the walls represent the difference between graphite carbon/silica walls, as carbon walls are strongly attractive and silica walls are weakly repulsive. However, most silica-based porous materials have cylindrical pores.

Kim and Steele [37] also looked at phase change at solid boundaries, studying the effect corrugation had on the monolayer of methane on graphite. Their small scale simulations of 289 molecules showed that increased corrugation leads to pre-transitional effects that are not present in solidification against smooth walls.

1.5.2 Adsorption/Desorption in Pores

Adsorption is the process by which a fluid adheres in a thin film to a solid or liquid with which it has contact. As an example, the following discussion considers the effect of the conditions for filling and emptying of a silicate nanotube, as studied by Gelb [38]. The first thing to remember is that classical statistical mechanics laws do not allow a first-order phase transition to take place within short-range one-dimensional systems, even for the case of meso scale pores, despite their three-dimensional structure. Bundles of pores or tubes add to the system's

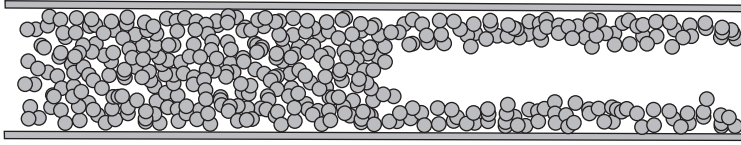


Figure 1.20 Phase regions for adsorption filling of a pore.

dimensionality, which alters the behaviour due to the long-range interactions. This can result in a first-order change of phase within such a cluster due to the presence of neighbouring tubes. These interpore effects are difficult to characterize in real materials and are therefore not, at present, widely investigated by simulations [28]. The filling of a pore involves three basic components, a high density phase representing the filled part of the pore, a low density part representing the multilayer adsorption and the interface between the two, as shown in Figure 1.20.

As would be expected from continuum scale observations of surface tension, the interface between the ‘wet’ walls of the pore and the ‘filled’ region is almost hemispherical. Higher temperature adsorption results in a thicker layer at the walls through the adsorption layer, resulting in a lower surface tension and an increase in the number of interfaces within the pore. The effect of inhomogeneity of phases along the length of a pore becomes negligible when there is no hysteresis present between adsorption and desorption, and leads to a rounding-off of the phase transition, similar to the effect of periodic boundaries on bulk fluid [38]. It is therefore acceptable to think of the phase transition within nano scale pores as almost first order and apply standard transition thermodynamics, as long as the temperature does not approach the critical point and the distance between phase interfaces is comparable to the pore diameter. The term ‘critical point’ used in capillary confined fluids has a different meaning to that of a bulk fluid, and is used to describe the point at which adsorption/desorption hysteresis disappears. As a consequence of the inhomogeneity along the pore, it is not possible to observe a critical point in the bulk fluid sense, or its associated properties. At lower temperatures, the adsorption layer is thinner and the interfaces are further apart, so small periodic cells are used whereas, for very high temperatures, the adsorption layer grows to such an extent and the interfaces are so close together that only one phase is present. The hysteresis, with respect to chemical potential during filling and emptying, is present in both experiment and simulation, but its effects are more pronounced in simulation, possibly due to the short time scale accessible. Longer pores have more capacity to exhibit inhomogeneity along their length which can present differences in nucleation on new phases and hysteresis loops. Pores with closed ends can have the effect of the closed end acting as an already nucleated dense phase while filling and affect the hysteresis loop.

The simulations performed by Gelb [38] were for adsorption of xenon on silica. A simplified model for silica was used, with the surface molecules modelled by

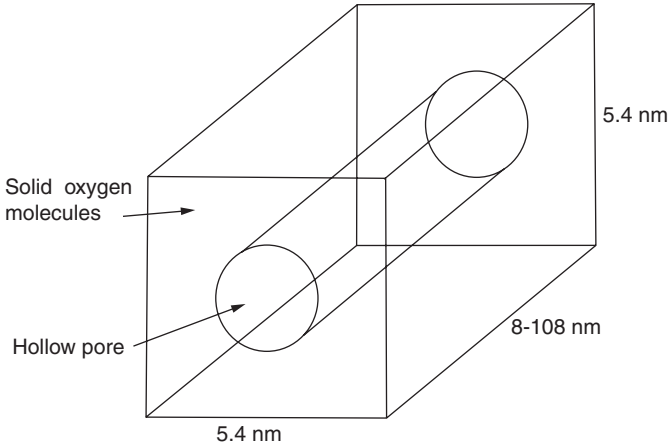


Figure 1.21 Cylinder oxygen atoms removed from the system to create a pore.

oxygen. Silicone molecules are not present on the surface of silica and are weakly interacting and were therefore removed from the model. The pore was created by defining a box, 5.4 nm square at one end with a length varying from 8 nm to 108 nm, full of a standard configuration of oxygen atoms for silica and removing a cylindrical volume of atoms from the centre to create the desired pore geometry (Figure 1.21). A small amount of relaxation was applied to the system after the removal of the cylinder in order to remove some of the translational symmetry experienced by the use of smooth continuum walls, although this was done at the cost of increasing the computational load of the simulation. Three geometries were explored in this investigation, a finite pore with two open ends, an infinite pore with periodic boundary conditions and a single-ended pore. The geometries were also modified in diameter and length for further comparison. The simulations were based on a grand canonical Monte Carlo (GCMC) method (constant chemical potential, volume and temperature) as it samples the correct ensemble for adsorption/desorption simulations and has been found to be reliable, despite inaccuracies when dealing with transport to and from the interface.

During the filling and emptying of long pores (108 nm) it was noted that equilibration became extremely slow at the top of capillary rise and the bottom of desorption drop and required up to thirty times as many more moves than usual. During the desorption of the long open-ended pore, the interface between the two phases moves steadily away from the open end, and there was no evidence of nucleation of either phase away from the interface. Desorption within an open-ended pore often results from the nucleation of the low-density phase within the high-density region, resulting in 'bubbles' forming. However, in this case, the interface also moves at an almost constant velocity.

The filling of the single-ended pore shows the reverse happening; the closed end acts as an already nucleated phase and the interface moves up the pore towards the open end at a relatively steady rate. Open-ended ‘infinite’ pores do not have the ‘head start’ of the closed end and must nucleate the start of the high-density phase before the filling process can properly begin. This means that capillary rise occurs at a higher chemical potential than closed-ended pores. Because of this higher potential, the closed-ended pore has a smaller width hysteresis loop than the open-ended tube, which also reduces the temperature at which hysteresis disappears. It was also found that the reduced hysteresis loop found with the single-ended pore occurs at a chemical potential almost exactly in the middle of the larger loop of the open-ended pore. Gelb [38] also noticed that at the ends of the pore, weaker repulsive interactions could be affecting the stability of the simulation as the interface approached the ends of the tube.

Open-ended and infinite pores were also compared using two different pore diameters of, 4 nm and 3 nm (see Figure 1.22). Although the hysteresis loop for the open-ended pore was smaller than for the closed-ended pore, it is still smaller than the loop for the periodic pore. The effects of the open-ended pore are more dramatic for the 4 nm diameter as a much higher chemical potential is needed to induce nucleation of a new phase, making the presence of the open end more important. The hysteresis experienced by the open-ended pores for both diameters is mainly on the desorption drop and not on the adsorption side. However, the capillary rise occurs at a slightly higher chemical potential, indicating that the open ends may be stabilizing the low density phase at the ends.

The final investigation performed by Gelb [38] looked into the effect of changing the length of the pore cell for the periodic/infinite pore. Three lengths were tested, 8 nm, 16 nm and 108 nm, and it was found that as the length was increased, the width of the hysteresis loop was reduced. This was attributed to the fact that the longer pores contained more density fluctuations, leading to a higher probability of nucleation of a new phase. This, however, could have been due to poor sampling resolution as the difference is fairly small and is most pronounced at a reduced temperature of $\tilde{T} = 0.927$. There was a fairly close agreement between the two longest pores, of 8 nm and 108 nm, which could indicate that the

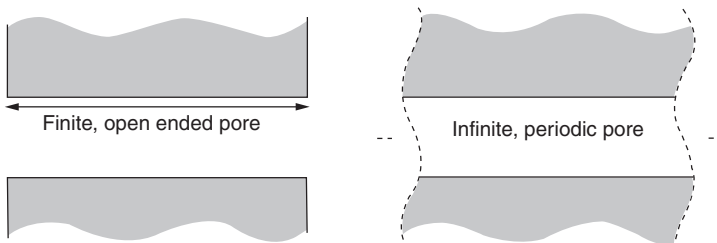


Figure 1.22 Infinite versus open pores.

difference in the hysteresis loops is not affected when the length becomes significantly greater than the pore diameter.

Gelb's [38] observations have been summarized below:

- Pore length has little effect on the adsorption/desorption hysteresis despite the added probability of nucleation, but the effect is greatest when the length is close to the pore diameter.
- Open ends on pores show much less desorption hysteresis for 3 nm diameter pores than for 4 nm diameter pores.
- Single-ended pores show almost no hysteresis due to the nucleation of phases at the end of the pores. Density also fluctuates greatly at pressures near condensation.
- Interpore correlation effects could yield a 'novel type of phase transition in two dimensions'.

The effect of the length of the tube is a fairly expected result. As long as the tube is long enough to separate the effects of the ends of the tube, the middle section shows little variation along its length. The difference in desorption hysteresis between pore sizes is mainly due to the nucleation of the ease of progression of the new phase, which is made easier by the effectively larger particles, due to the narrower pore. The lack of hysteresis shown in single-ended pores is mainly due to the closed end acting as a dense phase, giving a good start to phase nucleation.

1.6 SUMMARY

In this chapter a general overview of fluid behaviour on continuum and molecular scales was presented. The bulk, or continuum, properties have been discussed along with their origins from molecular mechanics. Several methods for solving for these continuum properties were presented in terms of the governing equations that quantify the relationships between them.

On the molecular scale, the origin of intermolecular forces and interactions has been presented and a wide variety of molecular simulation schemes have been discussed, from the deterministic molecular dynamics to the stochastic Monte Carlo method. Finally, the importance of these methods has been highlighted by considering the molecular examples in Section 1.5.

This chapter has shown the different approaches to fluid simulation that are needed as the scales of the system changes. The meso scale lies in between the continuum and molecular scales and must use elements from both to capture correctly the proper physics (from the molecular scale) and provide a description in terms of useful fluid properties (as characterized on the continuum scale).

2

Fluid Physics at Meso Scales

Aim. By the end of this chapter, the reader should be aware of and understand existing simulation techniques and their advantages/disadvantages when applied to fluid systems at meso scales.

2.1 INTRODUCTION

The focus of this chapter will be to present and discuss methods for combining information and physics from the continuum and molecular scales. The discussion begins with methods that couple continuum with molecular simulations. From this, two basic methods will emerge, where molecular simulations are used either to couple to the continuum region as a boundary condition (and vice versa) or by the molecular information being used to modify or enhance the continuum solution in a particular region.

Many of these methods consider solid systems or sparse gas dynamics, both of which can access larger length scales with molecular simulation than dense gases or liquids, due to the dynamics and distance between molecules. Existing meso scale methods will then be discussed, such as dissipative particle dynamics and the lattice Boltzmann method. The meso scale methods commonly used present a ‘top-down’ approach, the benefits of which and applications will be discussed.

The final section will discuss direct schemes from upscaling information from the ‘bottom-up’ approach to looking at schemes for extracting bulk properties from molecular dynamics, with a view to extract not only the properties but also the property distributions throughout the molecular domain.

2.2 TOP-DOWN APPROACH FOR MESO SCALE COMPUTATION

The meso scale region is defined as a scale in between the micro scale and molecular scale (approximately between 10^{-6} m and 10^{-8} m). The meso scale exists to cover the change in physics between the continuum approximated view and the discontinuous molecular description. Hence, the upper limit of the meso scale is set by the point at which the continuum approximating laws are violated. This can occur at a range of scales, depending on the state and properties of the fluid; e.g. a sparse gas invalidates the continuum laws at larger scales than a solid.

2.2.1 Continuum Limit

For the fluid to be considered a continuum, the laws described in Section 1.2.2 are summarized as follows:

- The fluid is continuous and infinitely divisible.
- The fluid is in thermodynamic equilibrium.

Because of the dependence of the continuum laws on the state of the fluid characterized by the rarefaction and energy of the molecules, the point of failure of these laws must be considered carefully. Travis *et al.* [39] show a comparison between Navier–Stokes hydrodynamics and molecular simulation, which displays different behaviour in terms of the velocity profile and heat flux profile. Due to the differences in density and kinetic theory, it is therefore necessary to consider the continuum to molecular transition separately for liquids and gases.

Gases have a very well developed kinetic theory, and consequently are better able to describe the transition from continuum mechanics to fully molecular flow.

2.2.1.1 Gas flows

To assess the validity of the continuum or molecular model for a gas, it is necessary to obtain a measure of the rarefaction of the gas at the scale of interest. To do this, the concept of mean free path is introduced. The mean free path is the average distance travelled by a molecule before it collides/interacts with another molecule. For an ideal hard sphere gas, the mean free path, λ , is a function of pressure, P , and temperature, T , as follows:

$$\lambda = \frac{k_b T}{\sqrt{2\pi} P \sigma^3}. \quad (2.1)$$

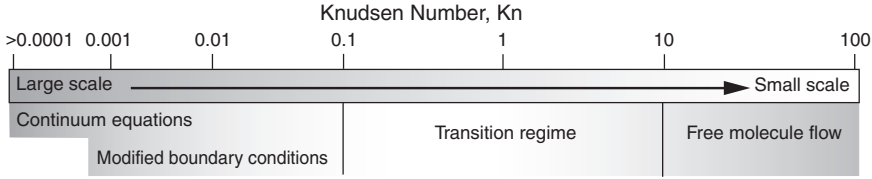


Figure 2.1 Range of Knudsen number for gas systems.

This provides a measure of the rarification of the gas. This can then be compared with the characteristic length of the flow field, l , which can either be taken as the characteristic dimension or the gradient of a bulk property, such as density

$$l = \frac{\rho}{|d\rho/dx|} \quad (2.2)$$

The ratio of the characteristic length to the mean free path of the gas is known as the Knudsen (Kn) number:

$$Kn = \frac{l}{\lambda}, \quad (2.3)$$

the value of which is used as a measure of the rarefaction of a gas with respect to the scale of the system, in order to test the validity of the continuum approximations. Typical values are shown in Figure 2.1 from the large scale continuum to molecular systems. A very small Kn number (< 0.001) describes a system that is well within the continuum laws, but as the Kn number increases the small scale effects of the fluid become more pronounced [40]. The first stage of the breakdown of the continuum approximations occurs at a Kn number of greater than 0.001 where areas of high gradient, such as boundaries, cannot maintain the continuous distribution of macroscopic properties. This is a result of the deviation from thermodynamic equilibrium, where there are insufficient collisions in the system for the energy to propagate smoothly in areas of high gradient such as at the boundaries. The low number of molecular interactions with the boundary means that the velocity and temperature of the solid and fluid are no longer the same at the interface, causing a violation of the no-slip condition (similarly the no-jump-in-temperature condition) that is assumed in continuum mechanics [41].

To account for this initial deviation from the classical equations, the linear Navier boundary condition [42] describes the slip and no-slip conditions by relating the difference in velocity between the wall and fluid ($u_{\text{fluid}} - u_{\text{wall}}$) to the strain rate at the wall ($\partial u / \partial y$)_{wall}:

$$u_{\text{fluid}} - u_{\text{wall}} = L_s \left(\frac{\partial u}{\partial y} \right)_{\text{wall}}, \quad (2.4)$$

with L_s being the slip length. This slip condition can be included in the continuum approximations as long as slip length L_s is known or obtained via molecular simulation or experiment. For normal large scale continuum simulations L_s is so small that the fluid and wall move at the same speed (no-slip condition), but as the Kn number of the system increases above a value of 0.001, the slip effect becomes more pronounced. The amount of slip that is allowed depends on the roughness of the surface over which the fluid is flowing and the interaction rate between the fluid and solid molecules.

A similar equation for the slip at the boundary, which includes temperature discontinuities, was presented by Smoluchowski [43]:

$$u_{\text{gas}} - u_{\text{wall}} = \frac{2 - \sigma_v}{\sigma_v} \mathfrak{L} \left(\frac{\partial u}{\partial y} \right)_{\text{wall}} + \frac{3}{4} \frac{\mu}{\rho T_{\text{gas}}} \left(\frac{\partial T}{\partial x} \right)_{\text{wall}}, \quad (2.5)$$

where σ_v is the momentum accommodation coefficient and \mathfrak{L} is the mean free path from above. The first term is a modified version of Equation (2.4) with the slip length being replaced by a description of roughness and scale, $[(2 - \sigma_v)/\sigma_v]\mathfrak{L}$. The second term represents the thermal creep, responsible for slip in the direction of increasing temperature along the surface [44]. Similarly, the equation to account for temperature discontinuities at boundaries is

$$T_{\text{gas}} - T_{\text{wall}} = \frac{2 - \sigma_T}{\sigma_T} \left[\frac{2\gamma}{\gamma + 1} \right] \frac{\mathfrak{L}}{Pr} \left(\frac{\partial T}{\partial y} \right)_{\text{wall}}, \quad (2.6)$$

where T_{gas} and T_{wall} are the temperatures of the fluid and wall respectively, γ is the specific heat ratio and Pr is the nondimensional Prandtl number. The thermal accommodation coefficient, σ_T , is similar to the momentum coefficient of Equation (2.5) and characterizes the material properties of the interface.

These equations can apply modifications to the continuum governing equations, but the violation of the no-slip condition is only the initial sign of the failure of the continuum laws and the approach to the limit of the continuum laws. However, Bing-Yang *et al.* [23] demonstrated that the Maxwell slip model fails as the surface roughness of the wall approaches the mean free path of the fluid for gas systems.

For higher Kn numbers, the violation of the continuum laws becomes more serious, as the effect of finite numbers of molecules affects the propagation of macroscopic properties further away from boundaries and wider areas of high gradient. Also the localization of mass and energy at molecular sites starts to bring statistical variations into the fluid properties. This type of breakdown occurs in the transition region between the continuum and molecular regions.

A transition region where continuum approximations cannot accurately predict the system behaviour is between Kn numbers 0.1 to 10. In this region, the mean free path and characteristic length of the gas are comparable, indicating the

importance of the underlying molecular physics of the system. In these systems, the continuum equations cannot be applied, even with boundary modifications.

For Kn number greater than 10, the mean free path of the gas is more than 10 times greater than the characteristic length of the system, and the fluid is well within the limits of and can only be described by molecular physics.

2.2.1.2 Liquid flows

The transition between the continuum and molecular regions for liquids goes through the same stages as for gases, but there is no parameter to act as a guide throughout the transition. The Kn number cannot be defined, as there is no concept of mean free path for liquid flows and molecules are in a constant state of collision and move over much shorter distances [40, 44]. The kinetic theory for liquids is not as well advanced as for dilute gases, making the transition difficult to measure. However, Loose and Hess [45] showed that thermal equilibrium, and therefore Newtonian behaviour, stops as the strain rate, $\dot{\gamma}$, exceeds twice the molecular frequency scale, τ :

$$\dot{\gamma} = \frac{\partial u}{\partial y} \geq 2\tau^{-1}, \quad (2.7)$$

where the molecular time scale is derived from molecular properties of mass, m , well depth, ϵ , and collision radius, σ , as

$$\tau = \sqrt{m\sigma^2/\epsilon}, \quad (2.8)$$

where u is the longitudinal velocity normal to y , and σ and ϵ are the characteristic length and energy scales for molecules of mass, m . However, under standard conditions the extremely small molecular time scale for liquids such as water puts the continuum/Newtonian limit extremely high.

Other studies by Pfahler *et al.* [46] showed the breakdown of the continuum description by comparing experimental data for the friction factor in a micro-channel liquid flow with the continuum description. They varied the speed and depth of the channel (100 μm wide by 0.8 μm and 1.7 μm deep) and plotted the friction factor as a function of the Reynolds number, comparing the results with those of Navier–Stokes predictions. They concluded that there was a well-defined point at which the behaviour of the liquid deviated from the predictions.

Liquid flows, however, remain difficult to classify in terms of the deviation from the continuum description. When compared to gases, the breakdown occurs at smaller length scales, due to the closer packing of the molecules. Equations (2.5) and (2.6) are also valid for fluids but, as described above, the exact point at which they apply is difficult to determine.

The discussion above shows that there is a limit at which the continuum approximations can no longer be considered accurate. Beyond this point it is necessary to include information from the molecular scale. Methods for the inclusion of this information will now be presented.

2.2.2 Top-Down Meso Scale Methods

This method of domain coupling has been mainly applied to structural problems where the particles of the molecular region are frozen with a near-zero mean square displacement. In the region of the interface, a finite element mesh is scaled to dimensions that coincide with the molecular lattice. The boundary between the two regions must ensure that there is a connection between the degrees of freedom in the continuum and molecular models that maintains all dynamic and conservation laws. The thickness of the interface is as small as possible so that the number of parameters linking the two domains is kept to a minimum. The domain coupling must also maintain the thermodynamics, static elastic and dynamic elastic responses of the material.

One method of coupling length scales in this way, developed to deal with crack propagation, was by Rafii-Tabar and coworkers [47] and resembles an iterative variation of the serial approach applied to crack propagation problems. With this approach, the continuum region is used to calculate the boundary conditions for the molecular region, which calculates the effective stochastic diffusion coefficient and growth at the crack tip for a short time interval, using a zero temperature molecular simulation. The average velocity that the tip travels is also calculated and all the molecular information is fed back into the continuum simulation for the next iteration. This approach uses a form of Langevin dynamics at the crack tip and finite element (FE) simulation for the continuum, with the molecules at the interface between the two representing the boundary conditions for the molecular region and having no thermal dynamics. So far this method has been limited to two-dimensional simulations with a molecular region not around 5000 molecules. This approach was also used by Ayton *et al.* [48], who used it to simulate flow through biological membranes.

A similar coupling scheme was also described by Abraham [49] in the MAAD program. In this method, finite element and molecular dynamic regions are linked by defining a region between the two called the 'handshake region' (Figure 2.2), with a Hamiltonian described by finite element cells and two/three body interactions crossing the boundary, each contributing half-weight. The displacements in the finite element region are updated by a molecular dynamic algorithm so as to ensure seamless transmission of displacements.

The hybrid models are very computationally efficient and give almost seamless coupling between areas of different length scales. However, direct coupling between molecular sites and continuum meshes is not suitable for fluids, as

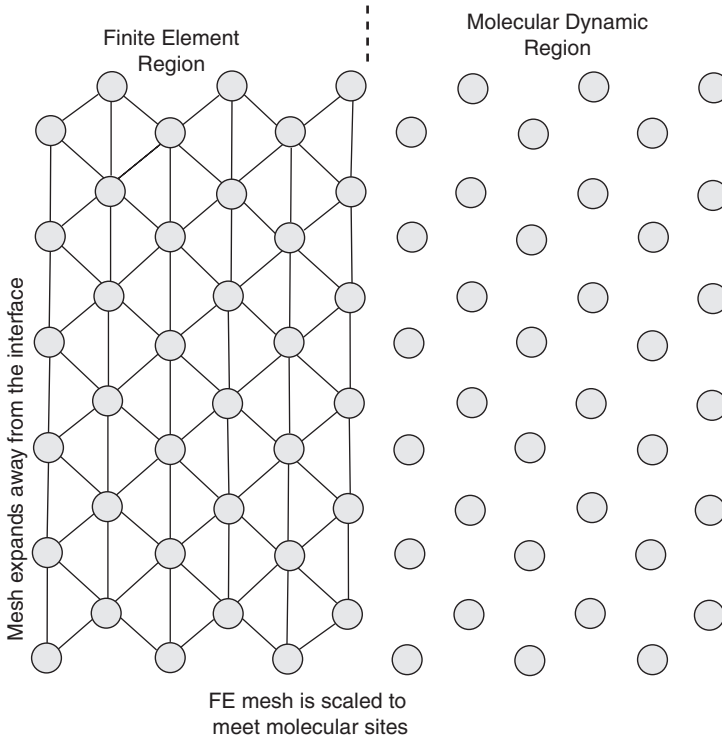


Figure 2.2 MAAD handshake region (FE/MD) [49].

the molecular sites in a fluid move constantly throughout the domain (thermal motion/diffusion) even if the fluid is at rest. Coupling between fluid domains requires an interface between the two that allows for the movement of molecules. For solids, the validity of the continuum equations can be extended, as the molecules are within a rigid structure and they move little, if at all, allowing the continuum laws to be valid at smaller scales. In fluids, however, the dynamic molecular structure cannot be treated in the same way. Garcia *et al.* [50] developed the coupling between the Navier–Stokes equations and direct simulation Monte Carlo (DSMC) models for dilute gases by using a Chapman–Enskog velocity distribution-based current generation scheme. This model considers only the scattering of molecules due to collisions; it is the diffusion that is vital to the model, as opposed to the simulation of cracks and solid systems, where diffusion is negligible and position is important. The method they developed is based around an adaptive mesh and algorithm refinement (AMAR) base, where they use DSMC to enhance the accuracy of the final stage of refinement (Figure 2.3). The simulation is detailed as follows. The continuum region covers the whole domain of the simulation, even

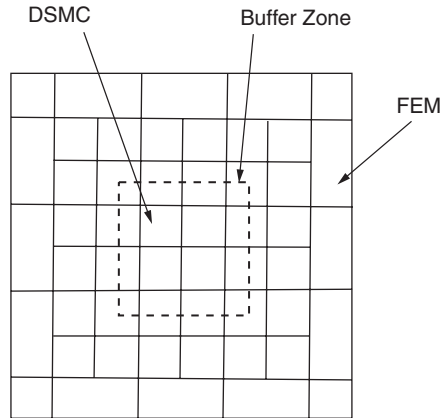


Figure 2.3 Direct simulation Monte Carlo used as the finest stage in an adaptive mesh and algorithm refinement method [50].

overlaying the DSMC region. The DSMC region is contained within a number of these cells and are surrounded by buffer cells. Buffer cells are controlled by the continuum solution at the end of a molecular time step, the molecules within the buffer zone are deleted and a new set of molecules are created using the hydrodynamic parameters of the continuum solution. The buffer cells are used by the continuum part of the solution for two reasons: the first is to monitor the flux through the boundary between the DSMC and continuum region, and the second is to influence the DSMC region by assigning the density and velocity of the created molecules. The time steps used are not the same in the DSMC and continuum solutions, as this would lead to instabilities, but they must both progress at the same rate. There are in general four molecular time steps, t_{part} , to every one continuum time step, t_{cont} , meaning that the DSMC simulation must perform four steps for every one of the continuum. The method follows the following routine:

1. The continuum region performs one step in time, t_{cont} , through all cells including those covering the DSMC region.
2. The molecules in the buffer region are replaced with particles determined by the hydrodynamic gradients (density/velocity/temperature) of the continuum cells that cover them. Molecules are given a velocity assigned by a distribution, as in the initialization stages of molecular dynamics, which is determined by the form of the continuum solver. If the simulations are based on the Euler equations, the Maxwell–Boltzmann distribution is used, and for Navier–Stokes equations the Chapman–Enskog distribution is used.
3. Momentum and energy corrections are made to all other particles, determined by their overlying continuum cells.

4. DSMC advances one molecular time step, t_{part} . Particles are allowed to pass freely in and out of the buffer zone.
5. Particles crossing the boundaries between cells contribute to a correction of the intercell flux between the continuum cells.
6. Repeat DSMC time steps (4 to 6) until the continuum time step, t_{cont} , is reached.
7. Conserved quantities, such as density, are used to correct continuum values.
8. Simulation then repeats steps 1 to 7 until the total time is reached.

This method uses molecular simulation laid over the continuum mesh to refine the continuum solution. As the molecules are created in the buffer zone at each time step, this causes problems of relaxation of the molecules at the beginning of each molecular iteration, which could influence the results, as the boundary conditions are essential to the solution of such a problem.

A similar approach was developed by Nie *et al.* [51], where a Navier–Stokes region was coupled to a molecular region to evaluate a channel flow with a fixed obstacle. The molecular region was placed around the obstacle.

The approach to the meso scale has been attempted in many ways, the most publicized being to couple continuum approximations with molecular information. This allows for the minimum volume considered by molecular simulation, thus improving the overall efficiency of the simulation. There are, however, some distinct problems associated with coupling these two simulation schemes. First, the continuum and molecular simulations have a different frame of reference. This is to say that the continuum region models the fluid in a steady state picture where variables like velocity, pressure and density take values relative to fixed positions in the system (Eulerian approach), whereas the molecular model considers the dynamics of the molecules within a fixed region (Lagrangian approach). This presents a barrier to the coupling of the two schemes that can be overcome, as will be shown, but can be especially difficult for dynamic fluid systems.

Second, there is a substantial gap between effective length scales considered by continuum and molecular simulations especially for dense gases and liquids. Consequently, the majority of coupling schemes have been developed for solid and fracture mechanics, which present a simpler problem as molecules are fixed to lattice sites, allowing a much simpler integration between molecular and finite element approximations. Other schemes work with relatively rarefied gases, with low Kn numbers, that allow the molecular simulation to operate at continuum dimensions, as the computational effort of molecular methods scale with the number of molecules in the system.

Another branch of ‘top-down’ simulation methods contains those that define new systems of governing equations and include a higher degree of molecular physics. These will be considered next.

2.2.2.1 Dissipative particle dynamics

A similar approach is known as dissipative particle dynamics (DPD) introduced by Hoogerbrugge and Kolesman [2]. This is effectively similar in concept to molecular dynamics, where the particles used move using Newton's laws, but the interaction laws are different from those used in molecular dynamics. Here, a single particle represents a group of molecules moving throughout the domain, and to account for the internal degrees of freedom of each 'area' of fluid, the interactions have fluctuating and diffusive components. DPD is typically used for simulating colloids [52] and complex fluids [53, 54], as its particle structure allows for the easy integration of large fluid particles and suspensions.

Dissipative particle dynamics was originally derived from a molecular dynamic framework, but the bulk particle interaction laws are closer to continuum equations and include modification to represent the molecular physics. This method is widely used mainly for simulations in the high end of the meso scales. Because of its representative particle approach, this method allows easy coupling with continuum particle methods such as smooth particle hydrodynamics.

2.2.2.2 Lattice Boltzmann method

The lattice Boltzmann (LB) method considers a fluid flow by solving the Boltzmann equation at many points over a discrete lattice/mesh. In this method, molecules exist as numbers possessed by each cell and flow is considered as the flux of molecules between cells. These lattice-based methods are mainly used to solve highly porous and complex geometries [1, 55] at the meso scale and for multicomponent flows [56]. Lattice Boltzmann simulations are best suited to simulations of sparse gas systems where molecular interactions rarely occur. A similar approach using the Boltzmann equation was developed by Naris *et al.* [57] which implemented a simplification for the collision integral.

The lattice Boltzmann and dissipative particle dynamics methods have been combined with smooth particle hydrodynamics to construct the DL meso software package [58]. This combination of methods has been very successful at modelling within the higher end of the meso scale. These methods allow the fluid to be modelled at meso scales, but they have their limitations. The LB and DPD methods make assumptions about the distribution of the molecular physics occurring within their elements/particles, and the actual internal molecular interactions are approximated. The molecular degrees of freedom are removed to save computational load.

An alternative approach to investigating fluid behaviour and capture fluid properties at the meso scale is from first principles of molecular interactions, or the 'bottom-up' approach. By directly modelling the molecular interactions within a fluid, it is possible to model a fluid in an environment that is closer to experimentation than simulation.

2.3 BOTTOM UP APPROACH FOR MESO SCALE COMPUTATION

As has been demonstrated in the previous section, the continuum approximations begin to fail within the meso scale region ($\leq 10^{-6}$ m). However, although the continuum assumptions fail, the bulk properties are still observable and have significant impact and meaning when a meso scale fluid is considered. This section demonstrates how meso scale fluid systems can be modelled from a ‘bottom-up’ approach, by considering the fluid physics from first principles of molecular interactions. These molecular simulations also demonstrate bulk behaviour, modelling the continuum properties from their molecular origins, as described in Section 1.2.1.

2.3.1 Molecular Dynamics Model

Molecular dynamic simulations model the individual molecules of a fluid by representing each individual molecule as a coordinate point in space, with a set of molecular properties attached to it that describes its mass, size and interaction strength. The general scheme for molecular dynamics is presented in Section 1.3 and this section will focus on the details of the simulation and its relevance to meso scale systems.

2.3.1.1 Molecular potential model

The most commonly used potential model in molecular dynamics is the Lennard–Jones potential (Figure 2.4). Intermolecular potentials are used as a simplified model of all the interactions that are present in real systems. The approximation is derived in different ways, either by experiment or from first principles of molecular dynamics. Experimental based potential models are generally based more on realism than provable mathematics. The actual potential model represents, in general, the short-range repulsive (Pauli/Coulomb forces) and long-range attractive (van der Waals/London) interactions, but in all Lennard–Jones models electronic degrees of freedom are neglected.

There are two basic parts of the Lennard–Jones potential, an attractive part and a repulsive part. This is described mathematically as

$$U_{r_{ij}} = 4\epsilon \left[\left(\frac{\sigma}{r_{ij}} \right)^{12} - \left(\frac{\sigma}{r_{ij}} \right)^6 \right], \quad (2.9)$$

where $U(r_{ij})$ is the potential energy between molecules i and j , with r_{ij} being the distance between them. Parameters σ and ϵ represent the collision radius and

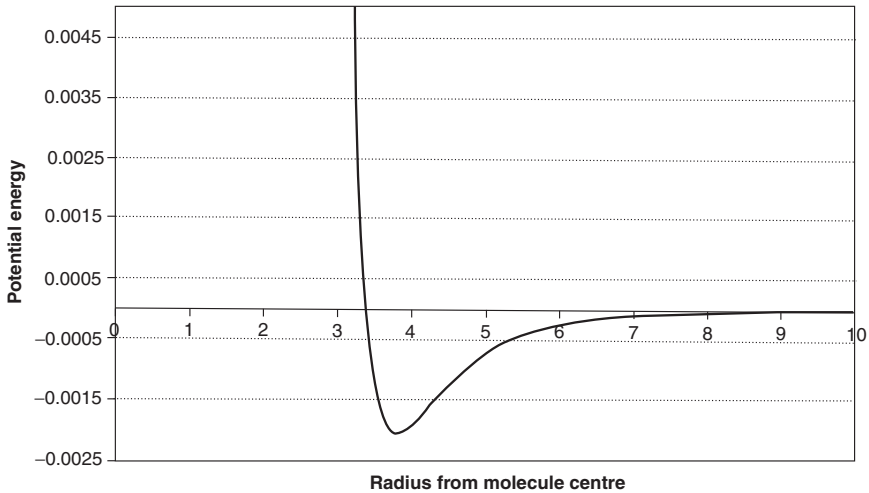


Figure 2.4 Lennard–Jones interaction potential for methane (CH_4).

well depth (strength of interaction) respectively. ϵ is commonly referred to in the form ϵ/k_b . Some common values for Lennard–Jones interactions are shown in Table 2.1.

When these soft sphere interactions take place in simulations it is necessary to shorten the range of the potential to prevent overlapping in periodic systems and to reduce the computational load. The cut-off is usually performed at two and a half times the molecular diameter, but is dependent on the system and is generally limited in periodic system to a maximum of half the distance between the two periodic boundaries.

The Lennard–Jones potential, despite its common use, should only be applied where there are no electrons available for bonding and there are only weak long range interactions. More complex materials such as metals and semiconductors require a more complicated many-body potential model rather than a pairwise model such as the Lennard–Jones. Many bodied potentials are affected by

Table 2.1 Lennard–Jones potential parameters.

	Well depth, ϵ/k_b (K)	Collision diameter, σ (nm)
C	28	0.34
Ar	124	0.342
CH_4	148	0.304
Kr	190	0.361
Xe	229	0.406

local environment density, assigning weaker bonding where many molecules are present. Even in rare gases, many body effects are present, but they are much less pronounced.

For systems containing multiple types of molecules, e.g. fluid mixtures, there are rules that combine the Lennard–Jones parameters of the two components, called the Lorenz–Barthelot mixing rules [59]. For the collision radius, the parameters are combined to give a single value for the evaluation of the Lennard–Jones potential between the two dissimilar molecules; for example, the radius for molecules numbered 1 and 2 is given as

$$\sigma_{1,2} = \frac{\sigma_1 + \sigma_2}{2}, \quad (2.10)$$

which takes the average of the two values. For the well depth, they are combined as follows:

$$\epsilon_{1,2} = \sqrt{\epsilon_1 \times \epsilon_2}. \quad (2.11)$$

For systems with many molecules, the searching through the flow domain for pairs of molecules, close enough to interact with nonnegligible Lennard–Jones potentials, can take a significant amount of time to process. Efficient schemes used to search for and keep lists of neighbouring molecules will now be presented.

2.3.2 Boundary Conditions

In the simulation of real systems, the molecules need to be contained in a controlled environment. Either geometric or computational constraints can limit the size of the simulation to a finite control volume, but molecules must be contained within the simulation cell and must have the ability to influence the system beyond the confines of the simulated volume. The method by which this is done must be carefully designed and applied. In molecular simulations where fluid boundaries are used, periodic boundaries are frequently used.

2.3.2.1 Periodic boundary conditions

Molecular simulation is currently only practical on a very small scale due to the computationally demanding particle-based techniques. It is therefore necessary in some situations to cut down the size of the simulation region to decrease the run time, similar to the way finite element analyses take advantage of symmetry. Periodic boundary conditions effectively surround the simulation cell with identical copies of the main cell, as shown in Figure 2.5.

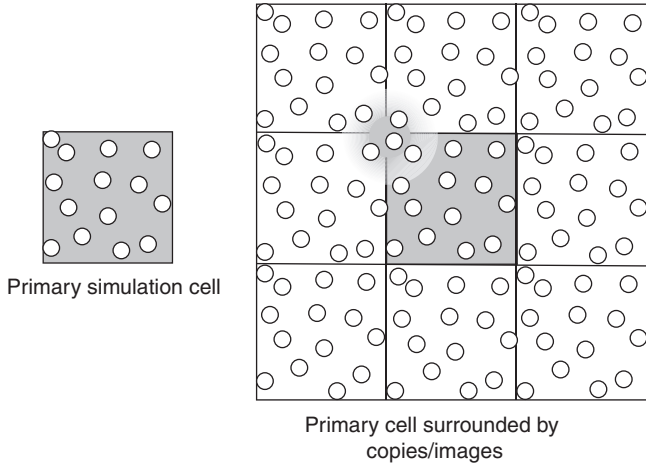


Figure 2.5 Periodic boundary conditions.

As a molecule passes over the boundary and out of the primary cell and into an adjoining image, at the same time an identical molecule with exactly the same properties passes in from the image on the opposite side into the primary cell. In the case of the soft sphere model, cross boundary interactions also need to be taken into account by finding the nearest image of an interacting particle. This is best illustrated by the one dimensional example in Figure 2.6, where it is shown that as the separation between two molecules becomes greater than $a/2$, the particle i is nearest to the image of the second particle, j . At the boundaries of the main

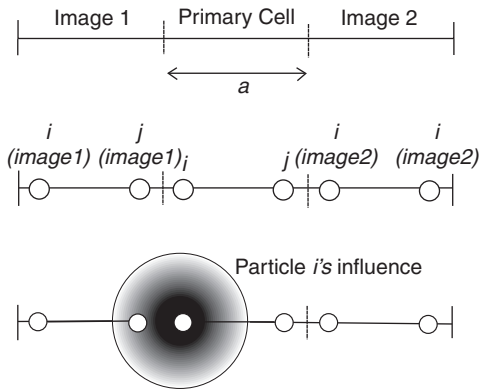


Figure 2.6 Soft sphere cross boundary interaction.

cell, the simulation sees and interacts with the opposite side of the same cell, effectively looping itself and creating the appearance of an infinite unconstrained simulation.

Periodic boundary conditions allow for the automatic conservation of flow properties. Mass is conserved perfectly; as there is no molecule deletion or creation by the boundaries, the molecules simply pass through the boundary as if it were not there. Similarly, energy is conserved and the boundary presents no obstacle to intermolecular interactions or molecule movement.

These periodic boundary conditions are for approximating a very large or infinite region of fluid with a relatively small simulation cell. There are also situations where it is necessary to confine a fluid to a region using solid walls or boundaries, and it is this situation that will be considered next.

2.3.2.2 *Wall boundaries*

For a molecular simulation of fluid with solid boundaries, it makes sense to apply a solid molecular wall with a similar interaction model by simulating all the frozen solid molecules in that wall. Although this is the most numerically accurate approach, it is also the most computationally demanding. Even for the case of a single-walled carbon nanotube, where there is only one layer of ‘solid’ molecules containing the flow, solid structures generally have a higher density and add a large number of particles to the simulation. There are several alternative strategies to save computation time, which will now be discussed.

Fortunately, there are several strategies available to model solid boundaries while maintaining all the information about a molecular wall. To reduce the computational load of a molecular wall, the wall molecules can be completely frozen, removing all degrees of freedom from the wall. This allows the molecular walls to retain their roughness/corrugation, but they lose the ability to absorb energy from the fluid as the cost of reduced computation time [60]. This also results in a stiffer wall interaction model as wall molecules cannot react to fluid molecule collisions, but significantly reduces the number of force interactions that need to be evaluated.

Over meso length and time scales, the collision rate with solid boundaries can be very high, which allows the molecular behaviour at boundaries to be applied as an approximation over many collisions. The main scheme for applying this is the diffuse boundary condition [61], which will be considered in the next chapter.

The above describes a molecular model for use at nano scales ($\approx 10^{-9}$ m), but the scales of interest are between 10^{-6} m and 10^{-8} m. Therefore this physics model must be able to provide information about the fluid on these larger scales. Methods for upscaling the physics and information from these molecular simulations will now be discussed.

2.3.3 Bottom-Up Meso Scale Methods

The main issue faced with bottom-up methods is the upscaling of information from the molecular model and the removal of degrees of freedom from the system to save computational resources. The first approach considered is the serial approach, where a very small molecular simulation describes the physical relationships behind a large scale fluid system.

A serial approach is used when the scales are only weakly linked together. Parameters are calculated at the smallest scale and the information is fed into the next scale up, where it is used to calculate a larger scale parameter, and so on until the largescale analysis can be performed.

This approach is best described by an example. Clementi [62] did a study of the tidal circulation in Buzzards Bay by starting with the quantum-mechanical simulation single water molecule. This information was then used to model the behaviour of a small cluster of molecules and then a database of interactions between the molecules was formed. The information contained in the database could then be used to describe an empirical potential to be used in a molecular dynamic simulation. The density and viscosity of water could then be calculated and fed into a continuum scale computational fluid dynamic simulation to predict the tidal movement of the bay. This shows how an accurate solution can be derived by upscaling information from the molecular to the kilometre scale. However, in the serial approach information only passes one way through the calculation and therefore its use is limited to situations such as the one described above where the scales are only weakly linked.

2.3.3.1 *Derived scaling*

The coupling techniques previously described involve coupling several regions of different scales. Now a method will be discussed that involves a single model that has a varying density in the same way that varying mesh densities are used in regular large scale finite element (FE) simulations. This negates the need to couple models together so the system can be simulated as a whole.

The best way to understand this approach is to imagine the simulation in two layers, one containing molecular information and covering the whole system at a fine scale and the other as a mesh, similar to FE, scaled from nodes corresponding to molecule sites close to the region of interest up to large scales where elements contain many molecules (Figure 2.7).

As the large scale elements contain many molecules, there is a large amount of information that is unnecessary, as in a region of low activity a lot of the data held by the parameters of each molecule is approximately the same. Therefore degrees of freedom need to be removed from the system to cut down on the processing of unnecessary information, which is done using the quasi-continuum method

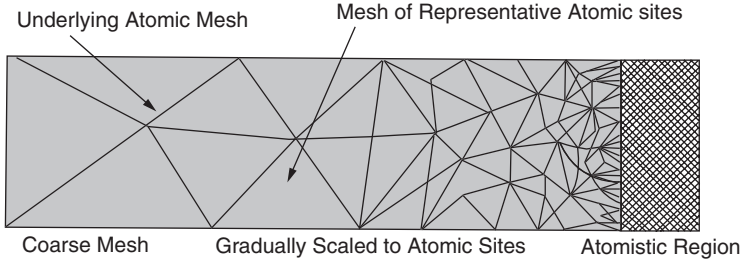


Figure 2.7 Constant density molecular layer (small dots) overlaid with an equivalent FE mesh.

described below. The cut-down molecular properties are then used to obtain the equations of motion by averaging molecules surrounding each node, resulting in the mean behaviour representing an area of molecules. This is similar to a standard FE simulation, but instead of the equations of motion being computed from a continuum model, the molecular model is used. As the size of the elements reduces, the number of molecules within each element reduces until the nodes of the mesh coincide with the sites of the molecules, where the equations of motion are derived from individual molecules and there is no longer a need to discard information. As can be seen, the less demanding element-based simulation gradually breaks down into the more demanding molecular simulation as the scale is reduced, providing almost seamless coupling.

Further away from a region of interest there is less activity and the resolution of the solution can be reduced to cut down computation time. This is done by increasing the size of the elements in the mesh, removing degrees of freedom from the molecules and averaging the properties to approximate the motion of the area. It was found that in some statistical models the Hamiltonian keeps its form as the degrees of freedom are removed; only the parameters change, so the parameters can be redefined as the scale of the mesh is changed by the use of an equation. The renormalization group equation [63] does just that and can update the Hamiltonian at any scale.

The method presented to reduce the number of degrees of freedom was created by Tadmor *et al.* [64] and later developed by Phillips and coworkers at Brown University, Providence, Rhode Island [65–68], called the quasi-continuum technique.

Quasi-continuum technique In areas at a distance from the area of study, where the displacement fields contain no steep gradients, the energy of the molecules local to each other possess approximately similar values. It is this approximation that is the key to the quasi-continuum method, which aims to reduce the processing time of the mid to large scale areas of the simulation. Assuming that this is

true, the local neighbourhood of molecules can be represented by the value of just one molecule. By doing this the number of degrees of freedom in the computation of the energy of the system can be dramatically reduced. The standard method for computing the system energy involves the summation of the energies of all molecules in the simulation, as below:

$$E_{\text{total}} = \sum_{i=1}^N E_i, \quad (2.12)$$

where

$$\begin{aligned} E_{\text{total}} &= \text{total energy,} \\ E_i &= \text{energy of individual molecule } i, \\ N &= \text{total number of molecules.} \end{aligned}$$

However, by representing an area of molecules with a single node/particle can reduce the computational demand dramatically. This is applied by choosing an finite element mesh with nodes defined by a quadrature rule over the relevant area as summing the energies of the molecules at the quadrature defined sites multiplied by weights proportional to the volume of representation of each representative molecule and the number of molecules in that area. This reduced sum contains far fewer terms than the energy equation described above, giving

$$E_{\text{total}} = \sum_{\alpha=1}^M E_{\alpha} \quad (2.13)$$

where

$$\begin{aligned} E_{\text{total}} &= \text{total local energy,} \\ E_{\alpha} &= \text{energy of representative molecule } \alpha, \\ M &= \text{total number of local representative molecules.} \end{aligned}$$

The molecules that are not included do not possess any properties of their own except their position vector. Only molecules local to the representative node contribute to the properties of the node, as shown in Figure 2.8.

By assuming that the deformation gradient is also homogeneous around the representative node, the local deformation gradient can be defined by F . The deformed configuration has Bravais lattice vectors, b , that are obtained from those in the reference configuration, B , as below:

$$Ba = Fba. \quad (2.14)$$

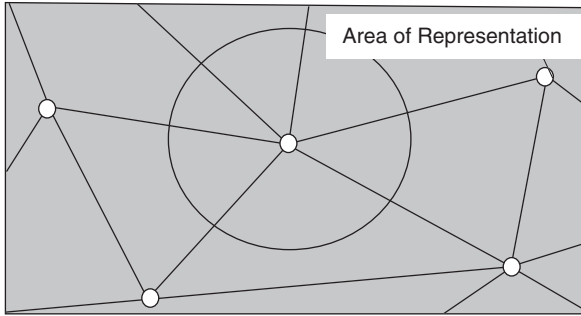


Figure 2.8 Lattice structure of molecules in regions of low gradients.

Once the Bravais lattice vectors are found, the formation of the energy equation reduces to basic lattice statics.

As the area of interest is approached, gradients increase causing the areas that can be assumed to have uniform energy to become smaller and smaller until there cannot be any assumptions about the homogeneity of neighbouring molecules. At this point the nodes of the mesh occupy all molecular sites. It is at this point that all quadrature weights become unity and every molecule is accounted for.

The computational cost of applying this method is relatively high and stays constant throughout changing mesh sizes. However, errors arise from the lack of continuity between cells. This becomes more dominant near the breakdown of the effective FE mesh where there are only a few molecules per cell and the position of the molecules becomes important. This leads to small added forces that can be accounted for. This method is generally used for two- or three-dimensional tests to model defective systems (cracks, dislocations and interfaces) and has recently been selected to study the effect of nano indentation [66].

So far, studies have been limited to solid problems as the lattice structure of a solid leads to an easily predictable deformation. This approach is difficult to apply directly to fluids as new laws for the removal of degrees of freedom will be needed.

2.3.3.2 Approximating methods

A wide range of methods are also available for upscaling molecular information from alternate applications. Molecular simulations rely on molecules being represented by data points with properties associated to them. Point approximating methods such as smooth particle hydrodynamics (SPH) and moving least squares (MLS) are capable of averaging data spread over a number of points. These methods show promise for the upscaling of information from molecular models.

Smooth particle hydrodynamics (SPH) SPH, first presented by Lucy [69], is a continuum particle method that solves continuum equations over a system of moving interpolation points [70, 71]. The property values at any point throughout the fluid relies on the properties of the surrounding points, and it is the method of sampling these properties that has most significance to this application. Instead of sampling the continuum properties, we seek to use this approach to extract the local bulk properties from the molecular motion at discrete nodes placed throughout the flow domain. The SPH method constructs average property values as a function of distance from each central point with the use of a weighting, or kernel, function.

Moving least squares The moving least squares approximation scheme relies on the construction of many least squares approximations applied over a large number of points [72]. This method is generally used for creating smooth surfaces over mesh structures in computer graphics. This method is generally applied as an approximation to all points in the system, taking each one in turn and constructing an approximation from its neighbours. The approximation in MLS is more advanced than the kernel averaging approach of SPH, where a polynomial function is fitted to the local property distribution.

This is similar to the approach taken by Liao and Yip [73], who used the underlying molecular information to fit a continuous predetermined temperature function described over the flow field to the molecular property distribution. Also, the equivalent continuum mechanics (ECM) method [74] used the meshless local Petrov–Galerkin method to solve for the local displacement in a solid molecular lattice.

Coarse-grained molecular dynamics Coarse-grained MD (CGMD) [75] was developed to deal with dynamic and finite temperature systems. In the cases concerning crack propagation, hybrid models work well and allow transfer of strain fields and elastic waves from one region to another, with minimal back-scattering. However, finite element based methods start to break down as scales reach molecular dimensions. One of the basic principles behind the finite element method assumes that the energy of each element is evenly distributed, but when the elements only contain a few molecules, the energies are localized in the nucleus (kinetic energy) and in the covalent bonds between the molecules (potential energy). CGMD provides an alternative to the finite element method that is slightly improved at large scales and greatly improved at small scales at the interface with the molecular dynamic simulation. In situations such as crack propagation or very small systems, high-frequency elastic waves have more of an effect; CGMD provides improved methods to deal with these, but these waves are negligible for larger systems and systems with less strong sources. CGMD constructs the coarse-grained structure with statistical techniques evaluating the interpolation of the

displacement field of the molecules and their equilibrium position, resulting in a weighted sum. This method acts as a replacement for the finite element method described before and shows significant improvement in the treatment of the elastic wave spectrum and small scale analysis. The computational demand is higher than regular finite element techniques, so it is used mainly where high performance is required or where the interface region is close to an area of interest.

2.4 SUMMARY

As has been shown in this and the previous chapters, the continuum equations are unable to account for the molecular scale effects that become important at the meso scales. It is therefore necessary to include this molecular information in the simulation model. This chapter has presented and discussed two approaches by which to include these effects, the ‘top-down’ and ‘bottom-up’ approaches.

The top-down approach uses molecular simulations only in regions where they are needed, as the final level of refinement in a mesh. This approach is useful when considering a large system possessing a few small areas where molecular scale detail is needed. However, several issues arise, especially when considering fluids. To couple a molecular region to a continuum mesh requires the continuum analysis to be valid with only a small number of molecules in each element. This is at the extreme of, and possibly past, the limits of the continuum approximation. Also, problems occur at the boundary between the two regions in fluid systems. The chaotic molecular motion of fluid molecules does not allow for simple boundary treatment at fluid boundaries, as the surrounding continuum region will not allow the use of periodic boundaries.

The chaotic nature of meso scale fluid systems leads to a bottom-up scheme, which is more suitable in most situations. Here, the physics of the system is governed by a molecular model, and information is upscaled and areas of low activity can be simplified. These methods are, however, very computationally demanding for large scale systems, but can present a very accurate solution. The way in which information is passed and degrees of freedom are removed is critical to the success of this approach. Approximation methods such as least squares and SPH are well suited to this application as they provide a reliable and well tested method for approximating information over many points.

In the next chapter, a method is developed specifically to tackle fluid simulation at meso scales.

3

Meso Scale Model Based on First Principles

Aim. The reader should understand how fluid modelling at the meso scale can be undertaken by employing molecular physics models to characterize bulk properties.

3.1 INTRODUCTION

The meso scale represents the range of scales in between the scales that can be defined by the continuum laws (typically $\gtrsim 10^{-6}$ m) and molecular physics (typically $\lesssim 10^{-9}$ m). The behaviour of fluid at these scales is neither fully described by the bulk continuum nor the molecular scale properties and physics. Continuum simulations are unable to model molecular scale effects, which presents a lower limit to the scale at which these approximations can be used. A molecular scale fluid model can predict the behaviour of fluid by considering thousands of molecular interactions, but provides no method of quantifying bulk effects, such as viscosity or temperature and velocity gradients, throughout the flow field.

Continuum mechanics, however, can describe and quantify these bulk properties, but molecular scale effects are ignored. The onset of molecular behaviour must be understood to recognize the point at which the continuum approximations fail.

The molecular dynamics simulations are able to predict the behaviour of the fluid accurately, but in order to describe the flow quantitatively, the bulk characterizing properties, such as pressure, temperature and velocity, need to be extracted. Such properties arise from the molecular interactions intuitively modelled by the molecular simulation, but are not quantified locally for at molecular scales they

are not well defined and have little meaning. At meso scales, these have increased importance as the bulk effects are visible and need to be considered in engineering applications.

In this chapter a bottom-up meso scale approach is developed and explained. A molecular model is implemented to control the physics of the fluid, along with tools and modifications to improve the efficiency when dealing with large numbers of molecules. Also, areas of low activity are simplified (such as solid boundaries) to improve efficiency further. This physics model then passes molecular information to the upscaling routines where it is used to characterize the bulk fluid effects in terms of useful engineering properties.

3.2 FLUID PHYSICS MODEL

To model meso scale fluid flows from first principles, the physics of the fluid behaviour must be considered at a scale smaller than the meso scale. For this, a molecular dynamics model is used to evaluate the system in terms of the molecular interactions. As it is intended for the model to work with dense as well as sparse fluids, the molecules interact via a soft sphere model with the nonbonded Lennard–Jones 12-6 potential. The use of molecular dynamic simulations has been highlighted in Section 1.4 and will be used along with the diffuse boundary conditions. The molecular model must be capable of simulating large numbers of molecules to allow access to meso scale systems of reasonable density (computational demand of a molecular simulation is heavily dependent not only on the number of molecules in the system but also on the number of neighbours possessed by each molecule, which is related to the fluid density).

To keep track of the neighbours of each molecule, an efficient book keeping scheme, the Verlet lists, is implemented for the molecular dynamics model.

3.2.1 Book Keeping

3.2.1.1 Verlet lists

The most common method used to search for and store possible interactions is known as the Verlet neighbour lists [76], and is described below. This method works by using two arrays, one that stores the actual interactions (*nlist*) and another that acts as an index (*npoint*), referencing the start points for the neighbour lists of each individual molecule.

Once these arrays have been initialized, a full search is performed for every molecule i for all other molecules within R_N . The search is performed within a radius that is larger than the cut-off radius R_C for the potential to include all particles that will interact with sphere i over the next n time steps (Figure 3.1).

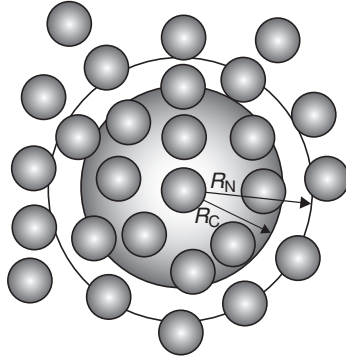


Figure 3.1 Interaction radius of the cut-off potential R_C and neighbour search R_N .

The difference between R_N and R_C is limited by the root-mean-square velocity of the simulation, with

$$R_N - R_C < n\tilde{v}h, \quad (3.1)$$

where R_C and R_N are the cut-off radius for the list and the potential respectively, n is the number of time steps between list updates, h is the time step length and \tilde{v} is the root-mean-square velocity for the simulation. This limits the thickness of the region so that a molecule from outside the neighbour list cannot travel into a sphere's interaction zone (R_C) without being included by an update of the list. This removes the need for the complete neighbour list to be repopulated at every time step; it is only updated periodically, saving a significant amount of computational time.

For any molecule in the system, i , the neighbour search is performed over all molecules numbered $> i$. This prevents the same pairwise interactions being recorded twice, in an interacting pair, as both will be in each other's interaction zone.

For a system of N particles, the pointer list, `npoint`, will contain N entries. The value stored for each molecule refers to the entry number of `npoint` at which the neighbour list for that molecule starts. Therefore, the number of entries in `npoint` is much higher as, depending on density, each particle has around 50 neighbours, which leads to an array of at least 15 000 entries for a system of 300 particles. This is illustrated in Figure 3.2.

An alternative to the Verlet lists was proposed by Sun and Ebner [77] where arrays were used to achieve the same effect. This used no extra memory and performance scaled with the number of molecules in the system. However, the reference locality was broken in these lists, reducing the performance for large systems.

Once the neighbour lists have been updated, they are used to evaluate the net force exerted on each molecule by its neighbours.

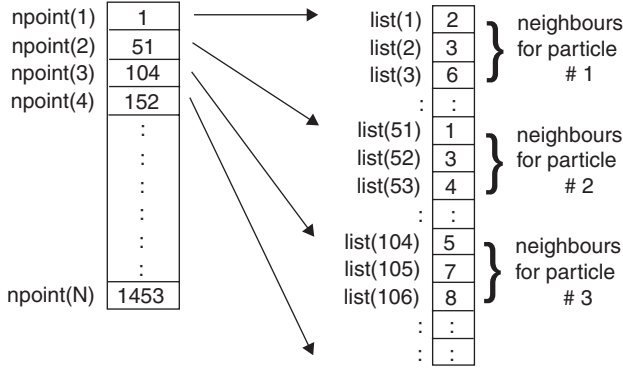


Figure 3.2 Verlet list book keeping scheme.

3.2.2 Force Interactions

The Lennard–Jones potential function is used for energy calculations and the force for each interaction is derived from the potential function

$$F_i = -\frac{\partial U(r_{ij})}{\partial r_{ij}}, \quad (3.2)$$

where F is the force acting between the two molecules (positive for molecule i and negative for molecule j ; Newton’s third law) and U is the potential function. This represents the force acting along the line between the centres of the two molecules, and the resulting force is applied in opposite directions to both molecules using Newton’s third law to save the same interaction being calculated again from the opposite direction. Applying the force of the collision to both molecules halves the number of collisions that need to be processed as each pair needs only to be evaluated once. This is done by only evaluating the entries in the list where $i > j$. The forces are converted to units of acceleration, enabling the time step part of the simulation to proceed.

3.2.3 Time Integration Scheme

Given an initial resultant force for each molecule, the first step in the time progression loop is to predict the new positions of all the molecules at the new time. There are several methods used to do this [24], and all are based on the simple finite difference algorithm.

3.2.3.1 Verlet algorithm

This is the most commonly used algorithm in molecular dynamic simulations, mainly because of its simplicity. The algorithm proceeds as follows:

1. Perform a Taylor series expansion of $r(t)$ forward and backward in time:

$$r(t + \Delta t) = r(t) + \frac{\partial r}{\partial t}(t)\Delta t + \frac{1}{2!} \frac{\partial^2 r}{\partial^2 t}(t)\Delta t^2 + \frac{1}{3!} \frac{\partial^3 r}{\partial^3 t}(t)\Delta t^3 + O(\Delta t^4), \quad (3.3)$$

$$r(t - \Delta t) = r(t) - \frac{\partial r}{\partial t}(t)\Delta t + \frac{1}{2!} \frac{\partial^2 r}{\partial^2 t}(t)\Delta t^2 - \frac{1}{3!} \frac{\partial^3 r}{\partial^3 t}(t)\Delta t^3 + O(\Delta t^4). \quad (3.4)$$

2. Add these two expressions together:

$$r(t + \Delta t) = 2r(t) + r(t - \Delta t) + \frac{\partial^2 r}{\partial^2 t}(t)\Delta t^2 + O(\Delta t^4). \quad (3.5)$$

Equation (3.5) is the general form of the Verlet algorithm.

It is easy to see that the truncation error varies with Δt^4 , making the prediction accurate to the third order, despite the absence of any third-order terms. However, there comes a problem when starting off the algorithm, as the approximation for $t + \Delta t$ relies on the current and previous time steps, $t - \Delta t$. At $t = 0$, it is common to use the backward Euler method to estimate a value for $r(-\Delta t)$.

3.2.3.2 Gear's predictor–corrector algorithm

The predictor–corrector algorithm devised by Gear [78, 79] is used to describe the progression of the molecules throughout the domain during the simulation time t , which is broken down into a finite number of short time steps. The time step is sufficiently small, so the forces and accelerations can be considered as constant. Forces and accelerations are updated once every time step. There are three basic steps in this algorithm, prediction, evaluation and correction:

- *Prediction.* Position, velocity, acceleration, third, fourth and usually fifth derivatives are predicted at $t + \Delta t$ from current time t using a simple Taylor series for each molecule in the time step:

$$\begin{aligned} r_i(t + \Delta t) = & r_i(t) + r_i^i(t)\Delta t + r_i^{ii}(t)\frac{(\Delta t)^2}{2!} + r_i^{iii}(t)\frac{(\Delta t)^3}{3!} \\ & + r_i^{iv}(t)\frac{(\Delta t)^4}{4!} + r_i^v(t)\frac{(\Delta t)^5}{5!}, \end{aligned} \quad (3.6)$$

$$\dot{r}_i(t + \Delta t) = \dot{r}_i^i(t) + \dot{r}_i^{ii}(t)\Delta t + \dot{r}_i^{iii}(t)\frac{(\Delta t)^2}{2!} + \dot{r}_i^{iv}(t)\frac{(\Delta t)^3}{3!} + \dot{r}_i^v(t)\frac{(\Delta t)^4}{4!}, \quad (3.7)$$

$$\ddot{r}_i(t + \Delta t) = \ddot{r}_i^{ii}(t) + \ddot{r}_i^{iii}(t)\Delta t + \ddot{r}_i^{iv}(t)\frac{(\Delta t)^2}{2!} + \ddot{r}_i^v(t)\frac{(\Delta t)^3}{3!}, \quad (3.8)$$

$$r_i^{iii}(t + \Delta t) = r_i^{iii}(t) + r_i^{iv}(t)\Delta t + r_i^v(t)\frac{(\Delta t)^2}{2!}, \quad (3.9)$$

$$r_i^{iv}(t + \Delta t) = r_i^{iv}(t) + r_i^v(t)\Delta t, \quad (3.10)$$

$$r_i^v(t + \Delta t) = r_i^v(t). \quad (3.11)$$

- *Evaluation.* The force evaluation at time t yields a net force on each particle, which is converted to acceleration ($F = ma$) and compared with the predicted acceleration from the previous step, resulting in an error signal:

$$F_i = \sum_{i \neq j}^N -\frac{\partial U(r_{ij})}{\partial r_{ij}} \hat{r}_{ij}, \quad (3.12)$$

where \hat{r}_{ij} is the unit vector between the centres of spheres i and j . This force is then converted to an acceleration by dividing by the mass of the particle and subtracting from it the predicted value for acceleration, $\ddot{r}_i(t + \Delta t)$, giving $\Delta \ddot{r}_i$.

- *Correction.* The error signal $\Delta \ddot{r}_i$ from the difference between the accelerations is multiplied by a stability factor and used to adjust the positions. The stability factor set depends on the time step to maximize the stability of the algorithm:

$$\Delta R_i^{ii} = \frac{\Delta r_i^{ii}(\Delta t)^2}{2!}, \quad (3.13)$$

$$r_i = r_i^p + \alpha_o \Delta R_i^{ii}, \quad (3.14)$$

$$r_i^i = r_i^{ip} \Delta t + \alpha_1 \Delta R_i^{ii}, \quad (3.15)$$

$$\frac{r_i^{ii}(\Delta t)^2}{2!} = \frac{r_i^{iip}(\Delta t)^2}{2!} + \alpha_2 \Delta R_i^{ii}, \quad (3.16)$$

$$\frac{r_i^{iii}(\Delta t)^3}{3!} = \frac{r_i^{iiip}(\Delta t)^3}{3!} + \alpha_3 \Delta R_i^{ii}, \quad (3.17)$$

$$\frac{r_i^{iv}(\Delta t)^4}{4!} = \frac{r_i^{ivp}(\Delta t)^4}{4!} + \alpha_4 \Delta R_i^{ii}, \quad (3.18)$$

$$\frac{r_i^v(\Delta t)^5}{5!} = \frac{r_i^{vp}(\Delta t)^5}{5!} + \alpha_5 \Delta R_i^{ii}. \quad (3.19)$$

The corrected positions are then fed back into the Taylor series approximation for the next time step, and the simulation can proceed.

Table 3.1 Coefficients of the fifth-order Verlet algorithm.

Order	Third	Fourth	Fifth
a_0	$\frac{1}{6}$	$\frac{19}{120}$	$\frac{3}{16}$
a_1	$\frac{5}{6}$	$\frac{3}{4}$	$\frac{251}{360}$
a_2	1	1	1
a_3	$\frac{1}{3}$	$\frac{1}{2}$	$\frac{11}{18}$
a_4		$\frac{1}{12}$	$\frac{1}{6}$
a_5			$\frac{1}{60}$

Values for stability factors α_i depend on the order of the Taylor series expansion [4] and are shown in Table 3.1. These values can be derived by studying the resulting stability matrices. The accuracy of the prediction relies on the order, k , of the expansion due to the truncation error, $O(\Delta t^{k-1})$.

The main advantage of this method is its versatility, which takes a single step forward in time but can be modified to become a multistep method by combining it with the Verlet algorithm. The algorithm can be extended by adding terms to the Taylor series or using the stability factor to maintain stability for a larger or smaller time step.

3.2.3.3 Velocity Verlet algorithm

The velocity Verlet Algorithm is similar to the Verlet algorithm, but is performed over two half time steps. The algorithm proceeds as follows:

1. Evolve velocities by half the total time step, $\delta t/2$:

$$v_i(t + \delta t/2) = v_i(t) + a_i(t)\delta t/2. \quad (3.20)$$

2. Use these projected half time step velocity values to evolve positions at the full time step, δt :

$$r_i(t + \delta t) = r_i(t) + v_i(t)\delta t + a_i(t)\delta t^2/2, \quad (3.21)$$

which becomes

$$r_i(t + \delta t) = r_i(t) + v_i(t + \delta t/2)\delta t. \quad (3.22)$$

3. Update the intermolecular forces and convert using Newtons law, $F = ma$, to achieve updated accelerations for all the molecules.

4. Complete the velocity time step:

$$v_i(t + \delta t) = v_i(t + \delta t/2) + a_i(t + \delta t/2)\delta t/2. \quad (3.23)$$

The velocity Verlet algorithm is the most compatible time integration method with thermostats and temperature controls, and is implemented into the model described above. This method also requires less storage than the predictor–corrector algorithm as only the position, velocity and acceleration vectors need to be stored between time steps, reducing the computational resources required. It is also simple and easily integrated, with a wide variety of thermostating methods.

Time step The selection of the optimal time step is crucial in molecular dynamics simulations. A large time step will progress the simulation time with minimal CPU (central processing unit) time. However, a time step that is too large can have two effects:

- Large time steps. The integration scheme assumes that the forces on each molecule are constant over the length of the time step. If the step is too large the deviation from this assumption causes errors in the calculation and conservation of energy.
- Very large time steps. Molecules may move large distances between successive steps and when close to other molecules may jump from low interaction to extremely high interaction forces where the molecules overlap. This can cause unphysically high forces and instability in the system. This behaviour often results in a complete breakdown of the molecular behaviour and energies, which tend to infinity.

The optimal time step will conserve energy and provide the greatest leap forward for the simulation time for each step. To examine this effect, the results of a simple investigation are presented. The system contains 114 molecules in a 2 nm wide periodic cube and the effect on average energy with a range of time steps is evaluated.

Figure 3.3 shows plots for kinetic and potential energy against a range of lengths of time step, varying from 0.5 fs to 25 fs. It was found that increasing

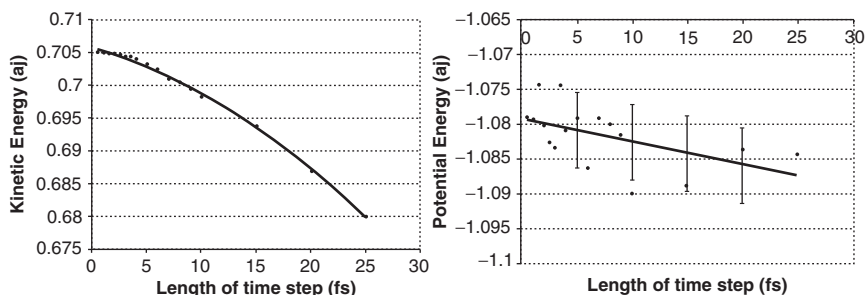


Figure 3.3 Graphs showing the effect of increasing the time step from 0.5 fs to 25 fs on kinetic energy (left) and potential energy (right).

the time step beyond 25 fs causes massive instabilities in the system and energy levels become extremely unphysical. The kinetic energy of the system is shown to drop by larger and larger amounts as the time step increases. The potential energy shows a slightly increasing trend (in terms of negative values) but noise of 0.5 % about the line of best fit.

As the time step approaches zero, the kinetic energy approaches a value of 0.7057 aj (attojoule, $J \times 10^{-18}$) and the potential energy approaches approximately -1.0792 aj. To obtain the best and most stable results, the system's energy should be as close as possible to these values. A time step of 2 fs can be seen to maintain energy levels to within 0.02 % for kinetic energy and ± 0.5 % for potential energy, while still progressing the simulation at an acceptable rate. A time step of 2 fs is used in all models presented in this book.

3.2.4 Boundary Conditions

Having achieved an efficient molecular physics model, the boundary conditions surrounding the fluid should also be efficient and appropriate to the scale of the system of interest. This is done with the implementation of the diffuse boundary conditions.

3.2.4.1 Diffuse boundary conditions

The diffuse boundary condition replaces a dynamic/static molecular wall with a smooth planar boundary with appropriate hydrodynamic conditions to replicate the scattering occurring from the corrugation, or roughness, of the molecular wall [61]. This effect is shown in Figure 3.4, where the figure on the left shows a single molecule approaching a molecular wall. Depending on whether it hits a wall molecule on its side or on top, it rebounds in a different direction. The figure on the right shows the effect of the diffuse boundary conditions, where the same effect of the molecular scattering is replicated over many molecular collisions.

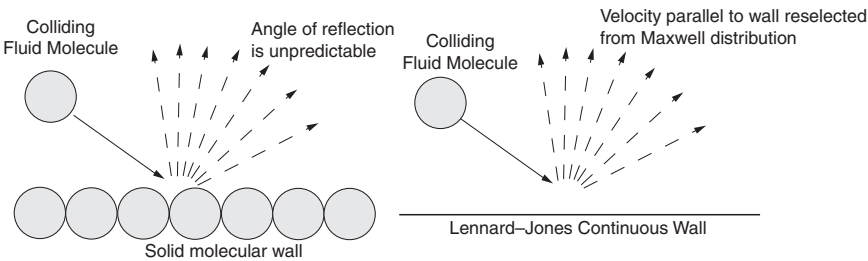


Figure 3.4 The diffuse boundary conditions.

The scattering is performed by selecting a proportion of molecules and re-selecting their component of velocity parallel to the wall from the Maxwell–Boltzmann distribution for the set temperature of the wall. The Maxwell–Boltzmann distribution for velocity is different from the speed distribution (Equation 1.50), and is defined as

$$g(v) = \sqrt{\frac{m}{2\pi k_b T}} e^{-mv^2/(2k_b T)} \quad (3.24)$$

which is shown in Figure 3.5.

The proportion of molecules selected for this ‘thermalization’ is set by the *tangential momentum accommodation coefficient*, f , for the solid.

Tangential momentum accommodation coefficient, f The tangential momentum coefficient is the proportion of molecules that go through the thermalization process in the diffuse boundaries. Its value can range from 0 to 1, to represent the degree of corrugation of the solid. Different degrees of corrugation occur for the following cases:

- $f = 0$. This is the extreme case, where none of the colliding molecules are thermalized by the solid. The colliding molecules maintain 100 % of their momentum parallel to the wall and are only affected by the intermolecular interaction potential perpendicular to the wall.

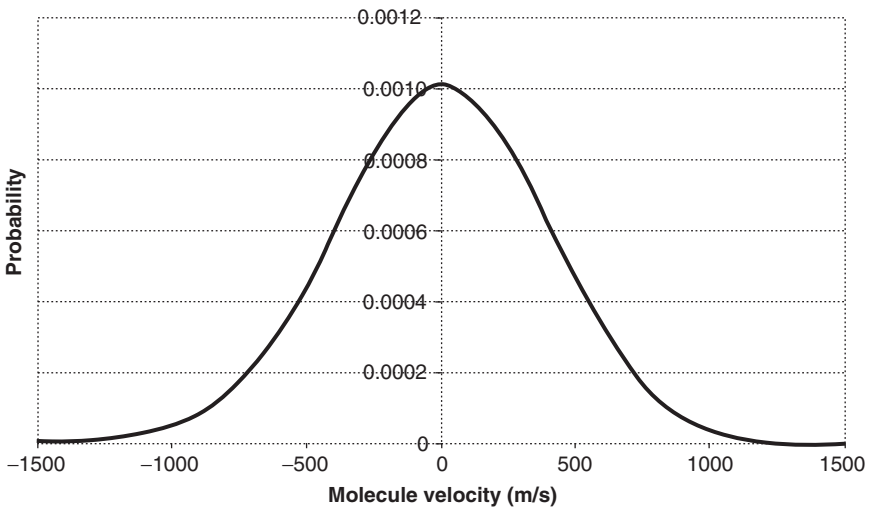


Figure 3.5 Velocity distribution molecules in a fluid system for a single component of velocity.

In this case the walls are perfectly smooth and there is no thermal exchange between the two.

- $f = x$. In the case of $f = x$, the proportion of colliding molecules, x , have their velocities parallel to the wall reselected from the Maxwell–Boltzmann distribution. This effectively removes $(x \times 100)\%$ from the momentum of the fluid close to the wall (as the average of the Maxwell–Boltzmann distribution is zero), thereby creating a drag force between the fluid and wall.

The Maxwell–Boltzmann distribution is a function of wall temperature, and the thermalized molecules enable the addition or removal of thermal energy from the fluid. This can be used as a method of thermostating the system or applying a temperature gradient or boundary condition to the flow.

The tangential momentum coefficient therefore acts to vary the exchange that occurs between the fluid and wall in terms of thermal and bulk kinetic energy. The reselection of the velocities also achieves molecular scattering of colliding molecules, similar to the effect of a fully molecular wall, but averaged over a large number of collisions.

- $f = 1$. This is the extreme case of perfect stick between the fluid and the wall. In this case, 100 % of the colliding molecules undergo the thermalizing process, removing all of the linear momentum of the fluid at the wall (as the average of the velocities applied will be zero). This represents the condition of no slip between the fluid and boundary, and the condition that the fluid and wall will be at the same temperature at the boundary. This is not to be confused with the no-slip condition used in continuum mechanics, as this extreme case is unlikely and results from strong interaction forces in a molecularly sparse solid, whereas the continuum no-slip condition occurs from an approximation of scale, as well as frictional effects.

Arya *et al.* [61] demonstrated that the tangential momentum accommodation coefficient was dependent on two dimensionless variables, the reduced roughness and the reduced energy. The reduced roughness

$$\frac{\sigma_{fw}}{L} \tag{3.25}$$

is the ratio of the fluid–wall Lennard–Jones interaction radius, σ_{fw} , and the lattice spacing, L . L is the diagonal spacing between solid molecule sites, shown in Figure 3.6.

The reduced energy is defined as the ratio of the Lennard–Jones well depth, ϵ_{fw} , to the thermal energy:

$$\frac{\epsilon_{fw}}{k_b T} \tag{3.26}$$

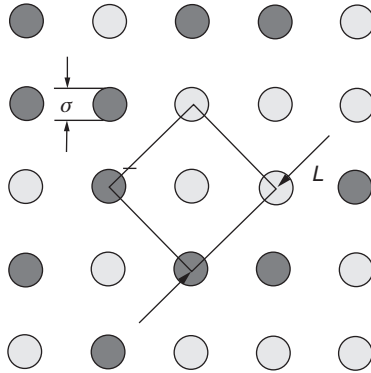


Figure 3.6 Example of a solid lattice displaying the lattice spacing parameter L and the wall molecule diameter σ .

They also found that f was dependent on the bulk velocity of the fluid, but this only has an effect at large velocities.

By studying a fully molecular boundary, Arya *et al.* [61] were able to plot values for a wide range of f . Values for f are also confirmed by the work by Sokhan *et al.* [60] who performed similar investigations for the tangential momentum accommodation coefficient for the flow between parallel plates. Values for carbon nanotubes have been studied in depth by Cooper *et al.* [80] and Bhatia *et al.* [81].

Implementation Because of the separate treatment of the parallel and perpendicular components of the colliding molecule, the diffuse boundaries require a more complex implementation than an interacting molecular wall. Because of the soft sphere nature of the simulation, there are no instantaneous collisions, only molecules that are interacting with the wall. It is therefore critical to clarify the definition and criteria that a molecule near a boundary must satisfy if it is to be considered as colliding. To be accepted as a colliding molecule, a molecule must be:

- within the repulsive zone of the walls interaction potential;
- experience a change of direction perpendicular to the wall.

The first criteria is tested by calculating the perpendicular distance, d , between the molecule and the wall, as illustrated in Figure 3.7. The section of boundary is defined by the line between two points, stored in the boundary vector b :

$$b = \begin{bmatrix} x_{b2} - x_{b1} \\ y_{b2} - y_{b1} \end{bmatrix} \quad (3.27)$$

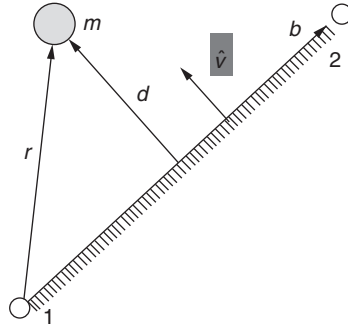


Figure 3.7 Calculating distance, d , between the molecule and the wall from the position vector, r , and the boundary vector, b ; d has unit vector \hat{v} .

and the position vector r is defined as the distance between the molecule (m) and the start of the boundary, at point 1:

$$r = \begin{bmatrix} x_{b1} - x_m \\ y_{b1} - y_m \end{bmatrix}. \quad (3.28)$$

The unit vector, \hat{v} , normal to the boundary is

$$\hat{v} = \frac{\begin{bmatrix} y_{b2} - y_{b1} \\ -(x_{b2} - x_{b1}) \end{bmatrix}}{\left| \begin{bmatrix} y_{b2} - y_{b1} \\ -(x_{b2} - x_{b1}) \end{bmatrix} \right|}. \quad (3.29)$$

To find the distance d , the dot product of the position vector and the unit vector \hat{v} is taken as

$$\alpha = |\hat{v} \cdot r| = \frac{|(x_{b2} - x_{b1})(y_{b1} - y_m) - (x_{b1} - x_m)(y_{b2} - y_{b1})|}{\sqrt{(x_{b2} - x_{b1})^2 + (y_{b2} - y_{b1})^2}}, \quad (3.30)$$

which can be simplified to

$$\alpha = \frac{x_m(y_1 - y_2) + y_m(x_{b2} - x_{b1}) + x_{b2}y_{b1} + x_{b1}y_{b2}}{\sqrt{(x_{b2} - x_{b1})^2 + (y_{b2} - y_{b1})^2}}. \quad (3.31)$$

Distance can then be calculated by multiplying α by the direction \hat{v} and the magnitude of r :

$$d = \alpha |r| \hat{v}, \quad (3.32)$$

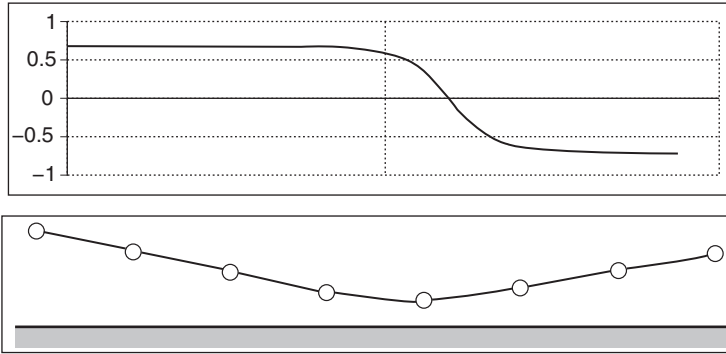


Figure 3.8 Variation of the dot product with the molecular distance from the wall.

Which can then be used to calculate the strength of the interaction between the molecule and the wall, which in turn can be used to detect the first criteria for a colliding molecule, as described above, as well as calculating the repulsive force.

The second criteria is evaluated in a similar way. By looking at the dot product of velocity and the unit vector perpendicular to the boundary, and monitoring its change between time steps, the point at which the molecule stops moving towards the boundary and starts moving away can be identified. At this point, the sign of the dot product changes, as shown in Figure 3.8. If a molecule is considered to collide with the boundary, by satisfying the criteria described above, it is then given a random number to be compared against the tangential momentum accommodation coefficient, f . If this test is successful and the molecule is accepted for thermalization by the wall, the parallel component of velocity is found, again by taking the dot product, but parallel to the boundary. This velocity is then randomly picked from the Maxwell–Boltzmann distribution (Equation (3.24)) for the temperature of the wall.

This boundary method provides a good approximation for solid boundaries right down to the molecular scale [82], and as the scale of the simulation increases and the number of collisions in the length and time scale of the system increases, the accuracy of the approximation also increases.

3.2.5 Modified Boundary Potential

As these diffuse boundaries are modelled as smooth planes, a standard Lennard–Jones interaction at the boundary does not take into account the depth of the solid. If the solid is more than one layer of molecules thick, the fluid may experience a stronger attractive force as the long-range attractive part of the potential of other solid layers reaches into the fluid domain. Figure 3.9 shows this effect; the smooth boundary is positioned at $x = 0$ and the effect of two layers within the solid is

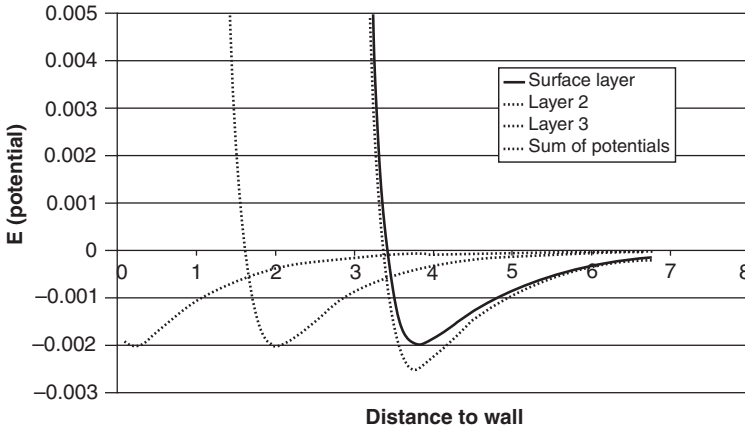


Figure 3.9 Total Lennard–Jones potential for three molecular layers.

shown. The resulting potential shows a much stronger attractive component. This must be taken into account by the interaction potential between the solid and fluid, and can be done by modifying the parameters, σ and ϵ , for the solid and fluid of interest.

This section has developed a molecular fluid model capable of efficient simulation of systems containing large numbers of molecules. However, this model handles the motion of individual molecules. The information from this model describes, but fails to characterize, the bulk fluid effects present in meso scale fluid systems. The characterization of these bulk effects and the description of the fluid in terms of its bulk properties is critical to engineering applications. The next section implements a method for extracting such information from the molecular system using the ensemble properties described in Section 1.2.1.

3.3 EXTRACTING LOCAL BULK PROPERTIES

The data possessed within the molecular flow model is chaotic and adjacent molecules can possess very different properties that average out over a large number of molecules to an approximately stable value. To allow the examination of bulk properties and their distribution throughout the flow domain, ensemble properties are assembled from local averages at discrete points through the flow field. Each point is assigned a subdomain from which to draw its information. The number of molecules within each subdomain can vary significantly for a large number to only a few. The approximating method must therefore be able to deal with these potential problems. The bin averaging method presents a crude approximation that has no refinement or weighting parameter, which gives noisy local averages even with a large amount of data, making it impractical for property distributions over

short simulation runs (time is critical, especially for simulations of large numbers of molecules, within the meso scale). The smooth particle hydrodynamics (SPH) method improves the approximation by applying a weighting (or kernel) function to the approximation. The least squares approximation uses the strength of the SPH method to fit a predetermined polynomial to the underlying property distribution. This is the most demanding of the three methods (and requires a small matrix inversion), but provides a good opportunity for high sampling resolution in time and space.

3.3.1 Approximation Method

The upscaling of information needs to be done in such a way that no important information is lost or altered. During this process some information is lost, as the point of upscaling is to remove unnecessary detail and degrees of freedom. Therefore, the information must be included into the assembly of the bulk properties. There are several well-known interpolating schemes available, such as moving least squares and smooth particle hydrodynamics that will be discussed along with the simple bin averaging scheme. The methods below aim to construct local ensemble averages of molecular properties at points placed throughout the domain, which together can be used to study the distribution of bulk properties over the whole domain.

The most simple method of assembling bulk property distributions is the bin averaging scheme.

3.3.2 Bin Averaging

The simplest way of averaging and upscaling molecular properties is the bin averaging scheme. This is where the molecular domain is divided into discrete cells and all the molecules in each cell are averaged to construct the ensemble properties for that cell (Figure 3.10). The bin averaging scheme has significant drawbacks. The resulting distributions can have significant variations, as adjacent molecules could be in different cells and two molecules on opposite sides of the same bin could have completely different properties but contribute equal weighting to the average. The resulting distribution is rough and contains a substantial amount of noise, and in order to be able to obtain smooth property distributions throughout the flow field, a large sample time is necessary. This reduces the time resolution of the samples that can be taken and can increase the overall time of the system to get a stable steady result.

The bin averaging is, however, easy to implement and is still widely used to investigate steady systems [60]. The drawbacks of this method lead to the search for a more refined approach that will allow for better time resolution and shorter sample times with less statistical noise.

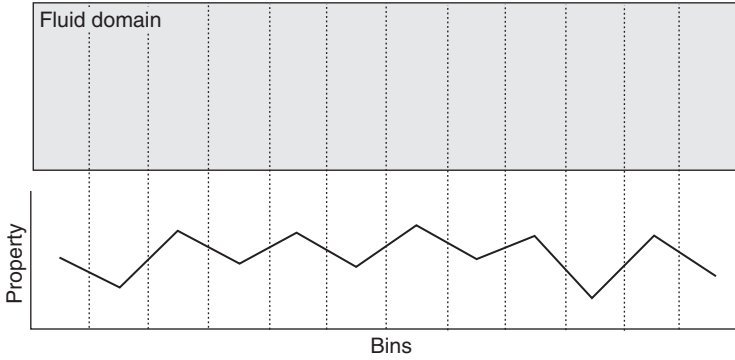


Figure 3.10 Bin averaging scheme.

3.3.3 Smooth Particle Hydrodynamics (SPH)

SPH, first presented by Lucy [69], is a continuum particle method that solves continuum equations over a system of moving interpolation points [70, 71]. The property values at any point throughout the fluid relies on the properties of the surrounding points; it is the method of sampling these properties that has most significance to this application. Instead of sampling the continuum properties, we seek to use this approach to extract the local bulk properties from the molecular motion at discrete nodes placed throughout the flow domain.

The sampling is done in a similar way to the molecular dynamics searching, where the molecules around each node are evaluated, but the properties of each node are given a weighting as a function of their proximity to the node. In this way the molecules closest to the node contribute more than the molecules further away, allowing the node to represent best the property value at that exact point in the flow field. The resulting distribution is much smoother than the bin averaging method, but is completely reliant on the strength of the weighting, or kernel function.

3.3.3.1 Approximation

The approximation is constructed using an integral for the function based on the delta function:

$$f(x) = \int_{\Omega} f(x') \delta(x - x') dx', \quad (3.33)$$

$$\delta(x - x') = \begin{cases} 1, & x = x' \\ 0, & x \neq x' \end{cases}. \quad (3.34)$$

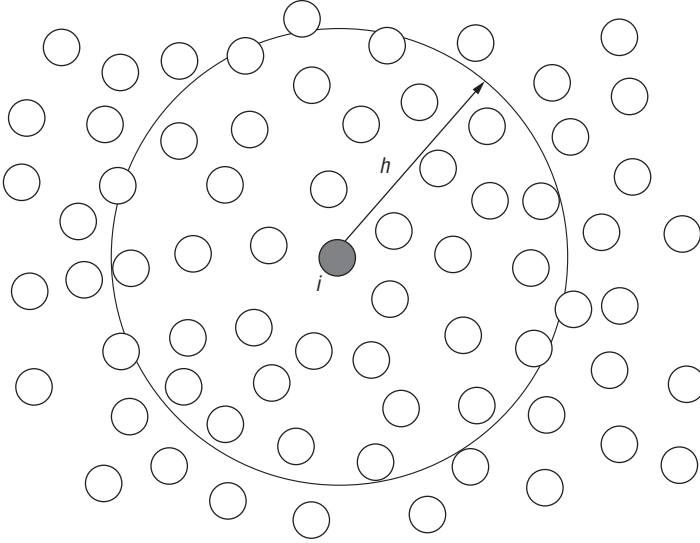


Figure 3.11 Smoothing length, h .

The first equation is exact as the function value is calculated at x , integrated over its volume. The delta function, however, is of no use when approximating many molecules so a weighting function is used instead. This replacement causes the function to become representative, and therefore approximate:

$$f(x) \approx \int_{\Omega} f(x')w(x - x', h) dx', \quad (3.35)$$

where $w(x - x', h)$ is the kernel weight function with h being the smoothing length, also known as the radius of the zone of influence, as shown in Figure 3.11. The kernel function is of critical importance to SPH as there is no assumption made about the distribution of data with which to form an approximation; it is solely the strength of the kernel that governs the accuracy. The integral is converted to a summation of a set of molecules to be used in a simulation, with the approximation of property $f(x)$ denoted by the addition of angled brackets $\langle f(x) \rangle$:

$$\langle f(x) \rangle = \sum_{j=1}^N f(x')w(x - x', h)\Delta V. \quad (3.36)$$

This sums the weighted contribution for all the particles, $j = 1, 2, 3, \dots, N$ within the smoothing length, or the zone of influence of the approximated point to achieve the approximate value at point i .

The derivative of a function, and hence the flux of a property, can also be represented by the SPH approximation by substituting $f(x)$ for $\nabla \cdot f(x)$ in the above equation:

$$\langle \nabla \cdot f(x) \rangle = \int_{\Omega} [\nabla \cdot f(x')] w(x - x', h) dx'. \quad (3.37)$$

3.3.3.2 Errors

As the approximation relies mainly on the strength of the kernel, to perform an error analysis Equation (3.37) is expanded in a Taylor series within the integral form:

$$\langle f(x) \rangle = \int_{\Omega} \{f(x) + f'(x)(x - x') + r[(x - x')^2]\} w(x - x', h) dx', \quad (3.38)$$

$$\langle f(x) \rangle = f(x) \int_{\Omega} w(x - x', h) dx' + f'(x) \int_{\Omega} (x' - x) w(x - x', h) dx' + r(h^2), \quad (3.39)$$

where r is the residual and the first integral, $f(x) \int_{\Omega} w(x - x', h) dx'$, can be simplified from the continuity conditions of the weighting functions discussed previously, where the integral of the kernel is equal to 1:

$$\int_{\Omega} w(x - x', h) dx' = 1. \quad (3.40)$$

The kernel is also an even function, so

$$\int_{\Omega} (x' - x) w(x - x', h) dx' = 0. \quad (3.41)$$

This reduces the error function down to

$$\langle f(x) \rangle = f(x) + r(h^2). \quad (3.42)$$

Therefore the error of the SPH kernel approximation of a function is of the order h^2 .

The smooth particle hydrodynamics (SPH) method adds a weighting (or kernel) function to the approximation, but as the SPH approximation is only based on the kernel, it is best suited to stable property distributions, where there is little noise and values change slowly and steadily throughout the subdomain.

3.3.4 Moving Least Squares

3.3.4.1 Method

The moving least squares approximation scheme relies on the construction of many least squares approximations applied over a large number of points [72]. It is generally used for creating smooth surfaces over mesh structures in computer graphics. It is generally applied as an approximation to all points in the system, taking each one in turn and constructing an approximation from its neighbours. This is best described in one dimension (Figure 3.12). In the whole domain there are nodes distributed with positions, x , so a start is made by selecting an arbitrary node, i . This node is then assigned a 'zone of influence' and all neighbouring particles contribute to the local approximation of the function. The distance from the central node, i , determines the strength of the influence a neighbour has on the approximation so that nodes closer to i have more influence than a node close to the limit of the zone.

These approximations are performed on every node, so that the end result is a system of particles with associated functions describing the approximation at each node. The combination of all of the local approximations leads to a global approximation over the whole simulation domain.

The moving least squares method applies a least squares approximation of the neighbourhood at points throughout the domain in order to construct a global approximation (Figure 3.13). In the molecular upscaling framework, the molecular properties are averaged at points defined by a coarse fixed grid over the domain. At each point the ensemble bulk properties are constructed as follows: a set of N molecules within a system, with individual positions x_i , y_i and z_i having

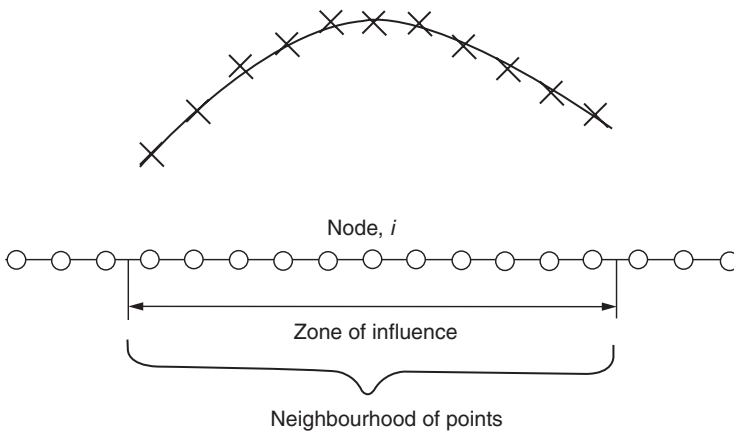


Figure 3.12 Least squares neighbourhood approximation.

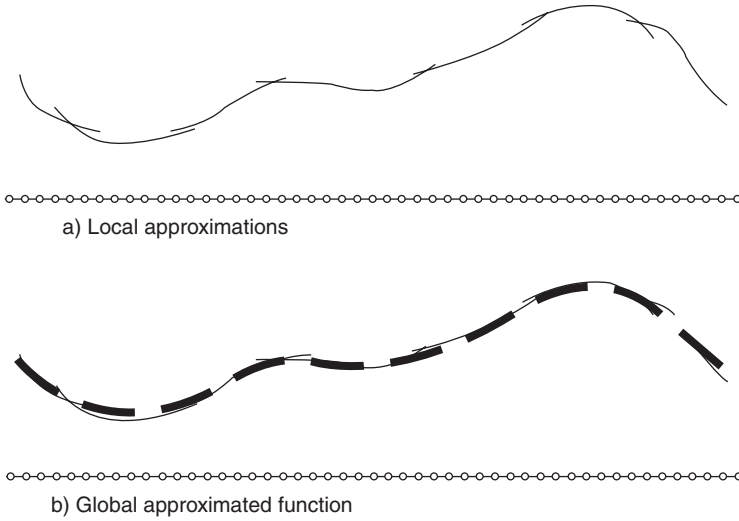


Figure 3.13 MLS local to global approximation.

associated parameter values u_i for $i = 1$ to N . The calculation will be illustrated using two dimensions for the purpose of simplicity and readability. Therefore, for a system of n neighbouring points with positions x_i and y_i ($i = 1, 2, 3, \dots, n$), the parameters are stored as

$$u^T = \{ u_1 \ u_2 \ \dots \ u_i \}. \quad (3.43)$$

The local approximation at the node (x, y) of U , U^h , is assumed to take the form of a polynomial over the local subdomain. For this example, the approximation will use a quadratic basis function

$$U^h = a_0 + a_1x + a_2y + a_3x^2 + a_4xy + a_5y^2, \quad (3.44)$$

which can be written in matrix form as

$$U^h = P^T a, \quad (3.45)$$

where P contains the basis function (which is in this case quadratic) and a contains the coefficients

$$P^T = \{ 1 \ x \ y \ x^2 \ xy \ y^2 \}, \quad (3.46)$$

$$a = \{ a_0 \ a_1 \ a_2 \ a_3 \ a_4 \ a_5 \}. \quad (3.47)$$

The coefficients must be found in order to complete the approximation, which is done by considering the function describing the error in the approximation at each molecule:

$$\text{Error} = [U^h(x, y) - U_i] \quad (3.48)$$

over molecules $i = 1, 2, 3, \dots, N$. Then sum the error over N local molecules using a sum weighted as a function of the molecules distance from the central node:

$$J = \sum_{i=1}^N w(x - x_i, y - y_i)[U^h(x, y) - U_i]. \quad (3.49)$$

Minimization of the weighted error function, Equation (3.49), leads to

$$(wP^T P)a = (wP^T)u, \quad (3.50)$$

$$Aa = Bu, \quad (3.51)$$

where

$$A = \begin{Bmatrix} w(x - x_1, y - y_1) \\ w(x - x_2, y - y_2) \\ \vdots \\ w(x - x_i, y - y_i) \end{Bmatrix} \begin{bmatrix} 1 & x & y & x^2 & xy & y^2 \\ x & x^2 & xy & x^3 & x^2y & xy^2 \\ y & xy & y^2 & x^2y & xy^2 & y^3 \\ x^2 & x^3 & x^2y & x^4 & x^3y & x^2y^2 \\ xy & x^2y & xy^2 & x^3y & x^2y^2 & xy^3 \\ y^2 & xy^2 & y^3 & x^2y^2 & xy^3 & y^4 \end{bmatrix}, \quad (3.52)$$

$$B = \begin{Bmatrix} w(x - x_1, y - y_1) \\ w(x - x_2, y - y_2) \\ \vdots \\ w(x - x_i, y - y_i) \end{Bmatrix} [1 \quad x \quad y \quad x^2 \quad xy \quad y^2], \quad (3.53)$$

$$U^T = [u_1 \quad u_2 \quad \dots \quad u_i], \quad (3.54)$$

$$a = \{a_0 \quad a_1 \quad a_2 \quad a_3 \quad a_4 \quad a_5\}. \quad (3.55)$$

Therefore the a coefficients can be found by solving

$$a = A^{-1}uB. \quad (3.56)$$

Once the coefficients have been calculated, they can be used in the original approximation for the local parameter values, Equation (3.44), to yield the approximated value of the bulk property U at the node at (x, y) .

3.3.4.2 Basis functions

The basis or approximating function used in the approximation depends on two conditions, the dimensionality of the system and the order of the approximation required. Basis functions are constructed using a form of Pascal’s triangle, as shown in Figure 3.14.

The triangle is shown in three dimensions with the first two levels shown. A linear basis function is constructed by summing all the components in the linear level and above:

$$P(x, y, z) = 1 + x + y + z. \tag{3.57}$$

The quadratic basis function is constructed in the same way, by summing all the components in and above the quadratic level:

$$P(x, y, z) = 1 + x + y + z + x^2 + y^2 + z^2 + xy + yz + xz. \tag{3.58}$$

These are the full basis functions for three-dimensional systems, so for systems with fewer dimensions simply set the coordinates that are not needed to zero and

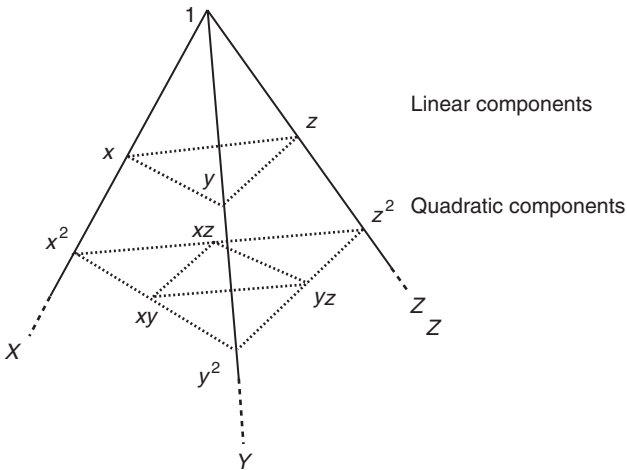


Figure 3.14 Basis function construction.

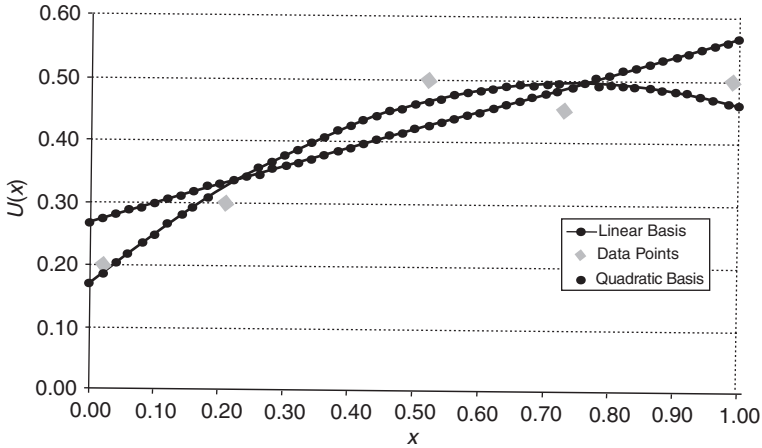


Figure 3.15 The difference between linear and quadratic basis functions for a one-dimensional example with five sample points (approximated around the centre point).

the basis reduces, for example, to two dimensions:

$$\text{for } z = 0, \tag{3.59}$$

$$P = 1 + x + y + x^2 + xy + y^2. \tag{3.60}$$

Higher-order basis functions can provide improved accuracy, but as the order increases the number of terms in the basis function increase substantially. Figure 3.15 demonstrates the difference between linear and quadratic approximations for a sample data set. Comparing the above examples of three-dimensional basis functions for linear and quadratic forms shows an extra six terms in the quadratic form. This may not appear as a great increase, but this increases the size of the A matrix from a 4×4 to a 10×10 matrix, which can add a significant amount of time to a simulation, especially when a large number of nodes are being solved. For this reason, cubic basis functions are rarely used as the A matrix is almost double the size of the quadratic version. A balance must be reached between accuracy and practicality.

3.3.4.3 Solving equations

In order to determine the coefficients for the local approximation, Equation (3.44), the solution to Equation (3.56) must be found. The equation is basically the matrix form of a set of simultaneous equations, so the analytical solution is fairly trivial and easy to solve by hand for one or two calculations by simply inverting the A

matrix. However, to be used in a simulation this solution to the equation must be found many times for every time step, a task that cannot be done by hand. There are many methods for solving such sets of equations, but LU decomposition is used in this case because it provides an efficient solution, without the need to invert large matrices.

LU decomposition In order to solve a system of equations of the form

$$Ax = B, \quad (3.61)$$

where A is an $N \times N$ matrix, B is a vector of size N and X is the vector of N unknowns. LU decomposition starts by decomposing matrix A into two diagonal matrices, one upper and one lower as follows, for $N = 3$:

$$A = LU, \quad (3.62)$$

$$\begin{bmatrix} A_{1,1} & A_{1,2} & A_{1,3} \\ A_{2,1} & A_{2,2} & A_{2,3} \\ A_{3,1} & A_{3,2} & A_{3,3} \end{bmatrix} = \begin{bmatrix} L_{1,1} & & \\ L_{2,1} & L_{2,2} & \\ L_{3,1} & L_{3,2} & L_{3,3} \end{bmatrix} \begin{bmatrix} U_{1,1} & U_{1,2} & U_{1,3} \\ & U_{2,2} & U_{2,3} \\ & & U_{3,3} \end{bmatrix}, \quad (3.63)$$

so that

$$\begin{bmatrix} A_{1,1} & A_{1,2} & A_{1,3} \\ A_{2,1} & A_{2,2} & A_{2,3} \\ A_{3,1} & A_{3,2} & A_{3,3} \end{bmatrix} = \begin{bmatrix} L_{1,1}U_{1,1} & L_{1,1}U_{1,2} & U_{1,3} \\ L_{2,1}U_{1,1} & L_{2,2}U_{1,2} + L_{2,2}U_{2,2} & U_{2,1}U_{1,3} + L_{2,2}U_{2,3} \\ L_{3,1}U_{1,2} & L_{3,2}U_{1,2} + L_{3,2}U_{2,2} & L_{3,1}U_{1,3} + L_{3,2}U_{2,3} + L_{3,3}U_{2,3} \end{bmatrix} \quad (3.64)$$

This gives $N \times N$ equations for $N \times N + N$ unknowns as the decomposition is not unique, but can be solved by Crout's method as follows:

$$Ax = LUx = L(Ux) = B, \quad (3.65)$$

$$B = Ly, \quad y = Ux. \quad (3.66)$$

Now solve for y using back-substitution:

$$y = \frac{1}{L_{i,i}} \left(b_i - \sum_{j=1}^{i-1} L_{i,j}y_j \right), \quad i = 1, 2, 3, \dots, N. \quad (3.67)$$

Use the result of y to solve for x using forward-substitution.

$$x = \frac{1}{U_{i,i}} \left(y_i \sum_{j=i+1}^N U_{i,j} x_j \right), \quad i = 1, 2, 3, \dots, N, \quad (3.68)$$

which results in the values of the original unknowns, x . LU decompositions, however, are still unable to solve for matrices with singularities (where the determinant is zero).

3.3.5 Weight Functions

The error function used to find the coefficients for the approximating function is calculated at each point and added as a weighted sum. The weighting function determines how important it is to get the error at that point to a minimum so that points closer to the central point are approximated with a higher accuracy than those further away. There are five criteria that all weighting functions must satisfy:

1. They must be > 0 within the subdomain of centre particle. Particles within the subdomain of the central point are allowed to influence the local approximation.
2. They must be $= 0$ outside the subdomain of centre particle. Particles outside the subdomain are not allowed to contribute to the local approximation.
3. The integral over the subdomain must be equal to one. This is known as the ‘consistency condition’, which is a condition that states that the weighting function is sufficient to interpolate the minimum requirement (constant function) exactly; e.g:

$$f(x) = c, \quad c = \text{constant}, \quad (3.69)$$

approximated as

$$\langle f(x) \rangle = f(x) = c. \quad (3.70)$$

Therefore

$$\langle f(x) \rangle = \int_{\Omega} f(x)w(x) dx = c, \quad (3.71)$$

which becomes

$$c \int_{\Omega} w(x) dx = c. \quad (3.72)$$

For this to be true, $\int_{\Omega} w(x) dx$ must be equal to one. When this condition is satisfied, the approximation is able to integrate, at least, the minimum of a constant function exactly..

4. They must decrease as the distance from the centre increases. The particles within the subdomain that are closer to the centre point are given a higher weighting in the approximation..
5. They must approach ‘Dirac’s delta function’ as the radius of the subdomain $r \rightarrow 0$. The delta function, accredited to Paul Dirac, is a function that has the value of infinity at $x = 0$ and zero everywhere else. It is simple to see that as the radius of the weight function decreases, the zone of influence shrinks around the central point, where it is a maximum, and zero elsewhere.

These conditions describe a weighting function that will give the best approximation close to the central point. The fifth condition is not always necessary as it is difficult to find a function that fits the other four criteria and not the fifth, but is included for completeness. An additional condition usually added is that the function is positive over all the subdomain; however, there are exceptions to this rule such as the weight functions used in point interpolation methods (PIM). There are three basic weighting functions in general use: the quadratic spline, Gaussian and exponential. All are a function of the radius from the central node, i .

In one, two and three dimensions,

$$r = x - x_i \quad \text{for one dimension,} \quad (3.73)$$

$$r = \sqrt{(x - x_i) + (y - y_i)} \quad \text{for two dimensions,} \quad (3.74)$$

$$r = \sqrt{(x - x_i) + (y - y_i) + (z - z_i)} \quad \text{for three dimensions,} \quad (3.75)$$

and the weighting functions are

Quadratic spline:

$$w(r) = 1 - 6r^2 + 8r^3 - 3r^4, \quad (3.76)$$

Gaussian:

$$w(r) = \exp^{-2.5r^2}, \quad (3.77)$$

Exponential:

$$w(r) = \frac{1}{100r}. \quad (3.78)$$

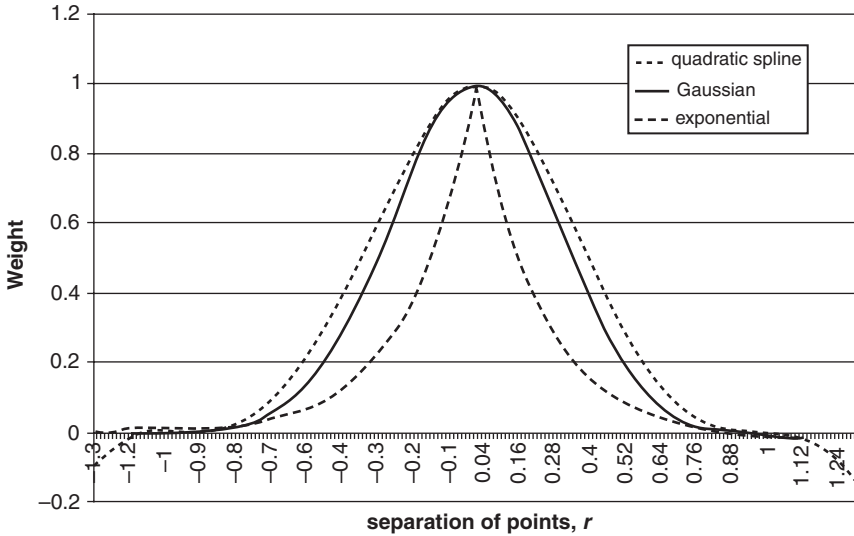


Figure 3.16 The three most common weighting functions: quadratic spline, Gaussian and exponential.

The choice of weighting function has a substantial influence on the local approximation generated by the MLS method, as will be shown in later chapters. The profiles of the weighting functions are shown in Figure 3.16.

3.3.6 Grid Structure Implementation

The least squares approximations are performed at nodes placed within the flow field. The three-dimensional molecular domain is overlaid with a grid of nodes, in either one, two or three dimensions, depending on the problem and the distributions of interest or expected.

Figure 3.17 shows a representation of a molecular region overlaid by a two-dimensional net of nodes, each having a zone of influence. Each molecule within the zone of a node contributes to the approximation at that node and is weighted as a function of its distance.

The molecular parameters are collected from the molecules at intervals during the simulation. Ensembles for density, pressure and temperature are stored in a separate A matrix and B (of the least squares approximation described above) vector for each node. As described in Section 3.3.4, the matrices are used to form the vector of coefficients of the fitted polynomial basis function

$$A = (wP^T P), \quad B = (wP^T), \quad (3.79)$$

$$Aa = Bu, \quad (3.80)$$

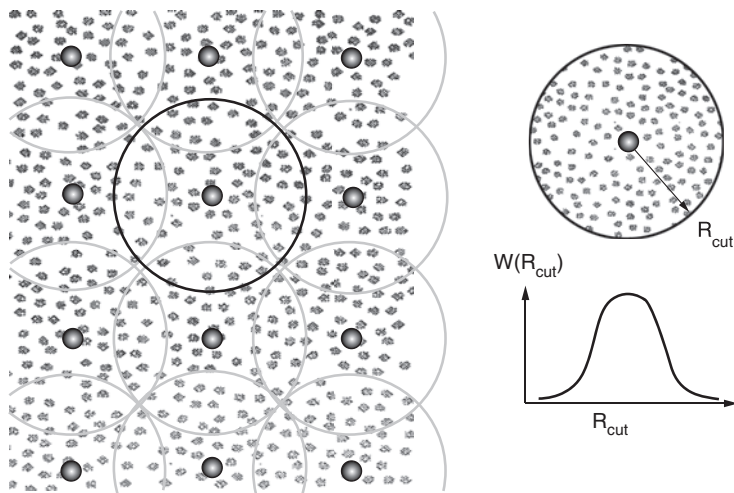


Figure 3.17 Net of approximating nodes placed over the molecular flow region. Molecules within each node subdomain contribute to the property average at that node with weighting $W(r_{\text{cut}})$, according to their proximity, R_{cut} .

where P is the basis function (a function of position of the molecule relative to the node) and w is the weighting function. For convenience, the B vector is combined with the vector of property values, u , which is a function of the phase space (position and momentum of the molecule) position of each molecule within the subdomain.

The sampling of the properties in no way influences the dynamics of the molecules in the molecular system, which are used purely to extract information from the molecular model. It is, however, important to consider the way in which the sampling is done in order to present the best data for the averages without losing information. It is also important to keep the number of sampling points to a minimum.

3.3.7 Sampling

When ensemble averages are constructed it is important to make the distinction between samples and ensembles. In this method, a sample is taken as an instantaneous snapshot of the local data at each node. Ensembles are generated using the data collected over a number of these samples over a period of simulation time. Molecular data collected in different ensembles can construct the different bulk fluid properties at these local points. A number of ensemble averages can be taken over the duration of the simulation in order to capture time-dependent effects, as well as providing a measure of the approach to the equilibrium state.

Each individual sample is combined into the A matrix and B vector, and a number of samples are used to make an ensemble average at the node, providing an



Figure 3.18 Highlighting the differences between samples collected to make up the ensemble averages, accumulated at points throughout the simulation time.

approximate value for the parameter over time as well as space in the simulation (Figure 3.18). The length of simulation time between samples and the length of time over which the approximations are computed is key to stability and accuracy in the ensemble averages.

The objective of the sampling is to provide the ensemble with data about the bulk state of the fluid, but information is not required about the behaviour of individual molecules. To ensure that it is the bulk behaviour and not individual molecular behaviour that is being fed into the ensemble, the information is expressed in terms of the local phase space. Phase space is a function of the position and momentum of all molecules in the system. For a local bulk fluid property, there is a region that contains all of the available phase space positions for the current state and time. By sampling as many points in the phase space available to the local molecules, the best description of the state of the fluid at that point can be found. If samples are taken too often, only a narrow portion of phase space can be sampled. If, however, there is time for the molecules to interact and move within the domain, the next sample may contain different data about the same available phase space volume. If the sample time is too long, the sampling becomes inefficient and reduces the amount of useful data that are collected during a simulation.

Similarly, if the ensemble averages of the samples are taken over a short period of time, there is insufficient sample data available to represent the available phase space to provide a stable ensemble average. If the averaging time is too long, then an unnecessary amount of information is contributed to the approximation and the time resolution is unnecessarily decreased.

In the next chapter, the effect of changing the sample and ensemble times is investigated and its effect on the resulting bulk properties that are extracted is found. These two sections have shown the implementation of a method designed to simulate meso scale fluid systems from a bottom-up approach. The developed method relies on a molecular scale fluid model and bulk properties are extracted from the underlying molecular motion. The next section examines the operation of the molecular model in more detail.

3.4 VERIFICATION OF PROPOSED MESO SCALE MODEL

The information in the above section has discussed how fluid can be modelled via the consideration of physics on a molecular scale. This section will provide

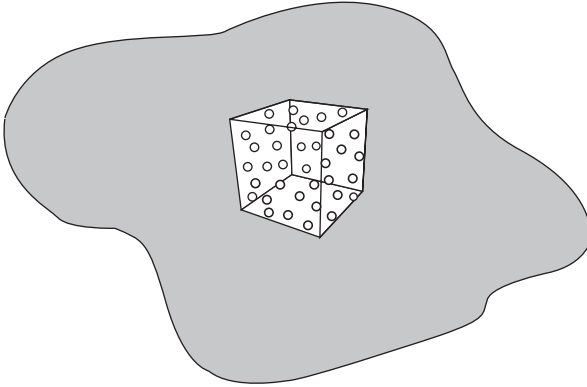


Figure 3.19 Cubic control volume considered away from any physical boundaries.

an example of a molecular dynamic simulation to demonstrate the operation of the developed model. For this, the example considered will be a cubic volume of methane molecules suspended away from any boundaries to allow the use of periodic boundary conditions in all three dimensions (Figure 3.19).

The 512 methane molecules (CH_4) used in this example interact via the soft sphere Lennard–Jones 6-12 potential and move according to Newton’s law via the Verlet algorithm as described above. Although this is a simple steady state system, this example can demonstrate the application of molecular dynamic simulations.

To start the simulation, the number of molecules and their properties are input into the initialization stage of the simulation. This allows a lattice of molecules to be created to fill the domain with the given number in order to generate the required density. The set temperature is then used to apply random velocities to the molecules according to the Boltzmann distribution.

The next part of the simulation is to equilibrate, or settle, the molecules, as the initial lattice is not a stable maintainable state, but a lattice makes for easy initial placement. During the breakout of this lattice, there is also large variations in molecular properties.

Figure 3.20 displays what happens when the molecules in the lattice are relaxed. Here, potential (PE), kinetic (KE) and total energies (E total) are plotted from $t = 0$ to $t = 1$ ps. During the equilibration period, the kinetic energy (and hence the temperature) is kept constant. This is because while the molecules are settling down they can be exposed to unphysical and high interaction forces, which can cause the energy of the system to become out of control. For this, simple velocity scaling is used.

Velocity scaling is a crude method of temperature control in molecular systems, where the kinetic energy of the molecules calculated using

$$E_{\text{KE},t} = \frac{1}{2}mv^2 \quad (3.81)$$

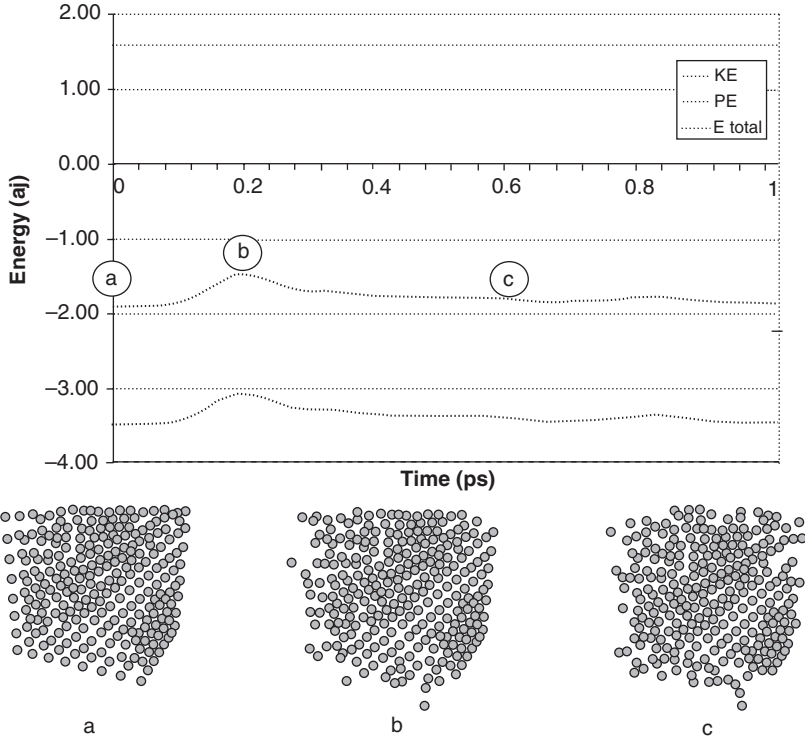


Figure 3.20 Top: kinetic, potential and total energies for initial stages of equilibration. Bottom: distribution of molecules at stages throughout the equilibration process: a, initial lattice; b, peak in potential energy; c, stabilization of a randomized system.

is compared to the kinetic energy of the initial temperature,

$$E_{KE,t=0} = \frac{3}{2} N k_b T. \quad (3.82)$$

The scaling factor is then

$$\alpha = \frac{E_{KE,t}}{E_{KE,t=0}}, \quad (3.83)$$

which is then used to scale all the velocities of all the molecules in the system using

$$v_i = v_i \alpha \quad (3.84)$$

to maintain the global kinetic energy at each time step.

This is a crude and unphysical approach to temperature control and is only suitable for steady state simulations to achieve equilibrium. For more complex simulations, such as those examined later, a more refined approach is required to control temperature.

Consequently, the only variation in energy comes from the potential energy component in the simulation. The plot of energies shown in Figure 3.20 is for the initial breakout of the lattice and three parts, a, b and c, are identified..

- The initial lattice (a) is the potential energy value computed from the initial positions of molecules..
- Molecules move with initial velocity and slack across periodic boundaries is taken up. The peak in potential energy (b) occurs from the momentum of particles crossing empty spaces..
- Potential energy begins to stabilize (c), molecules are constantly moving, colliding and exchanging momentum, but global potential energy is conserved. Fluctuations occur from molecules changing state, but the system is in the equilibrium state.

The equilibrium state can also be monitored using the order parameter described previously, tending from one at point a to zero at point c.

To check the thermodynamic state of the fluid, the velocity distribution in each of the three dimensions can be compared to the Boltzmann distribution, as shown in Figure 3.21. If the distributions match, then a stable thermodynamics state could be present, and when combined with the other equilibrium tests, it can identify when the whole system is stable. Figure 3.21 shows the instantaneous distribution of speeds of the molecules within the system and is shown against the exact distribution with 15 % error bars.

Once this equilibrium state has been reached, the production stage can start, which collects all the useful properties of the simulation. At the start of the production stage, the velocity scaling is removed, effectively freeing the simulation of any constraints. At this point the global ensemble averages can start to take data from the molecules in the system.

On the left of Figure 3.22 is a plot of the equilibrium stage, similar to Figure 3.20, but the time has been extended to 20 ps. Here, the initial peaks are present as the lattice structure breaks down, but then the potential energy remains approximately constant. On the right is the production run that follows the equilibration stage. In this case the production run has also been performed over 20 ps but the velocity scaling is removed. With the kinetic energy allowed to change, the constant exchange between potential and kinetic energies can be observed. In the equilibration stage, the fluctuations of the potential energy were directly translated on to the total energy because the kinetic energy was being continually rescaled. Now the kinetic energy has been released, the molecules exchange their kinetic and potential energies in perfectly elastic collisions, such that the net energy in the

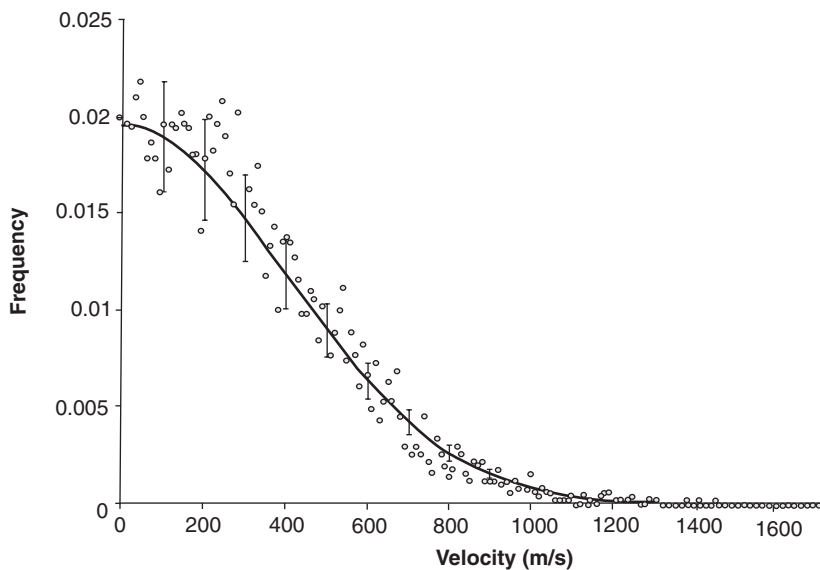


Figure 3.21 Distribution of velocities in a molecular simulation compared to a Boltzmann distribution, shown with 15% error bars.

system remains constant. It is during this period that the ensemble properties may be taken over the desired simulation time, as this is the period where the system is in steady state.

The simulations so far have been using a control volume of 512 molecules. Figure 3.23 shows a plot of the variation in the potential energy per molecule with respect to the number of molecules in the simulation. All simulations have

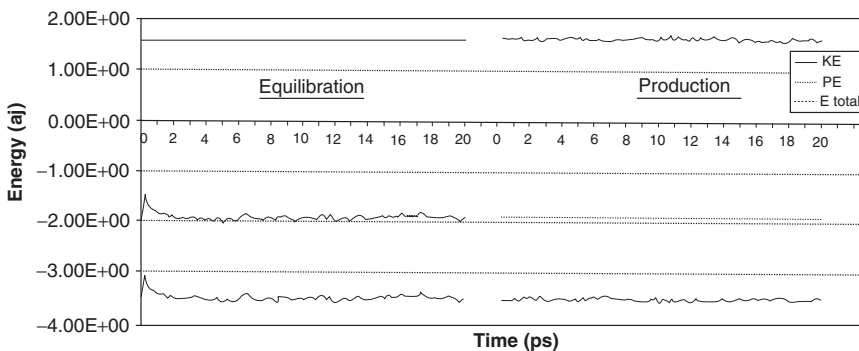


Figure 3.22 Potential (PE), kinetic (KE) and total energies during the equilibration and production stages of the simulation.

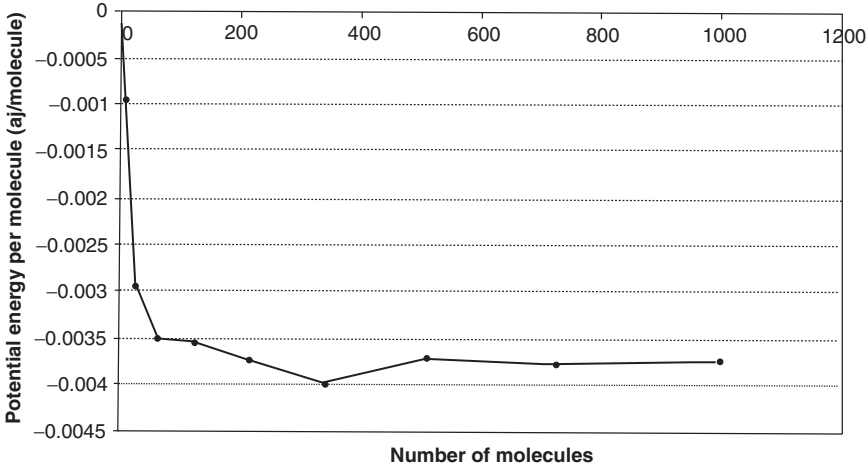


Figure 3.23 Average potential energy per molecule versus the number of molecules in the periodic cell.

the same density and the volume per molecule remains constant, but the average potential energy gathered in the simulation differs significantly. There is a clear region where there are enough molecules to predict the potential energy of the simulation correctly and the energy per molecule is approximately constant. Also from this graph, it is clear that increasing the system size from 512 molecules to 1000 would not have a significant effect on the results, and present a much higher demand on the computational resources.

If this potential energy is to be accepted as correct, there needs to be a benchmark with which to test the results for the simulation. This can be done by assembling an ensemble average for the pressure using a form of the virial equation of state summed over all the interactions and molecules. This equation of state allows the calculation of global pressure from the kinetic and potential energy in the system. The simulation of the above system yielded a global pressure of

$$P_{\text{sim}} = 44.28 \text{ MPa.} \quad (3.85)$$

which can be compared to the pressure obtained from an analytical equation of state, in this case the Lennard–Jones equation of state, which yields

$$P_{lj} = 44.53 \text{ MPa.} \quad (3.86)$$

This gives the difference in pressure between the simulation result and the analytical pressure to be 0.58 %, which gives confidence in the accuracy of the simulation model.

3.5 SUMMARY

This chapter has shown and explained a molecular physics based approach to meso scale fluid simulation. The molecular model is capable of handling very large numbers of molecules using processing power and memory requirements efficiently. This is further improved by the implementation of the diffuse boundary conditions, which allow the computational resources to concentrate on the highly dynamic part of the simulation, the fluid.

The bulk property averaging scheme allows the fluid properties and fluid effects displayed by the bulk of the fluid to be characterized as distributions within the flow field. The implementation of this method is in the form of a versatile node-based structure. Property interrogation nodes can be placed throughout the domain wherever needed and sample and ensemble times can be tuned to suit the current application. These parameters are covered in more depth in the case studies in the next chapter.

4

Enhancements to the Meso Scale Model

Aim. This chapter explores the limitations of the meso scale approach discussed in the previous chapter. Using these case studies the reader should see the depth of knowledge available from molecular models and how it may be used to characterize fluid systems.

4.1 INTRODUCTION

This chapter focuses on the further development of the meso scale approach discussed in the previous chapter. The development starts by extending the method to handle flowing fluids. When a fluid flows through a pipe or channel, the interaction between the fluid and solid molecules causes the molecules close to the wall to slow down, as has been discussed in the viscous fluid discussion in Chapter 1. This, combined with the internal collisions of fluid molecules causes a boundary layer to form. Capturing this boundary layer in the form of a velocity profile can tell us a great deal about the fluid behaviour, as will be seen in Chapter 5. The section discusses the generation and capture of fluid flow behaviour in molecular systems. The first issue to be discussed is the method of driving molecules to generate a flow.

This extended method is then explored and tested in a number of case studies. The first case studies focus on the parameters of the bulk property extraction scheme, examining the sample and ensemble length, radius of sub-domain and weighting function. These studies are performed on a fluid at rest and do not employ the thermal control element of the method.

The second section of case studies look at the collected bulk properties as distributions throughout the domain. A temperature gradient through a fluid confined between two parallel plates is considered on a fluid at rest. In this example thermal energy is propagated by the thermal motion of the molecules in the fluid. A study of a fluid flowing between parallel plates is also considered. This example employs both the thermostat and flow driving elements of the model, and is compared with results published in literature.

4.2 DRIVING FORCES

In order to generate a flow, there must be a driving force to push the molecules between one point and the next. A flow can be generated in a number of ways, varying in their complexity and computational demand. In the following section, methods for generating fluid/molecular flows will be presented and discussed, focusing on their application to meso scale systems.

The first method is the most demanding computationally, but presents the simplest concept. It relies on three components, a high-pressure reservoir, a low pressure reservoir and a test section that connects them, as shown in Figure 4.1.

The high-pressure reservoir is maintained at a constant high pressure by recycling the molecules that exit the test section into the low-pressure reservoir. This has the effect of keeping the low-pressure reservoir at a vacuum, but the high-pressure reservoir must be sufficiently large to smooth out the effect of molecules being inserted, which can lead to anomalies and discontinuities if they are inserted too close to the entrance of the test section, or overlapping another molecule.

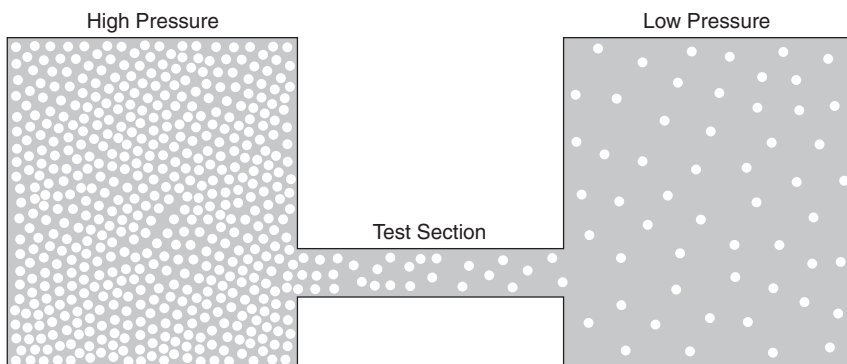


Figure 4.1 Schematic of molecules driven through the test section by maintaining two reservoirs at different pressures. The low-pressure reservoir is usually maintained at a vacuum.

This approach to flow generation needs a very large number of molecules, most of which are not within the test section and contribute little to the results of the simulation. This method does, however, allow pressure-driven flows to be directly modelled in a controlled and stable environment. However, in order to model the flow of fluid or molecules through a meso scale test section, the number of molecules needed would be prohibitively large.

Two similar, but reduced, approaches were developed by Liao and Yip [73] and Sun and Ebner [77]. The first, by Liao and Yip, is known as the reflecting particle method (RPM) [73]. This method removes the large reservoir and uses an extended part of the test section, with periodic boundary conditions at each end, to form a smaller reservoir in line with the flow. The high and low pressures are generated by using a selective membrane at some point along the flow, which allows molecules to pass freely across in one direction, but in the other direction a proportion of the molecules are reflected back. Figure 4.2 demonstrates the application of the membrane to model pressure-driven flow along a test section. The pressure difference can be controlled by altering the probability of reflection of the membrane.

The second approach is by Sun and Ebner [77] where the high- and low-pressure regions are created by replacing the periodic boundary conditions with a source region and a sink region. The sink is maintained at a vacuum by removing all molecules from the system that enter this region. The source region, at the opposite end of the cell, is a small volume with a movable boundary at the end. This boundary acts as a piston, reducing the volume of the source region and pushing the molecules into the volume considered by the simulation. Once the boundary has travelled a short distance, the density of the system is measured and the boundary resets to its original position; the void created fills with enough molecules of the same density. Molecules are added with velocities as described by the Maxwell velocity distribution at the temperature of the wall. This approach maintains a pressure gradient between the source and sink regions, causing a flow of molecules. The number of molecules injected and the volume

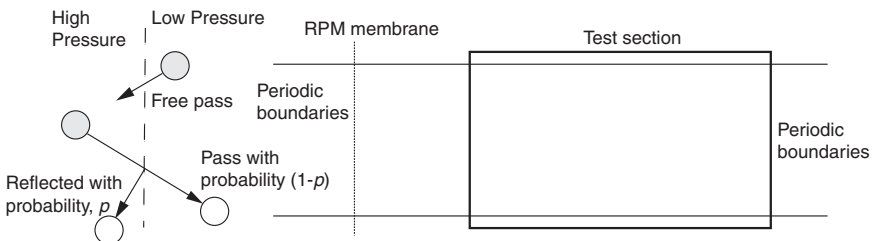


Figure 4.2 Left: the reflecting particle method, where molecules may pass freely in one direction, but are reflected with probability p when exiting the ‘high-pressure’ region. Right: the RPM membrane used to investigate channel flow. The test section must be clear of the membrane.

swept by the boundary is very small to minimize oscillations occurring as the new particles break out of the regular lattice used initially to position the particles. Sun and Ebner applied this successfully in two dimensions to study compressible flow [77] and has the potential to be applied in three dimensions.

By using these methods of applying a pressure gradient to drive the flow of molecules, force is transmitted in a very natural way, through the interactions of the particles. This is useful in modelling the reaction of a fluid to pressure gradients, as the pressure and density vary continuously along the length of the test section between the source and sink regions. However, this is not useful for considering steady, fully developed flows, which model the flow in channels with no density variation along their length (an infinitely long test section). These systems require a different approach.

To model fully developed flows, Sokhan *et al.* [60] modelled a driven flow between parallel plates by applying a uniform acceleration, in the required direction of flow, uniformly to all molecules in the system. The application of an acceleration is similar in a way to a gravitational effect pulling the molecules along the test section, although the acceleration is typically much larger. This, however, creates the problem that by applying an external force to the molecules energy is added to the closed system. As this external work is being done on the system in order to approximate the effect of a constant pressure gradient (effectively applied over an infinitely long section), the energy added to the molecules must be removed. The energy is removed by the application of a thermostat.

The simplest form of thermostat, velocity scaling, has been described in Section 3.4, but is far too crude for this application as temperature must be controlled throughout the duration of the simulation, even during the production phase.

4.3 THERMOSTATS

The aim of a thermostat is to maintain a control on the temperature, and hence kinetic energy, globally within the system. However, the way in which this is done is critical as controlling/altering the energy of molecules within the system affects the dynamic behaviour of the whole system. Control must be maintained without having an effect on the system behaviour. If energy is being added to the system in the form of an acceleration to model the effect of a pressure gradient acting in one direction, it should have the effect of influencing the proportions of energy within the system, but not change its global value.

4.3.1 Gaussian Thermostat

The Gaussian thermostat aims to control the temperature of the system by using Gauss's principle of least constraint [83]. The principle of least constraint states

that the constrained trajectories actually followed should deviate as little as possible from the trajectories of the unconstrained equations of motion.

In the motion of the molecules in the system, the equation of motion is simply Newton's law,

$$F = ma, \quad (4.1)$$

which we wish to constrain to a constant global temperature, leading to the formation of a constraint function that constrains the system temperature to the set temperature, as

$$g(r, v, t) = \frac{1}{2} \sum_{i=1}^N m v^2 - \frac{3}{2} N k_b T = 0, \quad (4.2)$$

which is the difference between the system temperature and the temperature set by value T . Differentiating once with respect to time gives the equation for the constraint plane

$$\sum_{i=1}^N m_i v_i a_i = 0 \quad (4.3)$$

Assuming that the unconstrained equations of motion lead the simulation away from the constraint surface, the equations of motion are corrected by considering the function of the square of the curvature [84], C :

$$C = \frac{1}{2} \sum_{i=1}^N m_i \left(a_i - \frac{F_i}{m_i} \right)^2. \quad (4.4)$$

The physical accelerations in the system correspond to the minimum value of C , so for an unconstrained system, $C = 0$ and the system evolves under Newton's equations. This leads to the constrained equation of motion:

$$a_i m_i = F_i - \lambda v_i m_i, \quad (4.5)$$

where λ is the friction factor applied to the molecules as scaling by their momentum and defined as

$$\lambda = \frac{\sum_{i=1}^N F_i v_i}{\sum_{i=1}^N m_i v_i^2} \quad (4.6)$$

Equations (4.5) and (4.6) are known and implemented together as the *Gaussian isokinetic equations of motion*. It is important to note that the scaling/friction factor is different to that used in the velocity scaling approach, and friction/scaling is applied as a function of the individual molecule momentum.

4.3.2 Nosé–Hoover

The Nosé–Hoover thermostat [85, 86] is a method of temperature control that is based on the inclusion of an extra parameter in Nosé–Hoover dynamics coordinate space [87]. This means the inclusion of the thermostat parameter, ξ , the second derivative of which is simply a function of the kinetic energy of the system and the temperature:

$$\ddot{\xi} = \frac{1}{Q} \left[\sum_{i=1}^N m_i v_i^2 - N_f k_b T \right], \quad (4.7)$$

where N_f is the number of degrees of freedom of the system. This equation for $\ddot{\xi}$ is the difference between the actual and set temperature of the system, which is multiplied by the reciprocal of a weighting function, Q , and can be defined as

$$Q = N_f k_b T \tau^2, \quad (4.8)$$

where τ^2 is the characteristic time scale of the motions of real particles [88]. This weighting function controls the application of the thermostat and can be adjusted for particular applications. A low weighting function can cause high-frequency oscillations in ξ , where as a high value it can overconstrain the system.

The Nosé–Hoover thermostat is used in this method because its level of control can be tuned to the specific system of interest using the mass parameter, allowing the thermostat to work effectively while applying the minimum of constraint on the system. It is, however more complex to implement it in the equation of motion; the implementation will be considered next.

4.3.2.1 Implementation in the proposed meso scale model

The thermostat parameter therefore has its own equation of motion and can be included in the velocity Verlet equations of motion of the molecules. The equations

of motion for the complete system proceed through the simulation time as follows:

1. Thermostat parameters and mass Q are computed:

$$\ddot{\xi}(t) = \frac{1}{Q} \left[\sum_{i=1}^N m_i v_i(t)^2 - N_f k_b T \right],$$

$$\dot{\xi}(t + \delta t/2) = \dot{\xi}(t) + \ddot{\xi}(t)\delta t/2,$$

$$\xi(t + \delta t) = \xi(t) + \dot{\xi}(t + \delta t/2)\delta t.$$

2. Molecular velocities and positions are updated, including the corrections from the thermostat parameter, using the velocity Verlet algorithm:

$$v_i(t + \delta t/2) = v_i(t) + [a_i(t) - v_i(t)\dot{\xi}(t + \delta t/2)]\delta t/2,$$

$$r_i(t + \delta t) = r_i(t) + v_i(t + \delta t/2)\delta t.$$

3. Molecular forces are updated using interaction and boundary forces, $F = ma$.
4. Complete the time step for the velocity of molecules and the thermostat parameter:

$$v_i(t + \delta t) = v_i(t + \delta t/2) + [a_i(t + \delta t) - v_i(t + \delta t)\dot{\xi}(t + \delta t)]\delta t/2,$$

$$\dot{\xi}(t + \delta t) = \dot{\xi}(t + \delta t/2) + \left[\sum_{i=1}^N m_i v_i(t + \delta t)^2 - N_f k_b T \right] \frac{\delta t}{2Q}.$$

This coupled equation is then solved using the iterative Newton–Raphson method.

These thermostats allow for the control of molecular systems, while presenting the minimum effect on the dynamics of the system. This allows for molecules to be driven by a pressure gradient, modelled by an acceleration applied to the molecules. However, with such a complex system operating, there needs to be careful benchmark tests made to make sure of the accuracy of the simulated molecules.

4.4 CASE STUDIES

To explore that capabilities of the developed approach, a number of case studies are presented. These are split into two sections, a study of the parameters of the bulk property collection scheme and an examination of temperature- and flow-driven systems. The initial simulations are performed with the thermostat disabled, and thus a temperature control is not necessary, but the simulation of a driven flow has the thermostat feature enabled.

4.4.1 Sampling

To study the parameters for the extraction of the ensemble averages, a molecular scale system is used to provide the most challenging bulk method. The reason for this is twofold: to reduce the computational load of the simulations to allow many simulations to be performed in a reasonable amount of time and, second, with only a few molecules, the least squared approximating nodes are starved for data, providing an excellent test for the performance of this approach at its weakest point, systems with low numbers of molecules.

To test the operation and sensitivity of these parameters, a simple molecular dynamics simulation is used as a demonstration, and is set up in a similar way to the simulation presented in Section 3.4. For this application, the limits of the system are set to a $15 \text{ nm} \times 15 \text{ nm} \times 8.3 \text{ nm}$ box, containing 5104 methane molecules interacting with a Lennard–Jones 12-6 potential. Periodic boundary conditions are applied in all three dimensions. The fluid is permanently at rest, with motion occurring only from internal thermal diffusion for the system temperature of 300 K. Within the molecular flow field a one-dimensional line of nodes was inserted along the y direction, at 0.5 nm intervals (shown in Figure 4.3).

As mentioned, the simulated fluid is at rest, so by recording the bulk velocity of the fluid in the x direction, the molecular velocities occurring by thermal diffusion should cancel out to yield an ensemble average of zero velocity at each of the nodes. With this knowledge, this system can be used to explore the effect of the parameters used to gather the least square approximations of the molecular behaviour. Investigations into the optimal number of time steps between samples, number of samples used in each ensemble average and the radius of the weighting function for each node are presented below. A study of the effect of the different weighting functions is also presented.

4.4.1.1 Case Study 1: length of time between samples

This investigation looks into the effect of coherence between samples and will identify when the molecules local to each node have had sufficient time to change

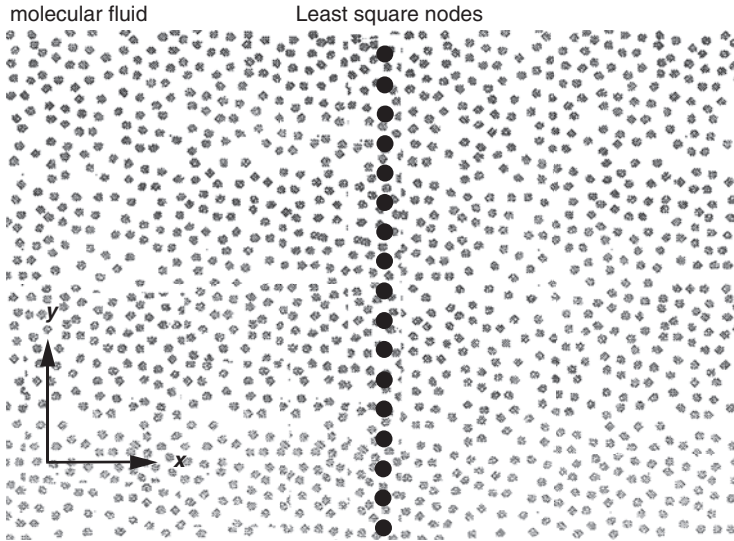


Figure 4.3 Simulation of a periodic molecular system, modelling fluid at rest; molecular properties are averaged by an array of one-dimensional nodes placed across the field.

their individual points in phase space so that the maximum number of available configurations in phase space is covered by each ensemble. The investigation proceeds as follows. The number of samples for each ensemble average taken at each of the nodes is kept constant at 20. The length of simulation time that elapses between each sample taken is varied between 25 and 400 time steps. The simulation time step is 2.0 ps, which relates to gaps between samples of 50 ps and 800 ps respectively.

Then 5104 molecules are placed in a lattice 15 nm by 15 nm by 83 nm, which is equilibrated to a stable point at rest at a temperature of 300 K, using periodic boundary conditions in all three dimensions. Temperature controls are removed and the molecules are left to maintain an equilibrium state. No external forces are applied to the molecules and only molecular motion/diffusion for the system temperature is present. The local velocity is monitored at 29 nodes arranged in a one dimensional array as shown in Figure 4.3, with each node having a cut-off radius of 1.0 nm. All simulations are performed from exactly the same starting point, with identical molecular data at the beginning of the production phase.

The fluid is at rest, so the bulk velocity of the fluid is zero. However, the molecules of the fluid are constantly moving throughout the fluid, diffusing with thermal motion. Poor phase space sampling will yield a nonzero value of velocity at the nodes and lead to larger variations in the ensemble values at the nodes. A more complete sample, of a wider portion of phase space, will lead to the thermal

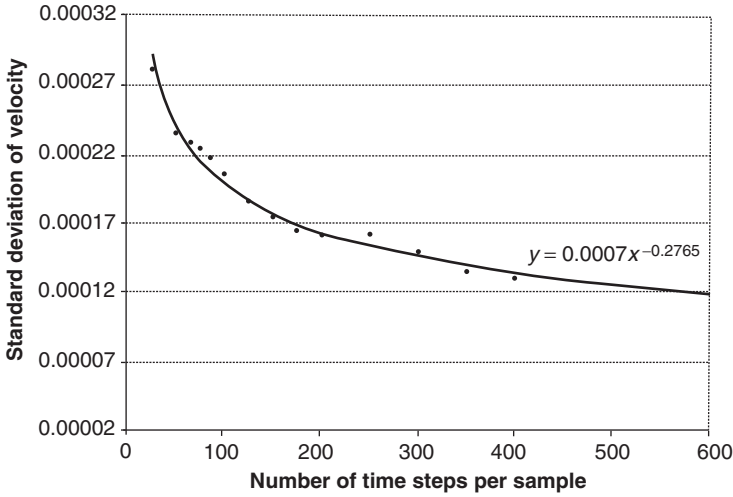


Figure 4.4 A graph demonstrating the relationship between the interval between samples and the standard deviation of the resulting one-dimensional velocity distribution. The equation of the best fit line is also shown.

motion of the molecules to cancel out, giving consistent values of velocity at the nodes. In this case, where there is no driving force applied to the fluid, the velocity at any point should be zero.

Figure 4.4 shows a plot of the average standard deviation (averaged over all nodes) of the values of velocity plotted against the number of time steps between each sample. It is necessary at this point to remember that the same number of samples are taken for each case so that every ensemble taken contains the same amount of data. The results show an exponential decrease in the standard deviation of the nodal values as the time between samples increases. This leads to the conclusion that samples taken at more than 200 time step intervals (400 ps) gives a good result, but the larger the time between samples the less variation there will be in the results. Increasing the sample interval to 400 time steps reduces the variation 18 % but the ensemble time increases by 200 %. The line of best fit is asymptotic to zero variation, indicating that the sample length could be extended indefinitely while still reducing the variation in the results. However, in practice a reasonable variation must therefore be accepted to allow for an acceptable resolution in time. For these cases, the variation is considered acceptable at 200 time steps or greater.

Figure 4.5 shows a plot of the average value of velocity (averaged over all nodes) plotted against the interval between samples. This shows the accuracy of the ensemble increasing as the time between samples increases, achieving an average velocity closer to the zero velocity specified. However, the data presented

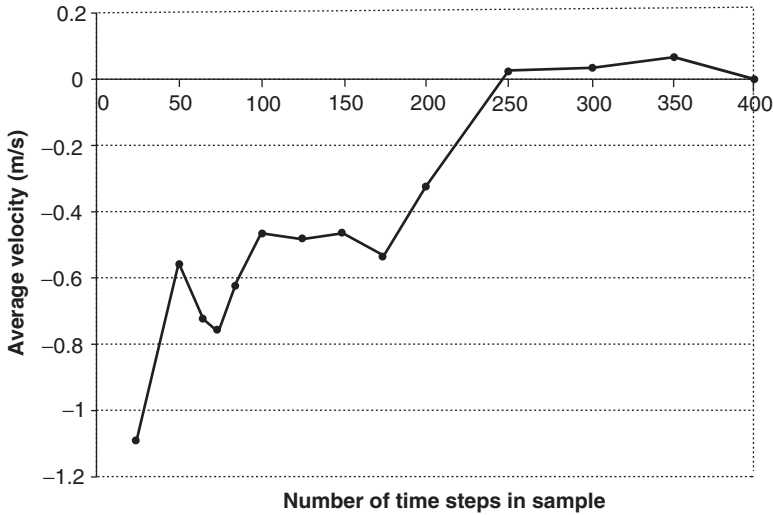


Figure 4.5 Graph showing the average value of velocity plotted against the number of time steps between samples.

contains a significant level of noise making a relationship difficult to determine, but the average velocity shows a definite trend to zero as the sample time increases, giving a very close approximation for sample times greater than 250 time steps.

Both of these graphs demonstrate the same result. The more time molecules are allowed in order to change state before being re-sampled, the better the interrogation of the available phase space performed by each of the local approximations. In both cases, the improvement is exponential, although the average velocity data are noisy. However, a longer time between samples reduces the resolution of the ensembles in terms of simulation time. This must be considered when long sample times are used. A way of increasing the time between samples is to take fewer samples per ensemble, which will be discussed in detail in the next case study:

4.4.1.2 Case Study 2: number of samples per ensemble

By performing a similar study, the effect of the number of samples collected per ensemble average can be investigated. Simulations were set up as described above, with the samples taken at regular intervals of 75 time steps, but the ensembles were constructed with between 2 and 40 samples.

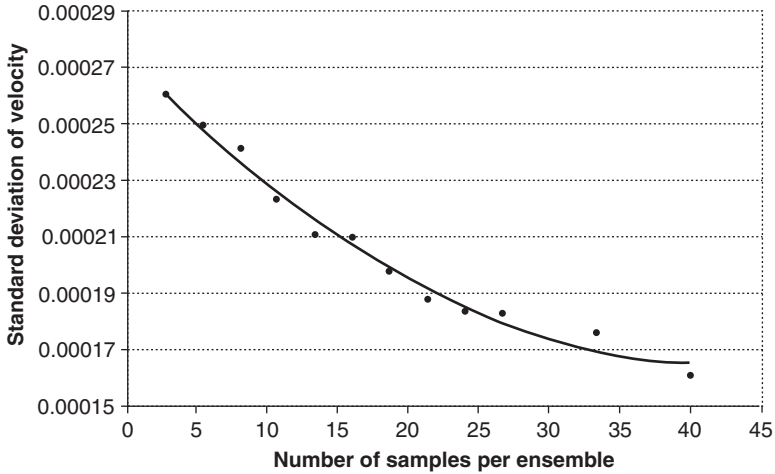


Figure 4.6 Graph standard deviation of velocity plotted against the number of samples per ensemble.

Figure 4.6 shows a plot of the average standard deviation of the collected ensemble velocity over all the nodes against the number of samples collected per ensemble average. The graph shows a similar relationship to sample timing study, with a slightly lower gradient, but as the number of samples increases in each ensemble, the variation in the results of this steady state system reduces to give more stable values. As the number of sample points increases, more points throughout the available phase space are sampled, leading to a better representation of the local ensemble by the approximation.

4.4.1.3 Case Study 3: time between samples versus number of samples per ensemble

The above study suggests that increasing the time between successive samples of the molecular data should be as long as possible in order to sample the widest available area of phase space. Similarly, to obtain bulk properties with the least amount of noise, there must be the maximum number of samples taken for each ensemble average in order to sample as many different points in the phase space as possible. However, in a realistic simulation example, there is a limit to the amount of simulation time that can be allowed between the ensemble averages being taken. This could be a limit on an ensemble taken for a steady system over a long period of time or short intervals for a dynamic system, where greater resolution in terms of time is required. In these cases, there is a maximum time over

which an ensemble can be taken. This means that within one ensemble a balance must be made between the number of samples used in each ensemble and the time between each sample taken.

To test the sensitivity of this tradeoff, the same example of fluid methane at rest, as described above, was used. The total ensemble time is limited to 20000 time steps, and the sample interval is varied between 100 and 1000 time steps to correspond to 200 and 20 samples per ensemble respectively.

Figure 4.7 shows a plot of the standard deviation of the ensemble velocity, averaged over three ensembles taken for the varying time between samples. In the previous results, it has been shown that the best and most stable results are obtained by leaving long periods between taking each sample and taking a large number of samples. However, for simulations with a finite time frame, there is a limit on this behaviour. As the length between samples increases, the number of samples that can be taken in the ensemble reduces, causing the variation in the results to increase as the time between samples increases. The results shown in Figure 4.7 are dominated by the variation caused by the reduced number of samples in the ensemble, and the variation expected to be caused by the short sample times does not have an observable effect in the sampled region.

From these results, it can be concluded that the largest acceptable time between samples is approximately 400 time steps for this case. To generalize this, 400 time steps represents 2% of each ensemble time, allowing 50 samples to be taken in each ensemble. Although the variation in the solution maintains a similar value for lower times between samples, the highest available values should be used to

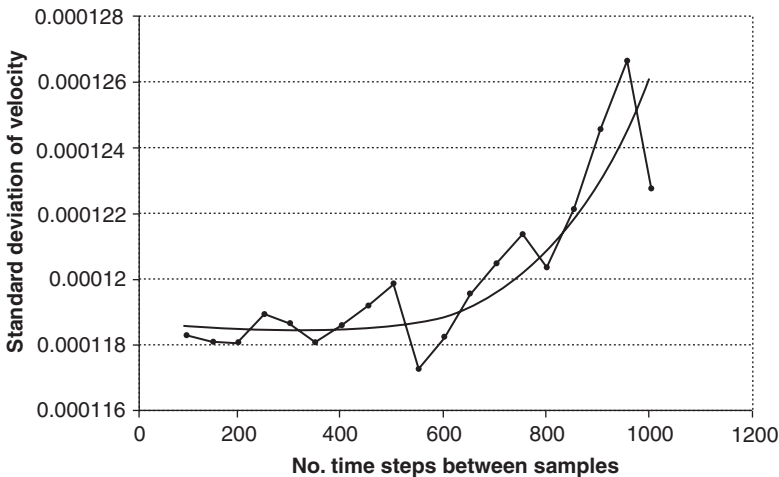


Figure 4.7 Plot to demonstrate the effect of trading off the length of time between samples against the number of samples per ensemble, for a fixed ensemble length of 20000 time steps.

achieve the best representation of the phase space, saving on the computational time involved with processing a higher number of samples.

4.4.1.4 Case Study 4: radius of weighting function

The radius of the weighting function governs the area or volume over which the approximation is constructed at each node. This parameter is critical, as a smaller radius gives better resolution in space at the cost of fewer molecules within each sample. Simulations were performed as above for the same sample times and number of samples per ensemble, and in this case only the radius associated with the nodes was altered. To give a idea of scale, the 29 nodes are spaced at 0.5 nm intervals across the 15 nm width of the simulation. The radius at each node is changed from 0.2 nm up to 2 nm. Figure 4.8 gives an approximate idea of scale, showing the radius in two dimensions. Figure 4.9 shows a plot of the standard deviation of the velocity obtained at each of the ensembles against the ratio of the node's radius to the diameter of the underlying molecules (for methane $\sigma = 0.381$ nm). This shows an increasing accuracy as the radius is increased, with an abnormally large value for a standard deviation at $R/\sigma = 0.5$. This is due to the radius being so small that only a single molecule can fit in the node's 'zone', making the node very sensitive to the properties of an individual molecule.

This can also be highlighted in the plot of the average velocity, shown in Figure 4.10, which reinforces the fact that one of the nodes has sampled a molecule with a speed that is on the higher side, as given by the Maxwell-Boltzmann distribution. This has had a dramatic effect on the value of one of the nodes. These results highlight that the radius of a node must be large enough to capture as many molecules as possible but be small enough to be able to capture any variations that may be present in the distribution of the property, leading to a compromise between resolution, stability and statistical error.

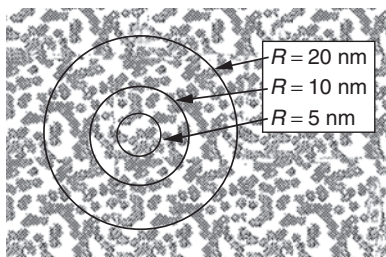


Figure 4.8 Two-dimensional example of the radius of a weighting function compared to the number of molecules present, for the example simulation.

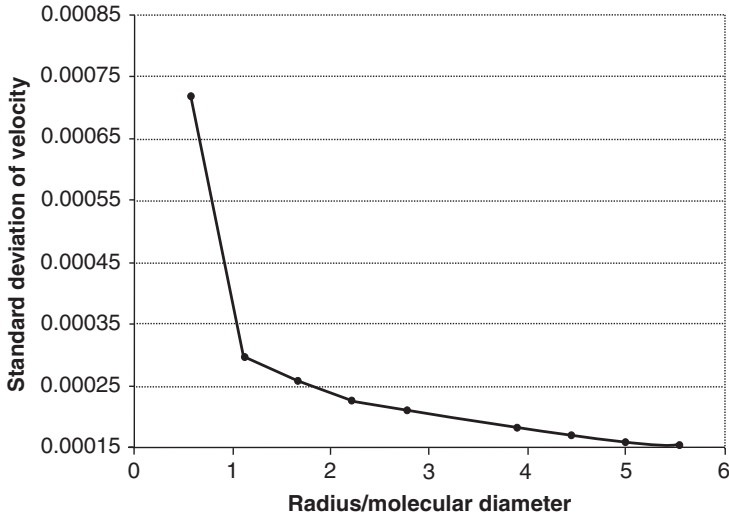


Figure 4.9 Standard deviation of velocity collected at the nodes, plotted against the ratio of the node radius to the molecular diameter.

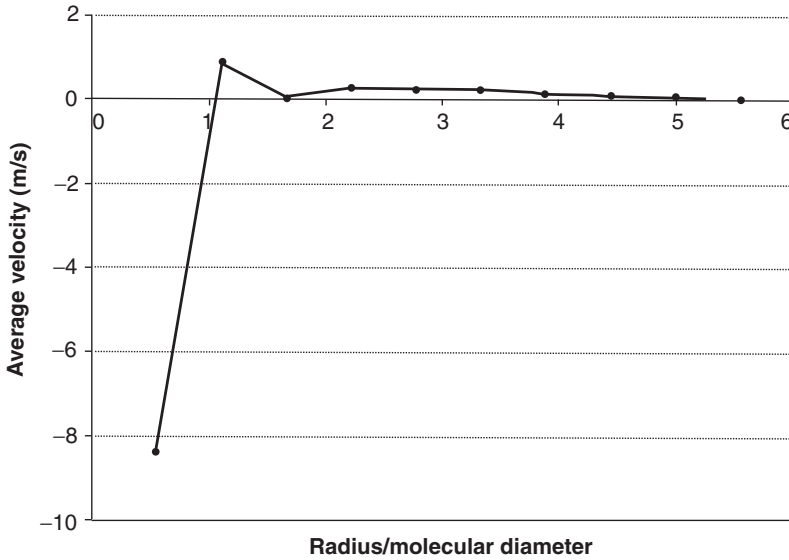


Figure 4.10 Average ensemble velocity plotted against the ratio of the node radius to the molecular diameter.

4.4.1.5 Case Study 5: weighting function

The weighting function plays a very important part in the property extraction, being the basis on which molecules are allowed to contribute to a node's ensemble average. By again performing the same test simulation, the effect of the different weighting functions highlighted in Section 3.3.5 (quadratic, exponential and Gaussian weighting functions) can be tested.

Figure 4.11 shows the values of the average ensemble standard deviation for the three weighting functions tested. From this, the Gaussian weighting function comes out on top, providing the most stable result, closely followed by the exponential function. In this application, the quadratic weighting function gives the most variation.

From these studies, it can be concluded that in order to obtain good stable results for the bulk properties collected at the least squares nodes, each sample must probe the available local phase space as comprehensively as possible. To do this, the ensembles must be constructed from as many samples as possible, and the samples must be taken with long intervals between them to allow the molecules to select a new phase space position. For this reason, a sample interval between 100 and 400 time steps should be used. However, these two parameters must be selected with the resolution of the distribution of properties, with respect to time, in mind. Similarly, for the nodal radius a larger radius will provide better phase space sampling but reduces the resolution in terms of the simulation space.

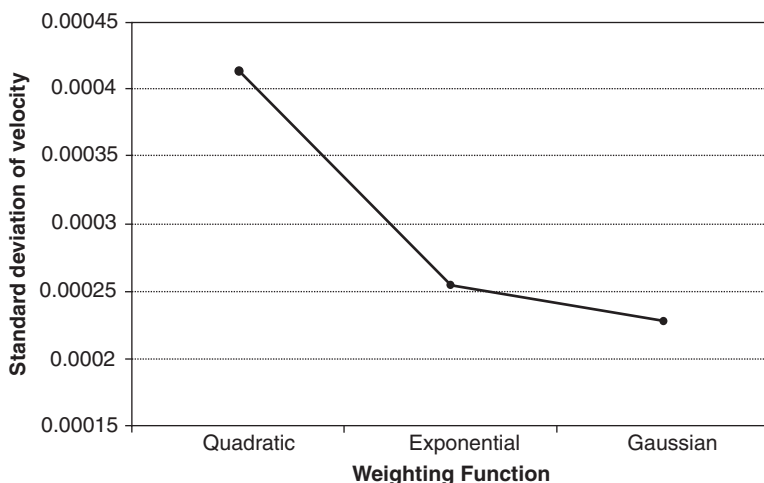


Figure 4.11 Values of standard deviation for each of the weighting functions.

The parameters for the bulk property collection must therefore be carefully chosen for the system of interest, especially for systems that include gradients and properties dependent on position and time within the simulation.

4.4.2 Gradient Study

In the previous section, the local averages have been extracted and evaluated for stable systems with approximately uniform properties throughout. This was used to study the effect of the parameters of the bulk ensemble approximations against a known value. In this section, systems involving properties that vary in space as well as time are considered. These provide more of a challenge, as spatial and temporal resolution of the nodes must be seriously considered and traded off against the stability and accuracy of the ensemble averages collected at the nodes.

Two distributed bulk properties will be considered. First, the distribution of temperature will be studied in a fluid at rest, contained between two parallel plates at different temperatures. The nodes will then monitor the distribution of temperature throughout the field, as the thermal energy propagates through the fluid via the molecular collisions. Second, velocity distributions will be studied within a flowing fluid field. As will be shown, the study of velocity distributions requires special treatment, as extra controls on the system are needed, which will be presented and validated against existing molecular simulations.

4.4.2.1 Case Study 6: temperature gradient

As an initial test of this method, the molecular simulation was performed on a fluid at rest. The fluid is trapped between two parallel plates of different temperatures, as shown in Figure 4.12. The plates are separated by 7.1 nm, with the left-hand wall having a temperature of 300 K and the right-hand wall having a temperature of 250 K. The fluid methane in the middle interacts with the wall via the diffuse boundary conditions. The tangential momentum accommodation coefficient was chosen to be $f = 0.81$, to simulate a sparse solid lattice of carbon molecules. A large value of f was used to achieve a large amount of variation of the temperature within the simulation domain to examine the ability of the bulk property extraction component to capture details of a relatively high gradient property.

The fluid molecules were equilibrated from their initial lattice and temperature of 275 K and settled to an equilibrium state. The temperature of the molecules were observed using 36 nodes placed at 0.2 nm intervals within the domain. The radius of interaction was set to 0.4 nm, and ensembles were taken over 50000 time steps (2 fs time steps).

The molecules were free to interact with each other, with the only temperature control being applied by the boundary walls. The resulting thermal profiles for

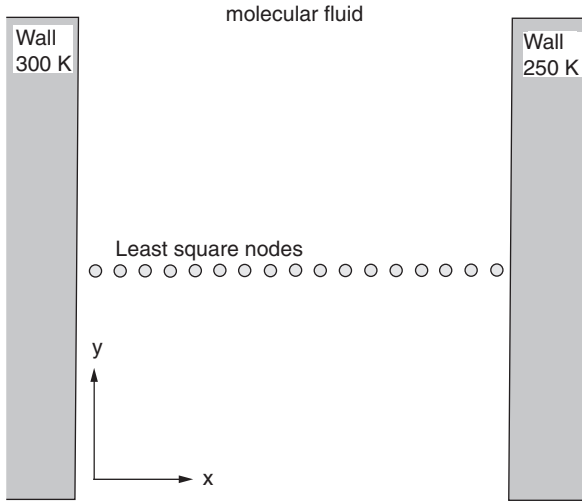


Figure 4.12 Schematic of fluid with the temperature gradient. The wall on the left is maintained at 300 K and the wall on the right at 250 K. An array of one-dimensional least squared nodes crosses the fluid between them to collect local values for temperature.

the steady state result are shown in Figure 4.13. From this graph, the temperature gradient extracted from the molecular model can be clearly seen between the average ensemble temperature collected near the left-hand wall and the value at the right-hand wall. In the centre of the fluid section, the temperature gradient is almost linear, but the gradient becomes steeper in a relatively wide region close to the walls. This is due to the slip and jump at the boundary, where a discontinuity is allowed. Error bars are shown at 0.5 %, indicating the variation between profiles extracted.

This simple example highlights how the least squares nodes can be implemented and used to interrogate a molecular domain, providing distributions of useful engineering properties. The next step is to move this method on to a more challenging system that can aid in the validation of the molecular mechanics model.

4.4.2.2 Case Study 7: velocity

This method allows the molecular model to simulate engineering systems at meso scale dimensions with large numbers of molecules. However, the accuracy of this model with its simplifications for boundary conditions and pressure gradients needs validation with existing work to ensure that the model is still accurate. The performance of a molecular simulation can be tested in a number of ways, and in this section validation results are presented to give an idea of the accuracy

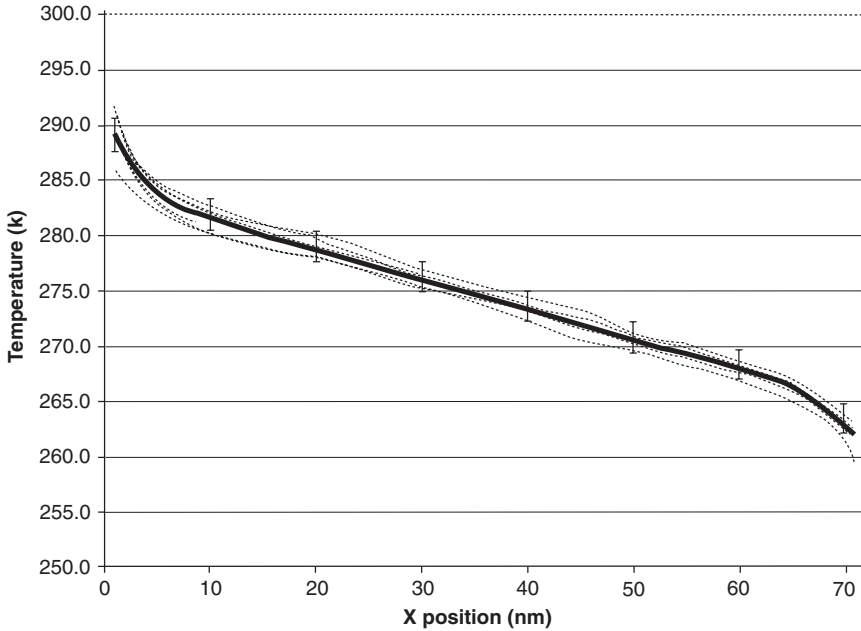


Figure 4.13 Temperature gradient for methane between two parallel plates at $x = 0$, maintained at 300 K, and at $x = 7.1$ nm, maintained at 250 K. The black line shows the average temperature profile shown with a 0.5 % variation.

of the method. There is almost no experimental data available for meso scale systems and computational restrictions limit comparisons on the continuum scales, so tests are performed at high-end molecular scales where information on simulations is readily available. This also allows the testing of the molecular model separately from the approximating (least squares) components.

The molecular dynamics model was tested against the molecular simulations performed by Sokhan *et al.* [60], whose simulations were performed using a model based on the DL_POLY [89] package. The system considers fully developed Poiseuille flow of methane through a graphite slit pore.

The system is simplified to methane molecules flowing between two parallel plates of graphite, which contain the molecules in the y direction and periodic boundary conditions in the x and z directions. The system dimensions are shown in Figure 4.14, with the graphite plates being separated by 7.1 nm; the lengths of the simulating cell in the x and z directions are 7.715 nm and 8.368 nm respectively. Into this volume was put 5104 methane molecules, corresponding to a reduced density of $\rho' = 0.61$ and interacting via a Lennard–Jones potential with a collision radius $\sigma = 0.381$ nm and a well depth $\epsilon/k_b = 148.1$ K.

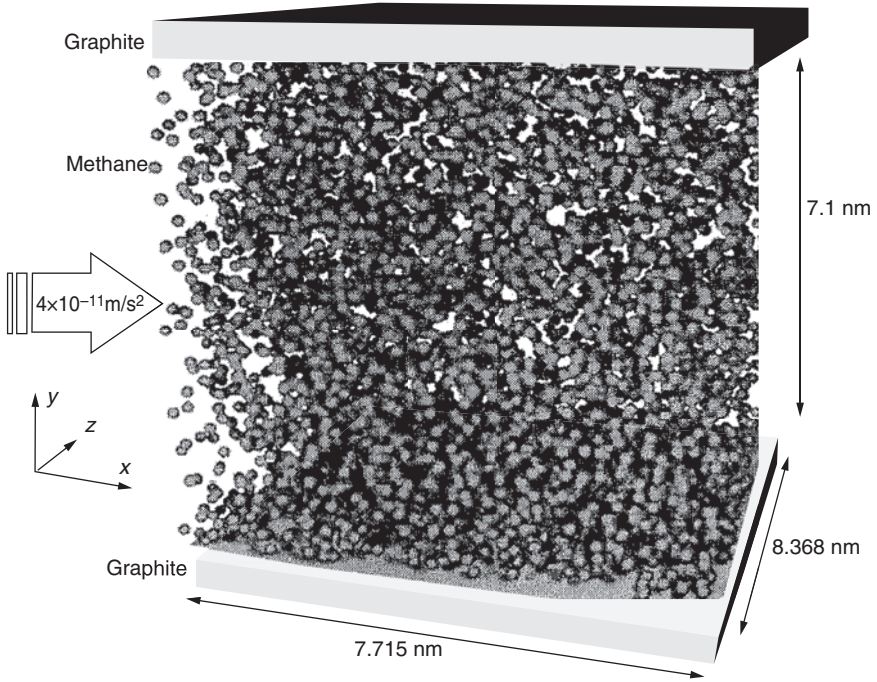


Figure 4.14 Cross-section of an artificially created slit pore.

The graphite plates were modelled in Sokhan's simulation using two fully molecular solid lattices of carbon atoms ($\sigma = 0.34$ nm and $\epsilon = 28$ K). The wall used in this simulation was modelled with diffuse boundary conditions, with a tangential momentum accommodation coefficient of 0.029, which was derived for this system in the same paper by Sokhan *et al.* [60] and confirmed by the work of Arya *et al.* [61] for methane on graphite.

Typically, the solid–fluid interaction parameters are computed using the Lorentz–Berthelot combining rule, which between the carbon and methane molecules leads to parameters $\sigma = 0.3605$ nm and $\epsilon/k_b = 64.39$ K. However, the work presented by Sokhan *et al.* shows results for different strengths of interaction between the wall and fluid molecules, so a stronger potential of $\epsilon/k_b = 148.1$ K was used to simulate a higher degree of wetting.

The fluid molecules are driven down the channel by applying a uniform acceleration to all molecules of 4×10^{-11} m/s. In Sokhan's simulations with flexible walls, the energy added via this acceleration could be removed and adsorbed by the wall molecules. However, in the case of the rigid molecular walls and the diffuse boundaries used in the present model, a Gaussian thermostat was used to perform the same task.

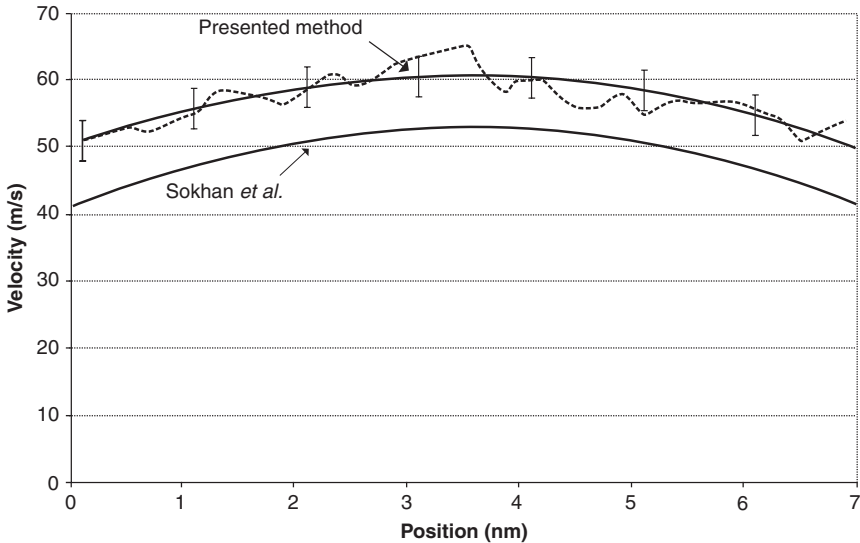


Figure 4.15 Comparison between the presented model and results published by Sokhan *et al.* [60]. Error bars are shown at ± 3 m/s.

The resulting velocity profiles are shown for comparison in Figure 4.15. The results from Sokhan were taken over a 1 ns period, whereas the results obtained by the presented method were constructed within a 0.1 ns long ensemble. The variation displayed by successive profiles extracted by the presented method is less than ± 3 m/s or 5 % of the average velocity; the variation of Sokhan's comparison is not known. The two velocity profiles show very similar curvature, but the results of Sokhan *et al.* [60] display a slightly lower average velocity than the results of the presented method. The similarity between the profile shapes means that the fluid molecules propagate the fluid energy in the same way, although the differences in the average velocity appear to be caused by differences in the boundary conditions applied. As an additional check extra validation tests were performed to test the system conformity to the thermal distributions.

The molecular dynamics of the fluid molecules was checked against the Maxwell–Boltzmann velocity distribution in each of the three dimensions, as well as the total speed distribution. Figure 4.16 shows the distributions from a short snapshot of the steady state simulation above, along with the exact versions of the distributions. All distributions show good agreement with the profile of the exact versions within 15 %, demonstrating that the molecules of the fluid conform to the correct thermodynamic state and that the thermostat is not having adverse effects on the velocity distributions.

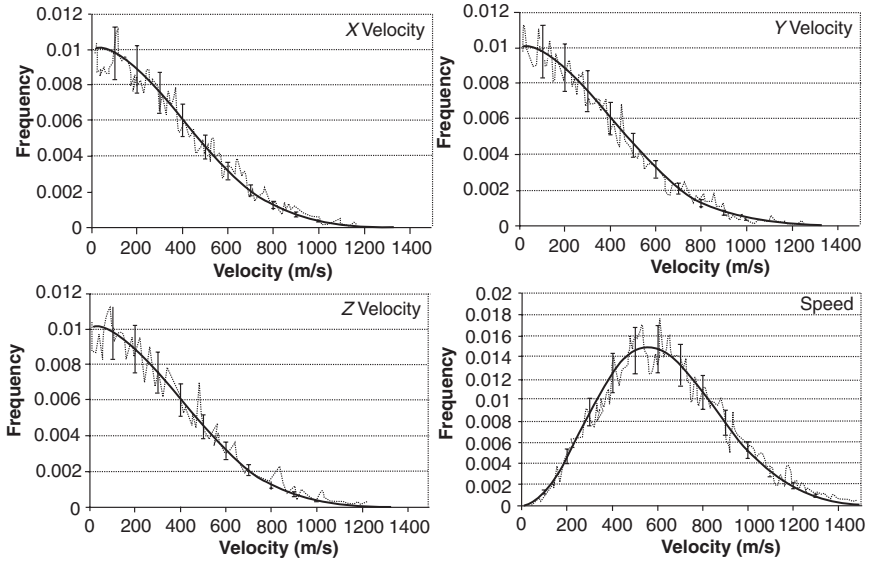


Figure 4.16 Distribution of X , Y and Z components of velocity, and the distribution of resultant speeds compared to distributions for temperature of 300 K with 15 % error bars.

The velocity distribution for the velocities assigned to the thermalized molecules at the boundary were also tested, to ensure that the thermalization was being performed correctly. Figure 4.17 shows the same level of variation as the bulk temperature distributions within the fluid.

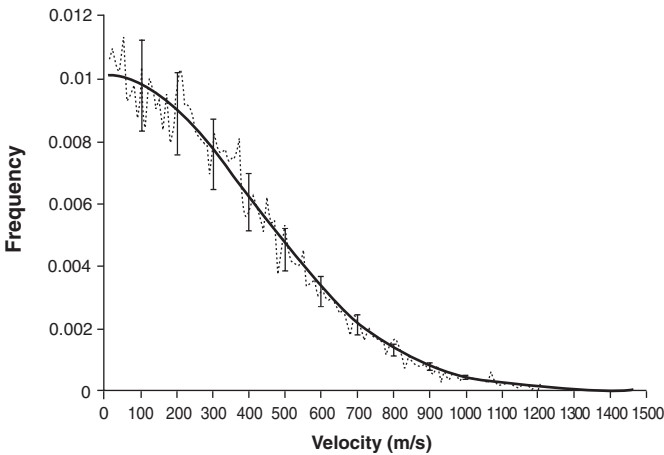


Figure 4.17 Velocity distribution of molecules thermalized by the boundary, shown against the velocity distribution for 300 K with 15 % variation

These results provide confidence in the developed meso scale molecular model. The simplifications applied to allow larger molecular systems to be accessed have not had an adverse effect on the mechanics, as shown by this molecular scale example compared to existing molecular simulation data from a well-established and developed code.

4.5 SUMMARY

In this chapter the method developed in the previous chapter has been extended to enable the simulation of flowing fluid systems. The generations of a flow have been implemented in the form of applying a representative acceleration to all molecules in the system. This addition of energy is balanced by a thermostating system designed to remove thermal energy from the simulation without affecting the dynamics of the molecules.

A number of case studies have been presented to look at the behaviour of the bulk property extraction scheme. These highlighted the importance of sample length and the size of the ensemble as well as their effect on the stability and resolution of the solution. Also highlighted was the tradeoff between sample and ensemble times for simulations within a restricted time frame.

Case studies involving property gradients were also considered. The temperature gradient simulation example highlights the thermal control that can be imparted on the fluid by the boundaries. This also highlighted the method's ability to capture bulk property distributions with high accuracy and resolution. The velocity profile case study results demonstrated good agreement with both published results and thermal distributions.

5

Modelling Fluid Regimes at Nano/Meso Scales

Aim. The reader should see how a fluid system can be explored using meso scale methods. This chapter also shows some of the current limitations faced by this meso scale approach.

5.1 INTRODUCTION

In this chapter, the application of the presented approach and how it may be used to extract useful data and properties from a fluid system dominated by molecular physics is discussed. To highlight its application, the bulk property extraction method is used to investigate flow regimes present in nano scale channel flows.

In the next section, flow regimes and the characterization of fluid flow in a continuum framework are discussed as a background to existing knowledge of fluid behaviour. Fluid flow from the molecular scale exists as a flow of molecules, but in meso scale systems the behaviour of both bulk and molecular flow becomes important. The third section presents a molecular fluid model for flow in a slit pore 15 nm high. The method developed in Chapters 3 and 4 is used to analyse the fluid at different flow rates by purely considering the bulk velocity distribution of the fluid. From this information the flow at high and low flow rates is compared, allowing the different flow behaviours to be analysed. To begin, continuum flow regimes will be discussed.

5.2 FLOW REGIMES

Fluid can flow in two basic forms, which were investigated by experiment by Reynolds (1842–1912) in the early 1880s [7]. These experiments highlighted the two different flows present in fluid systems, which will now be considered with the same approach as this experiment.

Figure 5.1 shows the setup of Reynolds experiments. A large tank of water has a long thin transparent tube, through which the water must pass to exit via the valve. The water is driven down the tube by the pressure difference between the pressure at the inlet to the tube in the tank and pressure of the outlet. The flow rate of the water along the tube can then be controlled by opening and closing the valve.

Dye is released into the centre of the flow along the tube via a thinner tube ending just inside the entrance. The dye is allowed to flow along the tube at the same speed as the water, and is used to visualize the internal behaviour of the fluid. By altering the flow rate of water passing down the transparent tube, Reynolds was able to study the way in which water flows through channels and tubes at varying speeds.

If the valve is only partly open, restricting the flow in the tube to only a small velocity, the thin stream of dye remains in the centre of the flow and is almost completely undisturbed (Figure 5.2). This is the observable result, at continuum scales, of the infinite molecular interchange occurring within the fluid, as has been discussed in Chapter 1. If multiple dye streams were employed at different places across the tube section, none would be disturbed, although those close to the boundary would move with a slower velocity. This gives the effect of the fluid being composed of layers of fluid moving parallel to each other, which is commonly referred to as *laminar flow*.

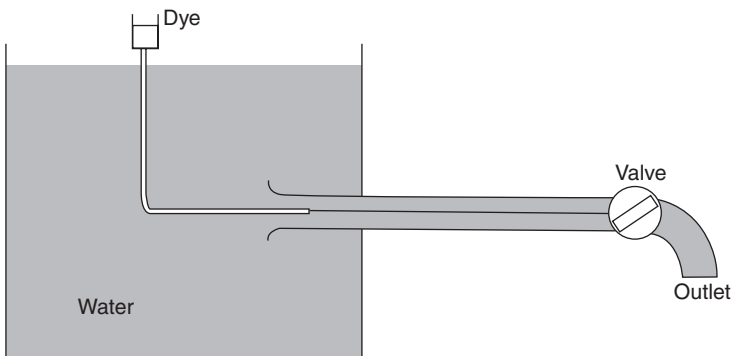


Figure 5.1 Apparatus used by Reynolds to study flow regimes.

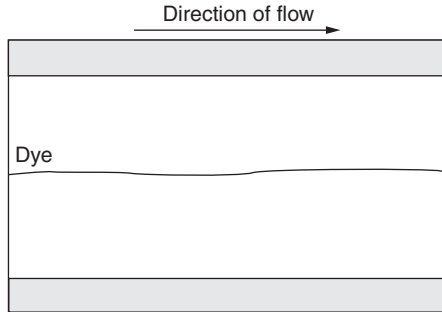


Figure 5.2 Parallel motion of a filament of dye within a laminar flow.

As the valve is opened further, the velocity of the fluid in the tube increases, and at some point the stream of dye begins to oscillate. If the valve were to be opened further, there comes a point at which the stream begins to diffuse at a distance away from the inlet. Further opening of the valve gives rise to a point at which a sudden breakdown of the dye stream at a distance from the inlet occurs, where the dye mixes almost completely with the water. Reynolds noticed that these disturbances only occurred at high flow speeds at a distance away from the inlet and that the mixing commenced suddenly.

The mixing of flow that occurs at these high flow rates is known as the *turbulent* flow regime. At this point, the fluid cannot be described in terms of layers of fluid at constant velocity across the channel, but particles of fluid (in terms of the continuum description of a fluid particle) mix across the width of the tube. The fluid particles in this flow regime have components of velocity that are not just in the direction of flow, and their paths criss-cross over each other in a seemingly unpredictable and chaotic way (Figure 5.3). In turbulent flow, the motion is irregular and conforms to no pattern in terms of frequency or formation of eddies, as the mixing occurs on a wide range of scales. However, there still remains a bulk

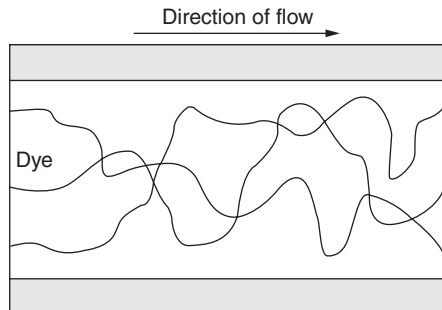


Figure 5.3 Chaotic mixing of filaments of dye within a turbulent flow.

average flow of fluid towards the outlet that the fluid particles follow, but they do not follow as pure a trajectory as fluid particles in a laminar flow.

Gotthilf Ludwig Hagen [90], a German physicist and hydraulic engineer, was the first to notice that the transition occurred in a tube at a specific velocity. He also noted that this velocity was dependent on the temperature of the fluid flowing through the tube, directly related to which is the viscosity. However, Hagen was unable to derive a general law to describe this behaviour.

Further experiments were performed using the above apparatus by Reynolds [7]. He noticed the inverse relationship between the transition velocity and the diameter of the tube. This led to the construction of the Reynolds number,

$$Re = \frac{\rho ul}{\mu}, \quad (5.1)$$

which is a function of density ρ , viscosity μ , velocity u and the characteristic dimension l (in this case the tube diameter). The relationship that Reynolds came up with was a measure with which to judge the transition to turbulence, but also taking advantage of the similarity of flows.

Reynolds noticed that large scale flows showed similar behaviour to that of flows of the same geometry, but on a smaller scale with a higher viscosity. This similarity of flows is used extensively in experimental investigations, and similar flows can be considered similar if they possess the same Reynolds number. The smooth, predictable nature of laminar flow allows it to be easily analysed mathematically. However, the complex and chaotic behaviour of turbulent flows does not allow for easy prediction. Turbulent flows are individual, and the exact dynamics of a turbulent flow is unrepeatable and is affected by dynamics on many scales. However, the behaviour of the fluid on small scales can be represented by statistical methods to provide an approximation of the multiscale mixing and eddy effects.

There are three basic models used for turbulent flow simulation on the continuum scale, DNS, LES and RANS. DNS (direct numerical simulation) presents the fullest simulation model turbulence and can be very accurate, but it is also very computationally expensive. RANS (Reynolds averaged Navier–Stokes) is the most simple, where turbulent terms are approximated as a function of the Reynolds number. LES (large eddy simulation and larger eddy simulation) presents a balance between the two, where the eddies on the scale of the simulation are evaluated fully and smaller scale eddies are approximated using a diffuse term.

5.2.1 Laminar Flow

Laminar flow can be described as fluid flowing in adjacent parallel layers, or laminae. Layers of fluid flow over each other, imposing shear or drag forces

on adjacent layers. Also the streamline followed by continuum fluid particles do not cross, but follow smooth predictable paths. This is the description commonly used for laminar flow at continuum scales. This description, however, is not valid at molecular scales as fluid layers and continuum particles cannot be described through the chaotic thermal motion of the molecules. It is therefore necessary to identify other distinguishing features to determine whether a flow is laminar in a molecular system.

For laminar, low speed flows, both Hagen and Poiseuille (1799–1869) found, through experimentation, a linear relationship between the head loss in a length of pipe and the flow rate of fluid. This head loss is the result of a linear relationship between the friction force experienced by the fluid from the wall imposing a velocity gradient on the flow. Here, the shear force between fluid layers results in a velocity gradient across the channel or pipe. This is quantified by the Hagen–Poiseuille equation for the flow rate Q in a cylindrical pipe of radius R :

$$Q = -\frac{\pi}{4\mu} \left(\frac{dp}{dx} \right) \int_0^R (R^2 r - r^3) dr, \quad (5.2)$$

which simplifies to

$$Q = -\frac{\pi R^4}{8\mu} \left(\frac{dp}{dx} \right). \quad (5.3)$$

The velocity at any radius of the pipe can also be calculated as

$$u(r) = -\frac{1}{4\mu} \left(\frac{dp}{dx} \right) (R^2 - r^2). \quad (5.4)$$

Velocity profiles of flows (see Figure 5.4) can be extracted from molecular simulations using the methods described in Chapter 4 and compared with those computed from the above equations. These equations, however, do not account for the slip between the solid and fluid at molecular scales [41]. On the continuum scale, it is assumed that there is no slip at the boundary and the fact that slip is present may have an effect on the linear relationship between the flow rate and pressure head. The velocity distribution of the flow in a channel or pipe, extracted from a molecular simulation, contains information about both the conformity to the laminar profile described by Hagen and Poiseuille and the flow rate in the tube. This information can be used to identify laminar behaviour through the chaotic molecular motion.

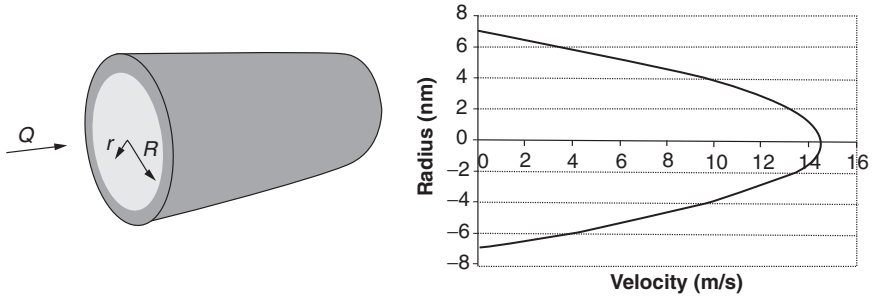


Figure 5.4 Velocity profile for laminar flow in a cylindrical pipe of radius R , as described by Hagen and Poiseuille [90].

5.2.2 Turbulent Flow

Turbulent flow occurs at high speeds, where the inertial terms of the Reynolds number dominate the viscous terms. In a turbulent flow regime, there is a high level of chaotic mixing and diffusion. From a continuum viewpoint, the paths followed by fluid particles are erratic and cross continuously as the flow is mixed up. On a molecular scale, the dynamics of the molecules does not appear to change significantly, as the chaotic random motion is present in both laminar and turbulent flows.

Experimental tests were performed by Henri Darcy (1803–1858) in 1857 [91] on turbulent flow in long pipes of different sizes, which resulted in the Darcy law for head loss in turbulent pipes. Due to the chaotic unpredictable nature, almost all models for turbulence contain some form of experimental results, as pure numerical analysis is not currently possible.

To identify a turbulent flow, observations of chaotic behaviour on its own is not sufficient at molecular scales, as it is present in laminar flow as well in the form of thermal motion. However, the mixing within turbulent flows occurs on a wider range of scales, which has the effect of increasing the energy losses internally within the fluid, where energy is dissipated away from the direction of flow. As a result, this increased instability in the fluid can be noted by observing the relationship between pressure loss and flow rate. The relationship should be similar to the laminar relationship, but with a lower gradient as the energy needed to drive the flow is higher. The increased energy perpendicular to the direction of flow should also increase the mixing of the fluid, leading to a different velocity profile that is more uniform across the centre of the channel.

This section has introduced continuum scale behaviour of the fluid in the form of two flow regimes, laminar and turbulent flow. These regimes can be easily observed, tested and simulated at continuum scales. However, as these simulation methods break down as the meso scale is approached, little is known about the

behaviour of molecular flows. In the next section, the method derived in Chapter 4 is used to extract information from a molecular simulation over a range of flow rates, to allow the behaviour of the flow to be analysed at different speeds.

5.3 FLUID FLOW CHARACTERIZATION FROM MOLECULAR SIMULATION

In this section, a molecular simulation is used to model the physics of a fluid passing through a slit pore of height 15 nm. Least square nodes are used to extract the bulk velocity distribution to provide information about the behaviour of the fluid at these scales. The slit pore is approximated by two parallel plates with diffuse boundary conditions in the y direction and periodic boundary conditions in the x and z directions.

In the following case, the velocity profile of the flow is extracted to measure the fluid response to increasing pressure gradients. The velocity gradient contains information about the flow rate of fluid along the channel which, for traditional laminar flows, should increase linearly with the increasing pressure gradient. However, at molecular scales, there is a definite amount of slip between the fluid and the boundary. This will affect the velocity gradient by raising the mean velocity in the channel as the frictional effect of the wall is reduced. The shape of the velocity gradient should maintain its Poiseuille profile approximately, allowing molecular variation, but with a nonzero velocity at the boundary, as shown in the validation tests in Chapter 4.

The system used in the tests is designed to replicate the flow of methane confined within a graphite slit pore. A two-dimensional schematic of the simulated three-dimensional system is shown in Figure 5.5. The pore walls are modelled as two single layers of carbon molecules in a graphite lattice, interacting via a Lennard–Jones potential. The Lennard–Jones parameters for methane were a collision diameter of $\sigma = 0.381$ nm, a well depth of $\epsilon/k_b = 148.1$ K and a molecular mass of 16.043 amu. The Lorentz–Berthelot mixing rules were used for the collision diameter, giving $\sigma = 0.3605$ nm for the carbon–methane interaction. The well depth used was $\epsilon/k_b = 148.1$ K, equal to the methane–methane well depth and similar to the methane wall used by Miyahara [35, 60], but the tangential momentum accommodation coefficient of the diffuse boundary was derived from the parameters of the carbon lattice, $f = 0.025$. The boundaries are fixed and possess no momentum, and therefore need no mass parameter.

The pore walls are 15 nm apart and infinite dimensions parallel to the pore are replicated using periodic boundary conditions in the x and z directions, with lengths 15 nm and 8.5 nm respectively.

Simulations were performed using a range of pressure gradients, simulated by applying a uniform acceleration to all fluid molecules. All tests were performed

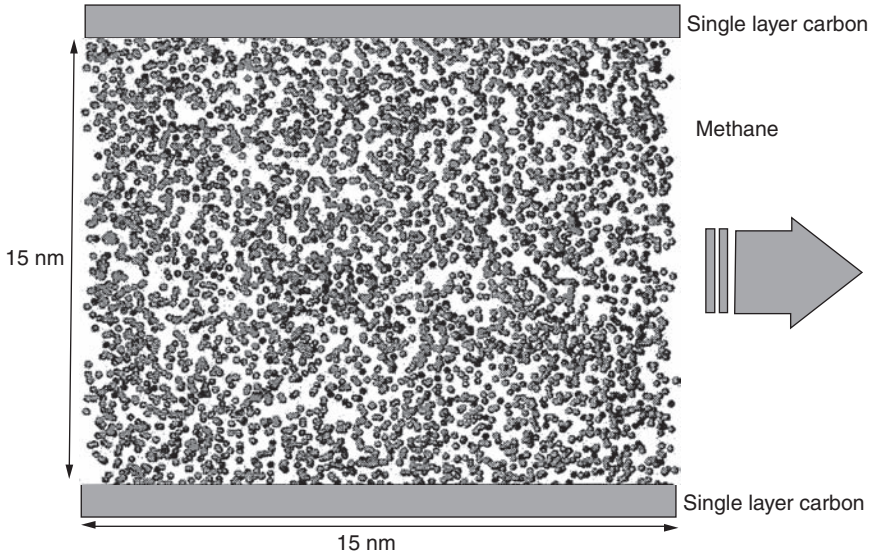


Figure 5.5 System to test flow regimes between parallel plates.

with the temperature at the wall maintained at 300 K and as the boundaries are solid and cannot remove sufficient energy from the system, the fluid temperature was maintained at 300 K using a Nosé–Hoover thermostat. The driving acceleration applied to the fluid was varied from $2 \times 10^{11} \text{ m/s}^2$ to $1 \times 10^{12} \text{ m/s}^2$ to test the response of the fluid over a wide range of flow rates.

The fluid response was measured using a one-dimensional array of nodes placed across the domain in the y direction, at 0.5 nm intervals. Samples of the x component of velocity (along the channel) of the molecules were taken every 200 time steps and ensemble averages were computed every 2000 time steps. By taking ensemble averages at these relatively short intervals, the progress of the simulation can be monitored using the velocity profile to check that a stable solution is reached for each run.

5.3.1 Characteristics of Low-Speed Molecular Flow

For the above model of a slit pore, the driving force along the pore ranged from $2 \times 10^{11} \text{ m/s}^2$ to $1 \times 10^{12} \text{ m/s}^2$. The resulting velocity profiles computed from the ensemble averages were recorded and the average velocity of the flow in each case was found. Figure 5.6 shows a plot of the resulting stable average velocity against the driving force applied to the flow.

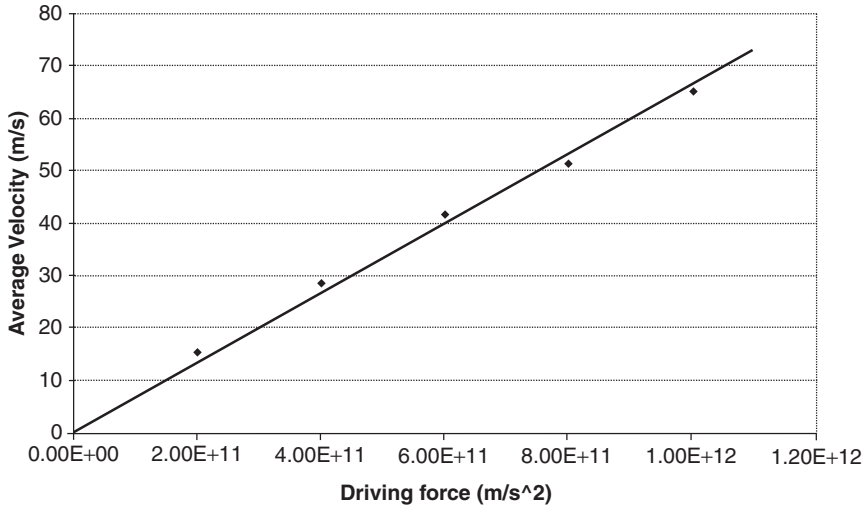


Figure 5.6 Average velocity in the channel plotted against the driving force (simulating pressure gradient) for low-speed flows.

The average velocity is plotted in Figure 5.6, as it is proportional to the flow rate of the fluid in the channel against the driving force applied to the flow. The graph shows a linear relationship between average velocity and the driving force, which passes through point (0,0). A degree of deviation is present from the linear line due to the short time over which the ensemble averages were taken, but a clear relationship is present.

In the chaotic molecular structure of a fluid, the molecules are continually moving with their own thermal velocity, conforming to the Boltzmann distribution. A useful comparison to draw is between the average of the thermal motion of the molecules and the average ‘bulk’ velocity of the flow. The average speed of a molecule in one direction can be computed from the Boltzmann equation as

$$v_{\text{average}} = \sqrt{\frac{T k_b}{m}}. \tag{5.5}$$

For a system temperature of 300 K, the average velocity due to thermal motion becomes [4]

$$v_{\text{average}} = 394.34 \text{ m/s}. \tag{5.6}$$

The lowest driving force tested in this system gives an average bulk velocity of 15 m/s, corresponding to a total of 3.8% of the average thermal velocity of molecules. Similarly, the largest velocity of 65.5 m/s corresponds to 16.6%,

both of which are very small compared to the magnitude of the motion of the molecules.

5.3.2 Characteristics of High-Speed Molecular Flow

By extending the range of driving forces applied, the bulk velocity extracted captured a change in the behaviour of the flowing molecules. Figure 5.7 shows a plot of the average velocity of the flow against the driving force for values up to $F/m = 5.0 \times 10^{13} \text{ m/s}^2$. On the left-hand side of the graph, the same data as the graph shown in Figure 5.6 is displayed. However, for larger driving forces, a change in the behaviour can be seen beyond this region.

Beyond the linear, slow-speed flow region (far left of graph), the same increase in driving force causes less of an increase in the average velocity. The fluid response reduces further until another approximately stable relationship is displayed for driving forces of between $1.2 \times 10^{13} \text{ m/s}^2$ and $5 \times 10^{13} \text{ m/s}^2$. This high-speed flow regime is present over a range of velocities from 190 m/s to 254 m/s, which when compared with the average thermal velocity of the molecules is 48.2% and 64.4% respectively. The low gradient of the graph in the high flow rate region of the graph indicated that a higher proportion of the energy given to the fluid by the driving force is diffused away from the direction of motion.

The range of driving forces tested was stopped at $5 \times 10^{13} \text{ m/s}^2$ because it was found that at higher values the thermostat interfered with the dynamics of the

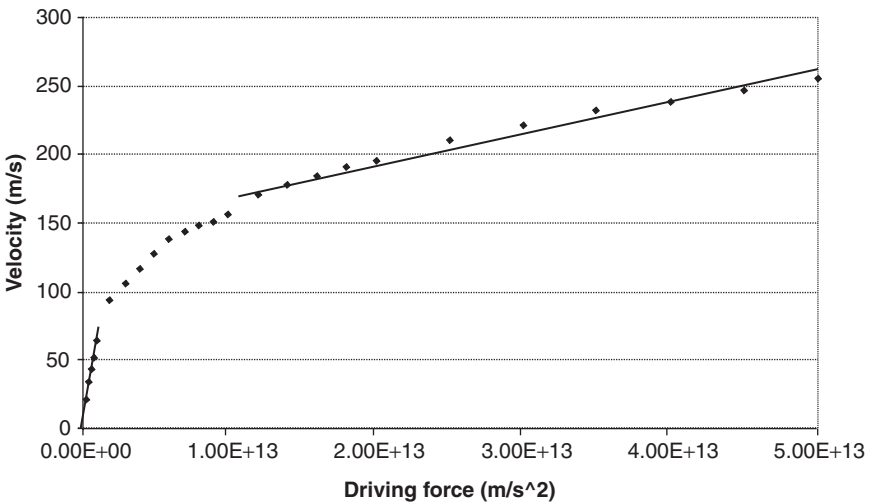


Figure 5.7 Average velocity in the channel plotted against the driving force (simulating pressure gradient).

simulation. At values of $6 \times 10^{13} \text{ m/s}^2$, the molecular motion becomes unstable, causing clusters of molecules to form. This is due to the system becoming over-constrained with molecules settling into a quasi-equilibrium state in which they change energy states as little as possible; however, they still maintain the global velocity distributions.

The results shown in Figure 5.7 demonstrate that the behaviour of different flow regimes can be captured and identified from a molecular simulation, where the high flow regime displays much higher losses than the low flow rate regime. The low-speed flow can be likened to a laminar flow, where losses are low, meaning that the exchange between layers parallel to the direction of flow should be minimal. In the high flow case, losses are higher and a higher level of interaction and exchange is expected to be perpendicular to the flow direction. This can be examined by comparing further data extracted during the simulations.

5.3.3 Comparisons and Data Analysis

To further aid in the characterization of these two regions, comparisons can be drawn between their behaviour. The presented method for obtaining the bulk properties has been used above to extract velocity profiles of the flow to plot the average velocity of the flow against the applied driving force. From these results, two regions have been identified: one that displays significantly higher losses than the other. Further analysis of these regions can be performed by comparing the velocity profiles extracted from simulations performed in each of the regimes. Figure 5.8 shows the velocity profiles extracted for driving forces of $2 \times 10^{12} \text{ m/s}^2$ and $4 \times 10^{13} \text{ m/s}^2$, corresponding to flows within the low and high flow rate regimes respectively. The velocity profiles were extracted using 29 nodes placed at 0.5 nm intervals across the channel, sampling at 75 time step intervals (2.0 fs time step), and each ensemble was measured over 0.4 ps.

The extracted profiles are shown in Figure 5.8. The profile extracted from the simulation with a low flow rate (bottom) displays a profile that is much more curved than the high flow rate profile. Accounting for the slip between the wall and the boundary, the profile is similar in shape to the analytical Poiseuille profile for describing laminar flow in pipes and channels. The profile is caused by the smooth propagation of energy throughout the system, where a molecule diffusing across the channel experiences many low-energy collisions, altering its thermodynamic state as it passes each point. Both profiles show the same degree of variation, $\pm 25 \text{ m/s}$. The variation is dependent on the thermal motion of the underlying molecules and therefore the same for high- and low-speed flows.

The high flow profile, on the other hand, displays a markedly different shape. For this flow regime, the molecules possess more energy and display a significantly flatter velocity profile, showing that there is less difference in kinetic

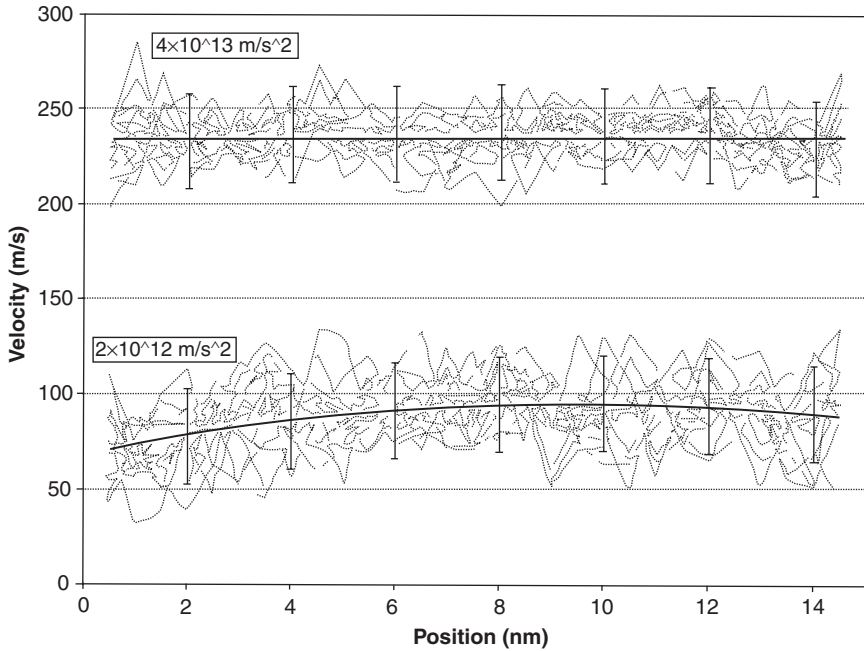


Figure 5.8 Velocity profiles extracted from molecular simulations for driving forces of $2 \times 10^{12} \text{ m/s}^2$ and $4 \times 10^{13} \text{ m/s}^2$. Flows at the two speeds show a variation of $\pm 25 \text{ m/s}$.

energy at neighbouring points through the simulation. This is in agreement with the continuum description of a turbulent flow with a flatter profile, as there is a higher degree of energy transfer between adjacent layers of fluid (mixing of energy), causing this velocity profile to form. This highlights the difference in the propagation of energy within the system, but does not indicate the propagation of mass within the channel.

An examination of the diffusion of mass within the system was performed using the following tests. The same simulation as above was set up and equilibrated to steady state for driving forces of $2 \times 10^{12} \text{ m/s}^2$ and $4 \times 10^{13} \text{ m/s}^2$, corresponding to the same low and high flow rates between parallel plates used above. All the molecules falling within a vertical band between $x = 3.0 \text{ nm}$ and $x = 5.0 \text{ nm}$ were selected and tagged at the start of the production stage. The simulation then proceeded for a short 282 fs period to allow the molecules to diffuse from their original positions, but not reach the periodic boundaries (for clarity). After this short time period the final distributions of the molecules can be plotted to determine the spread achieved as a result of diffusion.

Figure 5.9 shows the initial and final plots for the low and high flow rates for only those molecules tagged at the start of the simulation; all other molecules have

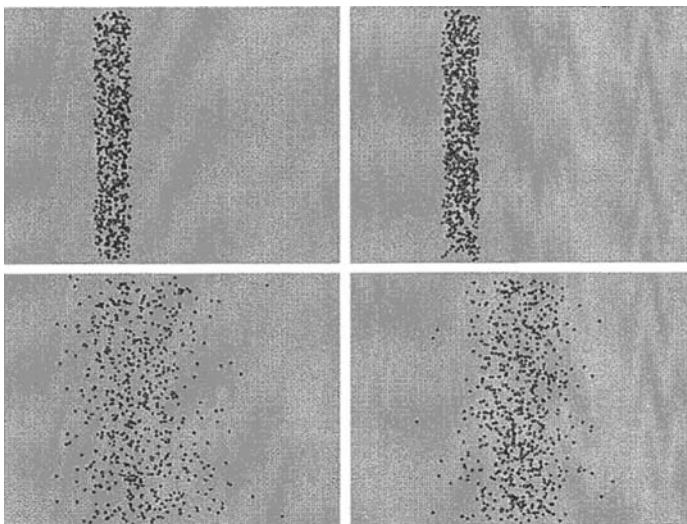


Figure 5.9 Initial and final distributions of molecules in the centre of the channel after 282 fs (the flow is from left to right). Left: low flow rate. Right: high flow rate.

been removed from the images. From these images, it is clear that the molecules in the high flow rate stream have moved further than those in the low flow rate stream. It is also noticeable that the high flow molecules have not dispersed as much as those in the low flow. This is confirmed by looking at a histogram plot of the distribution of the molecules, shown in Figure 5.10.

In Figure 5.10, the frequency has been normalized for the number of molecules in each band, as the low and high flow examples contained a slightly different number of molecules. These results highlight the fact that there is a substantial difference between the distributions of the two regimes. The standard deviation of the low flow rate simulation is 0.0443, whereas the high flow value is substantially lower, at 0.0302.

The same test performed with a horizontal band, between $y = 6.0$ nm and $y = 9.0$ nm, allows an examination of the way in which the molecules diffuse vertically, perpendicular to the solid boundaries. Figure 5.11 shows the initial and final plots. In these figures, the distribution of molecules in the low and high flow rates in the y direction is visibly the same in both cases. Figure 5.12 shows a histogram of the data collected, along with the initial position of the band. The graph shows that the majority of molecules have diffused in different directions in the low and high cases, but the distributions of the molecules after a short time are almost identical. The low flow rate gives a standard deviation of 0.0320 and the high flow rate gives a value of 0.0304.

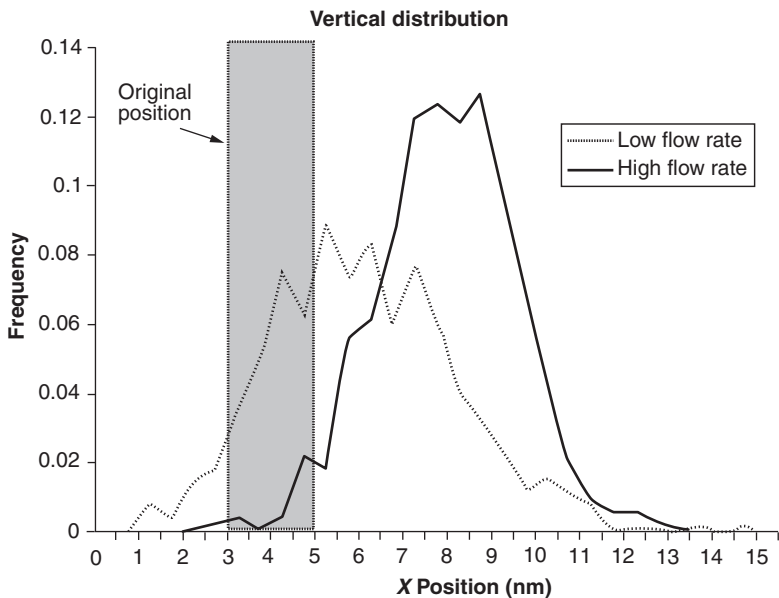


Figure 5.10 Graph comparing the distributions of the molecules in low and high flow rate simulations after 282 fs of simulation time.

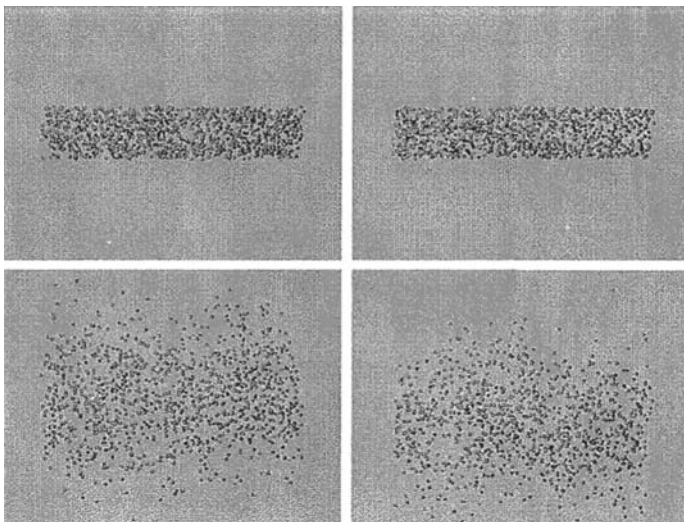


Figure 5.11 Initial and final distributions of molecules in the centre of the channel after 282 fs (the flow is from left to right). Left: low flow rate. Right: high flow rate.

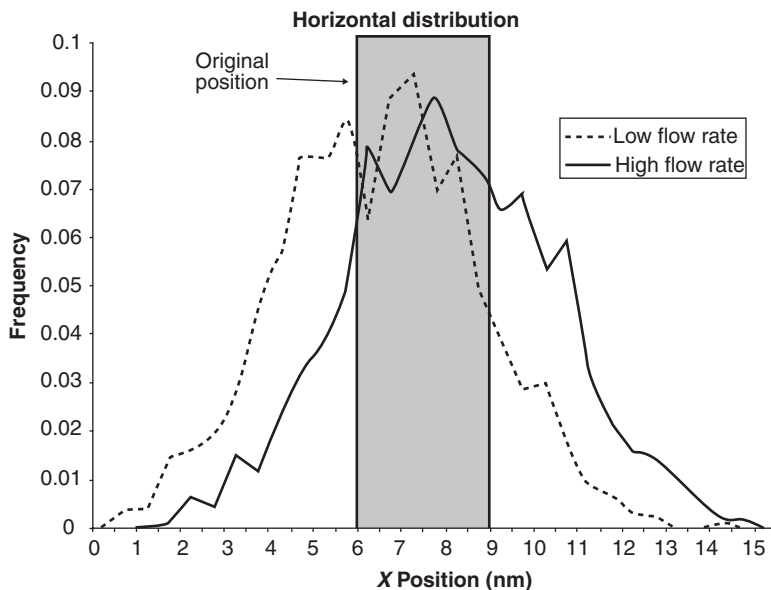


Figure 5.12 Graph comparing the distributions of the molecules in low and high flow rate simulations after 282 fs of simulation time.

These results give an indication over a small time frame of the diffusion of mass within the molecular system in the x (streamwise) and y (perpendicular to pore walls) directions. In the x direction, the molecules within the high speed flow diffuse less than those travelling in the lower-speed flow. However, there is little change in the diffusion of the molecules in the y direction due to the interaction with the solid boundaries. The molecules in the high flow case have a bulk motion that is a greater proportion when compared to the thermal motion of the molecules, which has the effect of ordering the molecules. Also, the increased energy being diffused perpendicular to the direction of motion has the effect of containing the molecules by the increased strength of the neighbour interactions (due to the increased energy perpendicular to the direction of flow). In the low flow case, the molecules have a much smaller component of bulk velocity and have more freedom to drift within the fluid domain.

The result is that as the speed of the flow increases, energy is distributed internally within the fluid. This is shown in Figure 5.7, where the energy lost identifies two regimes where a change of behaviour can be identified. Beyond this point, it can be shown in the comparison between the two velocity profiles in Figure 5.8 that for high flow rates the energy is diffused over a wider area across the channel, but the mass diffuses less. This is due to the increased molecular exchange between regions of fluid in terms of molecular interactions.

However, in the high flow case energy appears to be distributed in directions perpendicular to the direction of flow, showing turbulent behaviour. In a continuum framework, this would be accompanied by an increase in temperature across the channel. In this case, however, the thermal constraints imposed by the thermostat fix the average temperature of the channel. This overconstraining of the system could be a factor in the behaviour that has been extracted from the molecular dynamics. This is an area of meso scale simulation that needs more investigation and comparison with experiments for extra clarification, and may lead to the development of a new meso scale energy constraint system.

5.4 SUMMARY

In this chapter, it has been shown how bulk behaviour can be extracted from the simulation of the internal molecular interaction and how this information can be used to investigate fluid flow systems. This chapter has concentrated specifically on the extraction of bulk velocity of a fluid in a slit pore, but the same principles can be implemented for pressure, density and temperature distributions, either independently or investigated together, depending of the dynamics of the system of interest.

In the slit pore case study, the velocity profiles were extracted as ensembles of average velocity at nodal sites placed at regular intervals across the channel. The spacing of the nodes, together with the radius of influence associated with each node, allows for the provision of spatial resolution and clearly displays the curved velocity profile in the low flow rate case. In all the extracted profiles, a degree of statistical variation is present, and profiles are approximated as averages. This is due to the short ensemble time allotted for ensemble profiles to provide good temporal resolution and allow the approach to steady state to be monitored.

Using this approach, a change in behaviour could be captured, highlighting the possibility of two flow regimes being present. This combined with an analysis of the diffusion showed a reduction in the mass diffusion but an increase in the diffusion of energy within the fluid, which together with the consideration of the system energy constraints goes to account for the high losses in the high flow system. This example has highlighted how this method may be employed to extract useful data from a molecular physics dominated system and allows the analysis and characterization of a fluid system in terms of useful engineering properties and behaviour. Also highlighted are the energy constraint issues using the current thermostat systems.

6

Performance of Proposed Meso Scale Model

Aim: The reader should understand the computational performance issues faced by molecular physics models at these scales.

6.1 INTRODUCTION

In this chapter, the computational issues associated with performing simulations using the molecular model and bulk property extraction on meso scale systems are discussed. The next section details the performance issues faced with large scale molecular modelling and studies how the computational demands change as the system size increases. This section also highlights the importance of the consideration of density when considering large scale molecular simulations.

The third section contains a study of the flow along a slit pore of meso scale dimensions. Simulations contain between 20 000 and 100 000 molecules, and the impact this increased number of molecules and increased density has on the performance of the computation and the behaviour of the fluid is discussed.

6.2 ISSUES IN USING LARGE NUMBERS OF MOLECULES

In general, as the number of molecules increases in the system the computational time and resources required also increases. The number of molecules in a system can change in three ways, as a result of a change in density, a change in volume or

a change in both. Up to this point in this book, molecular simulations have been performed within cells of a maximum dimension of 15 nm, with a maximum of 5104 molecules. This has been in order to allow validation of the molecular model and the ability to explore the abilities of the bulk property extraction method with low numbers of molecules, where the method is weakest. In this section the resulting impact on the computational resources is discussed as a result of increasing the size of the molecular system to achieve meso scale dimensions.

First, the effect of an increase in the number of molecules at constant density (increased volume) is discussed.

6.2.1 Processing Large Numbers of Molecules

An increase in the system size has a number of knock-on effects within a molecular simulation. By increasing the number of molecules, the time to process the molecules and their interactions increases as well the memory needed to store their positions and lists of neighbours. Additionally, information on each molecule position, velocity and resultant force in all three dimensions must be stored during each time step.

In order to simulate meso scale systems that contain large (up to 100 000) numbers of molecules, the computational requirements of the simulation must be fully understood. To explore the limits of a molecular model, performance tests are performed to gain an understanding of the computational requirements in two ways. First, the effect of a simple increase in system size is tested by comparing the processing time of simulations with different numbers of molecules of the same density (volume altered). Second, these results will be compared to simulations of varying density in systems of the same volume. These tests will help an understanding of the issues important in simulating large molecular systems and the limits faced. These simulation tests are performed with a small number of molecules, between 14 and 5104 molecules. It is hoped that these small molecular numbers will display some overhead processing time of the standard computations and operations performed, giving a minimum computation time.

6.2.1.1 Constant density simulations

The simulations performed at constant density were performed using a cubic cell with periodic boundary conditions in all three dimensions. The side of the cubes tested were 1 nm, 2 nm, 3 nm, 4 nm, 5 nm, 6 nm, 7 nm, which contained 14, 114, 385, 913, 1783, 3080 and 5104 molecules respectively, as shown in Figure 6.1. This test explores the scalability of the molecular model and the extra requirements needed to simulate large molecular numbers. For each system, the time taken to reach 1ns of simulation time was recorded, along with the average number of neighbour interactions per molecule. In a molecular simulation, as the

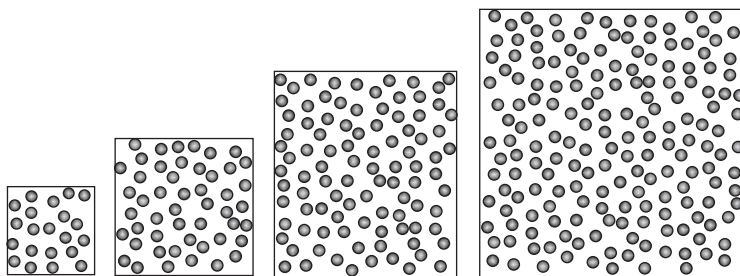


Figure 6.1 Simulations performed at constant density, over a range of volumes and numbers of molecules, to test computational requirements.

number of molecules increases, so does the size of the arrays required to store position and velocity of all the molecules. For each additional molecule in the system, the size of the array increases, thus increasing the amount of computer memory required. However, the size of the neighbour list arrays depends on the number of neighbour pairs in the simulation and changes with the number of molecules and the density of the simulation. The neighbour lists can be far longer than the molecular properties arrays, and because of their dependence on the number of molecules as well as the system parameters, can capture behaviour that may further increase the computational time and memory requirements.

Figure 6.2 shows a plot of the number of molecules against the average number of neighbours possessed by molecules within the system, over the different system

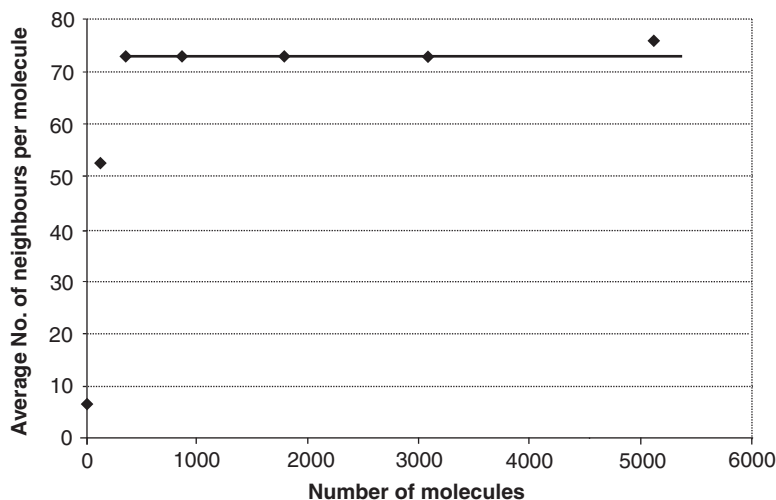


Figure 6.2 Plot of the number of molecules against the average number of neighbours per molecule for the constant density simulations.

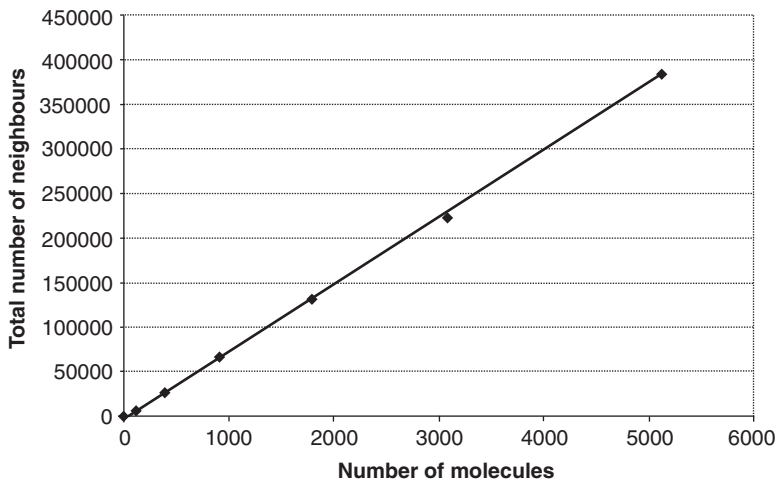


Figure 6.3 Plot of the total number of neighbours against the number of molecules for the constant density case.

volumes at constant density. This graph shows a constant 72.6 neighbours per molecule for simulations with above 385 molecules, and hence for systems with sides greater than 3 nm. The low number of neighbours for 14 (1 nm) and 114 (2 nm) molecules are due to the neighbour list cut-off radius being greater than 2 times the length of the periodic cell, as only a one-image buffer is considered in each dimension. However, this constant relationship is to be expected beyond the 3 nm system, due to the constant density. This presents a linear relationship between the number of molecules and the total number of neighbour pairs (Figure 6.3), steadily increasing the computational time needed to process all neighbour interactions.

Figure 6.4 shows a plot of the number of molecules against the time taken for the simulation to reach 1 ns. This graph shows a smooth relationship between the time needed to process the simulation and the number of molecules. The time increase added for each molecule added increases with the number of molecules. As shown in Figure 6.2, the number of neighbours per molecule is constant for the larger systems, but in this case extra time is spent searching through the extra molecules and constructing and processing the neighbour list interactions. Neighbour searches are performed periodically as described in Chapter 1, but the searches are performed over the whole system. By adding one extra molecule to a system of N molecules, the number of search evaluations being performed increases by N , and at this density the number of extra interactions to process increases by approximately 72.

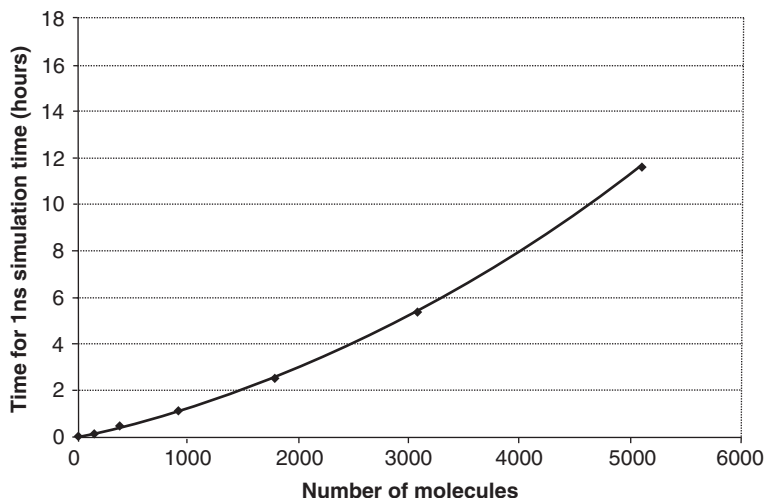


Figure 6.4 Plot of the number of molecules against time taken to reach 1 ns of simulation time for the constant density simulations.

Such computational costs can be reduced by implementing another stage of search/sorting that can be performed over smaller areas frequently, and over the whole system less frequently. This, however, would require more memory, thus trading off memory against computation time.

6.2.1.2 Constant volume simulations

To aid as a comparison with the above results for system sizes at constant density, simulations were performed over a range of molecular numbers at constant volume. Simulations were performed over a range of densities (Figure 6.5) within a constant volume cube of side 5 nm and periodic boundary conditions in all three dimensions.

The densities tested were 2.984, 24.29, 82.05, 194.6, 380.0, 656.4 and 1087. kg/m³ with 14, 114, 385, 913, 1783, 3080 and 5104 molecules of methane respectively. In these simulations, the number of molecules increases, which increases the time required to process and move the system molecules, and are subject to all the issues raised about computational time and resources as the constant density tests above. However, these simulations are performed at increasing density, which when compared to the results above, isolate the effect of increasing the length of the neighbour lists.

Figure 6.6 shows a plot of the number of molecules against the average number of neighbours per molecule possessed by each molecule in the simulation.

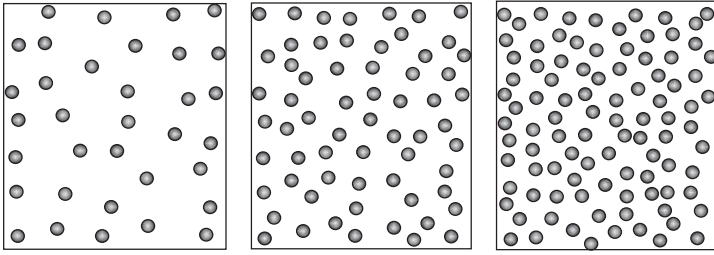


Figure 6.5 Simulations performed for different numbers of molecules at the same volume, with varying densities to test the additional computational resources required for high-density systems.

The graph shows a linear increase in the number of neighbours with the increase in the number of molecules present. This means that the neighbour lists are not only getting longer due to the increased number of molecules, as was shown in the constant density test results, but the length of the neighbour lists is also increasing because the number of neighbours possessed by each molecule in the system is increasing. This further increases the number of pairwise force evaluations required, extending the demand on memory storage and CPU processing.

Figure 6.7 shows a plot of the number of molecules against the time taken for the simulation to reach one nanosecond, for a range of system densities as specified above. Simulations were performed on a 3 GHz processor PC with 2 GB

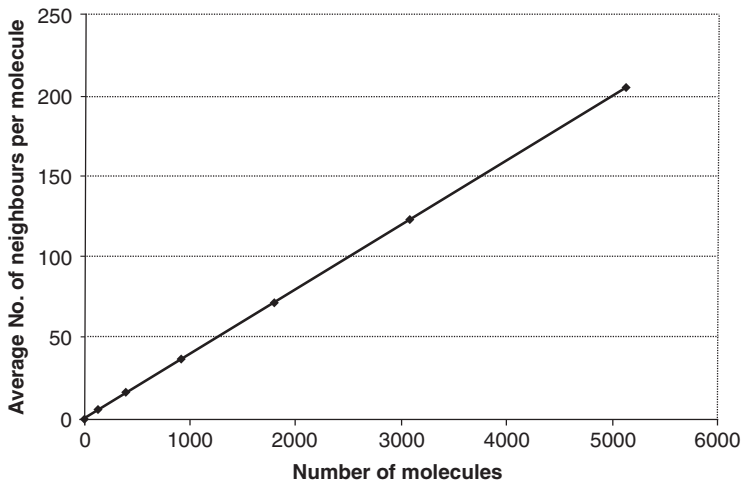


Figure 6.6 Plot of the number of molecules against the average number of neighbours per molecule.

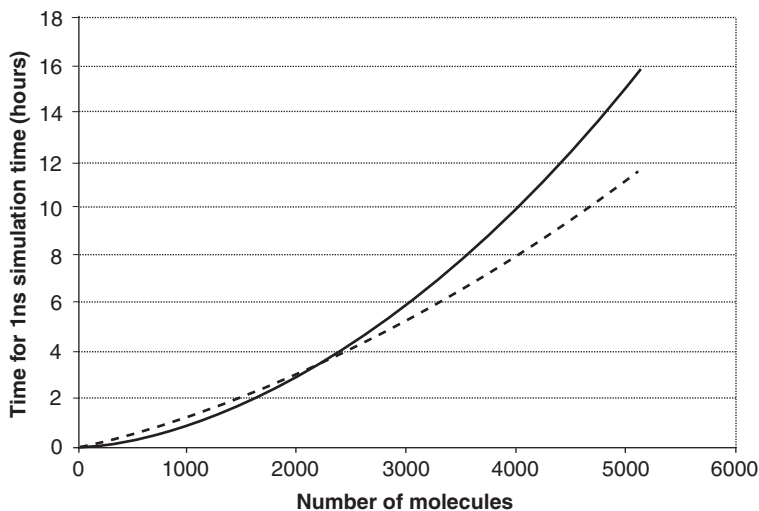


Figure 6.7 Plot of the number of molecules against time taken to reach 1 ns of simulation time for constant volume simulations (solid line) and constant density simulations (dashed line, Figure 6.4).

RAM (random access memory). The graph for the constant volume simulations (simulations of varying density, shown by the solid line) is shown against the results for the processing time of the constant density simulations (dashed line, Figure 6.4). The constant density simulations were performed in a 5 nm cube and the range of numbers of molecules used was the same in both constant density and volume simulations. As a result, the two resulting curves intersect at the system containing 1783 molecules.

This, however, creates an interesting point on the graph in Figure 6.7, where systems larger than 1783 molecules (constant density simulations performed at 380.0 kg/m^3) show that the higher-density simulations (solid line) require more computational time than the simulations containing the same number of molecules at a lower density (from the constant density simulations). This is due to the extended length of the neighbour lists and the number of extra interactions that need to be processed. However, for the simulations with less than 1783 molecules, systems with lower densities than the constant density simulations show that a shorter length of processing time is needed to process the interactions within the system, as the neighbour lists are shorter. This demonstrated the importance of considering the density of a molecular simulation when considering the resources required by a simulation.

The above study highlights the issues present in simulating large numbers of molecules. Although these simulations have been undertaken using a maximum of

only 5104 molecules, they show the reaction of the system to changes in volumes and density in terms of performance. It is particularly important to understand these concepts with small system sizes, as the only difference between these tests and large-massive systems (apart from larger numbers) is the reduced proportion of time spent on overhead calculations and linear operations.

These results highlight the importance of considering the density of the simulation as well as the number of molecules being processed, as a high-density simulation (or one with high density regions) can significantly increase the processing time and memory requirements. Also highlighted is the tradeoff that is possible between CPU resources and memory, which can be made during the search routines. This can utilize a larger memory usage to speed up the time taken searching for neighbouring pairs within the simulation domain with a tree-like search structure.

These issues are key, as the results indicate that there is a limit on the available simulation domain at meso scales in terms of both molecular numbers and density, which depend on the computing power available.

6.2.2 Boundary Conditions

In this molecular model, the solid molecular boundaries have been replaced with an approximating continuous wall to remove solid molecules from the simulation in order to reduce computational cost. These diffuse boundary conditions replicate the scattering/corrugation effect of a molecular wall over a large number of collisions by thermalizing a proportion of the colliding molecules. As the characteristic length and time of the system increases, the number of collisions occurring with the wall over this time and length scale increases. As a result, the wall approximation is being performed over a larger number of collisions, and provides a much better approximation. The boundary conditions have been validated against fully molecular walls at molecular scale dimensions with results published by Sokhan *et al.* [60], in Chapter 4. This validation of the model with a low collision rate over the time and length scale of the simulation gives confidence in the validity of the boundaries at larger scales where the collision rate is higher.

6.2.3 Bulk Property Extraction

At meso scale dimensions, bulk properties become much more defined and stable as their definition improves and importance rises, but they are still below the limit at which they can be evaluated by the continuum governing equations. The parametric study performed in Chapter 4 highlights the fact that the ensemble averages of properties collected is improved by sampling the widest range of available phase space positions. A molecular system with meso scale dimensions

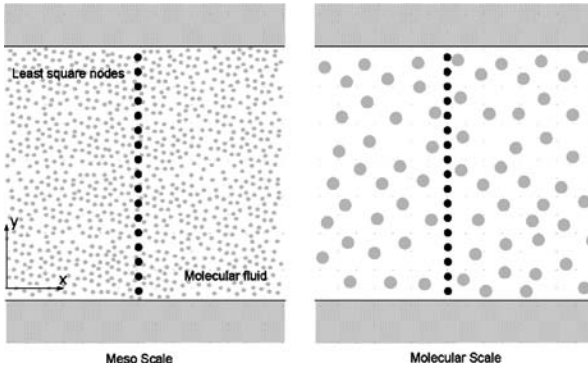


Figure 6.8 Extracting bulk properties from systems with a high number of molecules (left) and a low number of molecules (right).

containing a large number of molecules allows a greater number of molecules to be included in the influence zone of each node as the resolution of the system moves up to meso scale resolutions, when compared to a system of molecular scale dimensions of the same density (Figure 6.8).

6.3 MESO SCALE SIMULATIONS

The small scale tests performed up to now have tested the lower limits of this method for extracting bulk ensemble properties from molecular simulations. The results may be less accurate because the ensemble averages have low numbers of molecules. Nevertheless, the method provides a framework that allows the characterization of bulk effects from a molecular model. These bulk fluid properties have a definitive meaning above the molecular scale over large numbers of molecules. The bulk properties have a definite definition on a continuum scale, but there are a wide range of governing equations that can predict bulk fluid behaviour at these scales. The aim of this method is to capture the behaviour of these properties at meso scales, where they have meaning but cannot be characterized by continuum equations. It is particularly important to characterize the fluid in terms of meaningful properties relevant to solving engineering problems occurring at the meso scale. In this section simulations are performed at meso scale dimensions to examine the way in which the behaviour of this method, and the dynamics of the molecular model, change when a large number of molecules is used.

The system used is similar in form to the slit channel used previously to aid comparison with smaller systems; this is shown in Figure 6.9. The slit channel is approximated by two parallel sheets of graphite separated by 93 nm, with modified boundary potentials to approximate an infinite solid comprised of

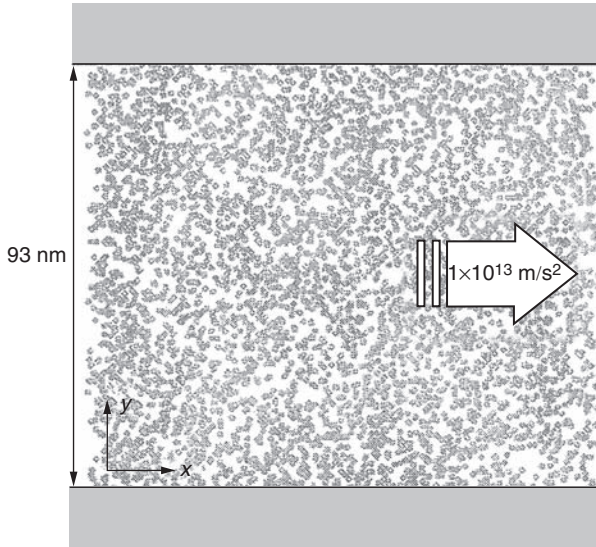


Figure 6.9 Approximated slit pore, showing the flow of methane molecules between parallel graphite planes.

parallel graphite layers. The walls themselves were approximated using the diffuse boundary conditions with a tangential momentum accommodation coefficient of $f = 0.029$ [60,61]. Periodic boundary conditions are applied in the x and z directions at 93 nm and 40 nm respectively. An acceleration of $1 \times 10^{13} \text{ m/s}^2$ is used to simulate a pressure-driven flow in the x direction.

The available volume between the graphite walls was filled with methane molecules interacting with Lennard–Jones potential with a collision radius of $\sigma = 3.81 \text{ \AA}$ and a well depth of $\epsilon = 148.1 \text{ K}$. A range of densities was investigated of 1.58, 3.15, 4.73 and 7.89 kg/m^3 , corresponding to 20 000, 40 000, 60 000 and 100 000 molecules respectively. All simulations were performed with a fluid and wall temperature equal to 300 K. This model generates a flow of molecules along the slit pore, the behaviour of which was observed using a one-dimensional series of 46 nodes placed perpendicular to the direction of flow, in the y direction. The nodes, spaced at 2 nm intervals, captured the streamwise component of velocity.

The nodes collected molecular properties of molecules within a radius of influence of 2.5 nm, using the Gaussian weighting function in the least squares approximation. The Gaussian weighting function was shown to be the most capable in the parametric study in Chapter 4, and the nodal radius was chosen to allow for high resolution in order to allow the boundary layers at the solid interfaces to be captured.

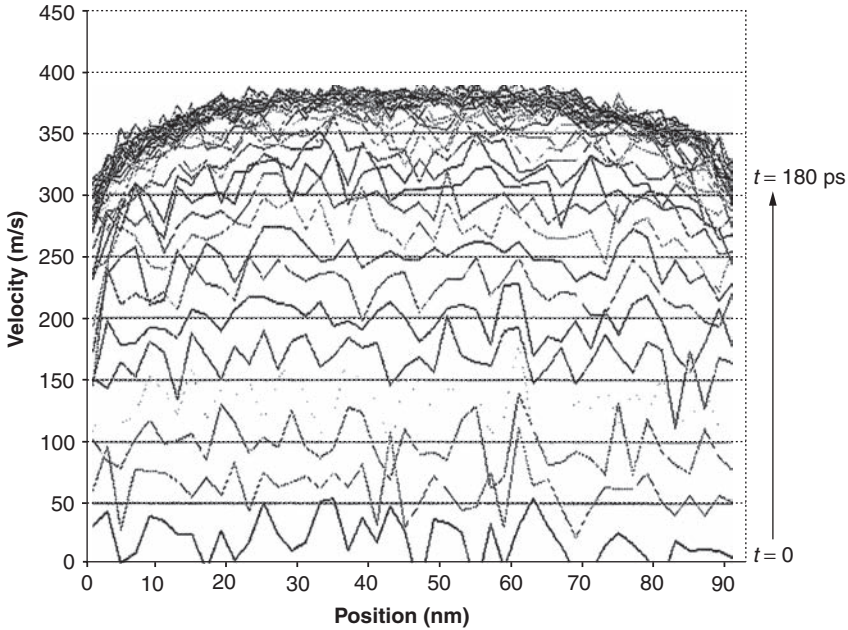


Figure 6.10 Bulk ensemble velocity profiles taken at 2 ps intervals. At $t = 0$ the fluid is at rest.

The time step used was 2 fs and samples were taken every 100 time steps. The ensemble averages were calculated over all nodes every 2000 time steps. The parametric study also found that larger times between samples and ensembles gave the best results, but for these simulations relatively short times were chosen to capture the development of the steady state solution.

Figure 6.10 shows the development of the solution for the low-density system containing 20 000 molecules. This graph clearly shows the system's progress to develop a steady state solution from $t = 0$ where the velocity of the system is zero, to the final equilibrium state after 90 000 time steps at $t = 180$ ps. At $t = 0$, the initial velocity increase between ensembles is large and the data contains a lot of variation, but as the simulation progresses the change in velocity between successive profiles reduces until the equilibrium state is reached. Once equilibrium has been reached, the successive velocity profiles are almost identical and show significantly less variation than at the start of the simulation, where diffusion is a higher component of the resultant velocity of the molecules.

The above simulation was repeated for systems of the same volume containing 40 000, 60 000 and 100 000 to examine the effect that a density increase has on large systems in terms of both the fluid behaviour and the performance of the simulation. All simulations were performed with the same approximated

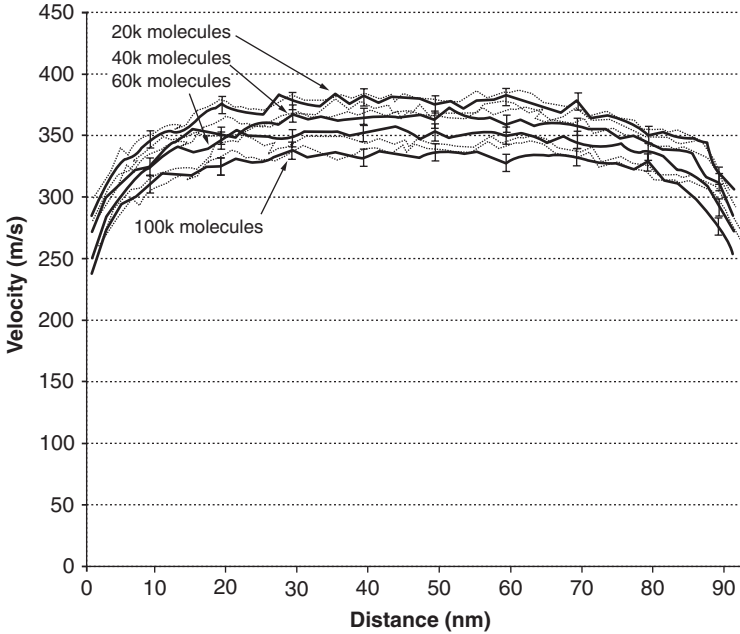


Figure 6.11 Steady state velocity profiles for slit channel systems with 20 000 (top), 40 000 (middle top), 60 000 (middle bottom) and 100 000 (bottom) molecules, corresponding to densities of 1.58, 3.15, 4.73 and 7.89 kg/m³. For clarity the average profile is shown with ± 7 m/s.

pressure gradient of 1×10^{13} m/s² and using the same parameters for collecting the ensemble properties.

The resulting steady state profiles are shown in Figure 6.11 for the four different densities. The average of four extracted profiles is shown with variations in each case of ± 7 m/s. From this graph the difference between the simulations of different densities can be seen. All of the results show boundary layer effects at both walls, but the velocity at the wall is slightly higher on the right-hand side of the graph. This is due to the distance between the nodes and the solid boundary, which is 1 nm on the left of the graph and 3 nm on the right. This has been done to highlight the errors that are introduced at the boundaries. If a node's 'zone of influence' extends beyond the boundaries of the fluid only a proportion of its available area may contain molecules; hence there are fewer molecules from which to sample the local behaviour. This leads to an increase in the variation in the results as fewer points in the available phase space are sampled, an effect that can be clearly seen when comparing the results of the four simulations on the left- and right-hand sides of the graphs. Here, the node placed at 3 nm from the boundary has its 2.5 nm 'zone' fully within the fluid domain and shows a clear distinction

between the four sets of results. The final node on the left, placed at 1 nm from the boundary, shows more variation as more of the node's 'zone' is outside the fluid domain. However, this node captures a lower velocity at the boundary, than the node on the right. This is an important effect to consider when placing nodes within the domain, as nodes closer to the boundaries give better information about the behaviour at the boundary, but only if the information is within an acceptable tolerance. This effect is minimized when the number of molecules is increased and as the percentage difference between the number of molecules in boundary nodes and the number of molecules in other nodes is reduced.

As the density of the simulation is increased, the average velocity in the channel decreases. In continuum terms, increasing the density of a simulation increases the Reynolds number. However, at molecular scales, the concept of Reynolds number is not well defined due to the variation of flow properties. A flow with a higher Reynolds number could potentially mean higher losses within the system, and Chapter 5 highlighted the fact that higher losses were found in systems with a high diffusion of energy and a lower diffusion of mass. Higher density simulations exhibit an increased number of collisions due to the increased number of neighbouring molecules.

6.3.1 Performance of Meso Scale Simulations

These meso scale simulations at different densities contain large numbers of molecules, from 20 000 to 100 000. The performance tests performed earlier in this chapter highlighted the high demand of high-density simulations, and as a result these tests were performed at relatively low densities. All simulations in this section were performed on a Xeon 3.2 GHz processor with 6 GB RAM. To examine the performance, similar data to previous tests were extracted in the form of neighbour pairs and simulation time.

Figure 6.12 shows a plot comparing the number of molecules in the simulation against the number of neighbour pairs per molecule. The graph shows the same linear relationship to that shown by the smaller scale variable density simulations in Figure 6.6, although in these tests the density is much lower (small scale density simulations were performed at a density of 72.8 kg/m^3).

Figure 6.13 shows a plot of the simulation rate of the variable density simulations at meso scales, which shows an exponential decrease in the number of time steps that can be performed per hour as the number of molecules in the system increases. In the 20 000 molecule case, 3483 time steps could be completed in an hour, but by increasing the number of molecules by a factor of 5, the number of steps that can be processed decreases by a factor of 21.4 to 163 per hour. This demonstrates the high cost of large systems of molecules. The computational cost could increase significantly for systems of higher densities.

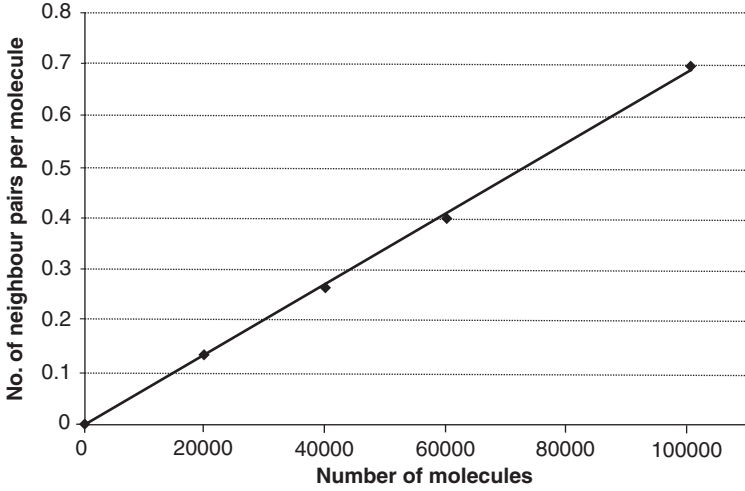


Figure 6.12 Number of molecules plotted against the number of neighbour pairs per molecule for the meso scale density simulations.

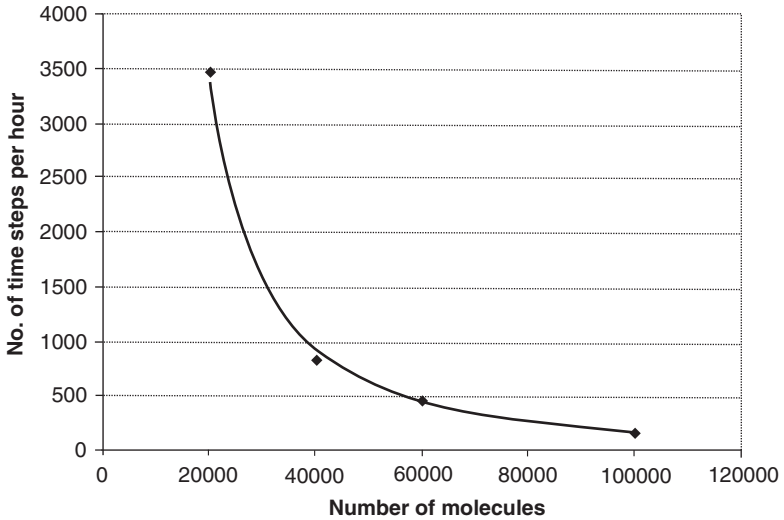


Figure 6.13 Plot of number of time steps achieved per hour against the number of molecules in the meso scale variable density simulations.

6.3.1.1 Predictions

Using the data collected in the above section, it is possible to predict the consequences of dramatically increasing the number of molecules. Figure 6.14 shows a plot of the number of molecules against the number of neighbour pairs for the same, constant volume, examples shown above. In this figure, the line of best fit has been extended to predict the number of neighbours present if there were one million molecules in the same volume. The figure shows that on average there would be approximately seven neighbour pairs per molecule. As has been shown above, the density of the system impacts strongly on the CPU time and resources required to complete each time step. Figure 6.15 shows a plot of the number of molecules against the number of time steps that can be completed per hour. This figure has used the line of best fit to predict the number of time steps completed per hour for a system containing one million molecules. The plot shows that approximately 2.2 time steps can be completed per hour. This dramatic reduction is due to the time required to process the movement of such a large number of molecules, the time searching through the domain for neighbouring molecules, and the evaluation of the forces between neighbour pairs (which is also increased as the high density of the system generates a larger number of force interactions to be processed). To perform the same 180 ps equilibration time with a one million molecule simulation would take approximately 4.6 years of continuous simulation time. This time could be seriously reduced with the implementation of

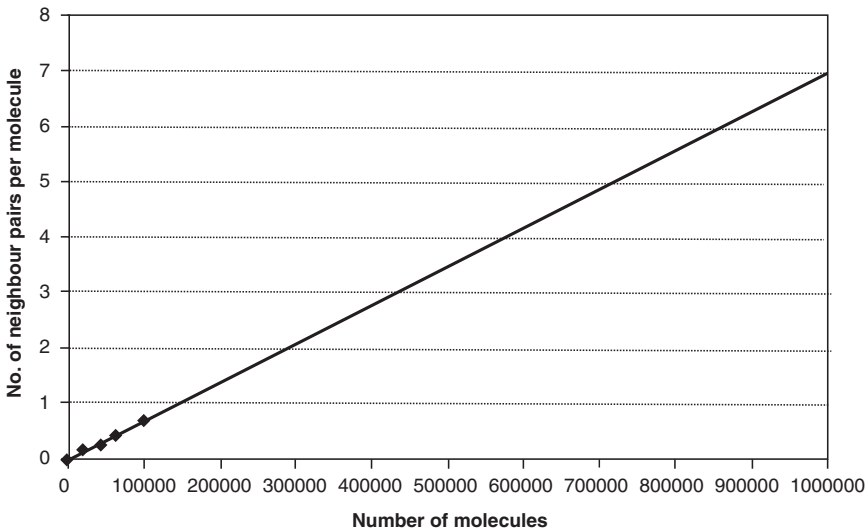


Figure 6.14 Plot predicted from previous data of the number of molecules plotted against the number of neighbour pairs per molecule for up to 1 million molecules.

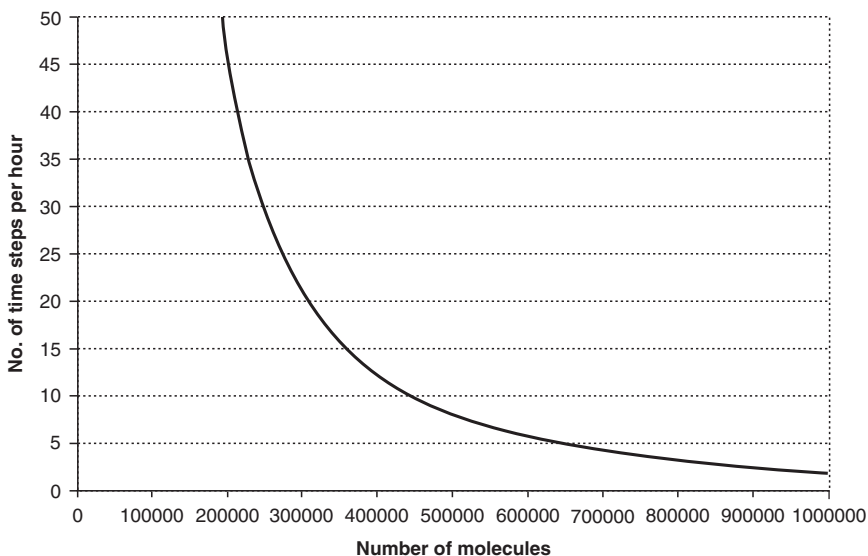


Figure 6.15 Plot predicted from previous data of the number of time steps achieved per hour against the number of molecules up to one million.

parallel processing and by performing searches for neighbour pairs over smaller subdomains rather than over the global system.

6.4 SUMMARY

This chapter has presented a large number of issues associated with modelling meso scale systems with a molecular model. At meso scales, the number of molecules begins to prohibit the range of systems that can be simulated. The limit on the molecular model is not in terms of scale and dimensions but in terms of the number of molecules and the density of the system. The penalty in terms of increased computational cost increases exponentially as the number of molecules or density increases.

From the bulk property extraction method point of view, as the number of molecules increases over the length scale of the simulation, the better the definition and the more stable the ensemble averages of the bulk properties become. A greater number of molecules improves the phase space sampling at each of the nodes, allowing a better resolution in time as well as space compared to the length scale of the simulation.

7

Experimental Aspects of Fluid Properties at the Nano/Meso Scale

Aim. By the end of this chapter the reader should be aware of and understand experimental techniques that can be used to study fluid systems at different scales and should also be aware of how events at the nano/meso scale can affect experimental results at the macro scales.

7.1 INTRODUCTION

So far this book has discussed many different methods for modelling the properties/flow of fluids at the nano scale. In this section, a practical example of where these models may be used to predict process parameters will be examined. The process considered here will be the membrane separation of nano-fluids. Nano-fluids consist of a solid/liquid mixture in which nano-sized particles (diameter < 100 nm) are suspended evenly in the base liquid [92]. The membrane separation of these fluids is based on the microhydrodynamics and interfacial events occurring at the membrane surface and inside the membrane. This immediately points to the requirement for understanding the behaviour and properties of the fluid at the nano-scale.

This chapter will outline the following:

- (a) colloidal interactions relevant to the process;
- (b) the use of the colloidal interactions in describing the properties of a nano-fluid, i.e. osmotic pressure, gradient diffusion coefficient and viscosity;

- (c) comparison of experimental results with theoretical predictions for the nano-fluid properties;
- (d) comparison of theoretical predictions with experimental results for the rate of frontal and cross-flow ultrafiltration.

Also considered in this chapter are other aspects of fluid behaviour arising from nano confinement, including their tensile and nano-rheological behaviour. Key experimental technologies for the study of fluids under such conditions are discussed.

7.2 COLLOIDAL INTERACTIONS IN NANO-FLUIDS

The interactions between the particles contained in a nano-fluid, or between these particles and an interface, control the operation of many industrially important processes and also determine the properties of the final products. In most aqueous-based nano-fluid systems there are three types of interactions that are usually operative:

- London–van der Waals or dispersion forces (ubiquitous);
- electrostatic or double-layer forces (when particles and surfaces are charged);
- steric interactions (short range for small molecules, long range for macromolecules).

Entropic effects are also important when considering the properties of nano-fluids.

In this chapter only electrostatically stabilized systems will be considered. The first properties that need to be quantified when trying to evaluate these systems are the size and charge. The size of nano-fluid particles can be determined by photon correlation spectroscopy [93, 94]. One of the characteristics of nano-particles is that they are in constant random thermal, or Brownian, motion. This motion causes the intensity of light scattered from the particles to vary with time. Large particles move more slowly than small particles, so the rate of fluctuation of the light scattered from them is also slower. Photon correlation spectroscopy uses the rate of change of these light fluctuations to determine the size distribution of the particles scattering light [94].

The zeta potential (and thus charge) can be obtained from electrophoretic mobility measurements [95]. Microelectrophoresis is the measurement of the movement of nano-particles, in dilute dispersion, when they are placed in an electric field. The measurement can be used to determine the sign of the charges on the particles and also their electrophoretic mobility, which is related to the surface charge and zeta potential [95].

In order to optimize processing it is also necessary to have knowledge of how the interaction properties are influenced by pH and ionic strength. For relatively

simple nano-fluids, quantification of the electrostatic and dispersion forces will give a complete description of the overall interactions. For more complex systems it is necessary to compare such initial predictions with experimental data to quantify the additional specific interactions. The atomic force microscope (AFM) probe techniques used in atomic force microscopy and AFM hybrid instruments is ideal to do this [96, 97]. These techniques can be used to measure the forces of interactions between surfaces and other particles in a range of process-relevant environments.

Colloidal interactions are responsible for strikingly influencing the transport properties of nano-fluids, such as gradient diffusivity and also viscosity, and the thermodynamic properties such as the osmotic pressure. The osmotic pressure is a key property in membrane separation processes as it controls the spatial distribution of particles in the concentration polarized layer and hence the rate of permeation. As a result, any fundamental attempt to model the filtration of nano-fluid systems requires adequate knowledge of the influence of colloidal interactions both on osmotic pressure and transport properties.

7.2.1 Particle–Particle Interactions

7.2.1.1 *Electrostatic interactions*

The electrical double layer, zeta potential and surface of shear Virtually all colloids in an aqueous dispersion acquire a surface charge and hence an electrical double layer. The Gouy–Chapman model [95] gives the simplest description of an electrical double layer which comprises a charged surface and a diffuse layer of counter ions, treated as point charges, in the solution. The distribution of the charges in the solution is described by the Poisson–Boltzmann equation (PBE). This model can be refined by taking the finite size of real ions into account [95], so that the diffuse layer in reality is assumed to start at the outer Helmholtz plane (OHP), which lies a small distance, d , away from the particle surface. The space charge in the electrolyte is now divided into two regions: (a) the compact or inner region very near the particle surface (up to the OHP) and (b) the diffuse layer where the PBE applies.

The detailed structure of the inner region of the double layer is not directly important in the modelling of ultrafiltration processes [98, 99], but the method by which the distance to the OHP is calculated will depend on the type of model used for describing the compact region. The position of the OHP is important as this is widely assumed to lie coincident with or very near to the surface of shear at which the zeta potentials are calculated from electrophoretic mobility data [95]. The zeta potential is then the potential at the beginning of the diffuse layer. For oxide surfaces, such as silica, a triple-layer model such as the Gouy–Chapman–Grahame–Stern model [95] is often used to describe the compact region. This model allows for a plane of (partially dehydrated) adsorbed ions on the particle surface and is

the most usual way that the high surface charge on the oxide is reconciled with the quite low diffuse double-layer potentials (zeta potentials) found. For the protein bovine serum albumin (BSA), the modified Gouy–Chapman model [95] where the OHP is located at the plane of closest approach of the hydrated counterions is probably more appropriate. This is because although some ion binding of the electrolyte ions does occur with the BSA surface, the number of ions bound is low [100] so an inner layer as described by the Gouy–Chapman–Grahame–Stern model would be inappropriate.

7.2.1.2 *Overlap of the electrical double layers: cell model*

When particles interact their diffuse double layers will overlap, resulting in a repulsive force that opposes further approach. The multiparticle nature of such interactions in concentrated dispersions can be taken into account using a Wigner–Seitz cell model [101] combined with a numerical solution of the nonlinear Poisson–Boltzmann equation in spherical coordinates [98]. A configurational force can then be calculated that implicitly includes the multibody effects:

$$F_{\text{ELEC}} = \frac{1}{3} S_{\beta} n^{\circ} kT \left(\cosh \frac{ze\psi_{\beta}}{kT} - 1 \right), \quad (7.1)$$

where S_{β} is the surface area of the Wigner–Seitz cell and ψ_{β} is the potential at the cell boundary.

From Equation (7.1) it can be seen that the configurational force will depend upon the numerical solution of the PBE to calculate ψ_{β} . The numerical solution of the PBE requires two boundary conditions. The condition that is used at the outer cell boundary is that of electroneutrality. A choice of boundary conditions is available at the particle surface. It is important to choose physically meaningful conditions at the particle surface that may depend on the colloidal material being considered. For metal colloids in a solution, a constant surface potential boundary condition is appropriate. A constant surface charge boundary condition may be appropriate when the surface charge is caused by crystal lattice defects, such as in clay minerals. In the case of biomaterials and oxide surfaces, the charge can be generated by surface dissociation reactions that are influenced by the solution conditions. This can be described by a boundary condition known as charge regulation [102]. A boundary condition where the zeta potential is held constant is also possible.

7.2.1.3 *London–van der Waals forces*

The most rigorous calculations of London–van der Waals forces are based on an analysis of the macroscopic electrodynamic properties of the interacting media.

For the present purposes a calculation procedure that is less exacting but accurately represents the results of modern theory is required. An effective approach is to calculate a value for the Lifshitz–Hamaker constant, which may be found if refractive index data for the pure substances in the colloidal dispersion are known over a range of wavelengths. A ‘Cauchy plot’ [103] may then be used to establish parameters that are used to calculate the Lifshitz–Hamaker constant. The attractive interaction energy, V_{ATT} , can then be calculated for two equal spheres of radius a at a distance D apart using [104]

$$V_{\text{ATT}}(D) = -\frac{A_{\text{H}}}{6} \left\{ \frac{2a^2}{D^2 + 4aD} + \frac{2a^2}{(D + 2a)^2} + \ln \left[1 - \frac{4a^2}{(D + 2a)^2} \right] \right\}, \quad (7.2)$$

where A_{H} is the screened, retarded Lifshitz–Hamaker constant [105]. The attractive force between two particles can be calculated from the interaction energy expression as

$$F_{\text{ATT}}(D) = -\frac{dV_{\text{ATT}}}{dD}. \quad (7.3)$$

7.2.1.4 Entropic pressure

The packing of particles at a high concentration leads to an entropic pressure, tending to disperse them. Various researchers have proposed equations to describe the hard sphere entropic pressure data produced by molecular dynamic calculations [106, 107]. The resulting continuous approximation that gave the best results for both high and low volume fractions is the Padé approximation of Hall [107],

$$\frac{P_{\text{ENT}}}{kT} = \left(\frac{3\phi}{4\pi(a+d)^3} \right) \left(\frac{1 + \phi + \phi^2 - 0.67825\phi^3 - \phi^4 - 0.5\phi^5 - X\phi^6}{1 - 3\phi + 3\phi^2 - 1.04305\phi^3} \right), \quad (7.4)$$

where

$$X = 6.028 \exp[Y(7.9 - 3.9Y)] \quad \text{and} \quad Y = \frac{\pi\sqrt{2}}{6} - \phi.$$

7.3 OSMOTIC PHENOMENA AND OSMOTIC PRESSURE

When a membrane that separates two fluid phases is impermeable to one (or more) of the components of one of the fluid phases, there is a net flow of diffusible components across the membrane, which is usually in such a direction that the non-diffusible component is diluted. This phenomenon is called ‘osmosis’. Osmosis is a process in which the solvent is transported through the membrane as a result of the difference in transmembrane concentration. If the system is not subject to any

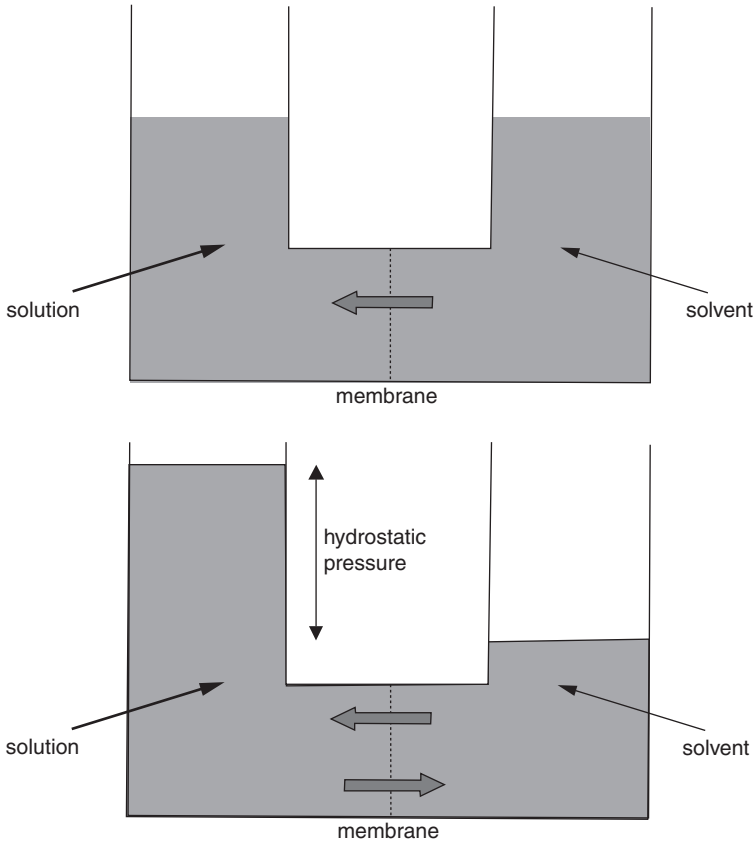


Figure 7.1 Illustration of osmosis and osmotic pressure.

external influence, such as removal of excess solvent, then a hydrostatic pressure difference is established, at which point net material transport reaches zero. This condition is known as ‘osmotic equilibrium’, and the corresponding pressure difference is referred to as osmotic pressure (see Figure 7.1). Osmotic equilibrium is a hydrodynamic equilibrium; solvent still passes through the membrane but the fluxes are statistically the same in both directions.

7.3.1 Measurement of Osmotic Pressure

7.3.1.1 Osmometers

All osmometers contain two compartments, which are separated by a membrane. Solvent is usually placed in one compartment and the solution in the other. There

are also arrangements for measuring the pressure in or applying a controlled pressure to either or both compartments. Pressure, in this context, may be either positive or negative. When there is no application of any controlled external pressure, the system reaches equilibrium with the pressure on one side of the membrane being higher than the other. The osmotic pressure is then obtained. The process to reach equilibrium is slow, taking quite a few hours or even longer [108]. Therefore some researchers use systems with applied pressure, the rate of approach to equilibrium is measured, often under controlled applied pressure, and the equilibrium position when the net flow is zero is determined by interpolation [109–111].

These two kinds of procedure for measuring the osmotic pressure may be broadly distinguished as the static method, in which systems are allowed to reach equilibrium, and the dynamic method, which uses systems with applied pressure. Figure 7.2 shows a schematic diagram of a static method membrane osmometer.

To measure the osmotic pressure of nano-fluids using the static method, the following experimental protocol is used. A nano-fluid of known concentration and background solvent conditions (pH and ionic strength for aqueous solutions) is loaded carefully into one chamber of the osmometer and then the pure solvent at the same conditions (pH and ionic strength) is placed in the other chamber. The nano-fluid chamber is then sealed, while the solvent chamber is left open to the atmosphere. After both sides of the osmometer are filled, the pressure in the nano-fluid chamber is followed and recorded via a computer. The pressure build-up is monitored until a steady state is reached (usually after about 3–6 hours). The equilibrium pressure is then recorded. The equilibrium pressure is taken to be the osmotic pressure of the nano-fluid at the given conditions. The whole apparatus is kept at a constant temperature throughout the experiment.

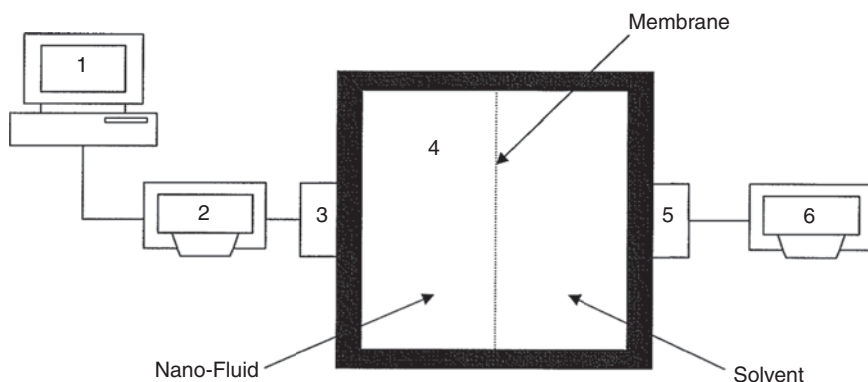


Figure 7.2 Schematic diagram of a static osmometer experimental setup: 1, computer; 2, pressure indicator; 3, pressure transducer; 4, osmometer cell (see Figure 7.3); 5, thermo-couple; and 6, temperature indicator.

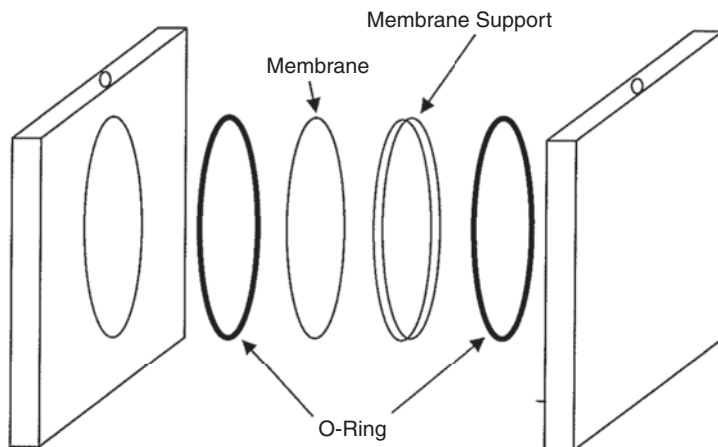


Figure 7.3 Osmometer cell.

The main advantage of membrane osmometry is that it yields a direct measurement of the osmotic pressure. However, there are several disadvantages when using a membrane osmometer to measure the osmotic pressure of a nano-fluid. There can often be problems with membrane leakage, membrane asymmetry, compression, solute contamination or temperature gradients. Ballooning of the membrane, which is caused by pressure differentials, is another problem. Dissolved air in the system can cause difficulties, so all solvents and solutions should be degassed before insertion. The measurements themselves take a long time as the sample and reference electrolyte require time to equilibrate. There can also be major practical difficulties in making highly concentrated nano-fluids for use in the membrane osmometer. Entry of the reference solvent into the nano-fluid in the osmometer results in dilution of the sample being measured, so analytical techniques for measuring the concentration of the final dispersion are also required.

7.3.1.2 Frontal ultrafiltration

Frontal (or dead-end) ultrafiltration experiments are usually carried out using a cell similar to that shown in Figure 7.4.

The whole experimental setup is shown schematically in Figure 7.5. The system is pressurized with nitrogen gas. The applied pressure is monitored by an on-line pressure. A digital electronic balance connected to a computer is used to continuously measure the weight of the permeate. A water jacket around the filtration cell body is used to keep the temperature of the system at 25 °C. Rates of filtration were determined by continuously weighing the filtrate on an electronic balance connected to a microcomputer.

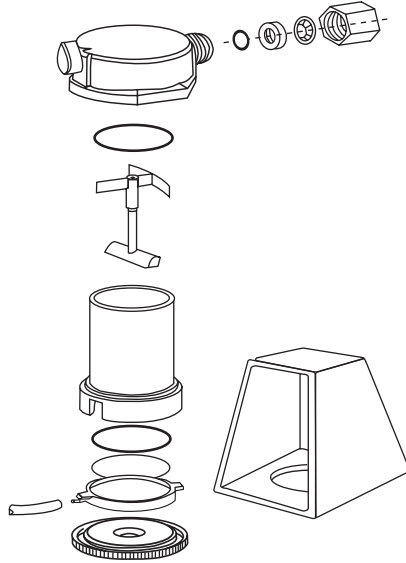


Figure 7.4 Amicon ultrafiltration cell (Model 8050), with a capacity of 60 mL, maximum operation pressure of 530 kPa, a membrane diameter of 43 mm and an effective membrane area of 13.4 cm².

During a frontal ultrafiltration experiment the volume filtered as a function of time is normally measured. From the recorded time versus volume data, the derivatives dV_i/dt_i and $dz_i/dt_i = d^2V_i/dt_i^2$ may be derived from Taylor's theorem [112]:

$$\frac{dV_i}{dt_i} = \left[\frac{t_i - t_{i-1}}{(t_{i+1} - t_i)(t_{i+1} - t_{i-1})} \right] V_{i+1} + \left[\frac{t_{i+1} - 2t_i + t_{i-1}}{(t_{i+1} - t_i)(t_i - t_{i-1})} \right] V_i - \left[\frac{t_{i+1} - t_i}{(t_i - t_{i-1})(t_{i+1} - t_{i-1})} \right] V_{i-1}, \quad (7.5)$$

$$\frac{dz_i}{dt_i} = \left[\frac{t_i - t_{i-1}}{(t_{i+1} - t_i)(t_{i+1} - t_{i-1})} \right] z_{i+1} + \left[\frac{t_{i+1} - 2t_i + t_{i-1}}{(t_{i+1} - t_i)(t_i - t_{i-1})} \right] z_i - \left[\frac{t_{i+1} - t_i}{(t_i - t_{i-1})(t_{i+1} - t_{i-1})} \right] z_{i-1}. \quad (7.6)$$

The osmotic pressure at any given time can therefore be evaluated using [113]

$$\Delta\pi_m(t) = \Delta P - \frac{\eta_s R_m}{A_m} \frac{dV}{dt}. \quad (7.7)$$

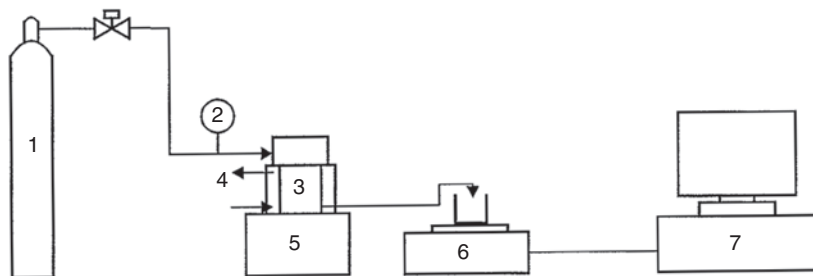


Figure 7.5 Schematic diagram of the batch ultrafiltration system: 1, nitrogen flask; 2, pressure transducer; 3, filtration cell; 4, water jacket; 5, magnetic stirrer; 6, electronic balance; and 7, personal computer.

These derivatives also enable the voidage, ε , of the nano-particles at the membrane surface at any given time to be calculated by a simple interpolation procedure [113]. The concentration of the particles corresponding to a given osmotic pressure can then be established as voidage is simply related to the nano-particle concentration.

In order to obtain a full osmotic pressure curve, frontal ultrafiltration experiments need to be carried out at several different pressures. This is due to the nature of numerical differentials taken from experimental data. Differentiation of numerical data may be an unstable process, i.e. any fluctuations in the original data will be amplified [112]; therefore, as the filtration proceeds with time, the smaller changes in volume with respect to time result in greater errors for the calculated flux. It is therefore best to use only the initial data from the first 5 minutes of filtration (approximately five to six points) to evaluate the osmotic pressure and concentration values, for after this instability may arise due to the numerical errors from the numerical differentiation. This method for measuring the osmotic pressure has the following advantages over conventional membrane osmometer measurements: (a) only very simple apparatus is required, (b) results are obtained quickly, (c) only small sample quantities are required and (d) only dilute initial samples are needed, as the ultrafiltration process creates a concentrated solution at the membrane, making sample preparation a simple task. However, this measurement is not a direct measurement and some calculations have to be performed in order to obtain the required data.

7.3.1.3 Results

Figures 7.6 to 7.8 show experimental results for the osmotic pressures of several different nano-fluids. The osmotic pressures were determined using the various different methods for measuring the osmotic pressure. The data for BSA were

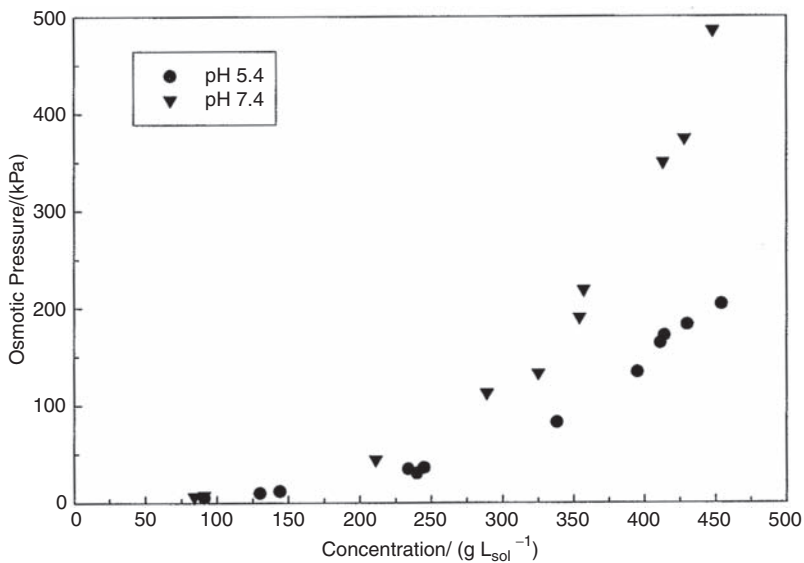


Figure 7.6 Osmotic pressure of bovine serum albumin (BSA) as a function of concentration at 25 °C and in 0.15M NaCl at pH 5.4 and 7.4 [111].

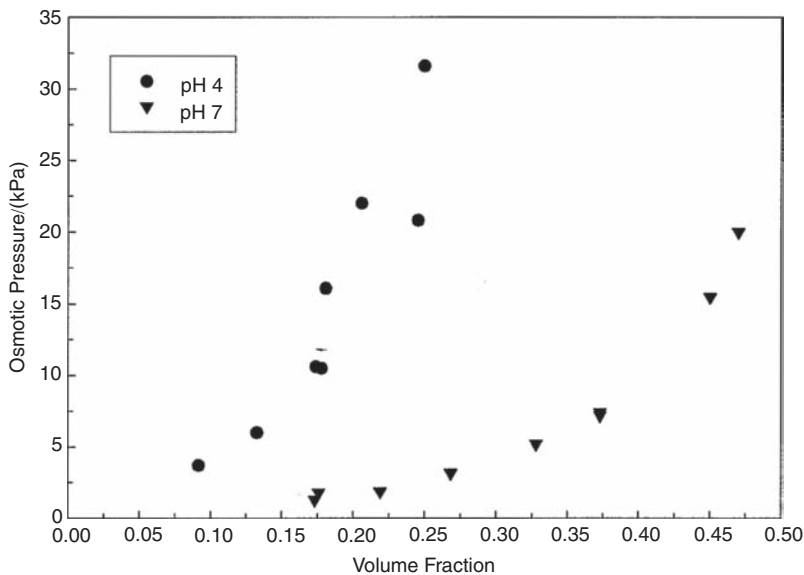


Figure 7.7 Osmotic pressure of recombinant human lactoferrin recombinant as a function of volume fraction at 25 °C and in 0.03M NaCl at pH 4.0 and 7.0 [114].

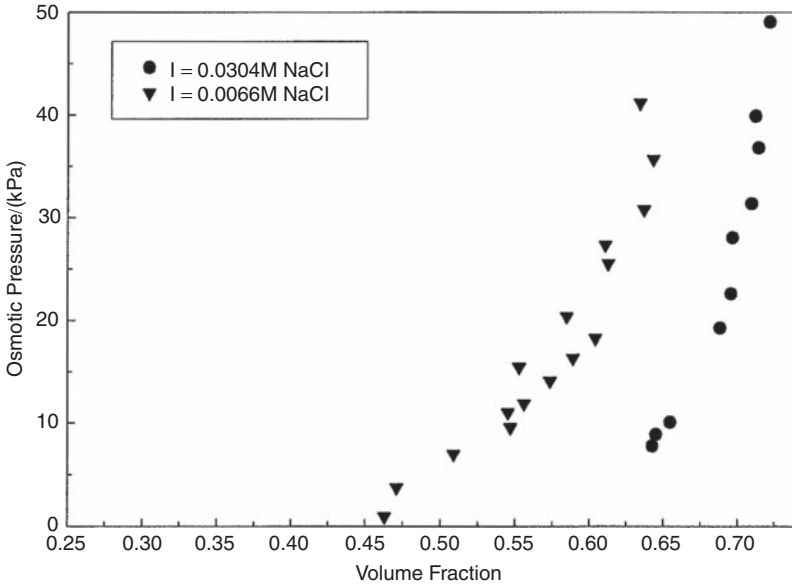


Figure 7.8 Osmotic pressure of silica as a function of volume fraction at 25 °C, pH 9.0 and at various ionic strengths [115].

determined using a dynamic osmometer [111], the data for lactoferrin was determined using a static osmometer [114] and the data for silica was determined via the ultrafiltration method [115]. Despite the examples shown here, osmotic pressure data are generally scarce in the literature and the data that do exist are usually confined to the dilute (low volume fraction) range, which is inadequate for many purposes. Osmotic pressures of dispersions of charged nano-particles depend on the nature, concentration and pH of the supporting electrolyte as well as on the nature, size and concentration of the nano-particles. This creates a problem for systematic investigations, as the methods by which osmotic pressures are measured are tedious and time consuming. This is where numerical simulation of the nano-fluid becomes important.

7.3.2 Numerical Calculation of the Osmotic Pressure for Nano-Fluids

7.3.2.1 Colloidal interaction approach

The osmotic pressure for proteins or other electrostatically stabilized nano-particles may be calculated accurately via the use of extended Deryaguin–Landau–Verwey–Overbeek (DLVO) theory [99, 114]. This allows the prediction

of the osmotic pressure for the whole concentration range for a given set of physicochemical conditions. By assuming a face centred cubic (f.c.c.) structure within a nano-fluid (there is considerable evidence that electrostatically stabilized nano-fluids exist in a regular packing form of minimum energy [98]), the osmotic pressure at any point in the dispersion may be calculated from the particle–particle interactions [99, 114],

$$\pi(\phi) = \frac{\sqrt{6}}{A_h} (F_{\text{ATT}} + F_{\text{ELEC}} + F_{\text{EXTRA}}) + P_{\text{ENT}}, \quad (7.8)$$

where $\pi(\phi)$ is the osmotic pressure, $A_h = 2\sqrt{3}(a + D/2)^2$ is the effective area occupied by a particle at a hypothetical plane, F_{ATT} is the attractive force between two particles, F_{ELEC} is the electrostatic force between two particles, P_{ENT} is the entropic pressure and F_{EXTRA} accounts for any extra interactions between particles (all these terms depend on particle separation and thus solution concentration).

7.3.2.2 Molecular dynamic approach

As described in Section 2.3.2, the nano-particles in a nano-fluid can be represented as a coordinate point in space, with a set of molecular properties being attached to it that describe its mass size and interaction strength. The main part of the model will revolve around describing the molecular potential between the nano-particles. In this case, we model the Coulomb repulsion between spherical particles is modelled by using the standard potential due to the mutual interaction of their electrical double layers [116]:

$$U(r_{ij}) = 4\pi\epsilon_0\epsilon_r a^2 \psi_0^2 \frac{\exp[-\kappa(r_{ij} - 2a)]}{r_{ij}}, \quad r_{ij} > 2a, \quad (7.9)$$

where ϵ_0 is the permittivity of vacuum, ϵ_r is the dielectric constant of the background solvent, a is the particle radius, ψ_0 is the electrostatic potential at the particle surface, κ is the Debye-Hückel parameter and r_{ij} is the separation distance between two particles i and j . In this case the potential at the particle surface can be related to the number of charges on the particle surface, Z , using

$$\psi_0 = \frac{Ze}{4\pi\epsilon_0\epsilon_r a(1 + \kappa a)}, \quad (7.10)$$

where e is the elementary electronic charge.

Once the molecular potential model is set up the molecular dynamics simulation may be performed and after a suitable length of time has passed to allow for

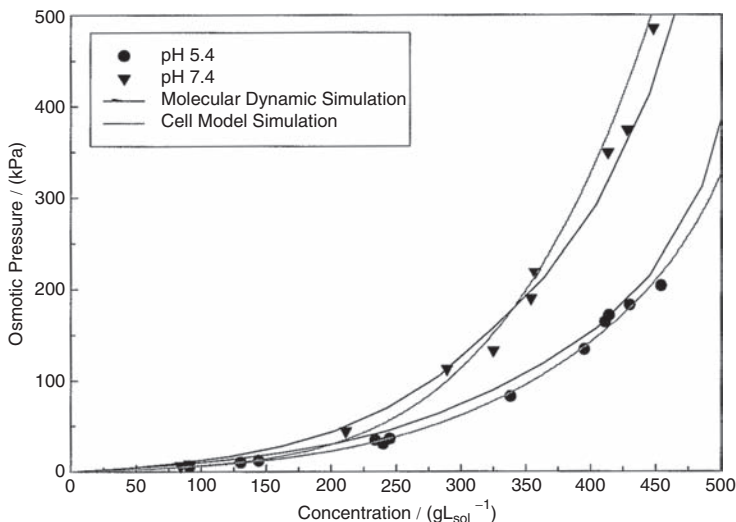


Figure 7.9 Comparison of predicted osmotic pressure values with the experimental data of Vilker *et al.* [111] for bovine serum albumin as a function of concentration at 25 °C and in 0.15M NaCl at pH 5.4 and 7.4.

equilibration, the pressure of the system may be extracted. This pressure is equivalent to the osmotic pressure of the system. In order to use this model, the value of the surface potential, ψ_o , or the number of charges, Z , is required. These values may either be determined experimentally or used as fitting parameters when comparing simulation results to experimental data.

Results of the osmotic pressure calculation, via the two different methods, for BSA particles in a 0.15M NaCl electrolyte solution are shown in Figure 7.9. The cell model method uses a charge regulation boundary condition when solving the Poisson Boltzmann equation, so only the pH, ionic strength and particle size ($a = 3.2$ nm for BSA molecules) are required as input parameters (all these properties are measured experimentally). The molecular dynamics model uses measured zeta potentials (at pH 7.4, $\zeta = -23.4$ mV; at pH 5.4, $\zeta = -5.1$ mV) and the particle size as input parameters. Excellent agreement between theory and experiment is obtained.

7.4 GRADIENT DIFFUSION COEFFICIENT

The Brownian motion of a single sphere in a liquid medium due solely to the thermal fluctuations of the molecular movements around the particle is described

by the well-known Stokes–Einstein equation,

$$D_{B_0} = \frac{kT}{6\pi\eta_s a_{\text{hyd}}}, \quad (7.11)$$

where D_{B_0} is the Brownian diffusion coefficient, a_{hyd} is the hydrodynamic radius of the particle, η_s is the viscosity of the fluid, k is Boltzmann's constant and T is the absolute temperature. However, the diffusion of a particle in a concentrated suspension is influenced by the presence of its neighbours. Moreover, there are two diffusion processes that need to be distinguished. The first of these processes is known as self-diffusion and describes the fluctuating trajectory of a tracer particle among others. The self-diffusion coefficient, D_s , is obtained via a time average of the position correlation function. The second of these diffusion processes is known as gradient or mutual diffusion. This is the macroscopic flux of particles produced by Brownian motion in the presence of a gradient in the total density of particles. The gradient diffusion coefficient, D_m , is the one that appears in Fick's law of diffusion. The tracer diffusion coefficient, D_s , and the gradient diffusion coefficient, D_m , coincide with the Brownian diffusion coefficient, D_{B_0} , at infinite dilution but differ in more concentrated suspensions.

Theoretically, the calculation of the gradient diffusion coefficient is a difficult task because the calculation of multiparticle interactions is complicated and not entirely resolved. Several methods have previously been used to predict the mutual diffusion coefficient (see for example, References [117] to [120]) but due to the dearth of adequate experimental measurements up to sufficient volume fractions, comparison between theory and experiment has been rare.

7.4.1 Experimental Measurement of the Gradient Diffusion Coefficient

Experimental measurement of the diffusion coefficient is usually performed by dynamic light scattering (otherwise known as photon correlation spectroscopy). Alternative methods to dynamic light scattering are not numerous and are rarely used. These methods include the capillary method [121–123], the porous barrier (membranes) method [121] and Gouy interferometric methods [124]. The advantages and disadvantages of these different types of methods have been discussed previously [125]. In this section the dynamic light scattering method will be considered.

Dynamic light scattering measurements can be performed using suitable experimental equipment. Within a dynamic light scattering measurement, the sample is placed in the path of a laser beam and the light scattered by the particles is detected by a photomultiplier. The light source used is usually a laser operating with vertically plane polarized light at a known wavelength. The measurements should be

carried out at a low laser power, so the results are not influenced by local heating of the samples, which would be caused by use of a more powerful beam. The scattering angle, θ , can also be varied. Variation of the scattering angle corresponds to a variation in the magnitude of the scattering vector, $q = (4\pi n_o/\lambda_o) \sin(\theta/2)$, which is important when analysing the data. The temperature of the samples is automatically kept at 25 ± 0.1 °C. By varying the concentration of nano-particles in the nano-fluid, the variation of the gradient diffusion coefficient with concentration may be obtained. However, one of the problems encountered with dynamic light scattering is that of multiple scattering at higher concentrations. It can be confirmed that the nano-particle concentrations used are not high enough to cause multiple light scattering by carrying out the experiments in two cells of different optical path lengths. If multiple light scattering effects were present, significant differences in the intensity autocorrelation function would be apparent for these two cells. However, this means that light scattering techniques are usually restricted to volume fractions below about 0.1.

7.4.2 Experimental Data Analysis

Most of the common light scattering equipment available operates in the homodyne mode of operation. The light scattered by the dispersed particles is coherently detected at a certain angle with respect to the incident radiation. Since the dispersed particles are in continuous Brownian motion, the observed scattered intensity, $I(t)$, will fluctuate along the time axis. Therefore, analysis as a function of time of these intensity fluctuations provides information on the motion of dispersed particles.

In a light scattering experiment, the time analysis is carried out with a correlator that constructs the time autocorrelation function, $G_2(\tau)$, of the scattered intensity [94]:

$$G_2(\tau) = [I(t) I(t + \tau)]. \quad (7.12)$$

This correlation function depends only on the time difference, τ , and is independent of the arbitrary time, t , at which the evaluation of $G_2(\tau)$ is started. The square brackets refer to an average value of the product, $I(t) I(t + \tau)$, for various times t .

For a dilute monodisperse solution, the scattered light intensity autocorrelation function, $G_2(\tau)$, can be related to the field autocorrelation function, $g_1(\tau)$ (the function of interest), via

$$G_2(\tau) = A(1 + B|g_1(\tau)|^2), \quad (7.13)$$

where A is, in principle, a time-independent constant proportional to the square of the time-averaged scattered intensity, called the baseline, and B is an

instrument factor ≤ 1 [94]. Hence, from the measured quantity $G_2(\tau)$ and baseline A , which is also measured, the normalized field autocorrelation function, $G_1(\tau)$, is determined [94]:

$$G_1(\tau) = \sqrt{B} g_1(\tau) = \left(\frac{G_2(\tau) - A}{A} \right)^{1/2}. \quad (7.14)$$

For the case of monodisperse particles, $g_1(\tau)$ is represented by a single exponential function [94]:

$$g_1(\tau) = \exp(-D_{\text{mon}} q^2 \tau), \quad (7.15)$$

where D_{mon} is the diffusion coefficient of the monodisperse particles being studied. In this case, $G_1(\tau)$ may be fitted to a simple exponential and the diffusion coefficient is easily evaluated.

For the practical case of polydisperse samples the field autocorrelation function of the scattered light for a homodyne experiment assumes the form [94]

$$g_1(\tau) = \int_0^\infty P(\Gamma) \exp(-\Gamma \tau) d\Gamma, \quad (7.16)$$

where Γ is the decay rate and is related to the effective diffusion coefficient, D_{eff} , by $\Gamma = D_{\text{eff}} q^2$ and $P(\Gamma)$ is the unknown distribution function of the decay rates [94]. The detailed analysis of such complex correlation functions is a difficult and not entirely resolved problem. Nevertheless, some valuable information can be extracted from the initial decay of the field autocorrelation function via the method of cumulants [126]. In the method of cumulants the factor $\exp(-\Gamma \tau)$ is expanded around $\exp(-\langle \Gamma \rangle \tau)$, where $\langle \Gamma \rangle$ is the mean decay rate, yielding a polynomial in time delay,

$$\ln G_1(\tau) = \frac{1}{2} \ln B + \sum K_n (-\tau)^n / n!, \quad (7.17)$$

where the n th cumulant is defined as

$$K_n = (-1)^n \lim_{\tau \rightarrow 0} \frac{d^n}{d\tau^n} \ln G_1(\tau). \quad (7.18)$$

For a system of polydisperse particles, the first cumulant defines an effective diffusion coefficient

$$D_{\text{eff}}(q) = \frac{K_1}{q^2}. \quad (7.19)$$

Therefore plotting K_1 versus q^2 should result in a straight line that passes through the origin and has a gradient that is equal to the effective diffusion coefficient, $D_{\text{eff}}(q)$.

Experimental data can now be obtained and treated in the following way:

- (a) For given concentrations of the nano-particles and electrolyte strengths the normalized field autocorrelation function can be measured at different scattering angles.
- (b) Taking the initial portion of the $\ln G_1(\tau)$ versus τ curve (at least 15 data points starting from the minimum time value) a straight line is fitted through the data (giving a correlation coefficient >0.95) to obtain K_1 , the first cumulant.
- (c) A curve of K_1 versus q^2 can now be plotted and a regression line that passes through the origin can be fitted through the points. The gradient diffusion coefficient is then determined from the regression curve gradient, which is equal to $D_{\text{eff}}(q)$ (Equation (7.19)).

Figure 7.10 shows how the first cumulant data, K_1 , determined at each scattering angle may be used to determine the gradient diffusion coefficient for a 10 g/L dispersion of BSA particles in a 0.01M KCl electrolyte. The gradient of the plot of K_1 versus q^2 yields the effective diffusion coefficient, $D_{\text{eff}}(q)$, in Equation (7.19). Figure 7.10 shows that the data are well represented by a straight line fit through the origin of the graph. For larger particles this linear dependence on the scattering angle is unlikely to be present as light scattering may be used to detect the structure factor of the dispersion [128], thus introducing into the diffusion coefficient determination, a dependence on the scattering angle, as shown by the data of Petsev and Denkov [117] for latex particles. However, for smaller particles where the length scales are often too small to be resolved by light, the linear relationship shown in Figure 7.10 is typical. It is, however, necessary to measure the light scattering at different scattering angles in order to check that this is the case and that no dependence on the scattering angle is apparent because if there was a dependence on the scattering angle then the gradient diffusion coefficient would be obtained via an extrapolation of a curve of D_{eff} versus q to the zero scattering vector, i.e. $D_m = D_{\text{eff}}(0)$ [117].

Figure 7.11 shows the overall results for the measured gradient diffusion coefficients for BSA at various ionic strengths and concentrations all at a constant pH. As with the osmotic pressure, it can be seen that the physicochemical conditions have a great effect on the gradient diffusion coefficient. Again by modelling the nano-fluid, predictions of the gradient diffusion coefficient may be obtained.

7.4.3 Gradient Diffusion Coefficient Calculation

The calculation of the gradient diffusion coefficient will be briefly outlined here as a thorough review of such calculations may be found elsewhere [127]. At finite

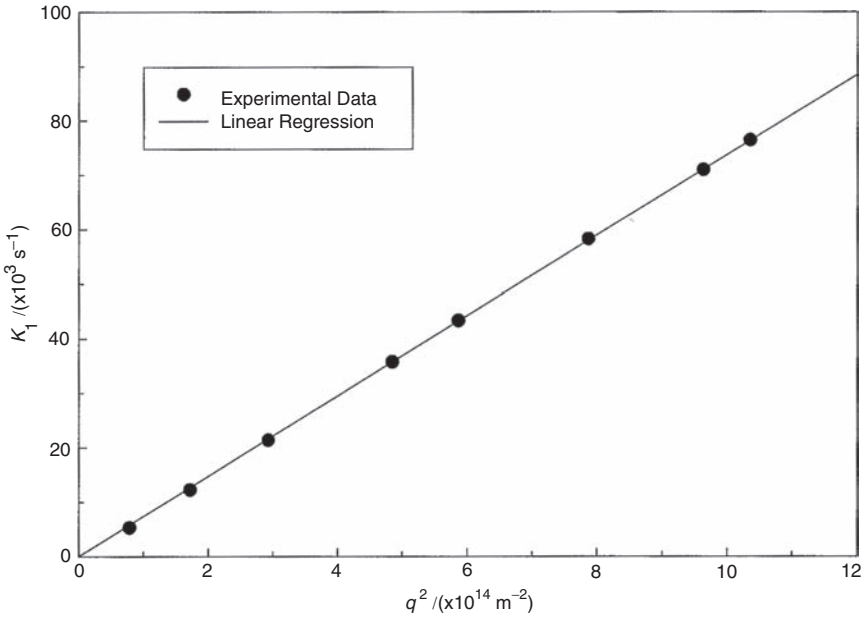


Figure 7.10 K_1 versus q^2 for BSA at a concentration of 10 g/L in 0.01 M KCl at various scattering angles [127].

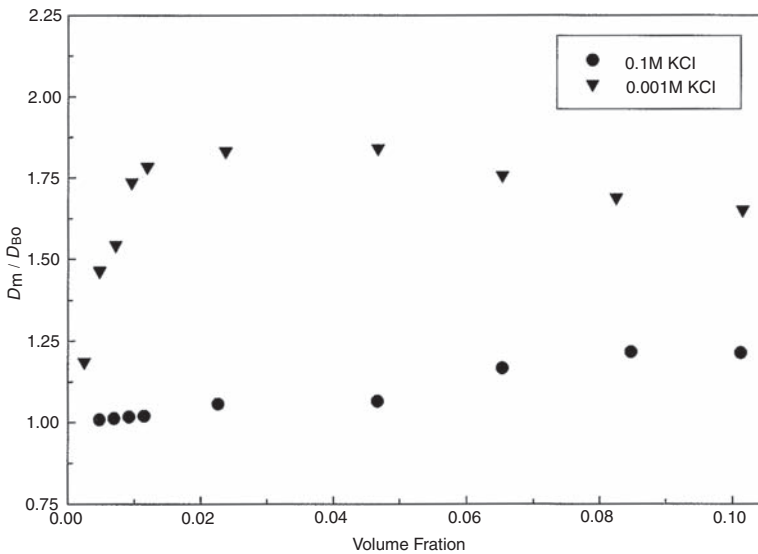


Figure 7.11 Experimental diffusion coefficients of BSA at pH 6.5 as a function of volume fraction [127].

concentrations, colloidal interactions and hydrodynamic interactions mediated by the fluid modify the dilute-limit value of the Brownian diffusion coefficient, D_{B_0} . The combined action of these interactions may be described by the generalized Stokes-Einstein equation [129],

$$D_m(\phi) = D_{B_0} \frac{K(\phi)}{S(\phi)}, \quad (7.20)$$

where $K(\phi)$ is the hydrodynamic interaction coefficient and $S(\phi)$ is the thermodynamic coefficient. This equation is valid over the entire range of volume fractions. The thermodynamic coefficient, $S(\phi)$, may be directly determined from the osmotic pressure, $\pi(\phi)$, as [130]

$$\frac{1}{S(\phi)} = \left[\frac{4\pi a_{\text{hyd}}^3}{3kT} \frac{\partial \pi(\phi)}{\partial \phi} \right]. \quad (7.21)$$

Prediction of the osmotic pressure thus allows the calculation of $S(\phi)$.

The hydrodynamic coefficient, $K(\phi)$, accounts for the fact that in concentrated suspensions the drag force exerted on a single particle deviates from Stokes' law because of the presence of the neighbouring particles. This coefficient describes the sedimentation velocity of an assemblage of spheres. This coefficient may be calculated for completely disordered hard spheres from [131]

$$K(\phi) = (1-\phi)^\alpha, \quad (7.22)$$

where $\alpha = 6.55$, and for completely ordered f.c.c. hard spheres from [127]

$$K(\phi) = 1 - 1.7876\phi^{2/3} - 0.0602\phi^{2/3} + 1.2989\phi - 0.6233\phi^{4/3} + 0.4842\phi^{5/3} - 0.3079\phi^2 \quad (7.23)$$

The point at which the order/disorder transition occurs is equivalent to the point at which the disordered system line, Equation (7.22), coincides with the ordered system line, Equation (7.23) [127]. Hence, α may be determined if the volume fraction of the order/disorder transition, $\phi_{o/d}$, is known, by equating Equations (7.22) and (7.23), taking logs and rearranging:

$$\alpha = \frac{\log\left(1 - 1.7876\phi_{o/d}^{1/3} - 0.0602\phi_{o/d}^{2/3} + 1.2989\phi_{o/d} - 0.6233\phi_{o/d}^{4/3} + 0.4842\phi_{o/d}^{5/3} - 0.3079\phi_{o/d}^2\right)}{\log(1-\phi_{o/d})} \quad (7.24)$$

For electrostatically stabilized dispersions, the value of α varies with the particle interactions [127]. In order to calculate the appropriate value for α ,

perturbation theory is used [127]. This entails a rescaling of the particle size due to the colloidal interactions [132]. The new particle size is determined via

$$d_{\text{eff}} = 2a_{\text{hyd}} + \int_{2a_{\text{hyd}}}^{\sigma} \left\{ 1 - \exp \left[-\frac{V_{\text{TOT}}(r)}{kT} \right] \right\} dr \quad (7.25)$$

In order to calculate the effective diameter via this method, the interaction potential, $V_{\text{TOT}}(r)$, needs to be known as a function of separation distance. This interaction energy is determined from the pair interaction force by numerically integrating the force distance curve,

$$V_{\text{TOT}}(r) = - \int_{\infty}^r F_{\text{TOT}}(r) dr, \quad (7.26)$$

where $F_{\text{TOT}}(r) = F_{\text{ELEC}}(r) + F_{\text{ATT}}(r)$.

Once the effective hard sphere diameter is known, the thermodynamic properties, such as the osmotic pressure, then correspond to those for a hard sphere suspension, with

$$\phi_{\text{eff}} = \phi \left(\frac{d_{\text{eff}}}{2a_{\text{hyd}}} \right)^3. \quad (7.27)$$

This method provides a basis for prediction of the order/disorder transition for electrostatically stabilized colloids as the hard sphere order/disorder transition is well known ($\phi_{\text{o/d}} = 0.55$ for hard spheres [130]). Consequently, an electrostatically stabilized colloidal dispersion will become an ordered f.c.c. solid when [130],

$$\phi_{\text{o/d}} = 0.55 \left(\frac{2a_{\text{hyd}}}{d_{\text{eff}}} \right)^3. \quad (7.28)$$

Therefore, knowing $\phi_{\text{o/d}}$ enables the calculation of α for an electrostatically stabilized solution from Equation (7.24), and thus the calculation of $K(\phi)$ for the disordered region from Equation (7.22). Once the value of $\phi_{\text{o/d}}$ is reached, Equation (7.23) then applies for the calculation of $K(\phi)$, even for charged suspensions [127].

The generalized Stokes–Einstein equation (Equation (7.20)) may also be modified to account for the influence of the secondary electroviscous effect on $K(\phi)$ [120],

$$D_{\text{m}}(\phi) = D_{\text{B}_0} \frac{\eta_{\text{s}}}{\eta_{\text{a}}} \frac{K(\phi)}{S(\phi)}, \quad (7.29)$$

where η_{s} is the solvent viscosity and η_{a} is the apparent solvent viscosity.

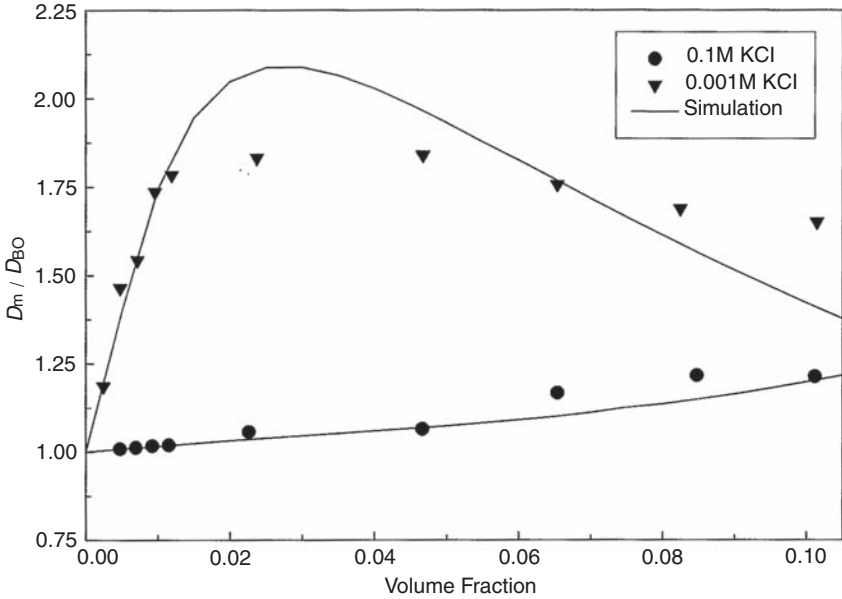


Figure 7.12 Comparison between theoretical predictions and experimental results for the diffusion coefficients of BSA at pH 6.5 as a function of volume fraction [127].

A comparison between gradient diffusion coefficient experimental data (measured by photon correlation spectroscopy [127]) and the theoretical predictions for the protein BSA is shown in Figure 7.12. Again good agreement between theory and experiment has been obtained.

7.5 VISCOSITY

In dilute nano-fluid systems the viscosity of the solution may be described by Einstein's equation [133],

$$\frac{\eta}{\eta_s} = 1 + [\eta]\phi + O(\phi^2), \quad (7.30)$$

where η is the viscosity of the solution, η_s is the viscosity of the pure solvent and $[\eta]$ is the intrinsic viscosity. For hard spheres the value of the intrinsic viscosity is precisely calculated as 2.5 [133]. The presence of electrical charges on the spheres, however, causes an augmentation of the intrinsic viscosity. This effect can be calculated theoretically (the currently accepted theoretical model being

that of Booth [134]), but it may also be determined experimentally by measuring the viscosity of a range of dilute solutions and plotting a graph of $\eta/\eta_s - 1$ versus ϕ . This results in a straight line passing through the origin with a gradient that is equal to the intrinsic viscosity.

For concentrated suspensions, correlations have been widely used to describe the viscosity of the system, one of the most commonly used being that of Krieger and Dougherty [133],

$$\frac{\eta}{\eta_s} = \left(1 - \frac{\phi}{\phi_{\max}}\right)^{-[\eta]\phi_{\max}}, \quad (7.31)$$

where ϕ_{\max} is the maximum packing fraction. For f.c.c. packed hard spheres, $\phi_{\max} = 0.7404$ and $[\eta] = 2.5$; therefore the index in Equation (7.31) becomes 1.85, which is close to the commonly quoted value of 2 [135].

However, in order to use this correlation experimental data are required. Also, when considering electrostatically stabilized solutions, the particle interactions will affect the values of ϕ_{\max} and $[\eta]$.

7.5.1 Viscosity Experiments

Tests and instruments to measure viscosity range from the simple to the complex. Viscosity can be measured using a falling ball test which measures the time required for a ball to fall through the test liquid contained in a temperature controlled glass tube (a small change in temperature can result in a large change of viscosity). When this test is done using a standardized falling ball viscometer, the absolute viscosity can be determined. Falling ball viscometers are used to measure the viscosity of Newtonian fluids.

Viscosity can also be measured with a simple device known as a glass capillary viscometer. The viscosity is determined by measuring the time needed for a known volume of fluid to pass through a small opening. The simplest glass capillary viscometer is probably the Ostwald-type capillary viscometer, used commercially in many applications.

The absolute viscosity of both Newtonian and non-Newtonian fluids can be measured using rotational viscometers. These viscometers measure viscosity by sensing the torque required to rotate a spindle at constant speed while immersed in the sample fluid. The torque is proportional to the viscous drag on the immersed spindle, and thus to the viscosity of the fluid.

The viscosity measurements shown in Figure 7.13 were obtained using an Ostwald type viscometer suspended in a water bath kept at a constant temperature of 25 ± 0.1 °C [136]. A range of dilute BSA solutions was used (0–20 g/L). The data shows the straight line relationship predicted by the dilute limit theory (Equation (7.30)), from which the intrinsic viscosity may be found. The intrinsic viscosity

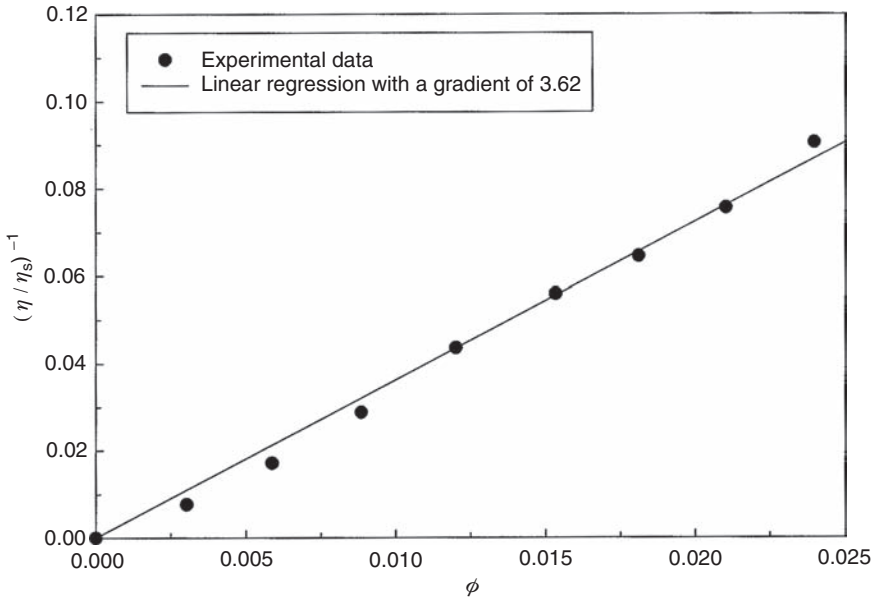


Figure 7.13 Experimental data for the intrinsic viscosity of BSA at pH 8.0 in a 0.03M NaCl electrolyte [136].

for this system at the given conditions (0.03M NaCl, pH 8.0) is 3.62. This value is comparable with the value of 3.75 measured by Kozinski and Lightfoot [137]. They also used an Ostwald viscometer to measure the viscosity of BSA solutions. In their experiments they used three different sizes of viscometers to determine whether non-Newtonian effects were present. The viscosity of BSA solutions was measured over a much higher range of concentrations (0–450 g/L) in two different types of buffer solution (0.5M arsenate buffer at pH 6.7 and 0.1M acetate buffer). No significant differences in the viscosity measurements were found between the different systems.

Figure 7.14 shows the experimental data of Kozinski and Lightfoot [137] plotted versus several different types of fit to their experimental data. This shows that many different types of expression can be fitted to experimental viscosity data (Equation (7.31) could also be fitted to these data). The behaviour of the viscosity versus concentration curve for these BSA dispersions is typical of that for concentrated nano-fluid systems. Figure 7.15 shows the viscosity for silica particles dispersed in a sodium chloride solution. The viscosity of these solutions was measured using a Carri-Med controlled stress rheometer with a cone and plate geometry. Again the viscosity measured here shows the same trend versus concentration/volume fraction as the BSA viscosity.

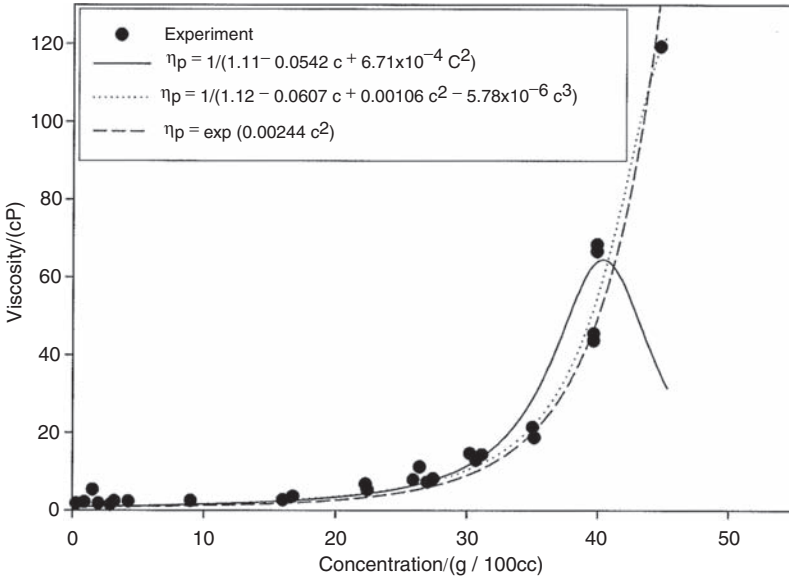


Figure 7.14 Viscosity of BSA solutions versus concentration [137].

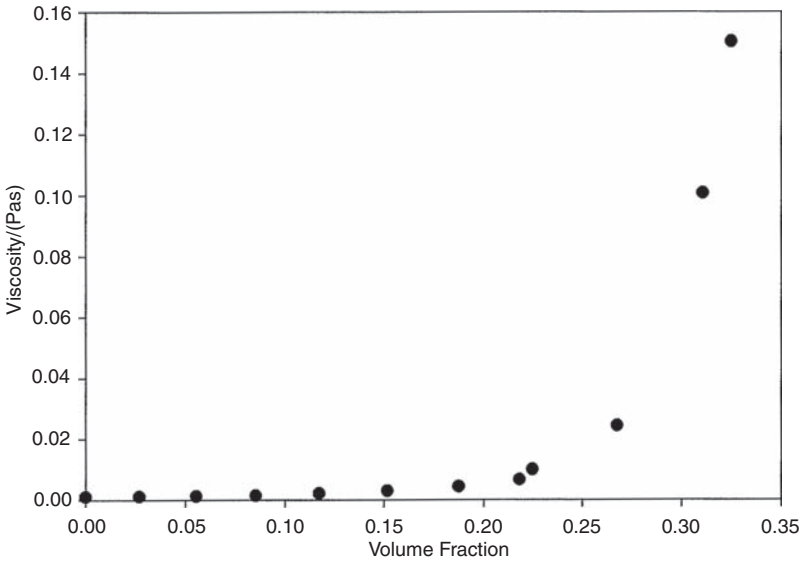


Figure 7.15 Viscosity of nano-silica particle solutions versus volume fraction (pH 8.9, 0.03M NaCl, $a = 9.71$ nm).

7.5.2 Viscosity Calculation

Experimental results such as those shown in Figures 7.14 and 7.15 are ideal for comparison with computer simulations. In order to predict the viscosity of a concentrated suspension it is necessary to take into account both the many body hydrodynamic interactions and the spatial distribution of the particles. However, in spite of many recent works, including theoretical, experimental and numerical approaches, the prediction of the viscosity of concentrated suspensions is still poorly achieved [135]. Many of the simulations are not dissimilar to computer simulations of liquids such as argon and chlorine [138]. They use Newtonian equations of motion and a Lennard–Jones type of particle–particle interaction law, the main differences being that the interparticle forces are smaller and the hydrodynamic resistance to motion is much greater for suspensions. Nonequilibrium molecular dynamics in particular is a technique that may be used to predict the viscosity of a suspension [139].

7.6 MEMBRANE SEPARATIONS

Membrane separation technology is a novel and highly innovative process engineering operation. Membrane filtration processes are nowadays used as an alternative to conventional industrial separation methods such as distillation, centrifugation and extraction, since they potentially offer the advantages of high selective separation, separation without any auxiliary materials, ambient temperature operation, usually no phase changes, small units, modular construction, simple integration into existing production processes and relatively low capital and running costs. The former advantages make membrane processes even more interesting for certain types of materials that have been inherently difficult and expensive to separate, such as:

1. Finely dispersed solids, especially those that are compressible, have a density close to that of the liquid phase, have high viscosity or are gelatinous.
2. Low molecular weight, nonvolatile organics or pharmaceuticals and dissolved salts.
3. Biological materials that are very sensitive to their physical and chemical environment.

The various membrane separation methods can be divided according to their separation characteristics, which may be classified by the size range of materials separated and the applied driving force (Table 7.1).

In general, three filtration modes can be distinguished: unstirred and stirred frontal (or dead-end) filtration and cross-flow filtration. In the unstirred frontal situation the solution is put under pressure without any agitation in the liquid.

Table 7.1 Classification of membrane separation processes for liquid systems.

Name of process	Driving force	Separation size range	Examples of materials separated
Microfiltration	Pressure gradient	~0.1–10 μm	Small particles, large colloids, microbial cells
Ultrafiltration	Pressure gradient	~5–0.1 μm	Emulsions, colloids, macromolecules, proteins
Nano-filtration	Pressure gradient	~0.5–5 nm	Dissolved salts, small organics
Reverse osmosis	Pressure gradient	<0.5 nm	Dissolved salts, small organics
Electrodialysis	Electric field gradient	<5 nm	Dissolved salts
Dialysis	Concentration gradient	<5 nm	Treatment of renal failure

Agitation can be provided with a stirring bar in the stirred dead-end mode. In the cross-flow situation the solution is pumped to flow tangentially over the membrane surface.

In the next section we will consider the ultrafiltration process for the separation of nano-fluids. Ultrafiltration separates solutes of the size (or molecular weight, Mw) of approximately 5 to 100 nm (or 2×10^3 to 2×10^5 Mw), using a pressure difference of usually 100 to 500 kPa as the driving force. At a fundamental level, ultrafiltration is a very complex process. The events leading to the formation of a cake at ultrafiltration membranes are taking place on a length scale of nanometres. The interactions between the particles at this scale are very important in the development of appropriate models. This immediately points to the requirement for understanding the colloid science of such processes.

7.7 MEMBRANE ULTRAFILTRATION MODELS

7.7.1 Frontal Ultrafiltration Model

This section reviews in outline a full description of the development of a theoretical model for frontal ultrafiltration [98, 140]. Only the most significant equations are described here.

The description of the filtration process starts with a D'arcy-type expression for flow through porous media:

$$\frac{1}{A_m} \frac{dV}{dt} = \frac{K_{\text{HAPP}}}{\eta_s} \frac{dp_y}{dy} \quad (7.32)$$

which relates the small element of cake thickness, dy , to the small volume of permeate, dV , passing through its formation. K_{HAPP} is taken as Happel's permeability coefficient [14] which is calculated from

$$K_{\text{HAPP}} = \left(\frac{2(a+d)^2}{9(1-\varepsilon)} \frac{3 - 4.5(1-\varepsilon)^{1/3} + 4.5(1-\varepsilon)^{5/3} - 3(1-\varepsilon)^2}{3 + 2(1-\varepsilon)^{5/3}} \right) \quad (7.33)$$

By performing a volume balance over the solids in the filter cake and allowing for the time dependence of the pressure, p_2 , at the membrane surface, a set of simultaneous equations can be developed which will describe the ultrafiltration process (a full derivation is given in References [98] and [140]):

$$\frac{d}{dt} \left(\frac{dV}{dt} \right) = - \frac{(dV/dt)^2}{V + A_m R_m (1/C_b - 1/(1-\varepsilon)) (1-\varepsilon) (\eta_s/\eta_A(\varepsilon)) K_{\text{HAPP}}(\varepsilon)} \quad (7.34)$$

$$\frac{dV}{dt} = z, \quad (7.35)$$

$$p_2(t) = p_3 + \frac{\eta_s R_m}{A_m} z. \quad (7.36)$$

These equations can be solved by a numerical predictor–corrector schema subject to the following boundary conditions:

$$\text{At } t = 0, \quad V = 0, \quad p_2(t) = p_1 \quad \text{and} \quad z = \frac{dV}{dt} = \frac{A_m}{\eta_s R_m} (p_1 - p_3).$$

The particle interactions are incorporated into these equations through the local voidage, ε , which varies with position in the filter cake and time, depending on the local interparticle interactions. The time-dependent boundary condition at the filter cake–membrane interface is given by

$$p_2(t) = p_1 - p_D. \quad (7.37)$$

7.7.2 Cross-Flow Ultrafiltration Model

Figure 7.16 shows a schematic representation of the ultrafiltration system being considered. To model the concentration polarization in thin channel ultrafiltration systems, it is adequate to use parabolic-type transport equations by using a boundary-layer-type approach [142]. Thus, for steady laminar flow in a thin

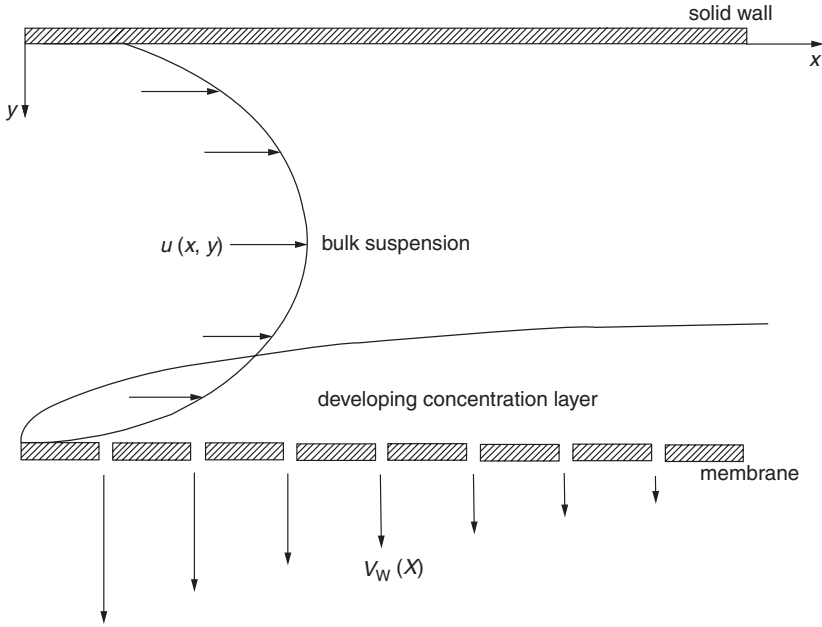


Figure 7.16 Schematic representation of ultrafiltration through one wall in a flat plate system.

channel ultrafiltration module with one porous wall, the appropriate governing equations are [142, 143]

$$\text{Continuity equation: } \frac{\partial u}{\partial x} + \frac{\partial v}{\partial y} = 0, \quad (7.38)$$

$$\text{Momentum equation: } u \frac{\partial u}{\partial x} + v \frac{\partial u}{\partial y} = -\frac{1}{\rho} \frac{\partial p}{\partial x} + \frac{\partial}{\partial y} \left(\frac{\eta}{\rho} \frac{\partial u}{\partial y} \right), \quad (7.39)$$

$$\text{Mass balance: } u \frac{\partial c}{\partial x} + v \frac{\partial c}{\partial y} = \frac{\partial}{\partial y} \left(D \frac{\partial c}{\partial y} \right). \quad (7.40)$$

It is worth noting here that u and v are the bulk flow velocities; i.e. the convective transport of the fluid and particles is the same. Notice that the properties of the nano-fluid, viscosity, density and diffusion coefficient, are included in these equations. Which equations are subject to the following boundary conditions:

At the inlet, $x = 0$:

$$c = c_o, \quad v = 0, \quad u = 1.5u_o \left[1 - \frac{(y-h)^2}{h^2} \right]. \quad (7.41)$$

These boundary conditions specify the inlet flow and concentration profiles. The inlet velocity profile may in principle be either uniform (plug flow) or parabolic (Poiseuille flow). The concentration profile of the feed at the inlet is assumed to be uniform.

At the non-porous wall, $y = 0$:

$$u = 0, \quad v = 0, \quad \frac{\partial c}{\partial y} = 0. \quad (7.42)$$

This boundary condition represents the no-slip condition as well as no-solute transport through the nonporous wall.

At the membrane wall, $y = 2h$:

$$u = 0, \quad v_w = \frac{\Delta P - \pi}{\eta_s R_m}, \quad \frac{\partial c}{\partial y} = \frac{\beta v_w c_w}{D_w}. \quad (7.43)$$

These equations give the conditions at the membrane wall for the momentum and solute continuity [136]. The no-slip condition is assumed at the membrane surface. The momentum equation is coupled with the solute continuity equation by the wall flux and solute mass balance of the convective-diffusive transport at the membrane surface with the solute rejection coefficient, β (for the ultrafiltration experiments considered here complete rejection of the solute is assumed i.e. $\beta = 1$). The local wall flux is determined by the axial transmembrane pressure drop, the concentration dependent local osmotic pressure drop across the membrane, and the effective membrane resistance.

No analytical solution is known for the system of equations, Equations (7.38) to (7.40), subject to boundary conditions, Equations (7.41) to (7.43). This system of equations can, however, be solved by a finite-difference method [144, 145]. A full description of the solution method can be found in Bowen *et al.* [146].

From the solution of Equations (7.38) to (7.40), the local permeate flux distribution, $v_w(x)$, along the channel length, x , is obtained. Thus, integrating the local permeate flux over a distance, l , the channel length from the inlet gives the average permeate flux, v_{av} :

$$v_{av}(l) = \frac{1}{l} \int_0^l |v_w(x)| dx. \quad (7.44)$$

Integrating along the whole channel length results in the steady state value, which can be measured experimentally [146].

In order to solve both the frontal and cross-flow ultrafiltration models, the properties of the nano-fluid are required: osmotic pressure, diffusion coefficient and viscosity over a range of concentrations.

7.7.3 Comparison of Experimental and Theoretical Data

Figure 7.17 shows the effect of the variation of the zeta potential (by variation of pH) at a constant ionic strength of 0.03M and an applied pressure of 400 kN/m². This figure illustrates the overall very good quantitative predictive ability of the developed model over the whole range of zeta potentials tested. It should be noted that the model predictions are physics based with no adjustable parameters. Very good agreement between theory and experiment was obtained. This is to be expected, as the main parameter involved in the frontal ultrafiltration model is the osmotic pressure and, as show in Section 7.3.2, the modelling of the osmotic pressure is in excellent agreement with experimental data. This method goes to show how modelling at the nano scale can be taken to predict process operation at the macro scale.

In Figure 7.18 model predictions have been compared to experimental cross-flow ultrafiltration data obtained for BSA [136]. Reasonable agreement

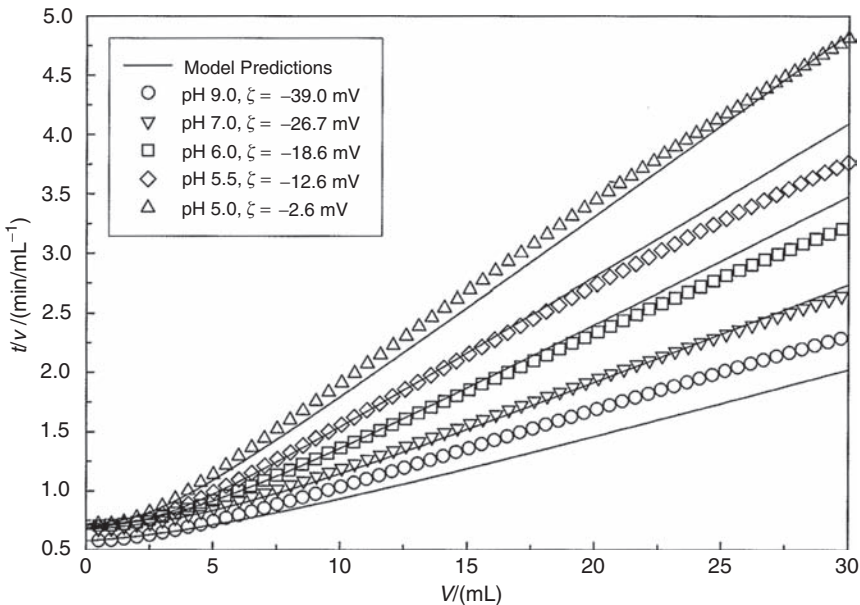


Figure 7.17 Time over volume versus permeate volume for varying pH at an ionic strength of 0.03M [140].

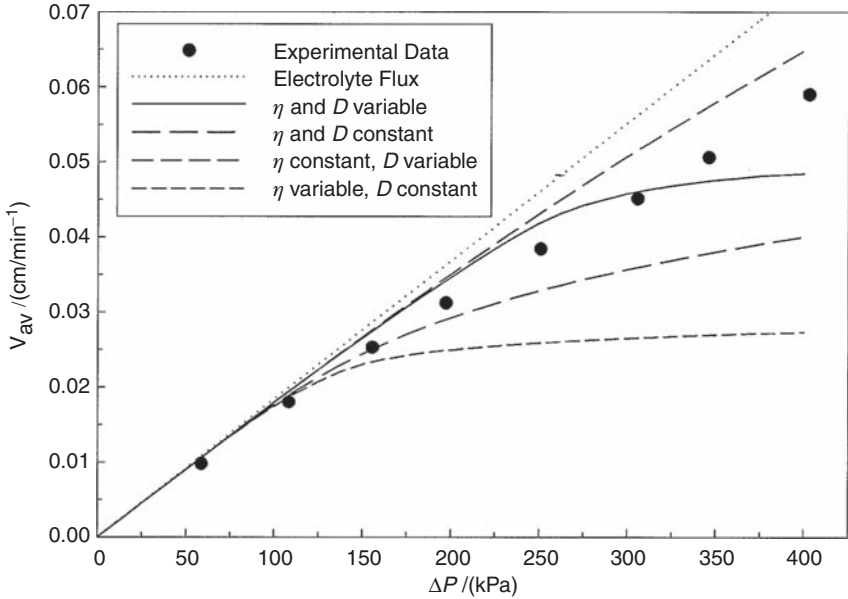


Figure 7.18 Permeate flux, v_{av} , versus applied pressure, ΔP , for a 10 g/L solution of BSA at pH 10.0 in a 0.03M NaCl electrolyte [136].

was obtained when all solution properties were allowed to vary, showing the importance of accounting for them properly. However, comparison between theory and experiment was not exact. This is most likely to be due to some uncertainty in the theoretical viscosity prediction, as the theoretical methods for predicting the osmotic pressure (Section 7.3) and the gradient diffusion coefficient (Section 7.4) have been compared to experimental data for these properties and have shown excellent agreement. Better predictions could be obtained by using a more sophisticated description of the rheological properties. Indeed, precise calculation of the rheological properties of charged colloidal systems remains a major challenge in colloid science. Even so, Figure 7.18 shows that the predictions obtained when allowing all the properties to vary are overall significantly better than the other predictions for the range of applied pressures considered.

7.8 TENSILE AND OTHER RHEOLOGICAL PROPERTIES OF LIQUIDS ON THE MESO SCALE

7.8.1 Metastability and Cavitation Phenomena

There has been considerable interest in the possible existence of a *separation-induced spinodal* and the associated phenomenon of *spontaneous cavitation*, the

term 'cavitation' referring to the formation of cavities (or cavitation 'bubbles') in a liquid when it experiences tension [147]. If the tension exceeds the liquid's cavitation threshold (or effective tensile strength) the liquid changes irreversibly into a two-phase system of liquid and a mixture of vapour and dissolved gas [148].

The rheological behaviour of thin liquid films is an important aspect of lubrication [149] and printing [150], processes that often involve meso scale (0.1–10 μm) thickness films undergoing rapid deformation between separating surfaces. In the case of fluid mechanical machinery these are usually solid surfaces, whereas in biomechanics they may be flexible surfaces, such as biological membranes. The 'cracking' of knuckle joints has been attributed to cavitation within meso scale lubricating films of synovial fluid [151], while surface damage in microelectromechanical system devices has been attributed to the cavitation of lubricant films [152]. The ability of liquids to sustain tension is an important factor in the survival of plants, in which the cohesion–tension (C-T) theory has been proposed to explain water transport [153]. The C-T theory assumes that water, when confined in small tubes with wettable walls such as xylem elements, can sustain a tension ranging from 3 MPa to 30 MPa. The liquid forms a continuous system in the water-saturated cell walls, from the evaporating surfaces of the leaves to the absorbing surfaces of the roots. During evaporation, the reduction in water potential at the surfaces causes movement of water out of the xylem, with water loss producing tension in the xylem sap that is transmitted throughout the continuous water columns to the roots.

In coating processes, cavitation film-splitting may result in the formation of rapidly stretching filaments, whose break-up leads to unwanted droplet deposition. Filament formation is also a feature of coating flows involving adhesive films [154], but descriptions of the process are still largely qualitative, invoking terms such as 'tack' [155, 156]. The tack of an ink film is primarily connected with the tensile forces developed in film-splitting [157], the function of cavitation being to limit the forces of separation of surfaces joined by a tacky liquid [158]. By definition, the tack of an ink film is the maximum tensile stress (or 'negative pressure') that it can withstand before splitting [150].

Due to the high deformation rates which typify many meso scale cavitation phenomena, significant viscoelastic effects may be anticipated. One such effect is a delay in the cavitation of viscoelastic liquids in micrometre-sized gaps, due to the development of normal stresses [159]. Others claimed that viscoelastic effects include a displacement of the point of cavitation from the centre of contact (where film thickness is a minimum) and enhanced film thicknesses [160]. Little is known about the influence of viscoelasticity in submicrometre liquid film cavitation, but the initial film thickness is a crucial factor; for sufficiently thin films, even ostensibly low rates of surface separation may provoke the high rates of fluid deformation necessary to generate enough tension (through viscous forces) to result in cavitation [161].

It is important to realize that in ultrathin films of water, cavitation may occur spontaneously, due to the antipathy between the liquid and hydrophobic

surfaces between which it is confined [162]. Spontaneous cavitation was first observed experimentally by Christenson and Claesson [162]. Theory predicts that vaporous cavities will only form in pure liquids as a result of large tensions, some 1300–1400 bar in the case of water [163], although a somewhat higher figure (ca. 1900 bar) results from an interpretation of the thermodynamic properties of stretched water known as the stability limit conjecture [164]. Experiments involving very small quantities of *pure* water have produced tensions close to this homogeneous nucleation limit [165] but they are not commonly observed. Thus the idea of bubble nucleation, and its manifestation as a liquid's *effective* tensile strength, F_c , has been introduced.

In some treatments, nuclei represent 'holes' in the liquid, which grow into macroscopic bubbles, but heterogeneous nucleation may involve microscopic impurities such as 'motes' of dirt or dust that act as nuclei. An energy barrier against nucleation arises because the liquid–gas transition is discontinuous and the interface between the two phases has a finite energy per unit area – the surface tension, S . Thus the formation of a bubble has an energy cost of $4\pi R^2 S$. When such a bubble forms, the energy of the whole system also contains the work of the negative pressure over the bubble volume, so that the total energy cost of forming the bubble is [166]:

$$\Delta E = 4\pi R^2 S + \frac{4\pi}{3} R^3 P. \quad (7.45)$$

At negative pressures, this energy has a maximum for a critical radius $R_c = 2S/|P|$.

The liquid pressure, p , exterior to a bubble of radius R will be related to the interior pressure, p_B , by

$$p_B - p = 2S/R, \quad (7.46)$$

where S is the surface tension. It is assumed that the concept of surface tension (or surface energy) can be extended down to bubbles or cavities a few intermolecular distances in size. If the temperature, T , is uniform and the bubble contains only vapour, then the interior pressure, p_B , will be the saturated vapour pressure, $p_V(T)$. However, the exterior liquid pressure, $p = p_V - 2S/R$, will have to be less than p_V in order to produce equilibrium conditions. Consequently, if the exterior liquid pressure is maintained at a constant value just slightly less than $p = p_V - 2S/R$, the bubble will grow, R will increase the excess pressure, causing the growth to increase, and rupture to occur. For some finite tension the liquid stretches without limit.

This may be considered in terms of the potential tensile strength of a pure liquid involving two molecules that are separated by a variable distance, r : equilibrium occurs at the separation r_0 and the attractive force is equal to $\delta\phi/\delta r$, where

ϕ is the potential energy associated with the intermolecular force which is a maximum at r_1 , where typically r_1/r_0 is calculated as 1.1 or 1.2. The application of a constant tensile stress equal to that corresponding to r_1 ruptures the liquid since, for $r > r_1$, the attractive force is insufficient to counteract that tensile force [148].

The pressure at which that happens is called the spinodal limit, at which the sound velocity becomes zero (i.e. the compressibility is infinite) and there is no barrier to nucleation. Thus for small tensions the energy barrier is large and the probability of bubble formation is low. A pure liquid may sustain tension for a prolonged period but it is important to realize that a liquid under tension is in a *metastable state* – it inhabits the region between the spinodal and the coexistence curve where liquid and vapour coexist. The spinodal parabola meets the coexistence curve at the critical point, but otherwise is separated from it by a finite distance [167]. In the absence of nucleation sites, the metastable fluid can be macroscopically long-lived, but it is not possible to proceed past the spinodal line and remain as one phase; at the spinodal the molecules may be regarded as self-nucleating.

Berard *et al.* [168] showed that the free energy of a bridging cavity is lower than that of liquid water when the surfaces are separated as far as micrometres and claim that the fact that such cavities are not observed as the two surfaces approach contact from far apart indicates that the liquid between them is metastable, i.e. that there is some barrier preventing cavitation. The theory for the long-ranged hydrophobic attraction relies upon this notion of induced cavitation – the force between two colloids in a near-critical or a near-spinodal fluid is attractive and long-ranged – and the connection between the spinodal attractions in the bulk and measured long-range attractions between hydrophobic surfaces is the observed cavitation [169].

Computer simulations by Berard *et al.* [168] on a Lennard–Jones liquid confined between hard walls showed cavitation at small separations and that there was indeed a spinodal separation. Approaching this separation it was found that the attractions were much stronger than the van der Waals attraction, and longer ranged. Qualitatively, a separation-induced spinodal can account for the measured hydrophobic attractions [170].

In the case of cavitation which results from the development of fluid mechanical stresses (as tension), Joseph [161] has pointed out that the concept of ‘negative pressure’ is not particularly useful, it being more pertinent to consider the state of stress experienced by a liquid. In so doing, it is convenient to decompose the stress into a deviator and mean normal stress, the most positive value of principal stresses being the maximum tension. In order to facilitate a comparison of a liquid’s cavitation threshold stress with the principal stresses at each point within the liquid, it is necessary to know the flow field. In terms of studying cavitation inception within meso scale liquid films, this requirement imposes stringent experimental demands as it requires a comparison of the cavitation threshold at each point in a liquid sample with the principal stresses there. For liquids in

motion, cavitation criteria must be based not on the pressure but on the stress, and a cavitation bubble will open in the direction of maximum tension in principal coordinates. An important point that emerges is that a liquid can cavitate as a result of experiencing a *shear* deformation, the resulting cavity being pulled open by tension in the direction defined by principal stresses.

7.8.2 Experimental Techniques

7.8.2.1 *Experimental studies of the tensile properties of meso scale fluid films*

Of the few experimental techniques capable of working at (or below) the meso scale, the various ‘force microscopes’, such as the surface forces apparatus (SFA), have been the most successful, but instances of their use in studies of thin fluid films are comparatively rare. Notable exceptions are provided by the work of Israelachvili and coworkers [171] who observed the growth and disappearance of vapour cavities in liquid films between separating mica surfaces in SFA experiments. The growth of a cavity was claimed to represent a ‘new’ cavitation damage mechanism, insofar as surface damage occurred during cavity inception [172]. This is an interesting finding given that by far the greatest effort in cavitation damage research has involved the study of bubble collapse and its consequences. Lord Rayleigh’s seminal analysis of the collapse of an isolated spherical void in an incompressible liquid [173] leads to the conclusion that, as the collapse nears completion, the pressure inside the liquid becomes indefinitely large. It is principally this ‘Rayleigh collapse’ mechanism (albeit extensively modified) that has led to the association of bubble collapse with cavitation damage [174].

Little is known about the dynamics of cavities formed in thin films but, due to their inevitably close proximity to the film’s bounding surfaces, significant departures from spherical symmetry may be anticipated [175]. The asymmetry of cavity collapse leads to potentially damaging phenomena, such as liquid jets [176], but the issue of cavitation damage due to cavity *growth* has received relatively little attention, despite the possibly damaging consequences to capillaries and small blood vessels of the intraluminal expansion of cavitation bubbles in the areas of laser angioplasty [177], electrohydraulic lithotripsy [178] and shock wave lithotripsy [179].

The atomic force microscope (AFM) enables imaging of the surface topography of both conducting and nonconducting materials with atomic resolution [180]. It has also been used to study nanomechanical, adhesion and viscoelastic properties [181, 182], the dynamic properties of systems such as membranes [183], the adhesion of a single biological cell to a surface [184] and the properties of liquids [185, 186].

Barrow *et al.* [187] have reported work in which an AFM was used to stretch (and, ultimately, to rupture) a thin film of liquid between a moving colloid sphere

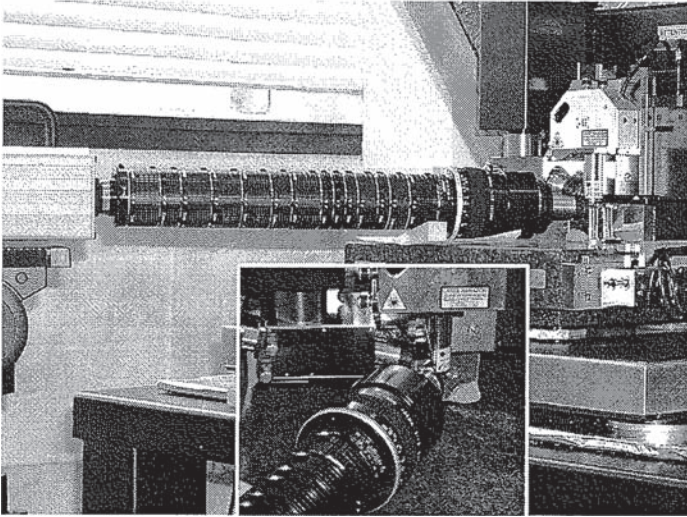


Figure 7.19 High-speed microphotographic (HSMP) system consisting of a microscope objective lens, a telephoto lens, a set of magnifying extension tubes and a Kodak HS4540 high-speed video camera. The HSMP system is aligned with the colloid probe mounted on the cantilever of a Digital Instruments DI 3100 AFM [187].

and a static, plane surface. Their experiments involved a novel high-speed video microphotographic system, which was used to record the development of fluid filaments following rupture of the fluid film (see Figure 7.19).

Figure 7.20 shows how the force between an AFM cantilever and a sample is recorded as a function of the scanner displacement, the latter being varied in this case using a piezoelectric crystal. A laser beam reflected from the back of the cantilever falls on to a photosensitive position detector (PSPD) photodiode whose output is used to detect changes in cantilever deflection. To generate a force–distance curve, the cantilever tip deflection is recorded as a function of the tip–sample separation as the piezo scanner raises the sample towards the tip and subsequently retracts away. In order to convert the resulting data into force as a function of true sample–tip separation, it is necessary to know the spring constant, K , of the cantilever and to define zero values of the force and of the separation distance.

In AFM work the cantilever tip geometry is often unknown. In the experiments reported by Barrow *et al.* [187] the tip was replaced by a ‘colloid probe’ of known geometry in order to facilitate a comparison of normalized data. The probes (Figure 7.21) were made by attaching $15\ \mu\text{m}$ diameter silica spheres to tipless cantilevers for which the values of K were $2.9\ \text{N/m}$ and $2.1\ \text{N/m}$, and whose resonant frequency (measured in the absence of a colloid sphere using the AFM’s noncontact, frequency-sweep mode) was $160\ \text{kHz}$ and $320\ \text{kHz}$ respectively. The

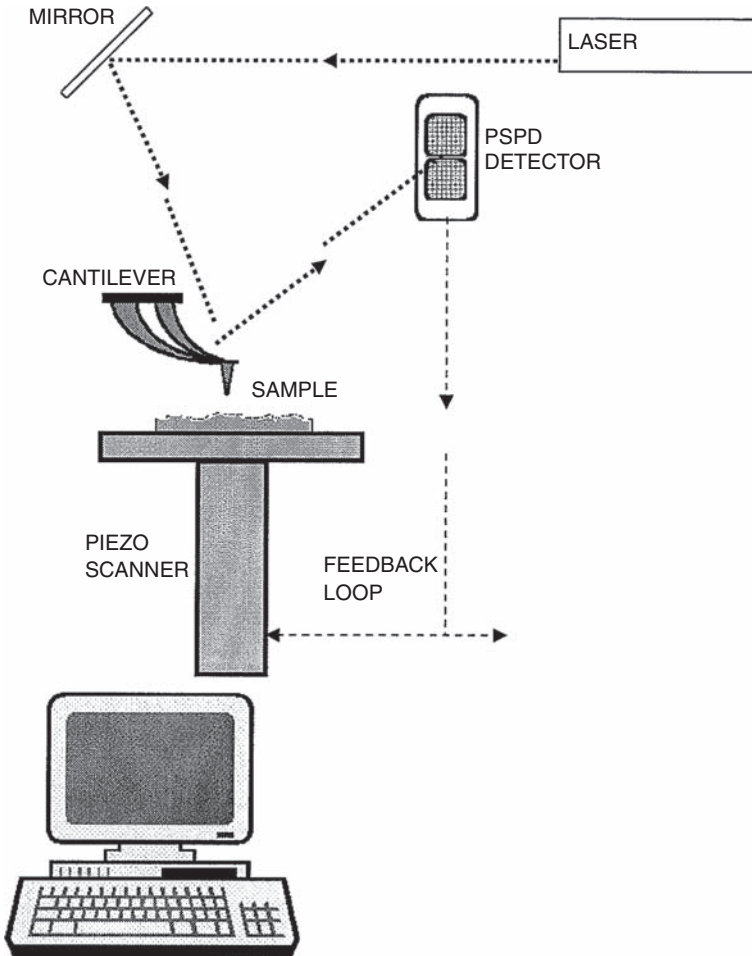


Figure 7.20 Basic arrangement of the AFM in which a laser beam reflected from the back of the cantilever falls on to a photosensitive position detector (PSPD) photodiode which detects changes in cantilever deflection.

optimal positioning of the sphere at the apex of the tipless cantilever, combined with its small mass, results in an insignificant modification of the spring constant of the bare cantilever [188]. Colloid spheres of this type have a maximum peak-to-valley roughness of 3 nm over an area of $0.45 \mu\text{m}^2$ [186]. The planar surface was prepared by oxidation of polished silicon wafers to give a 500 nm thick coating.

Typically these consist of an 'approach' and a 'retraction' stage (Figures 7.22 and 7.23), in which the maximum distance between the probe and the surface

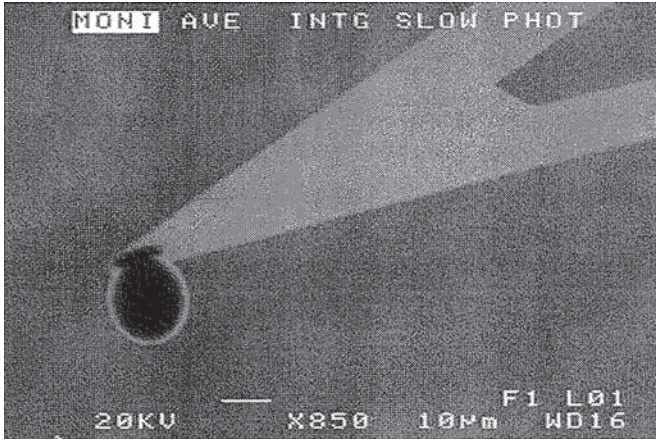


Figure 7.21 Scanning electron microscope (SEM) image of a spherical ‘colloid probe’ of the type used in the experiments.

over which force measurements are made is *ca.* $3 \mu\text{m}$. At the position denoted ‘*a*’ in Figure 7.22, the probe is initially located far from a nominally ‘dry’ surface (an unevenly distributed water moisture layer is present on surfaces in air with relative humidity greater than 20 %). At position ‘*a*’ the cantilever is undeflected, with the corresponding ‘zero-force’ PSPD output being constant. On approaching the surface, at a constant velocity, the PSPD output *decreases* at position ‘*b*’, this reduction corresponding to a *downward* deflection of the cantilever (an event

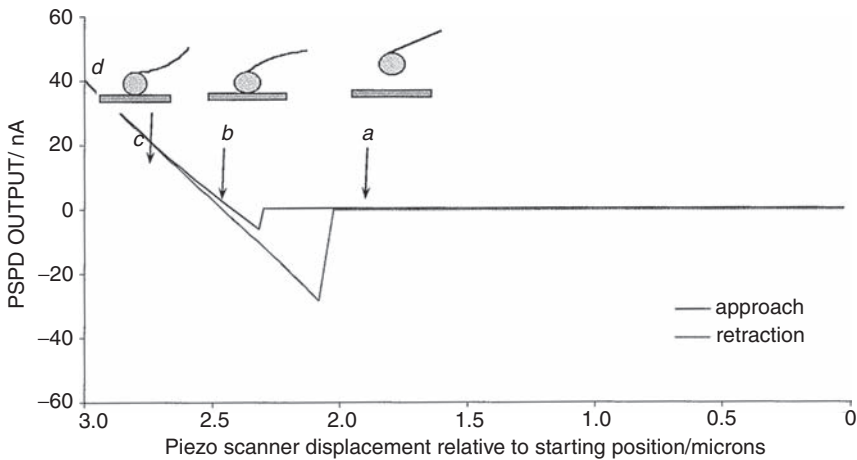


Figure 7.22 Typical force curves obtained for the approach and retraction of a probe to and from a nominally dry surface.

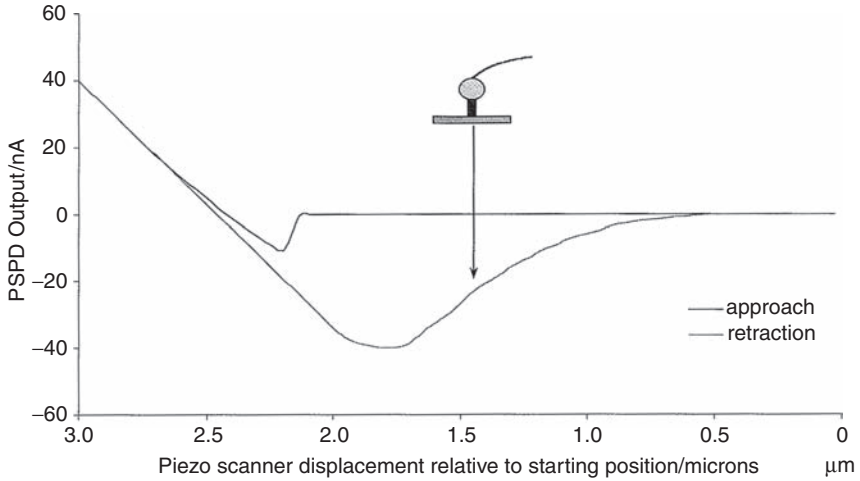


Figure 7.23 Typical force curves obtained for approach and retraction to and from a surface covered by a film of viscous liquid.

which is referred to as ‘snap in’). This is attributed to the action of capillary forces due to the presence of a surface layer of water moisture and to short-range attractive forces that act upon the probe prior to the establishment of a physical surface contact.

Between positions ‘*b*’ and ‘*c*’ the probe is arrested by the surface, but the other end of the cantilever is attached to the scanner column which *continues to descend*. Consequently, the cantilever deflection *reverses*, corresponding to a compressive force in region ‘*c*’. The scanner continues to descend until a predefined limit of compressive force is recorded (at ‘*d*’). By specifying a lower value of the limiting contact force (at ‘*d*’), a tolerable cantilever deflection is achieved. Following this phase of the ‘approach’ curve, the scanner retracts over a specified distance ($3\ \mu\text{m}$) relative to the final position of approach until the probe-surface contact is broken.

The general features of the corresponding curves obtained when a film of liquid (substantially more viscous than water) is placed on the surface are represented in Figure 7.23. Although the approach curve is similar to that shown in Figure 7.22, the retraction of the scanner is not accompanied by a ‘snap back’ to zero force. Rather, a more gradual reduction of tensile force is usually recorded, subsequent to the generation of the peak tensile force. This reduction is recorded over significantly greater distances than those previously noted for work involving a nominally ‘dry’ surface, this characteristic feature of the retraction curve being attributed to the formation of a liquid film that spans the gap between the probe and the surface. Thus, both the magnitude and the range of the measured tensile force increase significantly in the presence of a liquid film.

In Figures 7.22 and 7.23, the PSPD output is presented as a function of piezo position relative to the piezo's starting height, not to the planar surface. A change in PSPD output (relative to the zero-force) is produced by a deflection of the cantilever and causes an additional vertical displacement of the probe, which is *independent of scanner position*. In Figure 7.22, the region between 'c' and 'd' is referred to as the region of constant compliance in which the PSPD output is a linear function of the scanner position and the probe is considered to be in contact with the solid surface. It follows that within the region of constant compliance, the magnitude of the piezo displacement is equal to the magnitude of displacement of the probe *relative* to the piezo (corresponding to a compressive deflection of the cantilever). Under such circumstances, the relationship between the PSPD output and cantilever deflection is calculated from the gradient of the constant compliance region. This relationship is assumed valid for deflections corresponding to the development of tensile forces.

Barrow *et al.* [187] used their AFM–HSMP system to record a sequence of images at 1000 frames per second (f.p.s.) during retraction curve experiments on a sample of 12 Pa s silicon oil (see Figure 7.24). As the retraction curve proceeds, the liquid film splits rapidly prior to the formation of a microfilament, which is subsequently stretched by the continuing upward motion of the sphere. A provocative finding made in this work was that, under some circumstances, when the sphere and the surface were pulled apart sufficiently rapidly, an unexpected transient *decrease* of the sphere–surface separation was recorded.

The results of numerical simulations of cavitation bubble dynamics reported by Barrow *et al.* [187] suggest that the growth of a cavitation bubble within a liquid may result in the development of sufficiently large *negative* pressures to account for this phenomenon. The results of separate experiments involving acoustic pulse propagation within metre-long columns of liquid [189] and high-speed microphotography were used to show that the peak tensile forces recorded in the AFM experiments corresponded to the development of tensile stresses that are commensurate with the fluid's effective tensile strength (or 'cavitation threshold'). The results of this study, the first to apply the AFM in cavitation bubble dynamics work, provided evidence in support of the mechanism mooted by Israelachvili and coworkers [190], i.e. that in the cavitation of liquids within confined spaces, such as situations involving meso scale films, the growth of a cavity may be more damaging than its subsequent collapse.

7.8.2.2 *Experimental studies of the nanorheological properties of meso scale fluid films*

The rheological properties of adsorbed polymer layers at the nanoscopic level can be obtained from a force-sensing apparatus such as a surface force apparatus (SFA) or an atomic force microscope (AFM), by adapting these techniques to

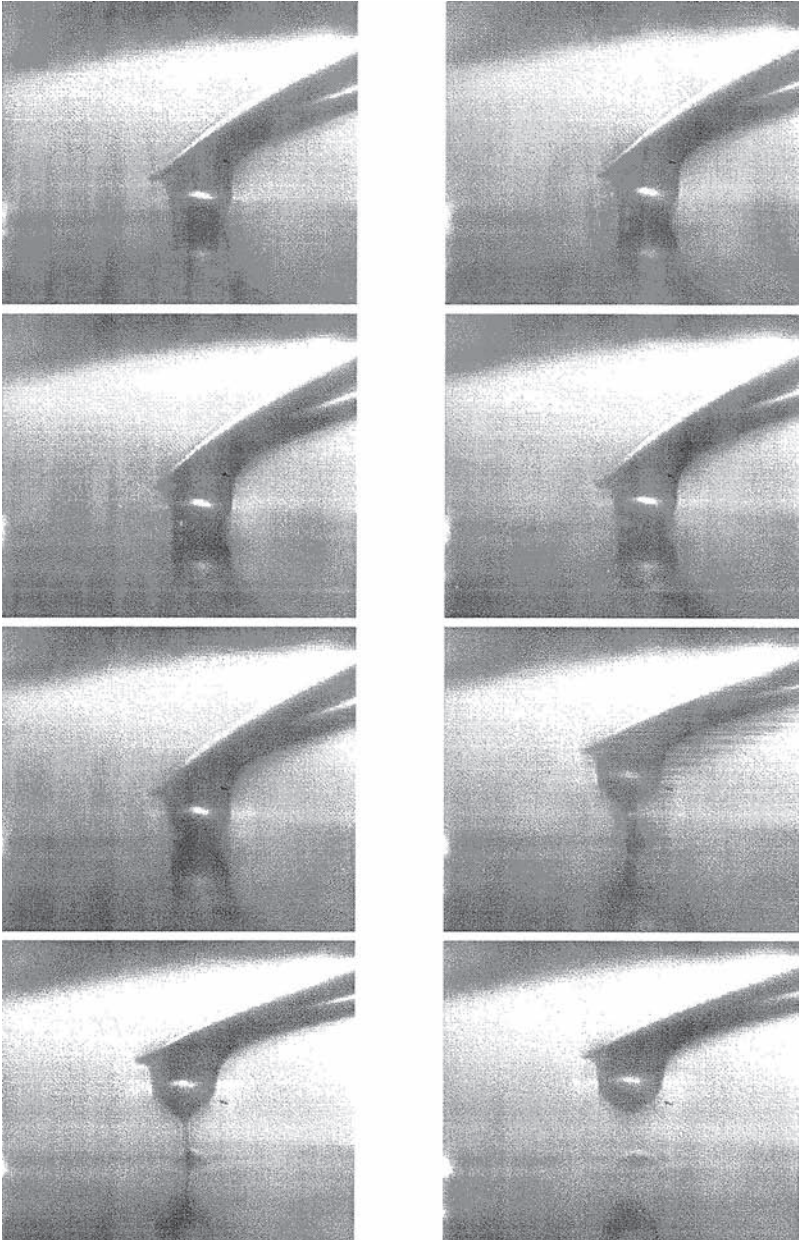


Figure 7.24 A sequence of images recorded at 1000 frames per second (f.p.s.) during AFM retraction curve experiments on a sample of 12 Pa s silicon oil. The liquid film splits rapidly prior to the formation of a filament, which is subsequently stretched by the continuing upward motion of the sphere.

act in a dynamic mode, thus effectively enabling them to act as rheometers. This technique, described as ‘nanorheology’ by Suraya *et al.* [191], involves applying a small-amplitude sinusoidal motion to one surface. This driving signal creates an oscillatory motion of the fluid within the gap due to hydrodynamic forces, which induces the second surface to respond by oscillating at the same frequency. However, due to viscous effects, the amplitude of the oscillation is attenuated and the phase is shifted relative to the driving motion. For a purely viscous medium, the response signal will be 90° out-of-phase, while a fully elastic response would be precisely in-phase (if the driving frequency is lower than the resonant frequency) with the driving signal. For polymer-coated surfaces in relative motion in a dilute polymer solution, a viscous response may be seen at very large surface separations. However, when the separation distance is a few times the thickness of the polymer layers, they begin to deform; the viscoelastic nature of the system becomes more apparent and the phase shift then becomes smaller, while the response amplitude becomes larger.

Suraya *et al.* [191] note that there is no direct method of determining the stress and the strain from the raw data, since these dynamic experiments only measure the hydrodynamic force in terms of phase and amplitude. Consequently, a mechanical model is required to interpret the detected motions in terms of physical stress and strain. To interpret experimental data, some nanorheological studies between polymer-coated surfaces have used the hydrodynamic lubrication equation, which describes the hydrodynamic force that arises from the flow of a Newtonian liquid of viscosity η , between a bare plane and a spherical surface of radius R , at a separation distance h_0 apart, moving at a relative velocity U , given by

$$F = 6\pi\eta U \frac{R^2}{h_0}, \quad (h_0 \ll R). \quad (7.47)$$

This equation also applies for a linear viscoelastic fluid, in which case the velocity, force and viscosity are treated as complex quantities. This approach provides a quantitative description of the rheological properties of the fluid between the two surfaces if that fluid is a continuum. However, when the fluid between the two surfaces is not uniform, such as when there is an adsorbed polymer layer, only qualitative information can be obtained.

Suraya *et al.* [191] have reported the use of this oscillatory AFM technique to investigate the viscoelastic properties of adsorbed hydroxypropyl guar (HPG) layers. Polymer-coated surfaces exhibit static interactions arising from bridging and steric behaviour. In addition, there are also dynamic interactions that arise from the rheological behaviour of the adsorbed polymer layers. The oscillations were performed at frequencies between 300 Hz and 1 kHz, with applied oscillation amplitudes of 2 nm. Qualitative data analysis was carried out using complex viscosity and complex modulus transfer functions based on a hydrodynamic lubrication model.

The results indicated viscous behaviour at large surface separations and viscoelastic behaviour in the region of polymer layer overlap, as would be expected for adsorbed polymer layers. The adsorbed HPG layers also showed an indication of frequency-dependent viscoelastic behaviour and ‘shear thinning’ (in terms of a reduction of viscosity with frequency). The experiments revealed an unanticipated correlation between the apparent thickness of the adsorbed layers and the viscoelastic properties of the system, this being attributed to the shear thinning behaviour of the layers. The future development of such nanorheological techniques is likely to prove important as they will provide an improved understanding of macroscopic properties in terms of phenomena that are observed on the nanoscopic scale.

7.9 SUMMARY

A discussion of various experimental measurements and techniques that depend on fluid flow and properties at the nano/meso scale is presented. These measurements range from macro scale measurements, such as rates of membrane filtration, down to nano scale measurements performed using the atomic force microscope (AFM). Comparison between simulation and experiment is shown for several cases.

8

Future Advancement

Aim. This chapter summarizes the approaches considered in this book and the current challenges faced in the meso scale simulation of fluid systems. Some suggestions are given for further work required in the area.

8.1 FUTURE ADVANCEMENT

The work presented in this book has highlighted techniques for how to tackle simulation of fluid in meso scale systems. In the development of a complete molecular-based meso scale simulation method there are several issues that need to be tackled to improve the efficiency and robustness and increase the scale and complexity of systems that can be simulated. None of these issues are trivial and present significant scope for further research. The main issues are detailed below:

- *Search efficiency.* Much of the time spent processing the molecular model is spent searching for neighbours within the domain. As the system size increases as compared to the interaction radius of the individual molecules and the number of molecules, the proportion of time spent searching throughout the domain for neighbour pairs increases. This efficiency could be significantly increased by the implementation of a second level of search routine, where frequent neighbour searches are performed over smaller subdomains of the flow field. Research is needed to identify efficient search techniques that are relevant for extremely large numbers of molecules that are constantly moving and mixing together.
- *Parallel implementation.* To allow the meso molecular model access to larger systems containing upward of one million molecules, this method would require

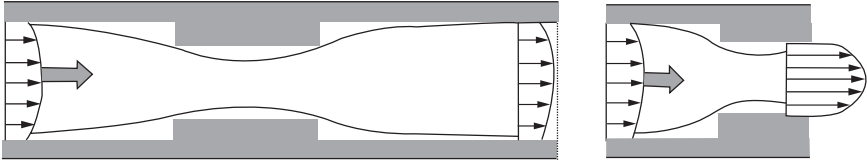


Figure 8.1 Left: flow restriction modelled with current periodic boundary conditions and molecular energy conserved. Right: modified boundaries allow a different type of problem to be simulated.

parallelization to take advantage of multiple processor machines. This will enable the storage and faster processing of large numbers of molecules and longer neighbour lists to reduce the computation time per molecule. This is also compatible with methods of improving search routines, as a form of domain decomposition would be required. Due to the chaotic nature of fluid simulation, data storage and communication must be efficiently maintained to make the most of the available resources.

- *Meso scale boundary conditions.* For most engineering problems, the typical periodic boundary condition used in MD simulations, that the fluid properties must be identical on opposite sides of the simulation cell, is unrealistic, as illustrated in Figure 8.1. The figure on the left shows the type of system that can be simulated using periodic boundary conditions. The limitation of these conditions is that the fluid at opposite sides of the simulation cell must be at identical states to prevent violation of thermodynamic laws. In order to simulate the change in fluid properties at intermediate sections, e.g. a restriction, the inlet and outlet conditions will need to be exactly the same and, hence, far away from the restriction to apply periodic boundary conditions. This means that independent conditions cannot be applied to the boundary to solve common fluid flow situations that occur in engineering problems. For example, the boundary condition as shown in Figure 8.1 (right) cannot be evaluated using periodic boundaries. However, maintaining the invisibility of the boundary to the fluid molecules presents a significant challenge.
- *Investigate and develop energy/temperature controls.* This book has identified that the current temperature controls are insufficient to deal with increases in temperature due to changing internal dynamics. Examples highlighted in Chapter 5 showed that the temperature of the high flow system was not allowed to increase as would be expected for a turbulent system. This needs more investigation and possibly a new method for applying system controls and would significantly expand the range of systems that can be simulated, allowing the effective use of reduced boundary conditions.

References

- [1] H. R. Wu, Y. L. He, G. H. Tang and W. Q. Tao, Lattice Boltzmann simulation of flow in porous media on non-uniform grids, *Prog. Comp. Fluid Dyn.*, **5**,(1/2), 97–103, 2005.
- [2] P. J. Hoogerbrugge and J. M. Kolesman, Simulating microscopic hydrodynamic phenomena with dissipative particle dynamics, *Europhys. Lett.*, **19**, 155, 1992.
- [3] J. F. Douglas, J. M. Gasiorek, J. A. Swaffield and L. B. Jack, *Fluid Mechanics*, 5th edition, Pearson Education, 2005.
- [4] J. M. Haile, *Molecular Dynamic Simulation, Elementary Methods*, Wiley-Interscience, 1997.
- [5] Sir J. Jeans, *An Introduction to the Kinetic Theory of Gases*, Cambridge, 1967.
- [6] *Oxford English Dictionary*, 2nd edition, Oxford University Press, 1989.
- [7] O. Reynolds, An experimental investigation of the circumstances which determine whether the motion of water shall be direct or sinuous, and of the law of resistance in parallel channels, *Roy. Soc.*, **44**, 52–105, 1883.
- [8] J. D. Van der Waals, *On the Continuity of the Gaseous and Liquid States*, Dover Publications, 2004.
- [9] F. London, On centers of van der Waals attraction, *J. Phys. Chem.*, **46**, 305–317, 1942.
- [10] M. Massimi, *Pauli's Exclusion Principle*, Cambridge University Press, 2005.
- [11] G. Dharmadurai, Solid state density equations if state for fluids, *J. Phys. III France*, **6**, 505–509, 1996.
- [12] D. Keffer, Thermodynamic properties of a single component fluid, *Uni. Knoxville*, March 2001.
- [13] D. Frenkel and B. Smit, *Understanding Molecular Simulation*, Vol. 1, Accademic Press, 2002.
- [14] M. Lewerenz, *Monte Carlo Methods: Overview and Basics*, Vol. 10, John von Neumann Institute for Computing, 2002.
- [15] N. Metropolis, A. Rosenbluth, M. Rosenbluth, A. Teller and E. Teller, Equation of state calculations by fast computing machines. *J. Chem. Phys.*, **21**, 1087–1092, 1953.

- [16] C. Pangali, M. Rao and B. Berne, On a novel Monte Carlo scheme for simulating water and aqueous solutions, *Chem. Phys. Lett.*, **55**, 413–417, 1978.
- [17] H. Gould, J. Tobochnik and W. Christian, *Introduction to Computer Simulation Methods: Applications to Physical Systems*, 3rd edition, Addison-Wesley, 2006.
- [18] D. Levesque, A. Gucquel, F. Lamari Darkrim and S. Beyaz Kayiran, Monte Carlo simulations of hydrogen storage in carbon nanotubes, *J. Phys.: Cond. Mat.*, **14**, 2985–9293, 2002.
- [19] R. Radhakrishnan and K. Gubbins, Effect of fluid–wall interaction on freezing of confined fluids: towards the development of a global phase diagram, *J. Chem. Phys.*, **112**(24), 11048–11057, 2000.
- [20] K. Travis and K. Gubbins, Computer simulation of isothermal mass transport in graphite slit pores, *Mol. Sim.*, **27**, 405–439, 2001.
- [21] R. Tuzun, D. Noid, B. Sumpster and R. Merkle, Dynamics of fluid flow inside carbon nanotubes. *Nano. Tech.*, **7**, 241–246, 1996.
- [22] R. Cracknell, D. Nicholson and N. Quirke, Direct molecular dynamic simulation of flow down a chemical potential gradient in a slit shaped micropore, *Phys. Rev. Lett.*, **74**(13), 2463–2466, 1995.
- [23] C. Bing-Yang, C. Min and G. Zeng-Yuan, Rarefied gas flow in rough micro channels by molecular dynamic simulation, *Chin. Phys. Lett.*, **21**(9), 1777–1779, 2004.
- [24] F. Ercolessi. *A Molecular Dynamics Primer*, International School for Advanced Studies, Italy, 1997.
- [25] B. Yoon, Anisotropic phase transition of hard spheres confined in hard walls, *Bull. Korean Chem. Soc.*, **22**(12), 1375, 2001.
- [26] B. Yoon, Analytical expressions for the radial free space distribution function of the hard sphere system and the phase transition, *Chem. Phys. Lett.*, **243**(1-3), 35–38, 1995.
- [27] B. Peterson, K. Gubbins, G. Heffelfinger, U. Marconi and F. van Swol, Lennard–Jones fluids in cylindrical pores: nonlocal theory and computer simulation, *J. Chem. Phys.*, **88**, 6487, 1988.
- [28] R. Radhakrishnan and K. Gubbins, Quasi-one-dimensional phase transition in nanopores: pore–pore correlation effect, *Phys. Rev. Lett.*, **79**(15), 2847, April 1999.
- [29] M. Meyer and H. Stanley, Liquid–liquid phase transition in confined water: a Monte Carlo study, *J. Phys. Chem. B*, **103**, 9728–9730, 1999.
- [30] P. Poole, U. Essmann, F. Sciortino and H. Stanley, Phase diagram for amorphous solid water, *Phys. Rev. E*, **48**(6), 4605–4610, 1993.
- [31] S. Gatica, G. Stan, M. Calbi, J. Johnson and M. Cole, Axial phase of quantum fluids in nanotubes, *J. Low Temp. Phys.*, **120**(5/6), 337–359, 2000.
- [32] G. Stan and M. Cole, Low coverage adsorption in cylindrical pores, *Surf. Sci.*, **395**, 280–291, 1998.
- [33] J. Dash, M. Schick and O. E. Vilches. Phases of helium monolayers: search and discovery. *Surf. Sci.*, **299**, 405–414, 1994.
- [34] M. Cole, V. Crespi, G. Stan, C. Ebner, J. Hartman, S. Moroni and M. Boninsegni, Condensation of helium in nanotube bundles, *Phys. Rev. Lett.*, **84**, 3883, 2000.
- [35] M. Miyahara and K. Gubbins, Freezing/melting phenomena for Lennard–Jones methane in slit pores: a Monte Carlo study, *J. Chem. Phys.*, **106**(7), 2865–2880, 1997.

- [36] M. Maddox and K. Gubbins, A molecular simulation study of freezing/melting phenomena for Lennard–Jones methane in cylindrical nanoscale pores, *J. Chem. Phys.*, **107**(22), 9659–9667, 1997.
- [37] H. Kim and W. Steele, Computer simulation study of the phase diagram of the methane monolayer on graphite: corrugation effects, *Phys. Rev. B*, **45**(11), 6226–6233, 1992.
- [38] L. Gelb, *The Ins and Outs of Capillary Condensation in Cylindrical Pores*, Florida State University, 2002.
- [39] K. Travis, B. Todd and D. Evans, Departure from navier–stokes hydrodynamics in confined liquids, *Phys. Rev. E*, **55**(4), 4288–4295, 1997.
- [40] M. Gad el Hak, *Liquids: The Holy Grail of Microfluidics Modelling*, Virginia Commonwealth University, 2004.
- [41] E. Lauga, M. Brenner and H. Stone, *Handbook of Experimental Fluid Dynamics*, Springer, 2005.
- [42] C. J. Maxwell, On stresses in rarefied gasses arising from inadequacies of temperature, *Phil. Trans. Roy. Soc. I*, **170**, 231–256, 1897.
- [43] M. von Smoluchowski, Ueber warmeleitung in verdunten gasen, *Annalen der Physik und Chemi*, **64**, 10130, 1898.
- [44] M. Gad el Hak, The fluid mechanics of microdevices – the Freeman scholar lecture, *Fluids Eng.*, **121**, 5–33, 1999.
- [45] W. Loose and S. Hess, Rheology of dense model fluids via non-equilibrium molecular dynamics: shear thinning and ordering transition, *Rheologica Acta*, **28**, 91–101, 1989.
- [46] J. Pfahler, J. Harley and B. Bau, Liquid transport in submicron channels, *Sensors and Actuators*, **A21–A23**, 431–434, 1990.
- [47] H. Rafii-Tabar, L. Hua and M. Cross, A multi-scale atomistic-continuum modelling of crack propagation in a two-dimensional macroscopic plate, *J. Phys.: Cond. Mat.*, **10**, 2375, 1998.
- [48] G. Ayton, S. Bardenhagen, P. McMurtry, D. Sulsky and G. Voth, Interfacing molecular dynamics with continuum dynamics in computer simulation: toward an application to biological membranes, *IBM J. Res. Dev.*, **45**(3/4), 417–426, 2001.
- [49] F. Abraham, Dynamically spanning the length scales from the quantum to the continuum. *J. Mod. Phys. C*, **11**(6), 1135–1148, 2000.
- [50] A. L. Garcia, J. B. Bell, W. Y. Crutchfield and B. J. Alder. Adaptive mesh and algorithm refinement using direct simulation Monte Carlo, *J. Comp. Phys.*, **154**, 134–155, 1999.
- [51] X. Nie, S. Chen, W. N. E. and M. Robbins, A continuum and molecular dynamics hybrid method for micro- and nano-fluid flow, *J. Fluid Mech.*, **500**, 55–64, 2004.
- [52] E. S. Boek, P. V. Coveney, H. N. W. Lekkerkerker and P. van der Schoot, Simulating the rheology of dense colloidal suspensions using dissipative particle dynamics, *Phys. Rev. E*, **55**(3), 3124, 1997.
- [53] P. V. Coveney and K. E. Novik, Computer simulations of domain growth and phase separation in two-dimensional binary immiscible fluids using dissipative particle dynamics, *Phys. Rev. E*, **54**(5), 5134–5141, 1996.
- [54] A. G. Schlijper, P. J. Hoogerbrugge and C. W. Manke, Computer simulation of dilute polymer solutions with the dissipative particle dynamics method, *J. Rheol.*, **39**(3), 567–579, 1995.

- [55] J. Tolke, M. Krafczyk, M. Schulz and E. Rank, Lattice Boltzmann simulations of binary fluid flow through porous media, *Philos. Transact. A Math. Phys. Eng. Sci.*, **360**(1792), 535–545, 2002.
- [56] M. M. Dupin, I. Halliday and C. M. Care, Multi-component lattice Boltzmann equation for mesoscale blood flow, *J. Phys. A*, **36**, 8517–8534, 2003.
- [57] S. Naris, D. Valougeorgis, F. Sharipov and D. Kalempa, Discrete velocity modelling of gaseous mixture flow in MEMS, *S.Latt. M.Struc.*, **35**, 629–643, 2004.
- [58] R. Qin, DL meso. http://www.ccp5.ac.uk/dlmeso/DL_MESO.html, September 2006.
- [59] M. P. Allen and D. J. Tildesley, *Computer Simulation of Liquids*, Oxford University Press, 1997.
- [60] V. Sokhan, D. Nicholson and N. Quirke, Fluid flow in nanopores: an examination of hydrodynamic boundary conditions, *J. Chem. Phys.*, **115**, 3878, 2001.
- [61] G. Arya, H. Chang and E. Maginn, Knudsen diffusivity of a hard sphere in a rough slit pore, *Phys. Rev. Lett.*, **91**(2), 026102, July 2003.
- [62] E. Clementi, Global scientific and engineering simulations on scalar, vector and parallel LCAP-type supercomputers, *Phil. Trans Roy. Soc. A*, **326**, 445–470, 1988.
- [63] K. G. Wilson and J. B. Kogut, The renormalization group and the expansion, *Phys. Rep.*, **12**, 77–199, 1974.
- [64] E. B. Tadmor, M. Ortiz and R. Phillips. Quasicontinuum analysis of defects in crystals, *Phil. Mag. A*, **73**, 1529–1563, 1996.
- [65] V. B. Shenoy, R. Miller, E. B. Tadmor, R. Phillips and M. Ortiz, Quasicontinuum models of interfacial structure and deformation, *Phys. Rev. Lett.*, **80**, 742, 1998.
- [66] V. B. Shenoy, R. Miller, E. B. Tadmor, D. Rodney, R. Phillips and M. Ortiz, An adaptive finite element approach to atomic-scale mechanics: the quasicontinuum method, *J. Mech. Phys. Solids*, **47**, 611, 1999.
- [67] D. Rodney and R. Phillips, Structure and strength of dislocation junctions: an atomic level analysis, *Phys. Rev. Lett.*, **82**, 1704, 1999.
- [68] R. Miller, M. Ortiz, R. Phillips, V. Shenoy and E. B. Tadmor. Quasicontinuum models of fracture and plasticity, *Eng. Frac. Mech.*, **61**, 427, 1998.
- [69] L. B. Lucy, A numerical approach to the testing of the fission hypothesis, *Astro. J.*, **82**, 1013–1024, 1977.
- [70] J. Feldman, *Dynamic Refinement and Boundary Contact Forces in Smoothed Particle Hydrodynamics with Applications in Fluid Flow Problems*, PhD Thesis, School of Engineering, Swansea University, June 2006.
- [71] J. J. Monaghan, Smoothed particle hydrodynamics, *ARAA*, **30**, 543–574, 1992.
- [72] E. Fasshauer. *Computer Methods in Applied Mechanics and Engineering*, **193**, (12–14), 1231–1243, 2004.
- [73] J. Liao and S. Yip, Coupling continuum to molecular dynamics simulation: reflecting particle method and the field estimator, *Phys. Rev. E*, **57**(6), 7259–7267, 1998.
- [74] S. Shen and S. Atluri. Computational nano-mechanics and multi-scale simulation, *CMC*, **1**(1), 59–90, 2004.
- [75] R. E. Rudd and J. Broughton, Coarse-grained molecular dynamics and the atomic limit of finite elements, *Phys. Rev. B*, **58**, 5893–5896, 1998.
- [76] L. Verlet, Computer experiments on classical fluids. I. Thermodynamical properties of Lennard-Jones molecules, *Phys. Rev.*, **159**, 98, 1967.
- [77] M. Sun and C. Ebner, Molecular dynamics simulation of compressible fluid flow in two dimensional channels, *Phys. Rev. A*, **46**(8), 4813–4818, October 1992.

- [78] C. W. Gear, The numerical integration of ordinary differential equations of various orders, Technical Report 7126, Argonne National Laboratory, 1966.
- [79] C. W. Gear, *Numerical Initial Value Problems in Ordinary Differential Equations*. Prentice-Hall, 1971.
- [80] S. Cooper, B. Cruden and M. Meyyappan, Gas transport characteristics through carbon nanotubes, *Nano Lett.*, **4**(2), 377–381, 2004.
- [81] S. K. Bhatia, H. Chen and D. S. Sholl. Comparisons of diffusive and viscous contributions to transport coefficients of light gasses in single walled carbon nanotubes, *Molecular Simulation*, **31**, 643–649, 2005.
- [82] V. Sokhan, D. Nicholson and N. Quirke, Fluid flow in nanopores: accurate boundary conditions for carbon nanotubes, *J. Chem. Phys.*, **117**(18), 8531–8539, 2002.
- [83] D. Evans, W. Hoover, B. Failor, B. Moran and A. Ladd, Non equilibrium molecular dynamics via Gauss's principle of least constraint, *Phys. Rev. A*, **28**(2), 1016–1020, 1983.
- [84] D. J. Evans and G. P. Morriss, *Statistical Mechanics of Non-equilibrium Liquids*, Theoretical Chemistry Monograph Series, Academic Press, London, 1990.
- [85] A. C. Branka and K. W. Wojciechowski, Generalisation of Nosé and Nosé–hoover isothermal dynamics, *Phys. Ref. E. Stat. Phys. Plasmas, Fluids and Related Interdiscipline Topics*, **62**(3, Part A), 3281–3292, September 2000.
- [86] S. Nose, Constant-temperature molecular dynamics, *J. Phys.: Cond. Mat.*, **2**, SA115–SA119, 1990.
- [87] S. Nosé, A unified formulation of the constant temperature dynamics methods, *J. Chem. Phys.*, **81**(1), 511–519, 1984.
- [88] M. Tuckerman and M. Parrinello, Integrating the Carpparrinello equations. I. Basic integration techniques, *J. Chem. Phys.*, **101**(2), 1302, 1994.
- [89] W. Smith, T. R. Forester, I. T. Todorov and M. Leslie, *The DL_POLY 2 User Manual*, vol. 2.16, CCLRC Daresbury Laboratory, Daresbury, Warrington, UK, March 2006.
- [90] G. H. L. Hagen, Ueber die bewegung des wassers in engen cylindrischen, rohren, *Poggendorfs Annalen der Physik und Chemie*, **16**, 1839.
- [91] H. Darcy, *Recherches Experimentales Relatives au Movement de Leau dans les Tuyaux*. Imprimerie Nationale, Paris, 1857.
- [92] U. S. Choi, Enhancing thermal conductivity of fluids with nano-particles, *Trans ASME Fluids Eng. Div. (Publication)*, **231**, 99–105, 1995.
- [93] R. J. Hunter, *Foundations of Colloid Science*, Vol. 1, Oxford University Press, 1985.
- [94] B. Chu, *Laser Light Scattering: Basic Principles and Practice*, 2nd Edition, Academic Press, London, 1991.
- [95] R. J. Hunter, *Zeta Potential in Colloid Science*, Academic Press, London, 1981.
- [96] W. R. Bowen, N. Hilal, R. W. Lovitt and C. J. Wright, Direct measurement of interactions between adsorbed protein layers using an atomic force microscope, *J. Coll. Interface Sci.*, **197**, 348–352, 1998.
- [97] W. R. Bowen, N. Hilal, R. W. Lovitt and C. J. Wrigh, A new technique for membrane characterisation: direct measurement of the force of adhesion of a single particle using an atomic force microscope, *J. Membr. Sci.*, **139**, 269–274, 1998.
- [98] W. R. Bowen and F. Jenner, Dynamic ultrafiltration model for charged colloidal dispersions: a Wigner–Seitz cell approach, *Chem. Eng. Sci.*, **50**, 1707–1736, 1995.

- [99] W. R. Bowen and P. M. Williams, The osmotic pressure of electrostatically stabilized colloidal dispersions, *J. Coll. Interface Sci.*, **184**, 241–250, 1996.
- [100] G. Scatchard, I. H. Scheinberg and S. H. Armstrong Jr, Physical chemistry of protein solutions. IV. The combination of human serum albumin with chloride ion. *J. Amer. Chem. Soc.*, **72**, 535–540, 1950.
- [101] E. Wignery and F. Seitz, On the constitution of metallic sodium, *Phys. Rev.*, **43**, 804–810, 1933.
- [102] B. W. Ninham and V. A. Parsegian, Electrostatic potential between surfaces bearing ionizable groups in ionic equilibrium with physiologic saline solution, *J. Theo. Bio.*, **31**, 405–428, 1971.
- [103] D. B. Hough and L. R. White, The calculation of Hamaker constants from Lifshitz theory with applications to wetting phenomena, *Adv. Coll. Interface Sci.*, **14**, 8–41, 1980.
- [104] H. C. Hamaker, The London–van der Waals attraction between spherical particles, *Physica*, **4**, 1058–1072, 1937.
- [105] W. R. Bowen and F. Jenner, The calculation of dispersion forces for engineering applications, *Coll. Interface Sci.*, **56**, 201–243, 1995.
- [106] N. F. Carnahan and K. E. Starling, Equation of state for nonattracting rigid spheres. *J. Chem. Phys.*, **51**, 635–636, 1969.
- [107] K. R. Hall, Another hard-sphere equation of state, *J. Chem. Phys.*, **51**, 2252–2254, 1972.
- [108] X. Cao, *Colloid and Interface Aspects of Ultrafiltration*, PhD Thesis, 1999.
- [109] R. L. Merson and A. I. Morgan, Juice concentration by reverse osmosis, *Food Technology*, **22** 631–634, 1968.
- [110] H. Nabetani, M. Nakajima, A. Watanabe, S. Ikeda, S. Nakao and S. Kimura, Development of a new type of membrane osmometer, *J. Chem. Eng. Japan*, **251**, 269–274, 1992.
- [111] V. L. Vilker, C. K. Colton and K. A. Smith, The osmotic pressure of concentrated protein solutions: effect of the concentration and pH in saline solutions of bovine serum albumin, *J. Coll. Interfaces Sci.*, **79**, 548–566, 1981.
- [112] S. C. Chapra and R. P. Canale, *Numerical Methods for Engineers*. McGraw-Hill, Singapore, 1989.
- [113] W. R. Bowen and P. M. Williams, Obtaining the osmotic pressure of electrostatically stabilized colloidal dispersions from frontal ultrafiltration experiments, *J. Coll. Interface Sci.*, **233**, 159–163, 2001.
- [114] W. R. Bowen, X. Cao and P. M. Williams, Use and elucidation of biochemical data in the prediction of the membrane separation of biocolloids, *Proc. Roy. Soc. Lond. Series A—Mathematical, Physical and Engineering Sciences*, **455**, 2933–2955, 1999.
- [115] W. R. Bowen, P. M. Williams and J. Wilson, Quantifying extra interaction forces in charged colloidal dispersions from frontal ultrafiltration experiments, *Coll. Surf. A*, **231**, 67–83, 2003.
- [116] E. J. W. Verwey and J. Th. G. Overbeek, *Theory of the Stability of Lyophobic Colloids*, Elsevier, Amsterdam, 1948.
- [117] D. N. Petsev and N. D. Denkov, Diffusion of charged colloidal particles at low volume fraction: theoretical model and light scattering experiments, *J. Coll. Interface Sci.*, **149**, 329–344, 1992.

- [118] U. Genz and R. Klein, Collective diffusion of charged spheres in the presence of hydrodynamic interaction, *Physica A*, **171**, 26–42, 1991.
- [119] S. Walrand, L. Belloni and M. Drifford, Diffusion in concentrated micellar and hard sphere solutions, *J. Physique*, **47**, 1565–1576, 1986.
- [120] W. R. Bowen and A. Mongrue, Calculation of the collective diffusion coefficient of electrostatically stabilised colloidal particles, *Coll. Surf. A*, **138**, 161–172, 1998.
- [121] J. L. Anderson, F. Rauth and A. Morales, Particle diffusion as a function of concentration and ionic strength, *J. Phys. Chem.*, **82**, 608–616, 1978.
- [122] J. A. Quinn, C. H. Lin and J. L. Anderson, Measuring diffusion coefficients by Taylor's method of hydrodynamic stability, *AIChE Journal*, **32**, 2028–2033, 1986.
- [123] S. M. Selim, M. A. Al-Naafa and M. C. Jones, Brownian diffusion of hard spheres at finite concentrations, *AIChE Journal*, **39**, 3–16, 1993.
- [124] A. D. Cadman, R. Fleming and R. H. Guy, Diffusion of lysozyme chloride in water and aqueous potassium chloride solutions, *Biophys. J.*, **37**, 569–574, 1981.
- [125] E. L. Cussler, *Diffusion–Mass Transfer in Fluid System*, 2nd edition, Cambridge University Press, 1997.
- [126] D. E. Koppel, Analysis of macromolecular polydispersity in intensity correlation spectroscopy: the method of cumulants, *J. Chem. Phys.*, **57**, 4814–4820, 1972.
- [127] W. R. Bowen, Y. Liang and P. M. Williams, Gradient diffusion coefficients—theory and experiment, *Chem. Eng. Sci.*, **55**, 2359–2377, 2000.
- [128] R. H. Ottewill and R. A. Richardson, Studies of particle–particle interactions using polystyrene lattices and time average–average light scattering, *Coll. Poly. Sci.*, **260**, 708–719, 1982.
- [129] G. K. Batchelor, Brownian diffusion of particles with hydrodynamic interaction, *J. Fluid Mech.*, **741**, 1–29, 1976.
- [130] W. B. Russel, D. A. Saville and W. R. Schowalbe, *Colloidal Dispersions*, Cambridge University Press, 1989.
- [131] G. K. Batchelor, Sedimentation in a dilute dispersion of spheres, *J. Fluid Mech.*, **52**, 245–268, 1972.
- [132] J. A. Barker and D. Henderson, Perturbation theory and equation of state for fluids. II. A successful theory of liquids, *J. Chem. Phys.*, **47**, 4714–4721, 1967.
- [133] I. M. Krieger, Rheology of monodisperse lattices, *Adv. Coll. Interface Sci.*, **3**, 111–136, 1972.
- [134] F. Booth, The electroviscous effect for suspensions of solid spherical particles, *Proc. Roy. Soc. Lond. Series A—Mathematical, Physical and Engineering Sciences*, **203**, 533–551, 1950.
- [135] C. Allain, M. Cloitre, B. Lacoste and I. Marsone, Viscosity renormalization in colloidal suspensions, *J. Chem. Phys.*, **100**, 4537–4542, 1994.
- [136] W. R. Bowen and P. M. Williams, Prediction of the rate of cross-flow ultrafiltration of colloids with concentration-dependent diffusion coefficient and viscosity—theory and experiment, *Chem. Eng. Sci.*, **56**, 3083–3099, 2001.
- [137] A. A. Kozinski and E. N. Lightfoot, Protein ultrafiltration: a general example of boundary layer filtration, *AIChE Journal*, **18**, 1030–1040, 1972.
- [138] H. A. Barnes, J. F. Hutton and K. Walters, *An Introduction to Rheology*, Elsevier, 1989.
- [139] D. M. Heyes, Non-Newtonian behaviour of simple liquids, *J. Non-Newtonian Fluid Mech.*, **21**, 137–155, 1986.

- [140] W. R. Bowen and P. M. Williams, Dynamic ultrafiltration model for proteins: a colloidal interaction approach, *Biotech. Bioeng.*, **50**, 125–135, 1996.
- [141] J. Happel, Viscous flow in multiparticle systems: slow motion of fluids relative to beds of spherical particles, *AIChE Journal*, **41**, 197–201, 1958.
- [142] J. M. Kay and R. M. Nedderman, *Fluid Mechanics and Transfer Processes*, Cambridge University Press, 1985.
- [143] R. H. Davis and J. D. Sherwood, A similarity solution for steady-state crossflow microfiltration, *Chem. Eng. Sci.*, **45**, 3203–3209, 1990.
- [144] S. Ilias and R. Govind, A study on concentration polarization in ultrafiltration, *Separation Science and Technology*, **28**, 361–381, 1993.
- [145] S. Ilias, K. A. Schimmel and G. E. J. M. Assey, Effect of viscosity on membrane fluxes in cross-flow ultrafiltration, *Separation Science and Technology*, **30**, 1669–1687, 1995.
- [146] W. R. Bowen, A. Mongruel and P. M. Williams, Prediction of the rate of cross-flow membrane ultrafiltration: a colloidal interaction approach, *Chem. Eng. Sci.*, **51**, 4321–4333, 1996.
- [147] D. H. Trevena, *Cavitation and Tension in Liquids*, Adam Hilger, Bristol, 1987.
- [148] C. E. Brennen, *Cavitation and Bubble Dynamics*, Oxford University Press, 1995.
- [149] D. Dowson and C. M. Taylor, Cavitation in bearings, *Ann. Rev. Fluid Mech.*, **11**, 35–66, 1979.
- [150] Y. H. Zang, J. S. Aspler, M. Y. Boluk and J. H. De Grace, Direct measurement of tensile stress ('tack') in thin ink films, *J. Rheol.*, **35**, 345–361, 1991.
- [151] A. Unsworth, D. Dowson and V. Wright, Cracking joints. A bioengineering study of cavitation in the metacarpophalangeal joint, *Ann. Rheum. Dis.*, **30**, 348–358, 1971.
- [152] H. Spikes, The borderline of elastohydrodynamic and boundary lubrication, *Proc. Instn Mech. Engrs, Part C: J. Mechanical Engineering Science*, **214(1)**, 23–37, 2000
- [153] M. T. Tyree, The cohesion-tension theory of sap ascen, *J. Expl Bot.*, **48**, 1753–1765, 1997.
- [154] H. Lakrouf, P. Sergot and C. Cretan, Direct observations of cavitation and fibrillation in a probe tack experiment on model acrylic pressure sensitive adhesive, *J. Adhesion*, **69**, 307–359, 1999.
- [155] G. J. C. Braithwaite and G. H. McKinley, Microrheometry for studying the rheology and dynamics of polymers near interfaces, *J. Appl. Rheol.*, **9**, 27–33, 1999.
- [156] A. Zosel, The effect of fibrillation on the tack of pressure sensitive adhesives, *Int. J. Adhesion and Adhesives*, **18**, 265–271, 1998.
- [157] H. Strasburger, Tacky adhesion, *J. Colloid. Sci.*, **13**, 218–231, 1958.
- [158] W. H. Banks and C. C. Mill, Tacky adhesion—a preliminary study, *J. Coll. Sci.*, **8**, 137–147, 1953.
- [159] A. Ouibrahim, D. H. Fruman and R. Gaudemer, Vapor cavitation in very confined spaces for Newtonian and non-Newtonian fluids, *Phys. Fluids*, **8**, 1964–1971, 1996.
- [160] T. Narumi and T. Hasegawa, Experimental study on the squeezing flow of viscoelastic fluids. 1. The effect of liquid properties on the flow between a spherical surface and a flat plate, *Bull. JSME*, **29**, 3731–3736, 1986.
- [161] D. D. Joseph, Cavitation and the state of stress in a flowing liquid, *J. Fluid Mech.*, **366**, 367–378, 1998.

- [162] K. H. Christenson and P. M. Claesson, Cavitation and the interaction between macroscopic hydrophobic surfaces, *Science*, **239**, 390–392, 1988.
- [163] J. C. Fisher, The fracture of liquids, *J. Appl. Phys.*, **19**, 1062–1067, 1948.
- [164] R. J. Speedy, Stability-limit conjecture. An interpretation of the properties of water, *J. Phys. Chem.*, **86**, 982–991, 1982.
- [165] Q. Zheng, D. J. Durben, G. H. Wolf and C. A. Angell, Liquids at large negative pressure: water at the homogeneous nucleation limit, *Science*, **254**, 829–832, 1991.
- [166] H. Maris and S. Balibar, Negative pressures and cavitation in liquid helium, *Phys. Today*, **53** 29–34, 2000.
- [167] P. G. Debenedetti, *Metastable Liquids: Concepts and Principles*, Princeton University Press, 1996.
- [168] D. R. Berard, P. Attard and G. N. Patey, Cavitation of a Lennard–Jones fluid between hard walls, and the possible relevance to the attraction measured between hydrophobic surfaces, *J. Chem. Phys.*, **98**, 7236–7244, 1993.
- [169] P. Attard, Bridging bubbles between hydrophobic surfaces, *Langmuir*, **12**, 1693–1695, 1996.
- [170] J. L. Parker, P. M. Claesson and P. Attard, Bubbles, cavities and the long-ranged attraction between hydrophobic surfaces, *Phys. Chem.*, **98**, 8468–8480, 1994.
- [171] Y. L. Chen, T. Kuhl and J. Israelachvili, Mechanism of cavitation damage in thin liquid films: collapse damage vs. inception damage, *Wear*, **153**, 31–51, 1992.
- [172] T. Kuhl, M. Ruths, Y. L. Chen and J. Israelachvili, Direct visualisation of cavitation and damage in ultrathin liquid films, *J. Heart Valve Disease*, **3**, 117–127, 1994.
- [173] Lord Rayleigh, On the pressure developed in a liquid during the collapse of a spherical cavity, *Phil. Mag.*, **34**, 94–98, 1917.
- [174] M. S. Plessett and A. Prosperetti, Bubble dynamics and cavitation, *Ann. Rev. Fluid Mech.*, **9**, 145–185, 1977.
- [175] J. R. Blake and D. C. Gibson, Growth and collapse of a vapour cavity near a free surface, *Fluid Mech. I*, **11**, 123–140, 1981.
- [176] T. B. Benjamin and A. T. Ellis, The collapse of cavitation bubbles and the pressures thereby produced against solid boundaries, *Phil. Trans. R. Soc. A*, **260**, 221–240, 1966.
- [177] T. G. von Leeuwen, J. H. Meertens, E. Velema, M. J. Post and C. Borst, Intraluminal vapor bubble induced by excimer laser pulse causes microsecond arterial dilation and invagination leading to extensive wall damage in the rabbit, *Circulation*, **87**, 1258–1263, 1993.
- [178] R. Vorreuther, R. Corleis, T. Klotz, P. Bernards and U. Engelmann, Impact of shock wave pattern and cavitation bubble size on tissue damage during ureteroscopic electrohydraulic lithotripsy, *J. Urol. (Baltimore)*, **153**, 849–853, 1995.
- [179] P. Zhong, I. Cionta, S. Zhu, F. H. Cocks and G. M. Preminger, Effects of tissue constraint on shock wave-induced bubble expansion *in vivo*, *J. Acoust. Soc. Am.*, **104**, 3126–3129, 1998.
- [180] G. Binnig, C. F. Quate and G. Gerber, Atomic force microscope, *Phys. Rev. Lett.*, **56**, 930–933, 1986.
- [181] J. Domke and M. Radmacher, Measuring the elastic properties of thin polymer films with the atomic force microscope, *Langmuir*, **14**, 3320–3325, 1998.

- [182] D. Drakova, Theoretical modelling of scanning tunnelling microscopy, scanning tunnelling spectroscopy and atomic force microscopy, *Rep. Prog. Phys.*, **64**, 205–290, 2001.
- [183] W. R. Bowen, N. Hilal, R. W. Lovitt A. O. Sharif and P. M. Williams, Atomic force microscope studies of membranes: force measurement and imaging in electrolyte solutions, *J. Membr. Sci.*, **126**, 77–89, 1997.
- [184] W. R. Bowen, N. Hilal, R. W. Lovitt and C. J. Wright, Direct measurement of the adhesion of a single biological cell using atomic force microscopy, *Coll. Surf. A: Physicochem. Eng. Aspects*, **136**, 231–234, 1998.
- [185] M. C. Friedenbergl and C. M. Mate, Dynamic viscoelastic properties of liquid polymer films studied by atomic force microscopy, *Langmuir*, **12**, 6138–6142, 1996.
- [186] W. A. Ducker, T. J. Senden and R. M. Pashley, Measurement of forces in liquids using a force microscope, *Langmuir*, **8**, 1831–1836, 1992.
- [187] M. S. Barrow, W. R. Bowen, N. Hilal, A. Al-Hussany, P. R. Williams, R. L. Williams and C. Wright, A study of the tensile properties of thin fluid films in an atomic force microscope, *Proc. Roy. Soc. A: Mathematical and Physical Sciences*, **459**, 2885–2908, 2003.
- [188] J. E. Sader, I. Larson, P. Mulvaney and L. R. White, Method for the calibration of atomic force microscope cantilevers, *Rev. Sci. Instrum.*, **66**, 3789–3798, 1995.
- [189] P. R. Williams and R. L. Williams, On anomalously low values of the tensile strength of water, *Proc. Roy. Soc. A*, **456**, 1321–1332, 2000.
- [190] Y. L. Chen and J. Israelachvili, New mechanism of cavitation damage, *Science*, **252**, 1157–1160, 1991.
- [191] A. R. Suraya, P. F. Luckham and C. J. Lawrence, Shear thinning and frequency dependent behaviour of adsorbed polymer layers: Part I. Experimental aspects and a first order analysis, *J. Non-Newtonian Fluid Mechanics*, **148**, 57–64, 2008.

Index

- Adsorption 38–39
Atomic force microscope 161, 194–196,
199–201
Attractive interaction energy 163
- Backward Euler method 71
Basis functions 89, 95
Bernoulli equation 11
Bin averaging scheme 82
Boltzmann constant 4
Boltzmann distribution 4, 26–27, 97, 99,
135
Boltzmann equation 54
Boltzmann ergodic hypothesis 20
Boltzmann factor 24, 27–28
Boltzmann's constant 173
Bottom up meso scale methods 55, 96
Boundary condition 15, 50, 57, 150, 162,
186, 188
Boundary condition - diffuse 59, 68, 75,
119, 122, 133, 150
Boundary condition - periodic 21, 57, 105,
110, 121, 133, 144, 147, 204
Boundary condition - slip and no slip 47,
77, 133, 188
Boundary layer 103, 152, 154, 186
Bravais lattice vectors 62
Brownian diffusion coefficient 173, 178
Brownian motion 160, 172
- Canonical ensemble 21
Carbon nanotubes 25, 38, 59, 78
Cauchy plot 163
Cavitation 190–194, 199
Chapman - Enskog distribution 52
Characteristic length 3, 9, 16, 47–49
Clausius equation 18
Coarse grained molecular dynamics 64
Coefficient of viscosity 7
Collision radius 49, 55, 121, 152
Colloidal interactions 159, 161, 179
Compressible flow 106
Computational fluid dynamics 11
Computational time 143
Consistency condition 92
Continuity equation 12
Continuum approximations 8–11, 16,
46–50, 55, 132
Continuum limit 46
Convective - diffusive transport 188
Coulomb repulsion 171
Critical point 40
- Darcy law 132
Debye - Hückel parameter 171
Density 2, 3, 11, 94, 144–147
Density - electronic 17
Deryaguin - Landau - Verwey - Overbeek
theory 170

- Desorption 40
- Direc's delta function 93
- Direct numerical simulation 130
- Direct simulation Monte Carlo model 51
- Dissipative particle dynamics 54
- Dynamic light scattering 173

- Effective diffusion coefficient 176
- Electrophoretic mobility measurements 160, 161
- Electroviscous effect 179
- Euler equations 52
- Eulerian approach 53

- Field autocorrelation function 175
- Finite difference method 13, 70, 188
- Finite element method 14, 50, 57, 60–62
- Finite volume method 15
- Force 4, 5, 6
- Force - body 13
- Force - cohesive 8
- Force - configurational 162
- Force - dispersion 161
- Force - drag 7, 130, 178
- Force - driving 104, 112, 134, 136, 185
- Force - electrostatic 160–161
- Force - frictional 7, 131
- Force - hydrodynamic 201
- Force - inertial 7, 9
- Force - interaction 17
- Force - London 17, 55, 160, 162
- Force - Pauli 18, 55
- Force - van der Waals 16, 55, 160, 162
- Force - viscous dissipation 11
- Friction factor 49, 107

- Gaussian isokinetic equations of motion 107–108
- Gaussian Thermostat 106, 122
- Gauss's principle of least constraint 106
- Gouy - Chapman - Grahame - Stern model 161
- Gradient diffusion coefficient 159, 172–180
- Grand canonical ensemble 22

- Hagen - Poiseuille flow 131
- Happel's permeability coefficient 186
- Hard sphere model 25, 32, 178, 179, 180
- Helmholtz plane 161
- Hydrodynamic interaction coefficient 178
- Hysteresis loop 39–43

- Interaction potential 179
- Isobaric Isothermal ensemble 21

- Kinetic energy 3–6, 8, 28, 36, 75, 97, 99–100, 108, 137
- Knudsen number 47–48

- Lagrangian approach 53
- Laminar flow 128, 130, 137, 186–187
- Large eddy simulation 130
- Lattice Boltzmann method 54
- Lennard - Jones equation 18
- Lennard - Jones potential 35, 55–57, 68, 70, 97, 110, 121, 133, 152
- Lifshitz - Hamaker constant 163
- Lorenz - Barthelot mixing rules 59, 122, 133

- Maxwell - Boltzmann distribution 28–29, 52, 76–77, 80, 116, 123
- Maxwell slip model 48
- Mean free path 46, 48
- Membrane filtration 184
- Membrane separation 159, 184
- Metastable state 193
- Methane molecules 110, 121, 152
- Micro channel liquid flow 49
- Micro electrophoresis 160
- Microcanonical ensemble 20
- Microhydrodynamics 159
- Molecular dynamics simulation 25, 55, 57, 68, 97, 110, 119, 171
- Molecular frequency scale 49
- Momentum 4, 11–12, 19, 34, 95
- Momentum accommodation coefficient 48, 76, 78, 80, 119, 122, 133
- Monte Carlo simulation 19, 22–23, 37
- Moving least squares method 63, 82, 86–92

- Nano fluids 159, 161, 165, 189
 Nano-particle concentration 168
 Navier - Stokes equations 11–13, 51–53
 Newton - Raphson method 109
 Newtonian fluid 7, 131
 Newtons law 19, 54, 70, 73, 97, 107
 Newtons law of viscosity 7
 Nose' - Hoover Thermostat 108, 134

 Order parameter 30
 Osmometers 164
 Osmotic pressure 159, 161, 163–174, 178, 179

 Pade' approximation of Hall 163
 Particle - particle interactions 171, 178, 184, 186
 Permittivity of vacuum 171
 Phase change 36
 Photon correlation spectroscopy 160, 173, 180
 Point interpolation methods 93
 Poiseuille flow 121, 133, 137, 188
 Poisson - Boltzmann equation 161–162, 172
 Potential energy 97, 99–101
 Prandtl number 48
 Predictor - corrector algorithm 71, 186
 Pressure 4, 6, 11, 18, 101
 Pressure driven flows 105, 128, 133–136, 152
 Properties - continuum or bulk 2–3, 81–82, 95, 110, 114, 118, 135

 Quasi continuum method 60–61

 Rayleigh collapse 194
 Reflecting particle method 105
 Refractive index data 163
 Reynolds averaged Navier - Stokes method 130
 Reynolds number 9, 49, 130, 155

 Self diffusion coefficient 173
 Shear force 2

 Shear thinning 202
 Smooth particle hydrodynamics 54, 63, 82–85
 Soft sphere model 25, 32, 35, 68, 78, 97
 Specific heat ratio 48
 Steric interactions 160
 Stokes - Einstein equation 173, 178–179
 Stokes' law 178
 Strain rate 49
 Surface force apparatus 199

 Taylor series approximation 71–73, 85
 Taylor's theorem 167
 Temperature control 99, 106, 108, 110, 111, 119
 Temperature 3–8, 11, 18, 28, 94, 119
 Temperature - melting 36
 Thermal accomodation coefficient 48
 Thermal diffusion 110
 Thermodynamic coefficient 178
 Thermodynamic equilibrium 10
 Time step 74, 112
 Top down meso scale methods 50
 Tracer diffusion coefficient 173
 Turbulent flow 129, 132, 138

 Ultrafiltration processes 161, 166, 168, 170, 185

 van der Waals equation 18
 Verlet equations of motion 108
 Verlet lists and algorithms 68–74, 97, 109
 Visco-elasticity 191, 201–202
 Viscometers 181
 Viscosity 1, 6, 8, 9, 12, 130, 159, 161, 180–184
 Viscosity - dynamic 7
 Viscosity - kinematic 7

 Wall boundaries 59
 Weighting function 92, 95, 108, 110, 116, 118, 152
 Wigner - Seitz cell model 162

 Zeta potential 160, 161, 172, 189